once a dopant atom reaches the grain boundary it does not diffuse back into the grain); the diffusivity of the dopant is only a function of temperature and does not vary with concentration.

In order to treat the grain boundaries as a perfect sink for the dopant, we set the boundary condition $C(R_0) = C_e$ for all t, where C_e is the equilibrium dopant concentration at the annealing temperature (which is several orders of magnitude below the initial dopant concentration); the dopant concentration in the grain will not drop below this value during the anneal. We make an additional assumption that the equilibrium dopant concentration is not sufficient to bring about enhanced broadband infrared absorption, which is consistent with research on silicon doped with chalcogens at or below the equilibrium concentration [80]. Because the concentration in the grain will not decrease below C_e, we treat this value as a background concentration and express our concentration profile as $\tilde{C}(r,d) = C(r,d) - C_e$.

With these assumptions the concentration profile, $\tilde{C}(r)$, in the grain is given by

$$\tilde{C}(r,d) = -\frac{2R_0\tilde{C}_0}{\pi r}\sum_{n=1}^{\infty}\frac{(-1)^n}{n}\sin\left(\frac{n\pi r}{R_0}\right)\exp\left(-\left(\frac{n\pi d}{R_0}\right)^2\right), \tag{4.1}$$

where $\tilde{C}(r,d) = C(r,d) - C_e$ is the increased concentration above the equilibrium value at a distance r from the center of the sphere after a thermal anneal that produces a dopant diffusion length of $d = \sqrt{Dt}$. $\tilde{C}_0 = C_0 - C_e$ is the initial increased concentration above the equilibrium value. Equation 4.1, divided by $\tilde{C}_0$, is equivalent to 1 minus the equation for $C(r,d)/C_0$ for a sphere that is absorbing solute from a large volume of well-stirred liquid with a fixed concentration of C_0 (Chapter 6 of reference [107]).

We can determine the number of dopant atoms, $\tilde{N} = N - N_e$, above the equilibrium value in the sphere after a thermal anneal with diffusion length, d, by integrating Equation 4.1 over the volume of the sphere,

SIONYX1403000043.0045

SAMSUNG EX. 1002 - 688/4148

$$\tilde{N}(d) = \int_0^{R_0} \tilde{C}(r,d) 4\pi r^2 dr. \tag{4.2}$$

Then we can divide by the initial number of dopant atoms in the sphere that exceeded the equilibrium value, $\tilde{N}_0 = \frac{4}{3}\pi R_0^3 \tilde{C}_0$, to obtain the fraction, $\tilde{N}/\tilde{N}_0$, of supersaturated dopant atoms remaining in the sphere after annealing (a unit-less number between 1 and 0),

$$\frac{\tilde{N}(d)}{\tilde{N}_0} = \frac{\int_0^{R_0} \tilde{C}(r,d) 4\pi r^2 dr}{\frac{4}{3}\pi R_0^3 \tilde{C}_0}. \tag{4.3}$$

After integration the result is,

$$\frac{\tilde{N}(d)}{\tilde{N}_0} = \frac{6}{\pi^2} \sum_{n=1}^{\infty} \frac{1}{n^2} \exp\left(-\left(\frac{n\pi d}{R_0}\right)^2\right). \tag{4.4}$$

This equation is only a function of diffusion length, d, and the radius of the sphere, R_0. Equation 4.4 is plotted versus diffusion length in Figures 4.4 and 4.5 for six radii, R_0, (5, 10, 20, 40, 80, and 160 nm).

4.5.2 Comparison to diffusion theory

The six curves in Figure 4.4 were calculated with Equation 4.4 using radii that are similar to the grain sizes of femtosecond laser irradiated silicon [46]. In spite of the simplicity of our theoretical model, agreement is quite good. The theory and data agree well in general shape and order of magnitude for all three dopants. Our model does not take into account the possibility of grain growth, changes in diffusivity with concentration, or a change in activation energy when diffusing from the grain to the grain boundary. Below we discuss the deviations between the data and our theoretical model and speculate on possible explanations.

At large diffusion lengths (> 100 nm), the infrared absorptance of sulfur-doped samples begins to increase. This increase is also exhibited by samples irradiated in N_2 and

SIONYX1403000043.0046

SAMSUNG EX. 1002 - 689/4148

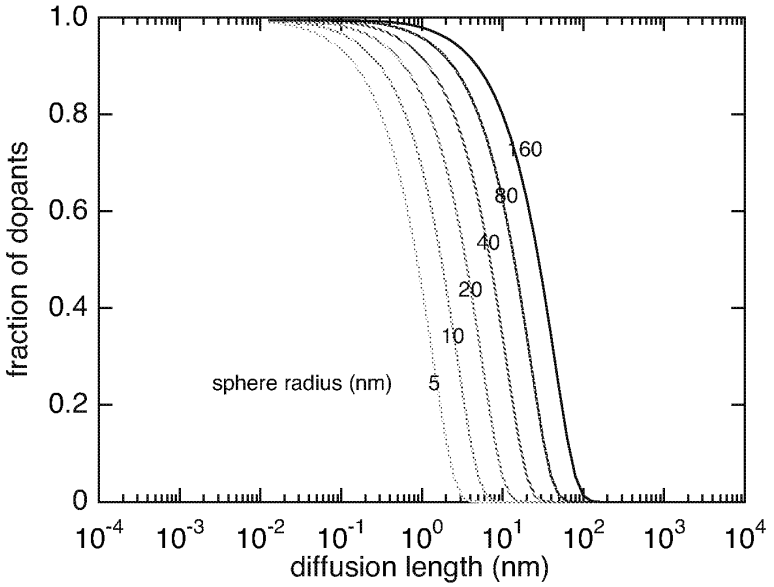


Figure 4.5: Plot of Equation 4.4, the fraction of supersaturated dopant atoms remaining inside a sphere of radius, R_0, versus diffusion length.

untreated silicon wafers after annealing. The cause of this increase is not known, but it is related to the original substrate and not the presence of the sulfur dopants. The samples annealed at high temperatures could have absorbed contamination from the vacuum furnace altering their infrared absorptance. This factor is likely to contribute to the deviation of selenium-and tellurium-doped samples from the theory by slowing their decrease in absorptance.

At small diffusion lengths, the absorptance data does not fall as fast as the theory curves and this deviation increases as diffusion length increases. One potential reason for this behavior is buildup of dopants at the grain boundaries. As more dopants diffuse from the crystalline grains to the grain boundaries, less space will be available causing diffusion from the grains to be increasingly more difficult. We can estimate the number of dopants that can fit in the free space available at the grain boundary as,

SIONYX1403000043.0047

SAMSUNG EX. 1002 - 690/4148

$$N_{GB} = \frac{1}{2}\rho_i a(4\pi R_0^2), \tag{4.5}$$

where ρ_i is the atomic density of the dopant (on the order of 3–4 $\times 10^{22}$ cm^{-3} for sulfur, selenium, and tellurium), a is the width of the grain boundary (on the order of the lattice parameter of silicon, 5.4 $\times 10^{-8}$ cm), and $4\pi R_0^2$ is the surface area of the grain. The factor of 1/2 indicates that each grain boundary is shared by two grains. We compare this value to the number of dopant atoms in the grain which can be expressed as,

$$N_G = \frac{4}{3}\pi R_0^3 C_i, \tag{4.6}$$

where C_i is the dopant concentration ($\sim 5 \times 10^{20} cm^{-3}$) and $\frac{4}{3}\pi R_0^3$ is the volume of the grain. For a grain size of $R_0 = 10$ nm, N_G/N_{GB} is 0.16. This value will increase as grain size increases. For a grain size of $R_0 = 60$ nm, N_G/N_{GB} is already greater than 1, indicating that buildup at the grain boundaries could slow diffusion for grains of this size and larger for concentrations on the order of 1 atomic %.

The infrared absorptance of the tellurium-doped samples decreases less steeply than the sulfur- and selenium-doped samples. The explanation for this behavior could be related to the diffusion path of each dopant. In single crystal silicon, tellurium atoms diffuse almost entirely substitutionally through the lattice while sulfur and selenium atoms diffuse both interstitially and substitutionally [90]. A theoretical study predicts that a high concentration of point defects (vacancies and self-interstitials) would become trapped during resolidification after femtosecond laser irradiation due to the high velocity of the resolidification front [108]. The greater concentration of defects in the nanocrystalline grains would allow for more substitutional diffusion of tellurium, effectively increasing its diffusivity. The increased number of defects could allow tellurium to also diffuse interstitially as well, lowering the activation energy of diffusion. The diffusion of sulfur and selenium may not be

SIONYX1403000043.0048

SAMSUNG EX. 1002 - 691/4148

affected by the presence of defects as they already diffuse much quicker and only partially along a subsitutional path. If the actual diffusivity of tellurium were larger and the actual activation energy lower, the data in Figure 4.4 would shift to the right and the slope would increase; both of these corrections would be in the right direction to bring the tellurium data in line with the sulfur and selenium data.

4.5.3 Diffusion theory using a lognormal distribution of grains

In the previous section, our model assumed that all grains are the same size. A more realistic approximation is a lognormal distribution of grain sizes,

$$y(R_0) = y_0 + A \exp\left(-\left(\frac{\ln(R_0/p)}{w}\right)^2\right), \tag{4.7}$$

where y is the number of grains with radius, R_0; p is the peak radius with height, A, and width, w; and y_0 is an offset that can account for the lognormal distribution approaching a nonzero value at large grain sizes. y_0 can also be thought of as a background number of grains present at all sizes.

In order to take a lognormal distribution of grain sizes into account, we perform a summation of theory curves calculated from Equation 4.4 for grain sizes ranging from $R_0 = 1$ to 5000 nm at 1 nm increments. The summation is weighted by volume,

$$\left(\frac{\tilde{N}(d)}{\tilde{N}_0}\right)_{lognormal} = \frac{\sum_{R_0=1}^{5000}\left(\frac{\tilde{N}(d)}{\tilde{N}_0}\right)_{R_0} y(R_0)(\frac{4}{3}\pi R_0^3)}{\sum_{R_0=1}^{5000} y(R_0)(\frac{4}{3}\pi R_0^3)}. \tag{4.8}$$

where $y(R_0)$ is the number of grains with radius, R_0, and $\left(\frac{\tilde{N}(d)}{\tilde{N}_0}\right)_{R_0}$ is the fraction of supersaturated dopants remaining in a sphere of radius, R_0, as a function of diffusion length. The sum, $\sum_{R_0=1}^{5000} y(R_0)(\frac{4}{3}\pi R_0^3)$, is the total volume of all the grains in the lognormal distribution.

SIONYX1403000043.0049

SAMSUNG EX. 1002 - 692/4148

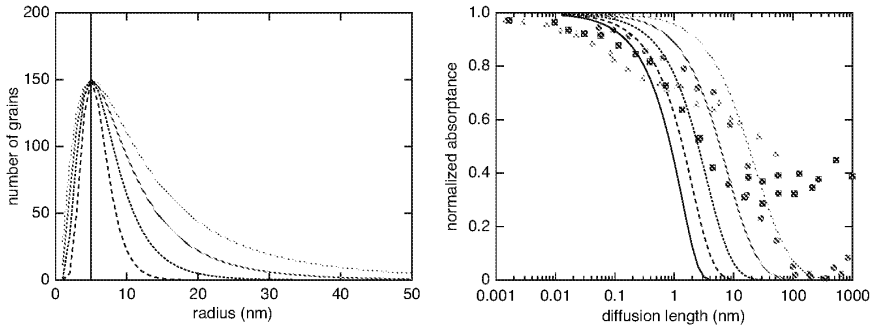


Figure 4.6: *Left:* Several log normal grain size distributions with $A = 150$, $p = 5$ nm, $y_0 = 0$ and $w = 0.5$, 0.75, 1 and 1.25. The solid black line indicates a monodisperse distribution of $R_0 = 5$ nm grains. *Right:* Plot of Equation 4.8 for the five distributions in the graph on the left.

Equation 4.8 is plotted in Figure 4.6 for a monodisperse distribution of 5-nm radius grains and four lognormal distributions with $A = 150$, $p = 5$ nm, $y_0 = 0$ and $w = 0.5$, 0.75, 1 and 1.25. As the width, w, of the lognormal distribution increases, the slope of the curve becomes smaller, more closely matching the slope of the data. This result is reasonable as larger grains will lose dopants slower than smaller grains; therefore, adding larger grains to the distribution decreases the slope of the fraction of supersaturated dopants remaining in the grains versus diffusion length.

Figure 4.7 shows the effect of adding a small offset, y_0, or background to one of lognormal distributions in Figure 4.6 ($A = 150$, $p = 5$ nm, and $w = 0.5$). The result is very sensitive to the magnitude of the background as the curve changes significantly for offsets ranging from $\sim 6 \times 10^{-7}$ to 4×10^{-5} of the peak value ($A = 150$ grains). Adding a background magnifies the effect of adding larger grains to the distribution. In Figure 4.7, the summation in Equation 4.8 is only performed from $R_0 = 1$ nm to 200 nm, as this more closely approximates the grain sizes observed in the resolidified surface layer. When $y_0 = 0$, the curve is similar to Equation 4.4 for $R_0 = 5$ nm and as y_0 becomes very large, the

SIONYX1403000043.0050

SAMSUNG EX. 1002 - 693/4148

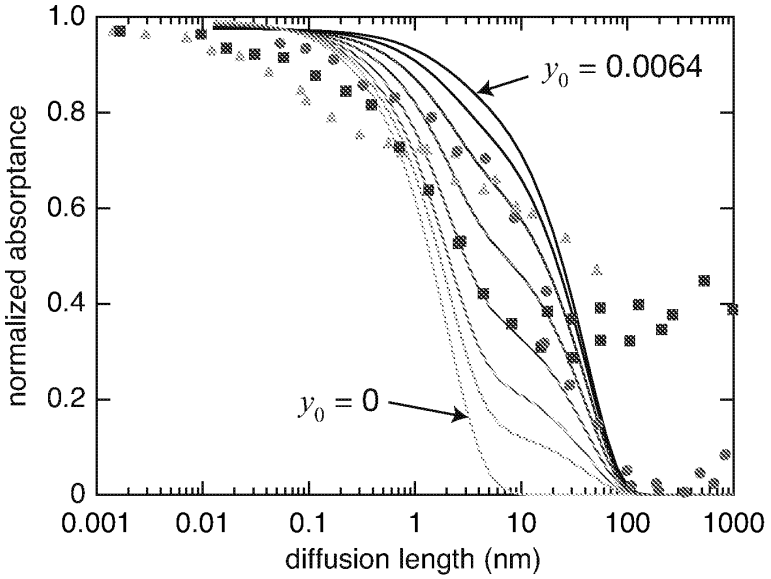


Figure 4.7: A comparison between the data and Equation 4.8 plotted for $A = 150$, $p = 5$ nm, $w = 0.5$ and $y_0 = 0$, 0.0001, 0.0002, 0.0004, 0.0008, 0.0016, 0.0032, and 0.0064. In this case, Equation 4.8 was summed over $R_0 = 1$ nm to 200 nm.

curve approximates Equation 4.4 for $R_0 = 200$ nm. From this analysis, we see that adding of a lognormal distribution of grains sizes to the theory further supports that diffusion of dopants to the grain boundaries is a plausible mechanism for the deactivation of infrared absorptance.

4.5.4 Diffusion theory with grain growth

At large diffusion lengths, the infrared absorptance of selenium-doped samples stops decreasing and levels off at 0.4 resulting in a marked departure from our model's prediction. In this section, we explore the effect that grain growth has on dopants diffusing to the grain boundaries. If the grain is growing, the dopants need to diffuse to a boundary that is moving away. If grain growth occurs at the same rate as diffusion or faster, it is

SIONYX1403000043.0051

SAMSUNG EX. 1002 - 694/4148

plausible that a concentration of dopant may become trapped in the grain. Actual grain size measurements before and after annealing would be needed to confirm that grain growth is responsible for the shape of the absorptance data of the selenium-doped samples.

In order to quantitatively assess the effect of grain growth on dopant diffusion we simplify the model for diffusion that we introduced in section 4.5.1. Equation 4.1 describes the concentration profile inside a grain if the grain boundary is treated as a perfect sink (at the grain boundary the concentration is held constant at C_e). To determine the new concentration profile, this boundary would need to move with the velocity of grain growth. In order to avoid complications with applying a moving boundary condition, we will assume the grain resides in an infinite medium with the same properties as the grain. This assumption reduces the grain boundary to an imaginary boundary, which can move with the velocity of grain growth without changing the shape of the concentration profile. Below we show that this assumption only slightly changes the shape and scale of the curves in Figure 4.5.

For a sphere of radius, R_0, and an initial uniform concentration, C_0 the concentration profile (from Chapter 3 of reference [107]) is given by,

$$C(r,d) = \frac{C_0}{2}\left\{\mathrm{erf}\left(\frac{R_0+r}{2d}\right) + \mathrm{erf}\left(\frac{R_0-r}{2d}\right)\right\}$$

$$-\frac{C_0}{r}\frac{d}{\sqrt{\pi}}\left\{\exp\left(\frac{-(R_0-r)^2}{4d^2}\right) - \exp\left(\frac{-(R_0+r)^2}{4d^2}\right)\right\}, \tag{4.9}$$

where C is the concentration at a distance, r, from the center of the sphere after a thermal anneal that results in a diffusion length of $d = \sqrt{Dt}$. We can determine the total number of dopant atoms, N, left in the imaginary sphere by integrating Equation 4.9 over the volume of the sphere,

SIONYX1403000043.0052

SAMSUNG EX. 1002 - 695/4148

$$N(d) = \int_0^{R_0} C(r,d) 4\pi r^2 dr. \tag{4.10}$$

Then we can divide by the number of dopant atoms initially in the sphere, $N_0 = \frac{4}{3}\pi R_0^3 C_0$, to obtain the fraction, N/N_0, of dopant atoms remaining in the sphere after annealing (a unit-less number between 1 and 0),

$$\frac{N(d)}{N_0} = \frac{\int_0^{R_0} C(r,d) 4\pi r^2 dr}{\frac{4}{3}\pi R_0^3 C_0}. \tag{4.11}$$

After integration the result can be simplified to,

$$\frac{N(d)}{N_0} = \frac{-2d}{\sqrt{\pi} R_0} + \operatorname{erf}\left(\frac{R_0}{d}\right) + \frac{d(R_0^2 - 2d^2)}{\sqrt{\pi} R_0^3}\left[\exp\left(\frac{-R_0^2}{d^2}\right) - 1\right]. \tag{4.12}$$

Equation 4.12 is plotted in Figure 4.8. We see that the result is very similar to Figure 4.5. The major difference is that the curves for the same size sphere have moved to larger diffusion lengths.

We now include grain growth. Normal grain growth [109] behaves the following equation,

$$R = \sqrt{R_0^2 + \alpha M t}, \tag{4.13}$$

where R is the radius after time, t; R_0 is the initial radius; M is the grain boundary mobility of the form $M_0 \exp(-Q/(kT))$ with a frequency of M_0 and an activation energy of Q; and α is a constant related to the grain boundary energy and geometric factors.

In order to include grain growth in our model, we assume the activation energy for the grain boundary mobility, Q, is approximately equal to the activation energy of diffusion of selenium, E_a. This approximation is valid as the value of Q has been reported [109,110] on the order of 2.4 eV. By making this assumption, the mobility of the grain boundary and

SIONYX1403000043.0053

SAMSUNG EX. 1002 - 696/4148

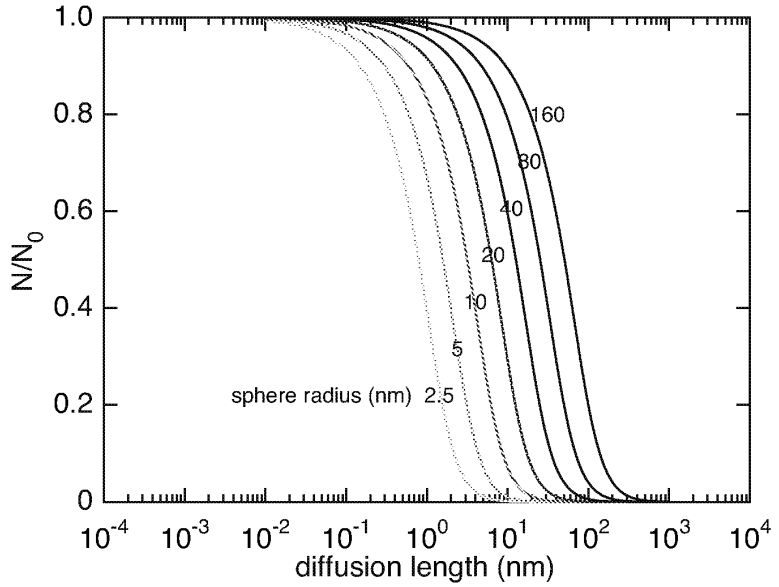


Figure 4.8: Plot of Equation 4.12 for various size spheres.

the diffusivity of selenium in silicon are proportional to each other by a constant, $M = \beta D$. We can now replace grain boundary mobility with selenium diffusivity in Equation 4.13,

$$R = \sqrt{R_0^2 + \alpha\beta D t}, \tag{4.14}$$

and make the following substitution, $d = \sqrt{Dt}$, yielding,

$$R = \sqrt{R_0^2 + \gamma d^2}. \tag{4.15}$$

Which gives the approximate grain growth as a function of the diffusion length of selenium in silicon, d. All of the constants have been collected into a new constant, γ.

Next we incorporate the grain growth formula into our calculation of N/N_0 in Equation 4.11:

SIONYX1403000043.0054

SAMSUNG EX. 1002 - 697/4148

$$\left(\frac{N(d)}{N_0}\right)_{gg} = \frac{\int_0^R C(r,d)4\pi r^2 dr}{\frac{4}{3}\pi R_0^3 C_0}. \tag{4.16}$$

The radius in the equation for $C(r,d)$ is kept at the initial sphere size, R_0, as this is the initial distribution of the dopant, but the volume integration is now performed from 0 to R; R being the new grain size as a result of grain growth (Equation 4.15). The subscript, gg indicates grain growth.

The result of the integration is,

$$\left(\frac{N(d)}{N_0}\right)_{gg} =$$

$$\frac{1}{2\sqrt{\pi}R_0^3}\left[2d\left(1-\exp\left(\frac{RR_0}{d^2}\right)\right)(R^2+RR_0+R_0^2-2d^2)-4dRR_0\right]\exp\left(\frac{-(R+R_0)^2}{4d^2}\right)$$

$$+\frac{R_0^3-R^3}{2R_0^3}\mathrm{erf}\left(\frac{R-R_0}{2d}\right)+\frac{R_0^3+R^3}{2R_0^3}\mathrm{erf}\left(\frac{R+R_0}{2d}\right) \tag{4.17}$$

which is a function of the initial sphere radius, R_0, the diffusion length of the dopant, d, and the constant, γ.

Despite many assumptions, our model—modified for grain growth—now matches the selenium data quite well. Equation 4.17 is plotted in Figure 4.9 for $R_0 = 4$ nm. The dotted lines represent different values of γ. The solid line is the best fit of the data, at $\gamma = 3.3$. The magnitude of γ determines the relative impact of grain growth on the diffusion of dopants out of the sphere. All curves begin to approach a different constant value of $(N/N_0)_{gg}$ at a diffusion length of 4 nm, which is determined by the initial grain size. For larger γ, $(N/N_0)_{gg}$ approaches a larger constant value.

SIONYX1403000043.0055

SAMSUNG EX. 1002 - 698/4148

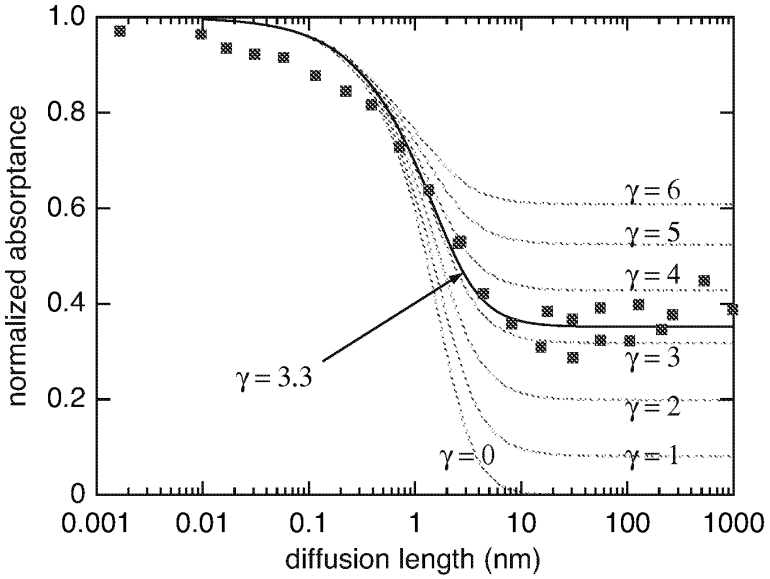


Figure 4.9: Comparison of normalized infrared absorptance for selenium-doped silicon to the theory curve for $R_0 = 4$ nm (from Figure 4.5) modified for grain growth (Equation 4.17) using various values of γ. The data matches the theory best for $\gamma = 3.3$.

Attempting to estimate γ based on the literature is difficult as the rate of grain growth in silicon varies greatly depending on the type of dopant and its concentration. Dopants can inhibit grain growth (as in the case of oxygen or chlorine [111]), have no effect (boron [109]) or greatly increase the growth rate (phosphorous [109]). It is possible the presence of tellurium may inhibit grain growth or other processes within the substrate at high temperature are altering the data. To our knowledge no grain growth studies have been performed using sulfur, selenium or tellurium-doped silicon. The grain growth shown by our model for $\gamma = 3.3$ is well within the observed ranges of grain growth for boron- and phosphorous-doped silicon [109]. The effect of grain growth is only apparent in the data for selenium-doped samples and not for sulfur or tellurium. In the case of sulfur, its fast diffusivity may wash out any effect of grain growth resulting in a value of γ close to 0.

SIONYX1403000043.0056

SAMSUNG EX. 1002 - 699/4148

4.6 Conclusion

Our analysis shows that the decrease in near-unity broadband infrared absorptance of supersaturated chalcogen-doped silicon after thermal annealing is likely caused by dopant diffusion. We observe that a characteristic diffusion length—common to all three dopants—leads to the deactivation of infrared absorption. If we assume the diffusivity of each dopant in our samples is similar to the bulk diffusivity reported in the literature, the grain size of the re-solidified surface layer is a probable source of this characteristic diffusion length, especially for a log normal distribution of grain sizes. We propose that a probable cause of the deactivation of infrared absorption is precipitation of the dopant at the grain boundaries. It is possible that other mechanisms, such as preciptiation of dopant particles within the grains in the form of clustering, also lead to the deactivation of infrared absorption. Further work on annealing studies of supersaturated chalcogen-doped silicon with different grain size distributions as well as in single crystalline silicon will help determine the relative contribution of each mechanism as a function of the silicon's microstructure and the dopant concentration.

4.7 Supplemental information

This section provides more experimental details, further clarification on the finer arguments in the earlier sections as well as more graphical representations of the data and theory for future reference.

4.7.1 Using an evaporated film as the dopant source

Previous to this work, the two methods used to incorporate dopants into the silicon substrate during femtosecond laser ablation was to perform the irradiation in a background

SIONYX1403000043.0057

SAMSUNG EX. 1002 - 700/4148

gas or disperse a powder film on the silicon with a solvent that then evaporates. Each of these methods has drawbacks. Due to expense and toxicity, it is difficult to obtain gaseous sources of many elements. In the case of a powder film, the resulting laser-structred surface is often nonuniform. By evaporating a film, we are able to expand the types of elements we can incorporate into the silicon. In the below sections, we discuss: the evaporation method, the effect that the film has on the resulting surface morphology, and the effect of film thickness and laser fluence on the resulting optical properties.

Details on the evaporation

Selenium and tellurium films were evaporated in a resistive thermal evaporator specifically set aside for use with "dirty" materials. Due to their extremely low vapor pressure, they are considered contaminants in vacuum systems; they can sublimate from the inside walls and contaminate future sample substrates. Their evaporation rate is also extremely sensitive to the resistive current flowing through the tungsten boat (R. D. Mathis, S3.005W). The general procedure for obtaining a relatively uniform film thickness was to slowly increase resistive current until an evaporation rate was detected by the crystal rate monitor, then increases in current proceeded extremely slowly and frequent adjustments were made to keep the evaporation rate between 10–20 A/s. If the current was not carefully monitored, the evaporation rate could increase to several hundred A/s within a few seconds resulting in a very nonuniform deposition.

Surface morphology

The surface morphology that results when irradiating a stationary spot on a sample coated with a film is very similar to the surface morphology that forms when irradiation is performed in a background gas. Figure 4.10, shows scanning electron microscope images of

SIONYX1403000043.0058

SAMSUNG EX. 1002 - 701/4148

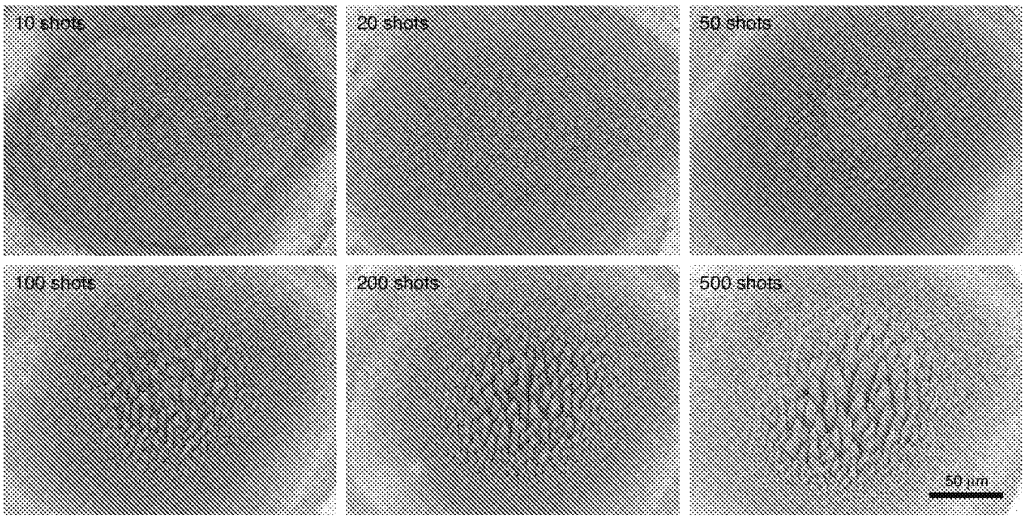


Figure 4.10: A series of scanning electron microscope images showing the evolution of surface morphology with an increasing number of shots. A 150-nm film of tellurium on silicon was irradiated with a fluence of 8kJ/m^2 in 500 Torr of N_2

a silicon substrate after irradiation with an increasing number of laser pulses in a stationary spot (each image is of a different spot on the silicon). The silicon substrate was coated with a 150-nm film of Te and irradiated in 500 Torr of N_2 with a fluence of 8kJ/m^2.

How doping happens when a film is used as the dopant source

We observed that the film in the center of the spot was broken and ablated away after only a single laser pulse. This observation sheds some illumination on how doping is achieved when a film is used. During irradiation the film is not driven into the substrate, but rather it is ablated away at the center of the irradiated spot due to the high fluence. However, since the beam is gaussian in space, there will be regions of lower fluence around the edges of the spot. The ablation threshold and therefore the melting threshold of tellurium is less than silicon. In regions of lower fluence the tellurium will evaporate but not ablate (there will be no net kinetic energy away from the surface) and at even lower fluences

SIONYX1403000043.0059

SAMSUNG EX. 1002 - 702/4148

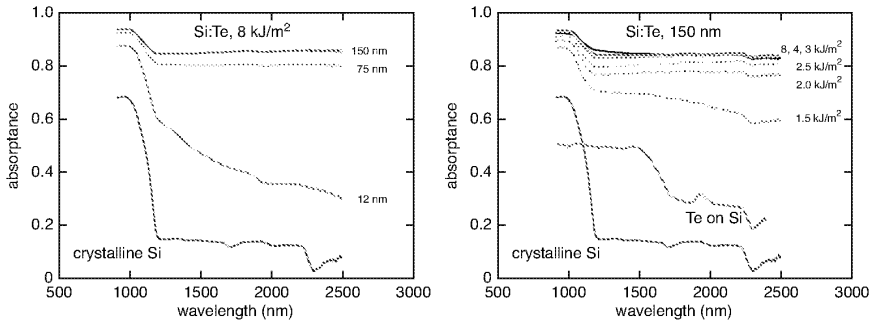


Figure 4.11: *Left:* The effect of film thickness on the infrared absorptance of silicon wafers coated with tellurium and irradiated with a fluence of 8kJ/m^2 in 500 Torr of N_2. *Right:* The effect of fluence on the absorptance of silicon wafers coated with a 150-nm thick film of tellurium and irradiated in 500 Torr of N_2.

the tellurium will melt. This will create an atmosphere just above the silicon wafer that is rich with tellurium atoms. As the next laser pulse comes it will ablate and melt silicon at the center of the irradiated spot and the nearby gaseous telllurium atoms will mix with the molten silicon and become trapped in the polycrstalline grains during solidification.

The effect of film thickness and laser fluence on optical properties

Figure 4.11 shows the absorptance for three film thicknesses of tellurium (12 nm, 75 nm and 150 nm). Irradiation was performed in 500 Torr of N_2 with a laser fluence of 8 kJ/m^2. The absorptance of the sample that was coated with a 150-nm thick film is very similar to the absorptance obtained when the irradiation is performed in a background gas of sulfur hexaflouride (see Figure 4.1), and was therefore used as the standard conditions in this experiment. The absorptance of the sample coated with only 12 nm of tellurium is similar to the absorptance of samples irradiated in N_2 gas (see Figure 4.1) and we conclude that minimal tellurium is being incorporated in the silicon substrate.

Figure 4.11 also shows the change in absorptance for a silicon wafer coated with

SIONYX1403000043.0060

SAMSUNG EX. 1002 - 703/4148

a 150-nm film of tellurium as fluence is varied. For fluences between 8 and 3 kJ/m^2, the absorptance is very similar. Although lower than the others, significant absorptance is still achieved with samples irradiated with a fluence of 1.5–2.5 kJ/m^2, which is below the ablation threshold of silicon (3 kJ/m^2). This is quite different than what is observed for samples irradiated in a background gas of sulfur hexaflouride where fluence has a strong affect on the infrared absorptance [46]. We attribute this behavior to the lower ablation threshold of tellurium.

Consider a tellurium coated sample being irradiated at a fluence below the ablation threshold of silicon. During irradiation, the sample is translated. This fact means that surface regions that were just irradiated with a low fluence are then subsequently irradiated with a higher fluence because the beam is gaussian in space. Tellurium at the edge of the irradiated spot will melt and refreeze with a new surface morphology that is established by capillary waves in the tellurium melt similar to the laser induced periodic surface structures discussed in Section 1.1.2. When the fluence exceeds the ablation threshold of tellurium, these small structures will evolve as more pulses of increasing fluence are incident, similar to the way all microstructures evolve during ablation as discussed in Section 2.1. Eventually the structures will grow large enough as the sample translates so that they act to concentrate the incident laser light in the valleys between the structures, effectively raising the fluence above the ablation threshold of silicon allowing the tellurium to be incorporated into the silicon at an average fluence that is below the ablation threshold of silicon.

4.7.2 Diffusion coefficients for sulfur, selenium and tellurium in silicon

The diffusion coefficients available in the literature are listed in Table 4.2.

SIONYX1403000043.0061

SAMSUNG EX. 1002 - 704/4148

Element	D_0 (cm^2/s)	E_a(eV)	T range (K)	Substrate	Method
S [87]	**0.92**	**2.2**	**1300–1650**	**Cz p-type**	**measured depth of p-n junction**
S [86]	0.0076	1.85	1250–1430	n-type	radioactive tracer implantation
S [84]	0.047	1.80	1328–1671	Fz n-type 300 Ω-cm	radioactive tracer implantation
Se [89]	**2.47**	**2.84**	**1073–1523**	**p-type**	**sheet conductivity**
Se [88]	0.95	2.60	1315–1515		sheet conductivity
Se [91]	0.11	2.42	1273–1523	Fz p-type 1–430 Ω-cm	sheet conductivity
Se [90]	0.3	2.60	1273–1538	Fz 5000 Ω-cm	sheet conductivity
Te [81]	0.5	3.34	1173–1523	Cz n-type	secondary ion mass spectroscopy
Te [90]	0.9	3.3	1318–1578	Fz 5000 Ω-cm	sheet conductivity
Te [85]	5.53	3.54	1149–1653	Fz n-type and p-type	radioactive tracer implantation
Te [85]	6.3×10^5	4.86			high T fit of above
Te [85]	**0.048**	**3.04**			**low T fit of above**

Table 4.2: Diffusion coefficients for sulfur, selenium, and tellurium in silicon. The bolded entries were used for the analysis in Figure 4.4

4.7.3 Absorptance spectra of chalcogen-doped silicon after annealing

Figure 4.12 provides the 75 absorptance spectra of sulfur-, selenium-, and tellurium-doped samples after the 25 anneals performed at temperatures of 575 K, 675 K, 775 K, 875 K, 975 K and times of 10 min, 30 min, 100 min, 6 hr, 24 hr. These 75 curves were averaged over the wavelengths 1250–2500 nm to create the data in Figure 4.2. The curves are presented here for future reference to the actual data.

4.7.4 Alternate graphs of optical data versus diffusion length

In this section, additional graphs are provided showing the change in optical properties versus diffusion length of the dopant.

SIONYX1403000043.0062

SAMSUNG EX. 1002 - 705/4148

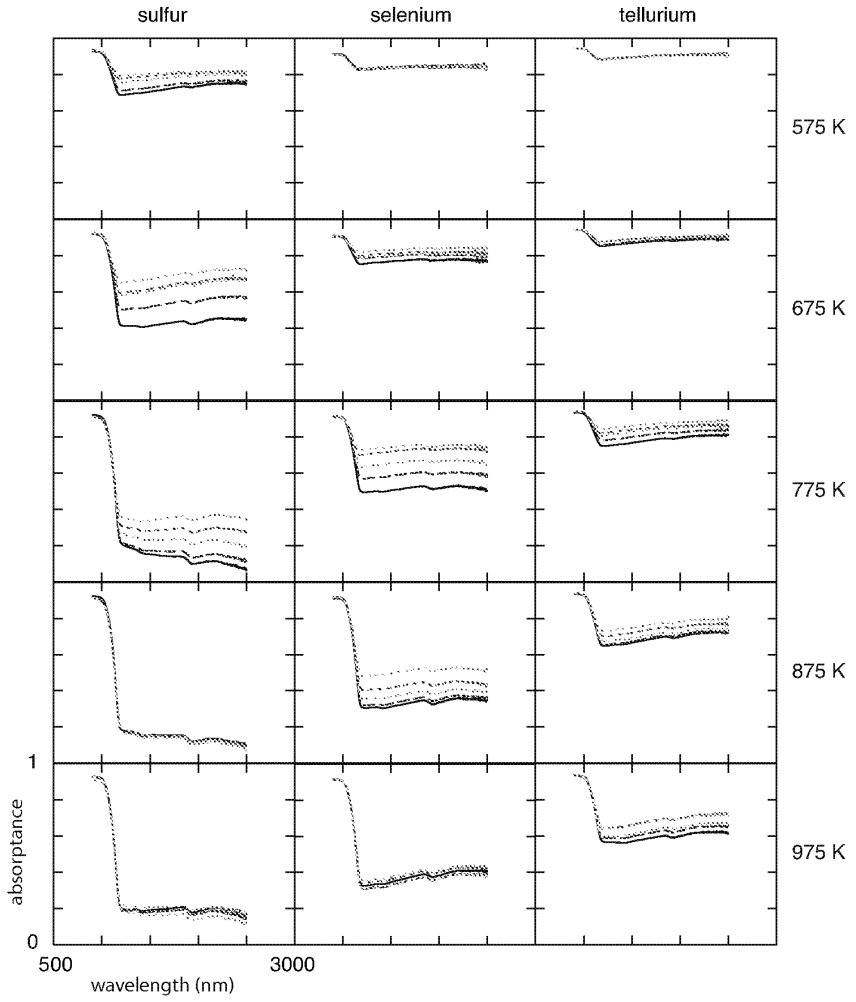


Figure 4.12: Absorptance spectra of chalcogen-doped silicon. Each column is the same dopant. Each row is the same temperature. Within a single graph the solid curve is an annealing time of 24 hr and the increasingly more dashed curves are annealing times of 6hr, 100 min, 30 min and 10 min.

Transmittance and reflectance versus diffusion length

Absorptance is calculated by measuring the transmittance and reflectance of a sample. In this section, we look at how these values directly change after the 25 anneals

SIONYX1403000043.0063

SAMSUNG EX. 1002 - 706/4148

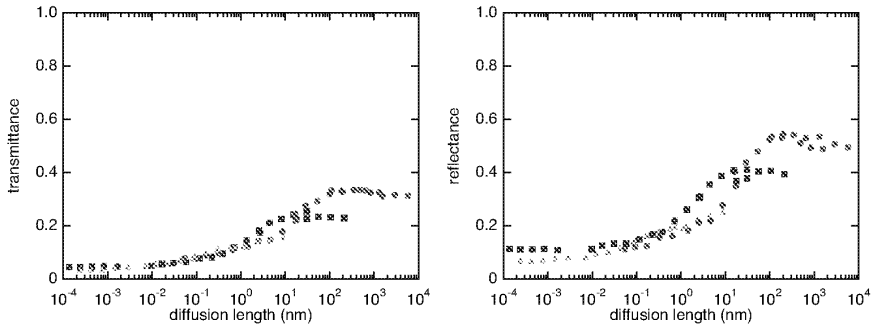


Figure 4.13: Transmittance and reflectance averaged over 1250–2500 nm for chalcogen-doped samples after the 25 anneals performed in Figures 4.2 and 4.12.

performed in Figures 4.2 and 4.12.

Figure 4.13 shows the actual reflectance and transmittance after each anneal versus diffusion length. At small diffusion lengths both the transmittance and reflectance are close to zero as the samples are highly absorbing in the infrared. At larger diffusion lengths, the transmittance and reflectance start to increase. In the case of sulfur, the transmittance and reflectance rise until they are close to the infrared transmittance and reflectance of the original unirradiated silicon wafer.

In order to determine whether the transmittance and reflectance are changing at the same rate with diffusion length, we replot the data from Figure 4.13 and normalize the values for transmittance and reflectance. We normalize reflectance by setting the minimum equal to the infrared reflectance after irradiation and setting the maximum equal to the infrared reflectance of the unirradiated silicon wafer. The same is done for transmittance. When the data is normalized in this manner, we get Figure 4.15. Figure 4.15 shows that the change in transmittance and reflectance after annealing occurs at the same rate. The graphs in Figure 4.15 are equal to one minus the normalized absorptance in Figure 4.4.

SIONYX1403000043.0064

SAMSUNG EX. 1002 - 707/4148

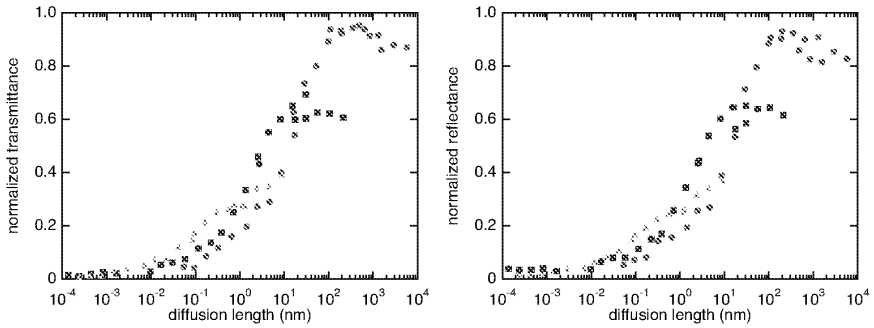


Figure 4.14: Normalized transmittance and reflectance averaged over 1250–2500 nm for chalcogen-doped samples after the 25 anneals performed in Figures 4.2 and 4.12.

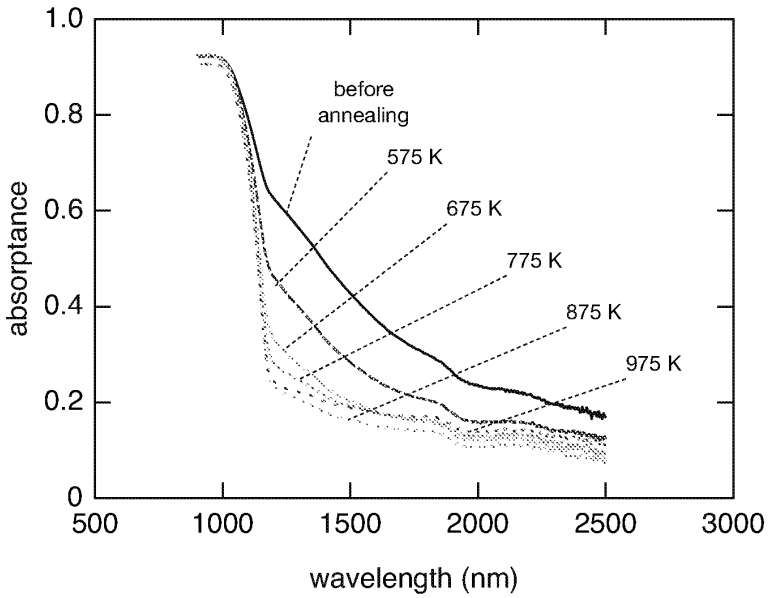


Figure 4.15: Absorptance spectra of samples irradiated in N_2 gas after annealing for 10 minutes at $T = 575$–975 K.

4.7.5 Absorptance spectra of samples irradiated in N_2 after annealing

Figure 4.15 shows the change in absorptance spectra for samples irradiated in N_2 gas and annealed for 10 minutes at $T = 575$–975 K.

SIONYX1403000043.0065

SAMSUNG EX. 1002 - 708/4148

Chapter 5

The photovoltaic potential of femtosecond laser irradiated silicon

In this chapter, we assess the potential of using femtosecond laser irradiated silicon as a photovoltaic device (*i.e.* a solar cell). In Section 5.1, we introduce the general field of photovolatic research. In Section 5.2, we discuss the advantages of using femtosecond laser irradiated silicon as a photovoltaic material. In Section 5.3, we introduce the basic electrical characteristics of a solar cell. In Section 5.4 we present the experimental results obtained from our efforts. The chapter concludes with a summary discussion of the results in Section 5.5. The reader may also wish to review Appendix A, which gives a more detailed description of the general operation of a solar cell.

5.1 Photovoltaic research

One of the main factors motivating photovoltaic research is reducing the manufacturing cost of solar cell technology. Because the sun is a nearly inexhaustible pollution-free source of energy, and solar cells have little to no operating cost with lifetimes on the order

SIONYX1403000043.0066

SAMSUNG EX. 1002 - 709/4148

of 30 years, the only monetary investment is the initial manufacturing cost. The fact that this still impedes the widespread use of PV electricity today shows how significant a factor it is. Once this barrier is removed, PV electricity will likely replace fossil fuels as the main source for grid-connected power stations. Fossil fuels are expendable with a limited supply, produce pollution, and have operating costs required to harvest and burn them [112, 113].

A typical solar cell array requires the following main systems depending on its application: solar cell modules, structural hardware (stands), storage system (batteries), inverter (converts from DC electricity to AC electricity) and connecting wires. The solar cell modules are estimated to be between forty and fifty percent of the total cost of the array. The rest of the cost comes from the remaining components which collectively are referred to as the Balance of Systems (BOS). The high cost of the solar cell modules—which are made up of several interconnected solar cells—allows scientific researchers who work on the performance of solar cells to have a major impact on the commercial viability of PV technology [112, 113].

One of the goals of PV research is to reduce the cost per unit of energy produced. This is estimated in \$/kWh. A kilowatt-hour is a unit of energy. It is obtained by taking the power needed for the application and multiplying it by the hours of operation. The \$/kWh can be estimated for any solar cell system by dividing the manufacturing cost by the energy produced over the lifetime of the system (20–30 years). This estimation is highly subjective and depends on the size of the system, the application and the location. Current estimates vary between 0.17 \$/kWh and 0.50 \$/kWh. The cost of electricity from power companies based on fossil fuels is currently at 0.03–0.05 \$/kWh. Even for the most favorable estimates, solar cell technology is not cost effective. In addition, using solar energy requires a huge investment up front and the pay-back times are on the order to 20–30 years. However, these numbers are encouraging as solar cell technology is within an order of magnitude of being

SIONYX1403000043.0067

SAMSUNG EX. 1002 - 710/4148

cost effective [112, 113].

Research on solar cells falls into two general categories,[1] both aimed at reducing the cost per kilowatt-hour. The first category involves using expensive materials and advanced processing techniques to obtain the highest possible efficiency. The increased efficiency will hopefully offset the extra cost. The second category involves using cheaper materials and cheaper processes. The lower quality material sacrifices efficiency, but this is hopefully offset by its low cost.

High efficiency, high cost solar cells

Solar cell systems that fall into the first category are single crystalline Si and GaAs used for space applications. The high purity required for high efficiency makes these materials very expensive. Nearly 50% of the material is lost when the bulk material is sliced into wafers. They are cost effective for space applications because weight is the limiting factor and solar cells are much lighter than any other fuel source. These solar cells are designed to have the highest efficiency possible, 24–25%, but are too expensive for most terrestrial applications [112, 113].

Lower efficiency, lower cost solar cells

The most prevalent material used in terrestrial applications is polycrystalline silicon wafers. It is cheaper to make than single crystal wafers and therefore falls into the second category. Their advantage is that they can be grown in thin slabs and less than 10 % of the material is lost to wafer slicing and polishing. Their efficiencies are $\sim$ 14 % depending on the manufacturer [112, 113].

[1] In addition to research on different solar cell materials, another active research area is solar cell design. Concentrator cells use glass or plastic lenses to focus sunlight (with magnifications of up to 1000 times) onto a small highly efficient solar cell. In tandem or multi-junction cells, different materials with different band gaps are stacked in series in order to absorb a larger portion of the sun's spectrum [112, 113].

SIONYX1403000043.0068

SAMSUNG EX. 1002 - 711/4148

Thin-film materials fall into the second category as they drastically reduce the cost of the material at the expense of efficiency. The most promising systems are Si, CdTe, and $CuInSe_2$. They are grown using many methods including physical and chemical vapor deposition techniques to a thickness on the order of micrometers. This process also results in very little loss of material. The thin film materials typically have a large number of defects resulting in efficiencies on the order of 10% and less. Commercial manufacture of thin film solar cells has only recently started on large scale [114, 115].

5.2 Laser irradiated silicon solar cells

In this section, we review the properties of femtosecond laser irradiated silicon and discuss the advantages and disadvantages of using it as a solar cell material. The previous work in Section 2.1, Figure 2.7, has shown that femtosecond laser irradiated silicon can be used as a photovoltaic device and that as a photodiode, it can convert wavelengths of light that are not normally absorbed by silicon into an electrical signal. These two results together indicate it is possible femtosecond laser irradiated silicon will be able to enhance current silicon-based solar cells by extending their usable spectrum.

From a photovoltaic standpoint, the most attractive property of femtosecond laser irradiated silicon is that it absorbs nearly all light that is emitted by the sun. The sun's spectrum at the earth above the atmosphere (AM 0) spans the range 0.25–2.5 μm (see Figure 5.1). The spectrum can be approximated by a black body radiating at a temperature of 5900 K. The spectral irradiance, M, emitted by a black body in the units of W m^{-2} μm^{-1} is given by,

$$M = \frac{2\pi hc^2}{\lambda^5} \frac{1}{\exp[\frac{hc}{kT\lambda}] - 1}, \tag{5.1}$$

SIONYX1403000043.0069

SAMSUNG EX. 1002 - 712/4148

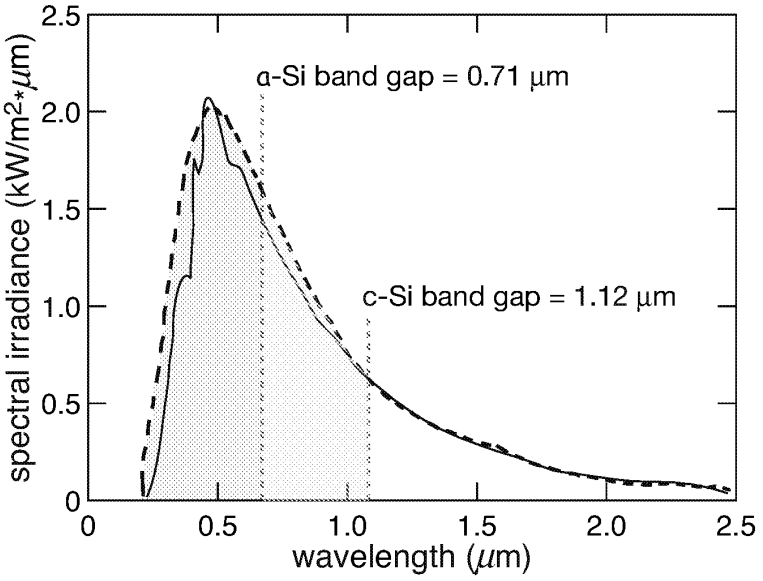


Figure 5.1: Solar spectrum of the sun at the earth above the atmosphere (solid line). Radiation from a black body at $T = 5900$ K (dashed line). The colored (grayed) regions under the curve represent the power/area that is available to amorphous silicon and crystalline silicon respectively due to their electronic band gaps.

where h is planck's constant (6.6260 $\times 10^{-34}$ m^2 kg/s), c is the speed of light (2.9979 $\times 10^8$ m/s), k is the Boltzmann constant (1.3807 $\times 10^{-23}$ m^2 kg s^{-2} K^{-1}) , T is the temperature of the black body in K and λ is the wavelength in μm. Crystalline silicon solar cells are transparent to wavelengths of light longer than 1.12 μm, due to their electronic band gap of 1.07 eV. By integrating Equation 5.1 from 1.12 μm to ∞ and dividing the result by the integration from 0 to ∞, we see that crystalline silicon solar cells are transparent to 23 % of solar energy. Thin film amorphous silicon solar cells have a larger bang gap of 1.75 eV [114] and are transparent to light longer than 0.71 μm. This value amounts to an even larger loss of solar energy, 53 %. These losses represent energy that is unavailable to typical silicon-based solar cells no matter how efficient they become. Because femtosecond laser irradiated silicon absorbs nearly all light emitted by the sun, it offers a chance to tap into

SIONYX1403000043.0070

SAMSUNG EX. 1002 - 713/4148

that lost energy.

Based on the above, femtosecond laser irradiated silicon would appear to be an attractive option for solar cells; however, absorption alone does not convert the photon into usable energy. Many materials, such as coal, absorb a large amount of sunlight. The key is that the absorption of the light needs to create current in an electrical circuit just as a standard electrochemical battery does. Solar cell operation is discussed in greater detail in Appendix A. Briefly, photon energy is used to create electron-hole pairs. These electron-hole pairs are separated by an electric field that is located internally within the solar cell due to a chemical composition gradient. The electron-hole pairs separate by either being created within the region of the internal electric field or by being created outside this region and then randomly diffusing into the region of the electric field. The separation of electron-hole pairs creates a current in the material which produces a current in an external circuit. The current is reduced by defects within the material that trap the electrons or holes before they are accelerated by the internal electric field [116].

By its very nature femtosecond laser irradiated silicon contains a high density of defects. Transmission electron microscopy shows the grain size is less than 50 nm. This is orders of magnitude smaller than for typical polycrystalline silicon solar cells, where the grain size is on the order of the thickness of the cell. In addition, after femtosecond laser irradiation, a high density of point defects (such as vacancies and dangling bonds) can become trapped in the resolidified crystalline material [108]. Point defects and grain boundaries can trap charge carriers and reduce the current that can be generated by the absorption of photons.

Because of the many defects in the laser modified surface, it is unlikely that femtosecond laser irradiated silicon will be able to improve upon the already high efficiency of single crystal silicon solar cells ($\sim$ 25 %) or even the lower efficiency of polycrystalline

SIONYX1403000043.0071

SAMSUNG EX. 1002 - 714/4148

silicon solar cells (~ 14 %). However, since thin film silicon already contains a large number of defects and exhibits a much lower efficiency (typically ≤ 10 %), it would seem to be a good candidate for use with our femtosecond laser irradiation process. We take a closer look at this material, in the next section.

5.2.1 Thin film silicon

Thin films of amorphous and microcrystalline silicon are typically produced by plasma-enhanced chemical vapor deposition using a mixture of silane (SiH_4) and hydrogen gases. The final film can contain a substantial amount of hydrogen (5–20 at.%) depending on the conditions. Amorphous silicon films can be grown using pure silane, but high dilution with hydrogen allows crystalline grains to form in the film [117]. The degree of crystallinity is varied by changing the silane concentration from 8% down to 4.5% where the film is completely crystalline with a grain size of $\sim 25\mu$m [115]. Further dilution leads to larger grains in the direction perpendicular to the film.

Amorphous and microcrystalline silicon are intrinsic but can be doped with phosphorous or boron during the deposition process. A standard *p*-*n* junction is not used. Due to the large amount of disorder (dangling bonds in amorphous silicon and grain boundaries in crystalline silicon) the diffusion length of charge carriers is typically less than 1 μm [115]. A standard *p*-*n* junction relies on the diffusion of photoexcited carriers from outside of the depletion region to its edge for generation of a portion of the photocurrent [116]. To reduce the loss of photoexcited carriers, thin film silicon is used in a *p*-*i*-*n* configuration. Thin highly doped *p*-type and *n*-type regions are placed on either side of a thicker intrinsic region setting up an electric field that spans the entire intrinsic region. The electric field imparts a drift force on photoexcited carriers reducing their chance of recombination [115]. In amorphous silicon, the hydrogen is needed to passivate dangling bonds which act as

SIONYX1403000043.0072

SAMSUNG EX. 1002 - 715/4148

recombination sites of photoexcited carriers [113].

5.2.2 Combining femtosecond laser irradiation and thin film silicon

The real advantage of femtosecond laser irradiated silicon is not just that it absorbs nearly all the wavelengths of light emitted by the sun, but that it does so in a laser modified surface film that is less than 500 nm thick. This makes it ideal for incorporation with thin film silicon. As we saw in the previous section, both amorphous and microcrystalline silicon contain a large number of defects, suggesting that the disorder in femtosecond laser irradiated silicon will not necessarily further reduce efficiency. Specifically, the microstructure of microcrystalline silicon seems to be very similar to femtosecond laser irradiated silicon.

One of the drawbacks of microcrystalline silicon is that it needs to be grown 2–3 times thicker than amorphous silicon in order to increase its light absorption. Even then, many of the longer wavelengths will not be absorbed as an absorption length of 6 μm is needed for wavelengths of light longer than 700 nm (see Figure 1.2). By incorporating a femtosecond laser modified layer on either the front or back of the film, all of these wavelength could be absorbed. Although the greater density of defects in femtosecond laser irradiated silicon will result in most of this absorption being lost to recombination in traps, even an increase in efficiency of thin film silicon solar cells of just several % would have a large impact on the photovoltaic industry.

Figure 5.2 is schematic representation of how femtosecond laser irradiated silicon can be incorporated into the *p-i-n* configuration of a thin film silicon solar cell. The intrinsic region of the solar cell can be grown thicker and then irradiated to produce the laser modified surface region.

In Section 5.4.6, we present results on the absorptance of femtosecond laser irradiated thin films.

SIONYX1403000043.0073

SAMSUNG EX. 1002 - 716/4148

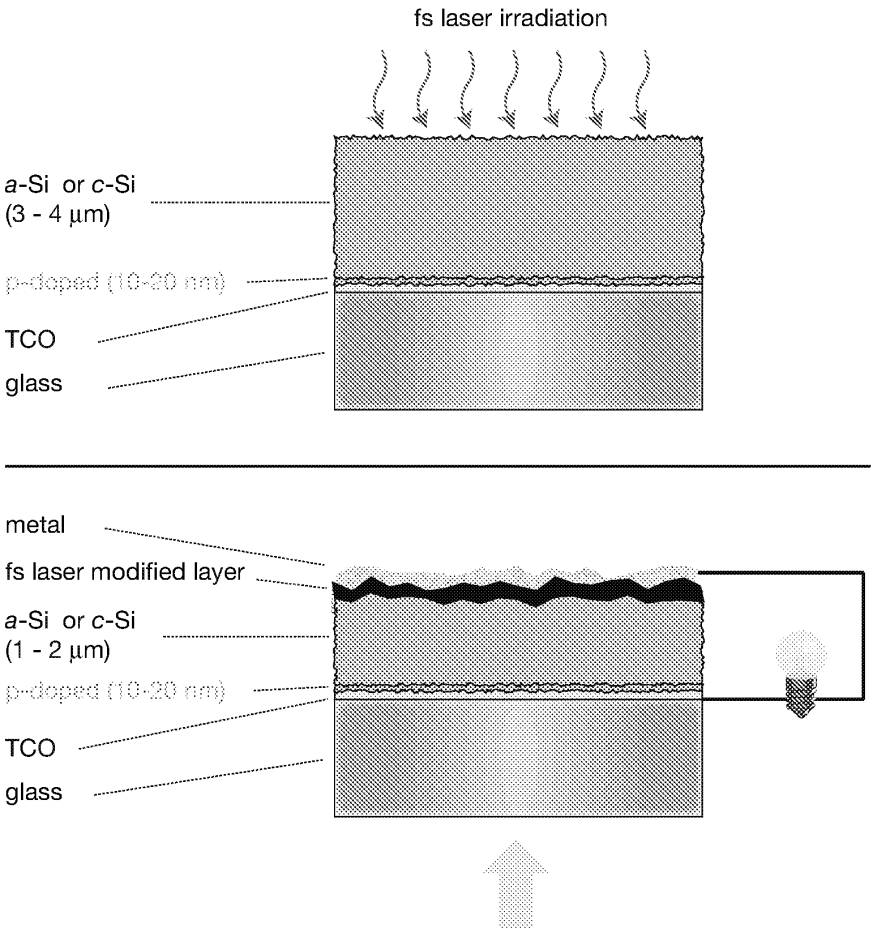


Figure 5.2: Schematic cross-section of the manufacturing process of a femtosecond laser irradiated thin film silicon solar cell.

SIONYX1403000043.0074

SAMSUNG EX. 1002 - 717/4148

5.3 The electrical characteristics of a solar cell

In a typical silicon solar cell, the silicon is several hundred micrometers thick. The n-type side faces the sun and the depth of the p-n junction is several hundred nanometers [116]. Due to silicon's indirect band gap, electron-hole pairs are generated throughout the entire depth of the solar cell when illuminated (see Figure 1.2). Those charge carriers generated in the depletion region (which is typically on the order of 100 nm thick) and those that diffuse to the depletion region will be accelerated by the internal electric field resulting in a generated photocurrent that is proportional to the intensity of the incident light.[2]

Dark and illuminated I-V curves of a commercial polycrystalline silicon solar cell are shown in Figure 5.3.[3] The commercial sample measured approximately 1 cm $\times$ 1 cm. The dark I-V curve of a solar cell behaves close to an ideal p-n junction (see Appendix A). The current approaches a very small and negative saturation current when reverse biased ($V < 0$) and increases nearly exponentially when forward biased ($V > 0$). Negative biasing increases the size of the depletion region of the p-n junction and likewise increases the internal voltage barrier. The saturation current comes from electron-hole pairs that are thermally excited in the depletion region. A forward bias decreases the size of the depletion region and the internal voltage barrier. As the internal voltage barrier decreases, more and more electrons can diffuse over the voltage barrier resulting in an exponentially increasing current [116, 118]. In practical applications, the voltage barrier needs to be decreased to near zero before any appreciable current flows. The voltage required to shrink the barrier to near zero is called the "turn on" or threshold voltage of the diode [119].

Several variables characterize the quality of a solar cell and are determined by mea-

[2]Since photons are generated throughout the bulk of a silicon solar cell, diffusion of excited charge carriers to the depletion region contributes to the generated current.

[3]These curves were acquired using the experimental setup described in the Section 5.4.1.

SIONYX1403000043.0075

SAMSUNG EX. 1002 - 718/4148

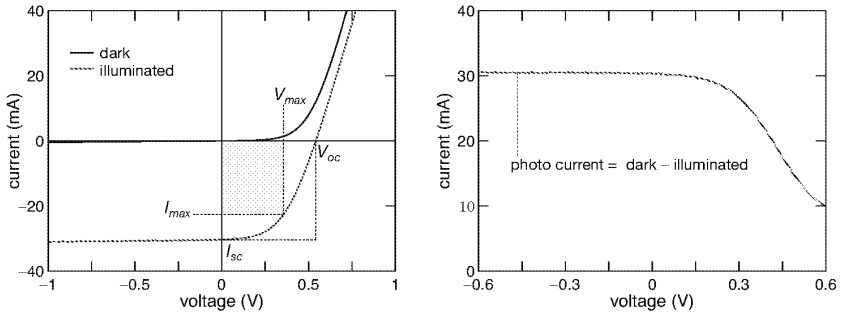


Figure 5.3: *Left:* Dark and illuminated current-voltage curves for a commercial polycrystalline silicon solar cell. The definitions of short circuit current (I_{sc}), open circuit voltage (V_{oc}), and the current (I_{max}) and voltage (V_{max}) that results in maximum power generation are indicated. *Right:* The generated photocurrent ($I_{ph} = I_{dark} - I_{illuminated}$) for a commercial polycrystalline silicon solar cell.

suring illuminated I-V curves. The open circuit voltage (V_{oc}) is the voltage that develops in a solar cell—unconnected to an external circuit—due to the separation of photo-generated electron-hole pairs. This value is measured by determining the voltage that needs to be applied to the illuminated solar cell in order to prevent the flow of current (see Figure 5.3). The short circuit current (I_{sc}) is the current that flows when the two sides of an illuminated solar cell are connected by a zero resistance conductor; this current is measured by forcing both sides of the illuminated solar cell to be at the same voltage. The two values can be determined with the same measurement by sweeping the applied voltage from a negative value to a sufficiently large positive value and recording the resulting current.

The only region of the illuminated I-V that has practical value for a solar cell is the part that resides in the fourth quadrant, where current is negative and voltage is positive.[4] This region represents connecting an illuminated solar cell to a load with a finite resistance (*e.g.* a light bulb). Varying the resistance of the load between zero and infinity, is equivalent

[4]The fact that the current is negative is due to convention and has no physical meaning. The positive direction of current flow is typically defined as from the p side to the n side and when the solar cell is generating power, the actual current flow is in the opposite direction.

SIONYX1403000043.0076

SAMSUNG EX. 1002 - 719/4148

to moving along the I-V curve from the point of short circuit current (resistance = 0) to the point of open circuit voltage (resistance = ∞). The power generated by the solar cell for any specific resistance is equal to the current in the circuit multiplied by the voltage in the circuit. We can determine the maximum power that the solar cell can generate by looking at the largest rectangle that can fit inside the illuminated I-V curve in the fourth quadrant (see the shaded rectangle in Figure 5.3). The current and voltage associated with the maximum power are termed I_{max} and V_{max}, respectively.

Another variable that characterizes the quality of a solar cell is the fill factor (FF),

$$FF = \frac{I_{max}V_{max}}{I_{sc}V_{oc}}. \tag{5.2}$$

The ideal shape of the I-V curve in the 4th quadrant is for the current to remain constant at I_{sc} until the applied voltage is very close to V_{oc}, where the current reduces quickly to zero. This allows for the highest power generation. The fill factor is a measure of how close the actual I-V curve comes to the ideal I-V curve. Graphically, the fill factor is the area of the shaded rectangle divided by the area of the larger dotted line rectangle in Figure 5.3.

The solar cell's efficiency, η (%), at converting solar power into electrical power is,

$$\eta = \frac{I_{max}V_{max}}{T_l A} \times 100\%, \tag{5.3}$$

where T_l is the intensity of the incoming light (in our case 100 mW/cm^2) and A is the area of the cell (in our case 1 cm^2). Substituting for the power, $P_l = T_l A$, of the incoming light and the using the equation for fill factor (Equation 5.2), we get,

$$\eta = \frac{(FF)I_{sc}V_{oc}}{P_l} \times 100\%. \tag{5.4}$$

For the commercial polycrystalline silicon solar cell in Figure 5.3 irradiated with

SIONYX1403000043.0077

SAMSUNG EX. 1002 - 720/4148

100 mW of light, $I_{sc} = 30$ mA, $V_{oc} = 540$ mV, $I_{max} = 23$ mA, $V_{max} = 350$ mV, $FF = 0.5$ and $\eta = 8.1$ %.

As we see from Equation 5.4 the values of I_{sc}, V_{oc} and FF determine the efficiency of the solar cell. These variables are affected by many factors. The short circuit current is the most direct measure of the concentration of defects within the solar cell material. A higher defect density, results in a larger number of charge carriers becoming trapped before contributing to an external current. Open circuit voltage is related to the internal voltage barrier of the *p*-*n* junction, which is a direct function of the band gap of the material and the temperature.[5] Open circuit voltage can be reduced by leakage paths of charge through the junction. This occurs at the edges of the solar cell but also through the center at breaks in the planar junction (*e.g.* at the grain boundaries of a polycrystalline silicon solar cell). These leakage paths can be characterized by the solar cell having a low shunt resistance (or low parallel resistance). The fill factor is similarly reduced by a low shunt resistance and high defect concentration [116].

A final parameter that can affect both short circuit current and fill factor is the diffusion length of the excited charge carriers. As we noted above, charge carriers that are generated outside the depletion region can diffuse to it and be accelerated by the internal electric field. In a typical silicon solar cell the diffusion length of charge carriers is much larger than the size of the depletion region. This is why the current remains nearly constant for an applied voltage of -1 V to 0 V in Figure 5.3, even though the depletion region is changing in size. If the diffusion length were equal to or less than the depletion region width, the measured current would vary greatly as the depletion region grew and shrank and both I_{sc} and FF would be affected.

[5]The correlation between the internal voltage barrier of a *p*-*n* junction and the band gap of the material is described in Chapter 4.2 of [116].

SIONYX1403000043.0078

SAMSUNG EX. 1002 - 721/4148

5.4 Photovoltaic experimental results and discussion

As we saw in Section 5.2.2, the ideal material to use for femtosecond laser irradiated solar cells would be thin film silicon. Here, we investigate the photovoltaic properties of femtosecond laser irradiated silicon wafers as crystalline silicon is a simpler model system. At the end of this section we explore the laser parameters needed to irradiate thin films of intrinsic silicon deposited on glass to show that their absorptance can be enhanced using femtosecond laser irradiation.

The following experimental results and discussion section will differ from those presented in Chapters 3 and 4. Our goal here is to create a record of the work performed for future reference. We include all relevant results, even though concrete conclusions cannot be drawn in some cases. Studying the photovoltaic properties of femtosecond laser irradiated silicon is an ongoing research project.

5.4.1 Measuring current-voltage (I-V) curves

As we learned in Chapter 2, the change in doping between the laser modified surface region and the bulk silicon substrate can create a diode. We use the following method to measure the current voltage characteristics of femtosecond laser irradiated silicon.

Following irradiation, samples are typically annealed in a vacuum oven or an inert gas flowing oven (see Section 5.4.2 for the effect of annealing). After annealing, the samples are dipped in an aqueous solution of 5 % hydrofluoric (HF) acid for 5 minutes to remove the 2–3 nm thick native oxide on the silicon. The HF acid terminates the silicon surface with H atoms and prevents oxide growth for a short period of time. The samples are then loaded into a thermal evaporator within 30 minutes in order to deposit metal contacts on the top and bottom of the sample. A 5 nm layer of chromium followed by 80–100 nm of gold creates a sufficient ohmic contact to the silicon. The chromium layer acts as a diffusion

SIONYX1403000043.0079

SAMSUNG EX. 1002 - 722/4148

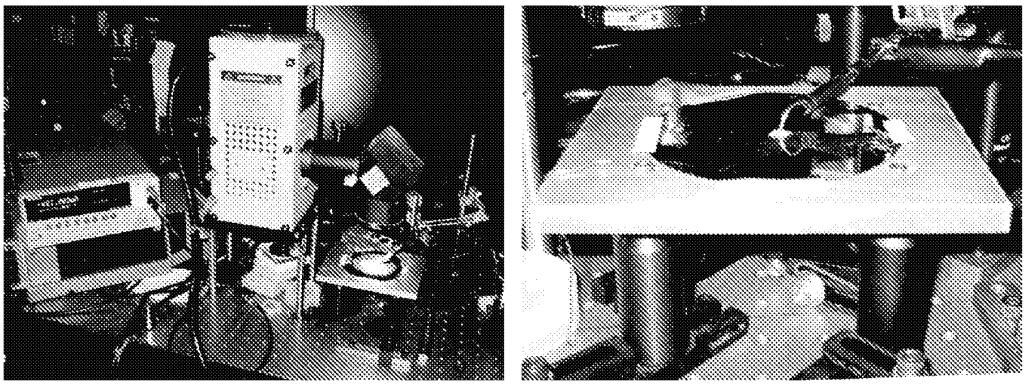


Figure 5.4: *Left:* Experimental setup for measuring dark and illuminated *I-V* curves. Including a Keithley multi-source meter, ThermoOriel Solar Simulator and probe station. *Right:* A close up of the probe station.

barrier due to the high diffusivity of gold in silicon.

During evaporation the samples are mounted on a metallic mask, so that the pattern of the top electrode (typically a 4 mm or 2 mm diameter circle) can be deposited on the irradiated surface. Then the samples are flipped over to deposit the bottom electrode on the entire back of the silicon wafer. In the latter experiments in this chapter, a special holder was built for use in the thermal evaporator that allowed samples to be turned over without breaking the vacuum, reducing the time required for depositing contacts by half. After removing the samples from the thermal evaporator, they are scribed with a diamond scribe and mechanically cleaved on all 4 sides to make sure gold does not connect the front and back of the sample.

Current-voltage curves were measured using a computer-controlled Keithley multi-source meter, which can source voltage and measure current (see Figure 5.4). A special probe station was built and placed under the output of a ThermoOriel Solar Simulator.[6] The

[6]The light source in the Solar Simulator is a 150 W xenon arc lamp. The spectrum of the xenon lamp is a good simulation of sun's spectrum except for several sharp peaks in the 800–1100 nm range. Filters can be used to suppress these peaks but not completely. An AM 1.0 filter was used to simulate atmospheric absorption.

SIONYX1403000043.0080

SAMSUNG EX. 1002 - 723/4148

bottom contact of the probe station is a 100-mm diameter, 500-μm thick, high conductivity silicon wafer coated with 200 nm of gold. A wire is soldered to the gold surface. The other end of the wire ends in a banana pin connection for connecting to the Keithley meter. Contact to the top electrode of the sample is made using a stainless steel probe mounted to a spring loaded arm. The optics of the Solar Simulator are focused so that an intensity of 100 mW/cm^2 hits the surface of the probe station.

5.4.2 The effect of annealing on the photovoltaic properties of sulfur-doped femtosecond laser irradiated silicon

Here we present our results on creating solar cells from femtosecond laser irradiated silicon and the effect of annealing on photovoltaic properties. We irradiated p-type, Si (100) wafers (ρ = 1–20 Ω-cm), using a fluence of 4 kJ/m^2 and 100 pulses/area in 500 Torr of SF_6. The spot size was 150 μm in diameter.

The samples were annealed to various temperatures between 575–1275 K in a gas flowing oven. After loading the samples into a quartz tube oven, it was heated to $\sim$ 373 K (100 C) and kept constant for 30 minutes while forming gas (90% N_2, 10% H_2) was flowed for 30 minutes to remove oxygen and water vapor. The samples were heated to the annealing temperature and held for 10 minutes. The gas flow was held constant for the entire anneal to prevent oxygen diffusion into the surface. After annealing, the samples were prepared for I-V curve measurement as described in Section 5.4.1. The top electrode was a 2-mm diameter circle. The samples were scribed and cleaved and the final dimensions of each sample was approximately 5 mm $\times$ 5 mm.

Figure 5.5, shows dark and illuminated I-V curves as well as photocurrent for the sample annealed for 10 minutes at 1075 K. The illumination intensity was 100 mW/cm^2. Since the sample was 0.25 cm^2, the incident light power was 25 mW, resulting in the

SIONYX1403000043.0081

SAMSUNG EX. 1002 - 724/4148

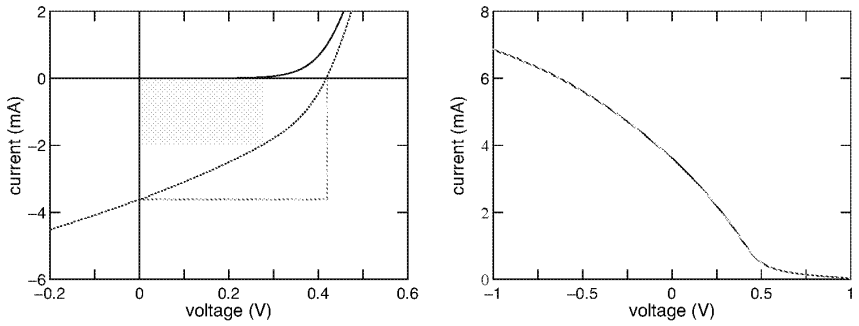


Figure 5.5: *Left:* Dark and illuminated current-voltage curves for a sample irradiated with 100 pulses/area at a fluence of 4 kJ/m^2 in SF_6. The sample was annealed for 10 minutes at 1075 K. *Right:* Photocurrent as a function of applied voltage. Area of the cell was 0.25 cm^2.

following photovoltaic properties: $I_{sc} = 3.6$ mA, $V_{oc} = 420$ mV, $FF = 0.36$ and $\eta = 2.2$ %. These values are significantly lower than the commercial solar cell shown in Figure 5.3, but the efficiency is comparable to our previous results discussed in Section 2.1.

Figures 5.6 and 5.7 show the dark and illuminated I-V curves for samples immediately after irradiation and after thermal anneals between 575–1208 K. The corresponding photovoltaic values of I_{sc}, V_{oc}, FF and η are given in Table 5.1. The values of I_{sc}, V_{oc}, and η all increase with annealing temperature until they reach a maximum at 1075 K. Annealing at higher temperatures only decreases these values.

Discussion of the effect of annealing

The values for I_{sc} and V_{oc} for our best solar cell (anneal $T = 1075$ K) are within less than a factor of two of the commercial polycrystalline silicon solar cell values from Section 5.4.1 (for 25 mW, $I_{sc} \sim 7.5$ mA and $V_{oc} \sim 550$ mV). The reduced efficiency of our samples seems to stem from the low fill factor.

In figure 5.8 we have graphed the values of I_{sc}, V_{oc}, FF and η versus annealing

SIONYX1403000043.0082

SAMSUNG EX. 1002 - 725/4148

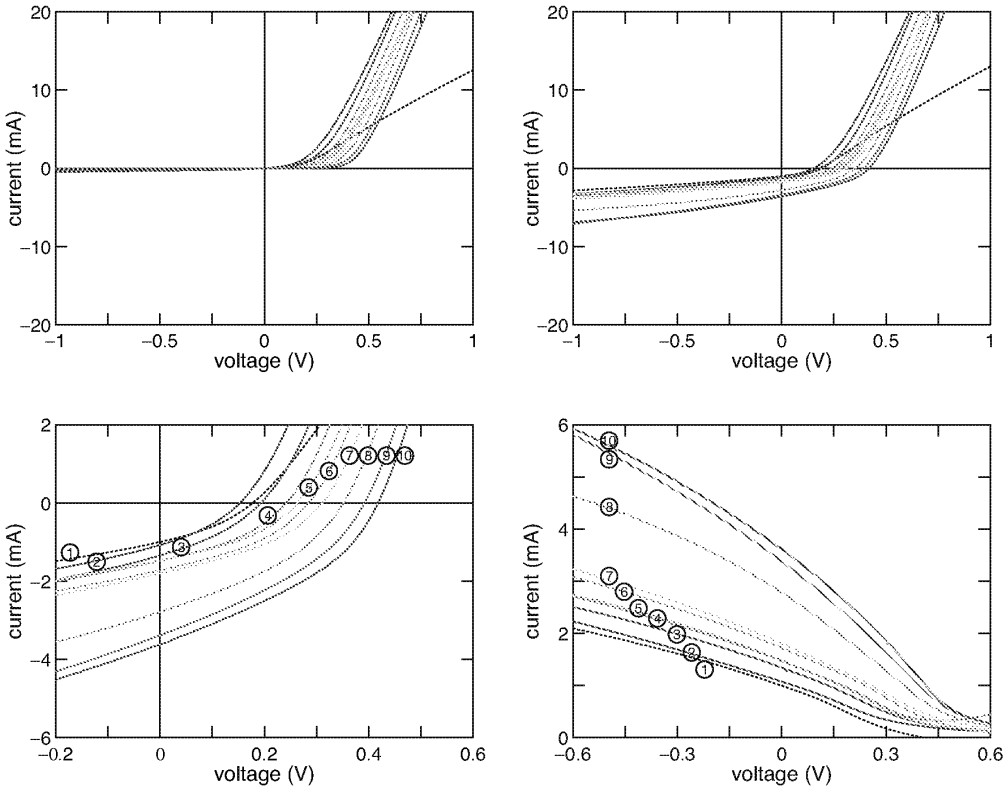


Figure 5.6: Dark (*upper left*) and illuminated (*upper right*) current-voltage curves for samples irradiated with 100 pulses/area at a fluence of 4 kJ/m^2 in SF_6 and annealed between 575–1075 K. *Lower left:* A closer look at the 4th quadrant. *Lower right:* Photocurrent as a function of applied voltage. The dotted line in each graph is the pre-annealed sample. Anneal temperature for each of the solid curves is listed in Table 5.1. Area of the cell was 0.25 cm^2.

SIONYX1403000043.0083

SAMSUNG EX. 1002 - 726/4148

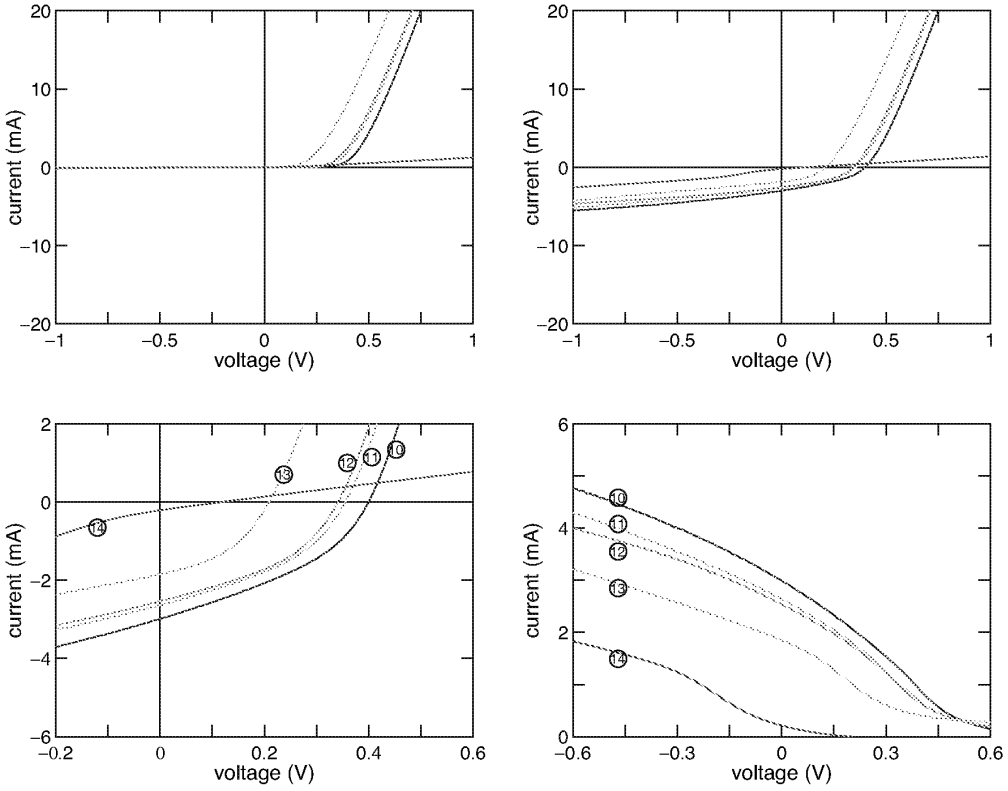


Figure 5.7: Dark (*upper left*) and illuminated (*upper right*) current-voltage curves for samples irradiated with 100 pulses/area at a fluence of 4 kJ/m^2 in SF_6 and annealed between 1075–1208 K. *Lower left:* A closer look at the 4th quadrant. *Lower right:* Photocurrent as a function of applied voltage. Anneal temperature for each of the solid curves is listed in Table 5.1. Area of the cell was 0.25 cm^2.

SIONYX1403000043.0084

SAMSUNG EX. 1002 - 727/4148

No.	Anneal T (K)	I_{sc} (mA)	V_{oc} (mV)	FF	η (%)
1	none	1.0	180	0.34	0.25
2	575	1.1	155	0.33	0.22
3	675	1.3	195	0.33	0.35
4	775	1.5	245	0.37	0.53
5	825	1.5	265	0.38	0.59
6	875	1.7	285	0.38	0.74
7	925	1.8	315	0.37	0.84
8	975	2.8	355	0.36	1.42
9	1025	3.4	395	0.35	1.87
10	1075	3.6	420	0.36	2.20
11	1108	2.6	360	0.39	1.49
12	1142	2.5	345	0.40	1.41
13	1175	1.8	210	0.41	0.64
14	1208	0.2	120	0.24	0.02

Table 5.1: Photovoltaic properties of samples irradiated with 100 pulses/area at a fluence of 4 kJ/m^2 in SF_6 and annealed between 575–1208 K. The sample number refers to the number used in Figure 5.6. Area of the cell was 0.25 cm^2.

temperature. The values of I_{sc}, V_{oc}, and η have been normalized with respect to the values obtained for the sample annealed at $T = 1075$ K. From this figure we can see that even though I_{sc} and V_{oc} increase with annealing temperature, FF stays roughly the same for every sample. We will now take a closer look at each of these solar cell parameters.

The observation that V_{oc} increases with annealing agrees well with our previous work discussed in Section 2.1. Hall measurements determined that the density of free electrons in the laser modified surface layer of p-type silicon ($\rho = 10$ Ω-cm) increased significantly after annealing to $T = 1075$ K; at this point the majority carriers in the surface layer was electrons rather than holes. The V_{oc} is a function of the magnitude of the internal voltage barrier of the p-n junction. The magnitude of the internal voltage barrier increases as the density of charge carriers increases in either side of the p-n junction (*i.e.*

SIONYX1403000043.0085

SAMSUNG EX. 1002 - 728/4148

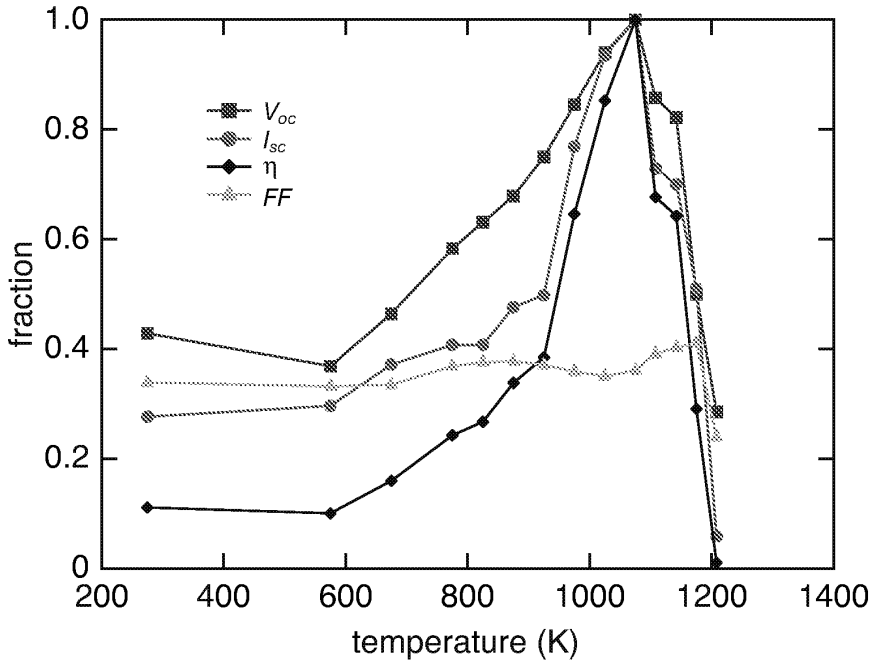


Figure 5.8: I_{sc}, V_{oc}, FF and η versus temperature for samples listed in Table 5.1 and displayed in Figures 5.6 and 5.7.

the internal voltage barrier of a heavily doped p-n junction is greater than a lightly doped p-n junction). So for our samples, V_{oc} increases because the internal voltage barrier of the junction is increasing. Additional evidence that the internal voltage barrier of our junction increases with anneal temperature can be seen in the dark I-V curves of Figure 5.6. As anneal T increases, the "turn on" voltage of the junction increases. As we discussed in Section 5.3, the "turn on" voltage is the voltage that needs to be applied to shrink the internal voltage barrier to zero.

In order to discuss the I_{sc} and FF exhibited by our samples, let us consider the nature of the junction. Figure 5.9 is a schematic cross-section of the junction. Based on our previous work, we know that the laser modified region becomes heavily n-doped upon

SIONYX1403000043.0086

SAMSUNG EX. 1002 - 729/4148

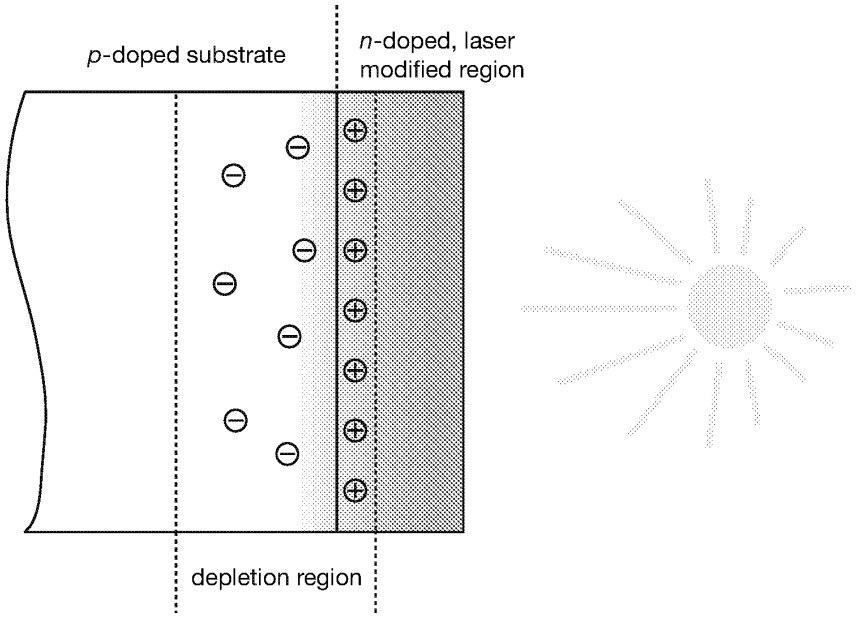


Figure 5.9: Schematic cross-section of the junction between femtosecond laser irradiated silicon and the underlying substrate. The gradient indicates where light absorption occurs.

annealing, creating a depletion region that will extend more into the p-substrate then into the n-type laser modified surface.[7] The region where light is absorbed is indicated by the gradient; most of the light is absorbed in the laser modified surface layer.[8]

The laser modified surface layer—where light absorption primarily occurs—contains a high density of defects (*i.e.* grain boundaries, vacancies, dangling bonds, etc.). The high defect density will result in photo-excited carriers having a short lifetime (and a short diffusion length) before they recombine. Only electron-hole pairs formed within a diffusion length of the depletion region will contribute to the photocurrent. The width of the depletion region grows and shrinks with applied voltage and due to the small diffusion length of

[7]For a description of this effect see reference [116], Chapter 5.2.

[8]As we know from Chapters 2 and 4, the laser modified surface layer is responsible for the near-unity absorptance; therefore, nearly all of the light will be absorbed in this surface layer.

SIONYX1403000043.0087

SAMSUNG EX. 1002 - 730/4148

the photo-excited carriers, the photocurrent will decrease as the applied voltage increases in the forward bias (reducing the fill factor). As we see in Figures 5.6 and 5.7, photocurrent is a strong function of applied voltage for all samples. In contrast, the photocurrent of the commercial cell (see Figure 5.3) is constant when the cell is reverse biased; for the commercial cell the diffusion length of excited charge carriers is much greater than the width of the depletion region.

Based on the above discussion, our samples' low fill factor is likely due to an extremely small diffusion length of carriers excited in the laser modified surface region. The fact that fill factor remains constant as annealing T increases indicates that the defect density in the laser modified surface region does not change enough to increase the diffusion length with respect to the size of the depletion region. Short circuit current, however, does increase with annealing. The increase in short circuit current could be due to several effects. As the laser modified surface region becomes more n-type with increased annealing temperature, the equilibrium (applied $V = 0$) width of the depletion region in the femtosecond laser modified surface layer might also increase. As a result, a larger volume of laser modified surface region—where a majority of the light is absorbed—will be present in the internal electric field and more photo-excited carriers will add to the photogenerated current. Also, annealing will heal defects within the section of the depletion region that extends into the laser modified surface layer; removal of defects in this region will increase the number of charge carriers that do not recombine and likewise the current will be increased.

Although a low shunt resistance in the solar cell would also reduce the fill factor and result in a back biased current that has a strong dependance on applied voltage, we do not observe such behavior. For the dark I-V curves shown in Figures 5.6 and 5.7, the current under reverse bias has very little dependence on applied voltage. If shunt resistance were responsible, we would expect the back biased current to show a similar dependence on

SIONYX1403000043.0088

SAMSUNG EX. 1002 - 731/4148

applied voltage in illuminated and dark measurements. This is not the case.

Due to the extremely small diffusion length of excited carriers in femtosecond laser irradiated silicon, it would benefit from being used in a *p-i-n* configuration such as is used for thin film silicon solar cells [115]. In Section 5.4.6, we explore irradiating thin films of silicon.

If we compare the annealing study performed here with the annealing study from Chapter 4, we see that the annealing temperature that results in the best photovoltaic properties (1075 K) is 200 K above the temperature at which the infrared absorptance is reduced to the absorptance of the original silicon wafer (875 K). Based on this, it appears that improvement in photovoltaic properties does not correlate with the decrease in infrared absorptance. The change in photovoltaic properties is likely related to changes in the lattice within the nanometer sized grains. These changes could include grain growth, diffusion of vacancies, healing of dangling bonds and changes in the coordination of sulfur dopants that remain in the grains even after annealing.[9]

5.4.3 The effect of HF acid etching on photovoltaic results

After annealing and before metal contacts are deposited, the samples are dipped in 5 % hydrofluoric (HF) acid to remove the native silicon oxide. Using the same wafers and experimental conditions as Section 5.4.2, we varied the etching time and examined the resulting photovoltaic properties. Listed in Table 5.2 are the values of I_{sc} and V_{oc} for various etching times. The annealing temperature was 1075 K. Based on the results, the etch appears to be an important step in manufacturing a good device, but the etching time is not critical.

[9]Not all of the sulfur atoms would necessarily diffuse out of the the crystalline grains even though the infrared absorptance has decreased to the original value; the concentration would remain at least as high as the solid solubility of sulfur in silicon ($\sim 10^{15}/\text{cm}^3$, [87]) at the temperature of the highest anneal.

SIONYX1403000043.0089

SAMSUNG EX. 1002 - 732/4148

Etch time	J_{sc} (mA)	V_{oc} (mV)
none	0.80	222
15 s	2.93	373
30 s	2.95	373
1 m	3.07	379
2 m	3.10	379
3 m	3.02	376
5 m	2.92	376
10 m	2.82	372

Table 5.2: Photovoltaic properties as a function of HF etching time.

5.4.4 The effect of H_2 gas and resulting surface morphology on photovoltaic results

As we saw in the Section 5.4.2, the efficiency of sulfur-doped femtosecond laser irradiated silicon is quite low in comparison to other silicon-based solar cells. This is likely due to the large number of defects present in the material as discussed in Section 5.2. In an attempt to passivate defects within the laser modified surface region with hydrogen atoms, we performed a study irradiating silicon in SF_6 gas diluted with various amounts of H_2 gas.

We irradiated p-type, Si (100) wafers (ρ = 1–20 Ω-cm), using a fluence of 5 kJ/m^2 and 200 pulses/area in six different background gas dilutions at a pressure of 500 Torr. The ratio of H_2:SF_6 pressure was varied in the following manner: 0:100, 10:90, 25:75, 50:50, 75:25, 90:10. The samples were then annealed to 1075 K for 30 minutes in a vacuum oven. The silicon substrate, laser parameters, annealing conditions, and evaporation of metal contacts were all chosen to be similar to the previous photovoltaic work [43] and is described in Section 5.4.1. Although in this case, for simplicity, the top contact was a 4-mm diameter circle, rather than the finger contacts shown in Figure 2.6.

SIONYX1403000043.0090

SAMSUNG EX. 1002 - 733/4148

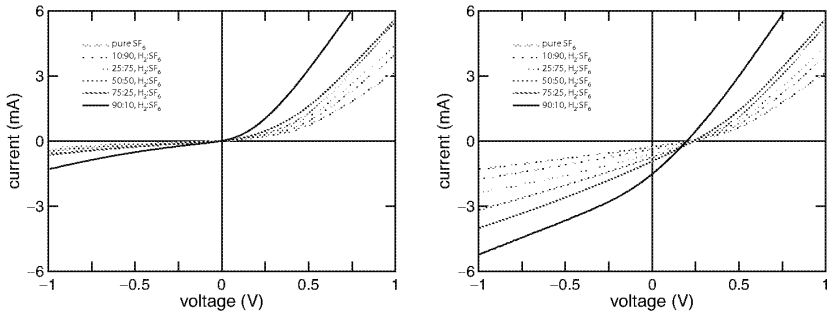


Figure 5.10: Dark (*left*) and illuminated (*right*) current-voltage curves for samples irradiated in a mixture of H_2 and SF_6. Samples are irradiated with 200 pulses/area at a fluence of 5 kJ/m^2. The results seem to indicate that incorporation of H improves photovoltaic properties; however further analysis shows that the effect is caused by a change in surface morphology, as a larger percentage of H_2 gas is used.

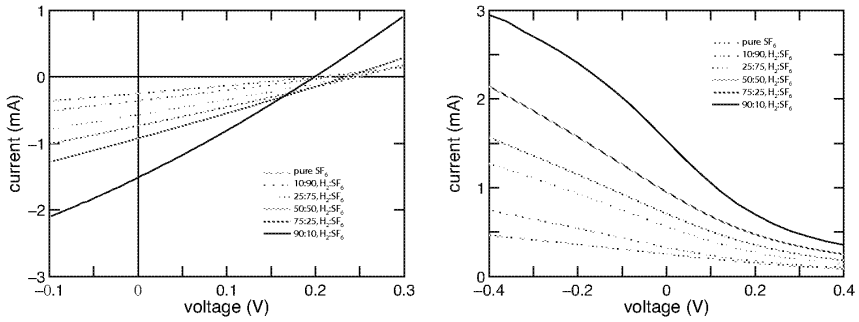


Figure 5.11: *Left* illuminated current-voltage curves for samples irradiated in a mixture of H_2 and SF_6. *Right* Photocurrent versus voltage curves of samples irradiated in a mixture of H_2 and SF_6. Samples are irradiated with 200 pulses/area at a fluence of 5 kJ/m^2. The results seem to indicate that incorporation of H improves photovoltaic properties; however further analysis shows that the effect is caused by a change in surface morphology, as a larger percentage of H_2 gas is used.

Figure 5.10 shows dark and illuminated current-voltage (I-V) curves from this initial study. The dark I-V curve shows that each sample behaves as a diode; the illuminated I-V curve shows that each sample responds to light. A closer look at the 4th quadrant is provided in Figure 5.11 along with a graph of the photocurrent versus voltage (photocurrent

SIONYX1403000043.0091

SAMSUNG EX. 1002 - 734/4148

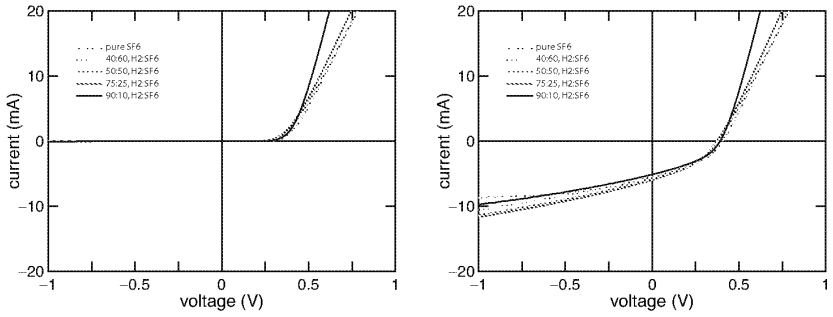


Figure 5.12: Dark (*left*) and illuminated (*right*) current-voltage curves for samples irradiated in a mixture of H_2 and SF_6. Samples are irradiated with 100 pulses/area at a Fluence of 4 kJ/m^2. The results show that with these laser conditions, H has no effect on photovoltaic properties.

= dark current − illuminated current).

Based on these results, it appeared that the incorporation of hydrogen improved the photovoltaic properties of the solar cells. As the percentage of hydrogen increased, the open circuit voltage, short circuit current and photocurrent all increased. However, when the experiment was repeated with slightly different laser parameters (fluence = 4 kJ/m^2 and pulses/area = 100) we discovered that the partial pressure of H_2 has very little effect on photovoltaic properties.

Figure 5.12 and 5.13 shows that the dark and illuminated I-V curves as well as the generated photocurrent are nearly identical for all partial pressures of H_2, when the samples are irradiated with 100 pulses/area at a Fluence of 4 kJ/m^2. Although all of the curves are similar in Figures 5.12 and 5.13 they show a marked improvement in photovoltaic properties over the same samples made with 200 pulses/area at a Fluence of 5 kJ/m^2 shown in Figures 5.10 and 5.11.

The key difference between 200 pulses at 5 kJ/m^2 and 100 pulses at 4 kJ/m^2 is the resulting surface morphology of the sample. Figure 5.14 shows the difference in surface

SIONYX1403000043.0092

SAMSUNG EX. 1002 - 735/4148

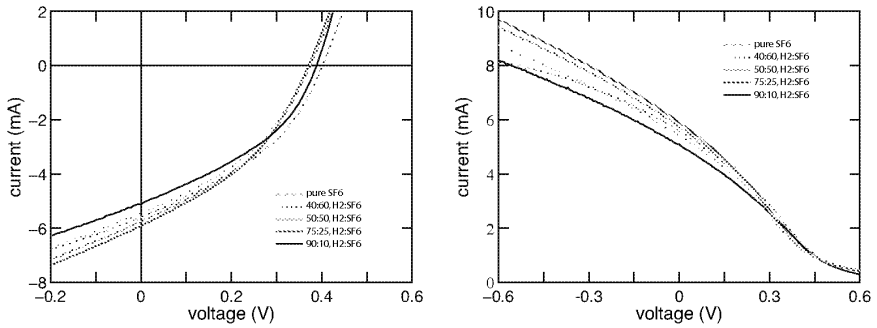


Figure 5.13: *Left* illuminated current-voltage curves for samples irradiated in a mixture of H_2 and SF_6. *Right* Photocurrent versus voltage curves of samples irradiated in a mixture of H_2 and SF_6. Samples are irradiated with 100 pulses/area at a Fluence of 4 kJ/m^2. The results show that with these laser conditions, H has no effect on photovoltaic properties.

morphology between 200 pulses/area at 5 kJ/m^2 and 100 pulses/area at 4 kJ/m^2. At 4 kJ/m^2, the surface is much smoother than samples irradiated at 5 kJ/ m^2. In addition, at 4 kJ/m^2 there is very little difference between the surface roughness of the samples irradiated in pure SF_6 versus the samples irradiated in 90% H_2. Although at 5 kJ/m^2, H_2 dilution causes a large change in surface morphology. The explanation for these observations is that previous work determined that spike formation occurs only for fluences greater than 4 kJ/m^2. In addition, we know that the resulting shape and size of the spikes depends on the type of gas. Based on these observations and the results presented in Figures 5.12 and 5.13, we can conclude that a lower surface roughness is better for photovoltaic performance.

There are several reasons that the above conclusion makes sense. A lower surface roughness will provide a less torturous path for charge carriers to travel from the laser modified surface region to the top metal electrode. In addition, the top metal electrode will form a more uniform layer on a surface with lower surface roughness. The second point is important for how we make contact to the top electrode in our experimental setup. We use a spring loaded metal probe to press down on the top electrode. We will achieve better

SIONYX1403000043.0093

SAMSUNG EX. 1002 - 736/4148

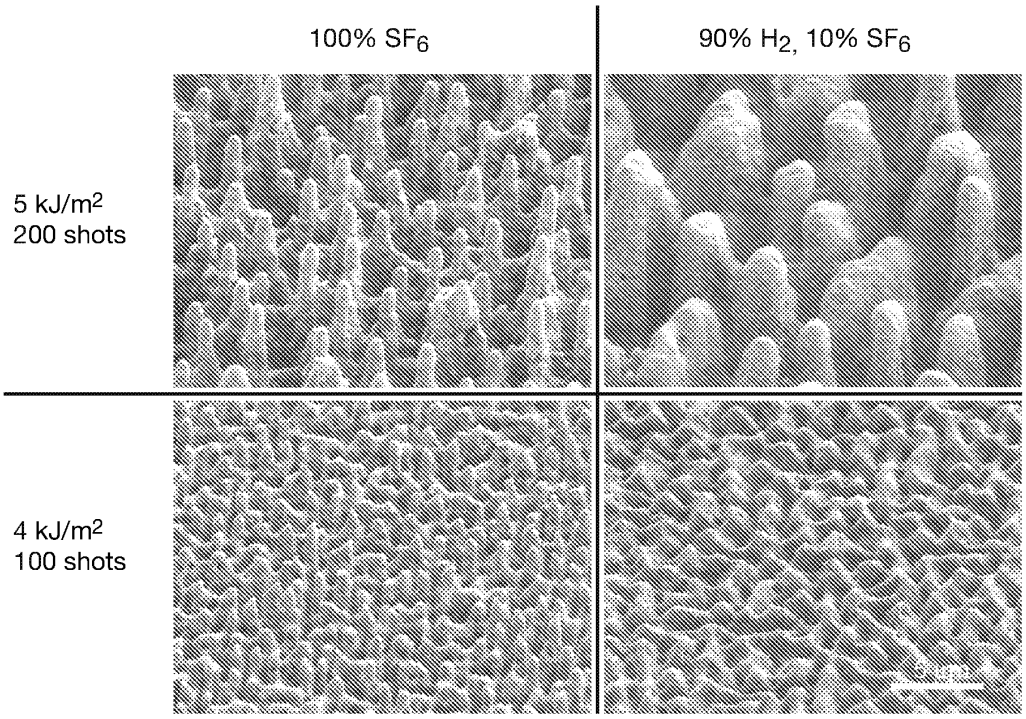


Figure 5.14: Surface morphology of samples irradiated with 200 pulses/area at a fluence of 5 kJ/m^2 (*top row*) and 100 pulses/area at 4 kJ/m^2 (*bottom row*). At 5 kJ/m^2 the there is a large difference in surface morphology between the samples irradiated in pure SF_6 and those diluted with 90% H_2; at 4 kJ/m^2, all samples look similar. Images taken with samples at 45°.

contact with a flatter surface morphology. Figure 5.15 shows the damage caused by our metal probe for both surface morphologies.

To conclude our discussion of the effect of H_2 gas and surface morphology on the photovoltaic properties of femtosecond laser irradiated silicon we present Figure 5.16. As the SF_6 is diluted by H_2, the surface slowly transitions from a surface morphology that is typical for SF_6 to the surface morphology that is typical for H_2. From our previous work we know that the surface features formed in H_2 are more blunt, larger and less densely spaced than those features formed in SF_6. So in effect, as we dilute with H_2 gas, we are creating

SIONYX1403000043.0094

SAMSUNG EX. 1002 - 737/4148

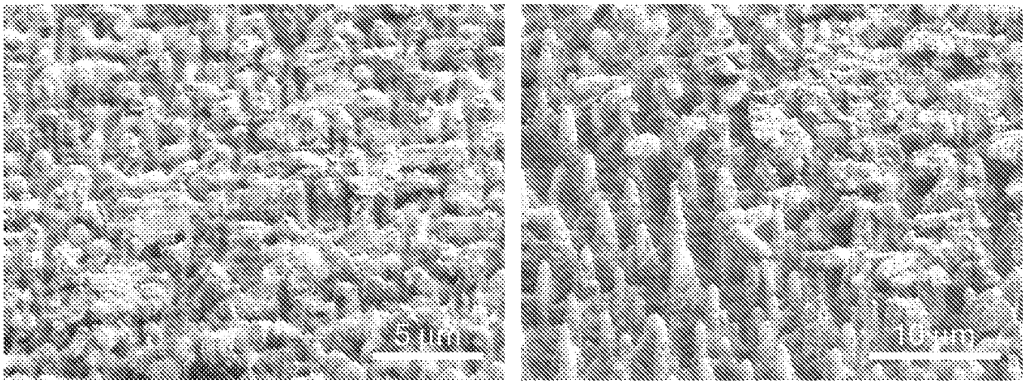


Figure 5.15: Images of the damage caused by contact of our metal probe with the top electrode of samples irradiated in pure SF_6 with 100 pulses/area at 4 kJ/m^2 (*left*) and 200 pulses/area at 5 kJ/m^2 (*right*). Images taken with samples at 45°.

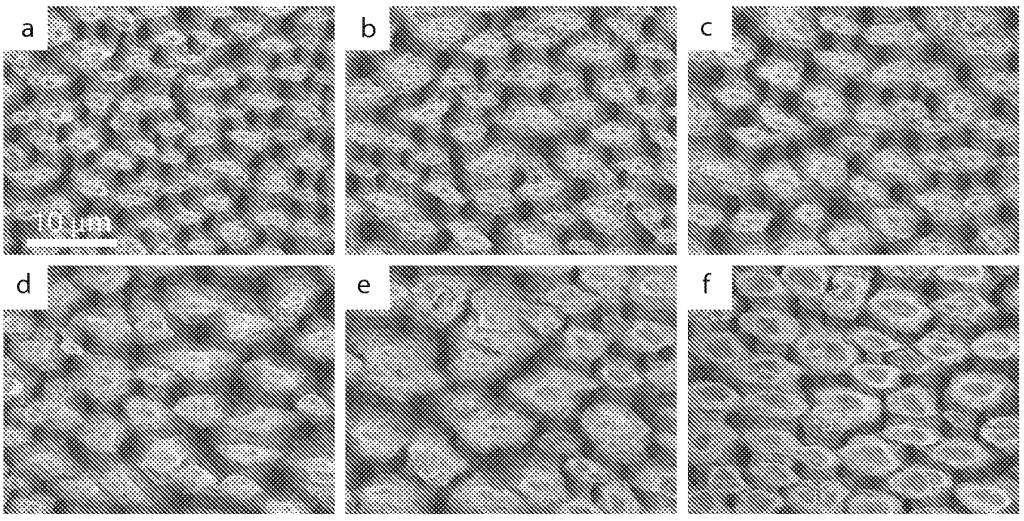


Figure 5.16: Surface morphology of samples irradiated with 200 pulses/area at a fluence of 5 kJ/m^2 at a pressure of 500 Torr for different ratios of H_2:SF_6 gas; (a) 0:100, (b) 10:90, (c) 25:75, (d) 50:50, (e) 75:25, (f) 90:10. Images are the top view of the samples.

a surface that has an overall lower surface roughness which is responsible for the increased photovoltaic performance indicated by Figures 5.10 and 5.11.

SIONYX1403000043.0095

SAMSUNG EX. 1002 - 738/4148

5.4.5 Creating a lower roughness laser-irradiated surface

Silicon irradiated in SF_6

As we determined in the previous section, a flatter surface morphology is better for photovoltaic properties. With this in mind, we set out to create the flattest surface possible that still absorbed a large portion of the sun's spectrum. We varied two laser parameters, fluence and pulses/area. Then we imaged the surfaces with a scanning electron microscope and measured absorptance using the same spectrophotometer used in Chapter 4.

First we chose a fixed fluence of 4 kJ/m^2 and irradiated samples with different pulses/area. We increased the spot size of the laser from the typical value of 150 μm to 250 μm full-width-half maximum (FWHM) but kept the step size the same at 75 μm (the step size being the distance between neighboring rows along which the center of the laser beam has traveled). By increasing the spot size, we reduced the step size to 1/3 of the spot size, with the goal being to create a flatter more uniform laser modified surface layer. The translation speed of the silicon wafer was 750 μm/s. In order to create a different number of pulses/area, a mechanical shutter was used to reduce the repetition rate of the laser (1000 Hz) to lower values (10–60 Hz) while keeping the translation speed constant. With this method the average number of pulses/area can be determined by,

$$pulses/area = \frac{\nu d^{spot}}{v}, \tag{5.5}$$

where ν is the repetition rate of the laser (or shutter), d^{spot} is the FWHM of the laser spot along the direction of translation and v is the translation speed. Then we fixed the number of pulses/area at 7 and varied the fluence from 4–12 kJ/m^2. The spot sized needed to be reduced to 180 μm in order to create the larger fluences and likewise we reduced the step size to 50 μm.

SIONYX1403000043.0096

SAMSUNG EX. 1002 - 739/4148

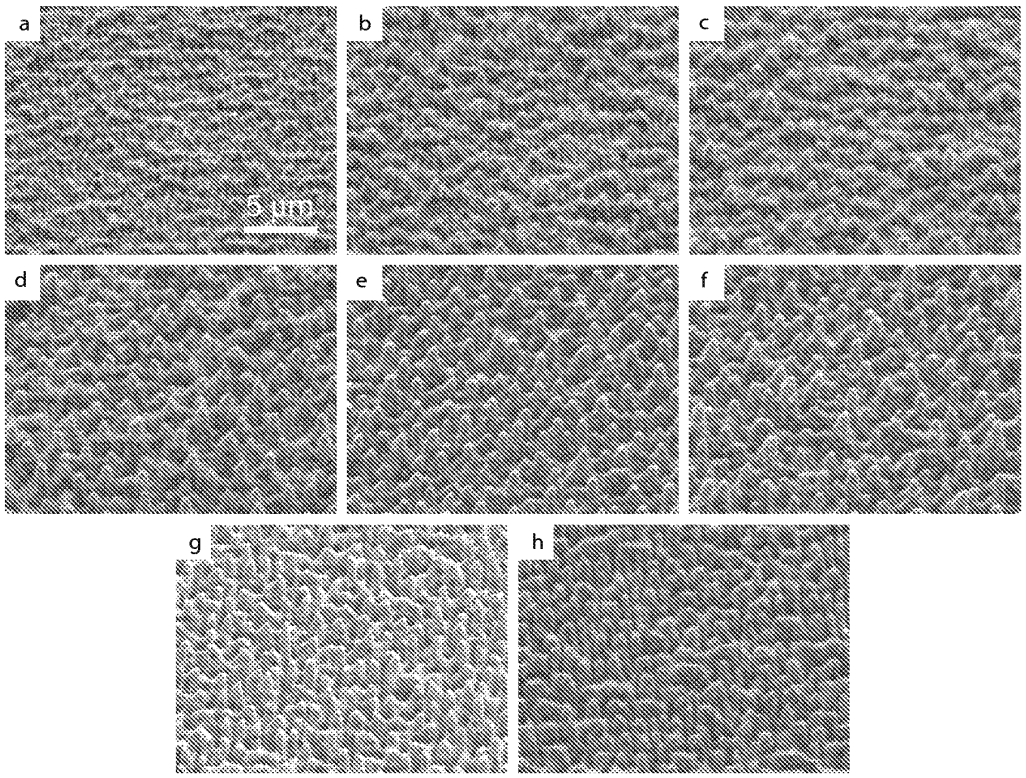


Figure 5.17: Surface morphology of samples irradiated with a fluence of 4 kJ/m^2 in 500 Torr of SF_6 gas for different pulses/area (a) 2, (b) 4, (c) 6, (d) 11, (e) 17, (f) 22, (g) 100, (h) 333. Spot size = 250 μm for all samples but (h) which was 150 μ. Images taken with samples at 45°.

Figure 5.17, shows scanning electron microscope images for samples irradiated with 2, 4, 6, 11, 17, 22, 100 and 333 pulses/area at a fluence of 4 kJ/m^2. The result is surprising. The surface roughness of the samples that were irradiated with 2, 100 and 333 pulses/area are all very similar; however, for the samples irradiated with 4–22 pulses/area, the surface features increase in size with increasing number of pulses.

This result changes our view of how spikes form. In our previous work [43], low numbers of pulses/area were performed for only a single fluence, 8 kJ/m^2 and the onset of

SIONYX1403000043.0097

SAMSUNG EX. 1002 - 740/4148

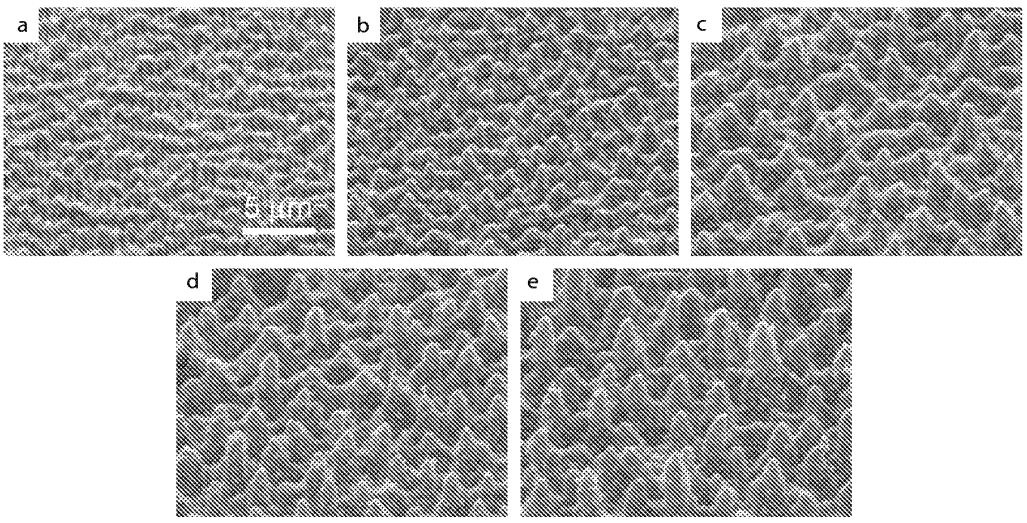


Figure 5.18: Surface morphology of samples irradiated with 7 pulses/area in 500 Torr of SF_6 gas for different fluences (a) 4, (b) 6, (c) 8, (d) 10, (e) 12. Spot size = 180 μm for all samples. Images taken with samples at 45°.

spike formation began between 10–15 pulses and spike height continued to increase up to 600 pulses. For a fluence of 4 kJ/m^2, only 500 pulses/area were performed and no spikes were observed. Based on these results, it was concluded that spikes do not form at a fluence of 4 kJ/m^2 [43]. However, the current results show this is not the case. Spikes do begin to form, but they then disappear after a large number of pulses. The reason for this result is unknown.

Figure 5.18, shows scanning electron microscope images for samples irradiated with 7 pulses/area at fluences of 4, 6, 8, 10 and 12 kJ/m^2. The size of surface features increases with increasing fluence.

Figure 5.19, shows the absorptance of each of the above samples shown in Figures 5.17 and 5.18. The data from the two studies are consistent with each other. The absorptance for the sample irradiated at 4 kJ/m^2 with 6 pulses/area in the fixed fluence

SIONYX1403000043.0098

SAMSUNG EX. 1002 - 741/4148

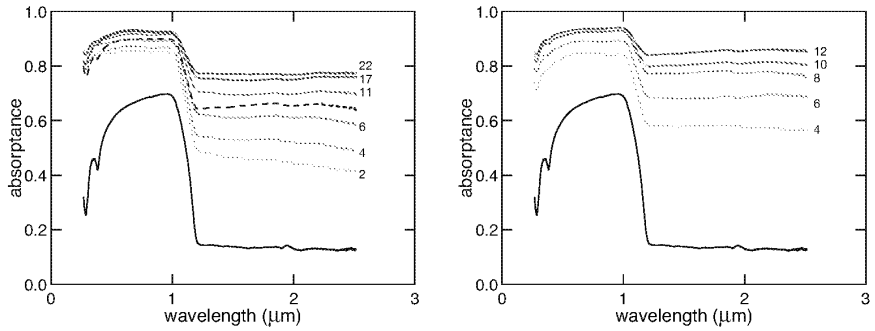


Figure 5.19: *Left:* Absorptance spectra of samples irradiated at a fixed fluence of 4 kJ/m^2 with varied pulses/area which are indicated. The dashed curve is for 333 pulses/area. *Right:* Absorptance spectra of samples irradiated with a 7 pulses/area for different fluences which are indicated in kJ/m^2.

study matches the absorptance of the sample irradiated at 4 kJ/m^2 with 7 pulses/area in the fixed pulses/area study. Absorptance seems to be correlated with the height of surface features in all cases, which is consistent with previous results [43]. The absorptance of the sample irradiated at 4 kJ/m^2 with 333 pulses/area is unusually low compared to our previous results and the results in Chapter 4 as well. The reason for this is unknown.

The conclusion of these two studies is that the surface roughness of samples irradiated with 100 pulses/area at a fluence of 4 kJ/m^2 is as flat as any that were created in this study. In addition, the absorptance of samples irradiated with 100 pulses at 4 kJ/m^2 is larger than any created in this study (for an example of the absorptance see Figure 4.1). As a result, 100 pulses/area and 4 kJ/m^2 were chosen as the standard conditions for many results in this chapter. These results are important as they illustrate the fact that surface morphology is a more complicated function of fluence and pulses/area than was previously thought.

SIONYX1403000043.0099

SAMSUNG EX. 1002 - 742/4148

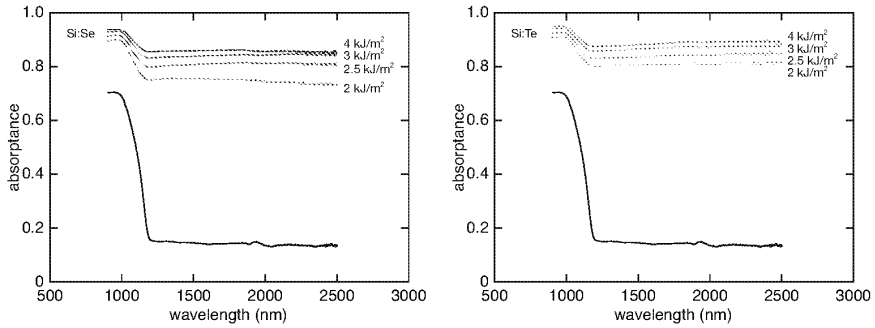


Figure 5.20: Absorptance spectra of samples coated with selenium (*left*) and tellurium (*right*) and irradiated with fluences varying from 2–4 kJ/m^2 with 100 pulses/area in a background gas of 500 Torr of N_2.

Obtaining low surface roughness for silicon coated with Se or Te and irradiated in N_2

In Figure 4.11, we saw that the infrared absorptance of tellurium-doped samples remained high at fluences as low as 1.5 kJ/m^2, below the ablation threshold of silicon. We concluded that the ablation dynamics are different for samples that are coated with a different material. In this section we investigate the optimal laser fluence for creating a highly absorbing surface layer with low surface roughness.

We irradiated silicon wafers coated with 150 nm of either selenium or tellurium in a background gas of N_2 at 500 Torr using 100 pulses/area for the following fluences: 4, 3, 2.5, 2 kJ/m^2. The films were deposited by thermal evaporation as described in Section 4.7.1. The resulting surface morphologies and optical properties are given in Figures 5.21 and 5.20.

The fluence that results in the minimum spike formation while retaining a relatively high infrared absorptance is 3 kJ/m^2 for selenium-coated samples and 2.5 kJ/m^2 for tellurium-coated samples.

SIONYX1403000043.0100

SAMSUNG EX. 1002 - 743/4148

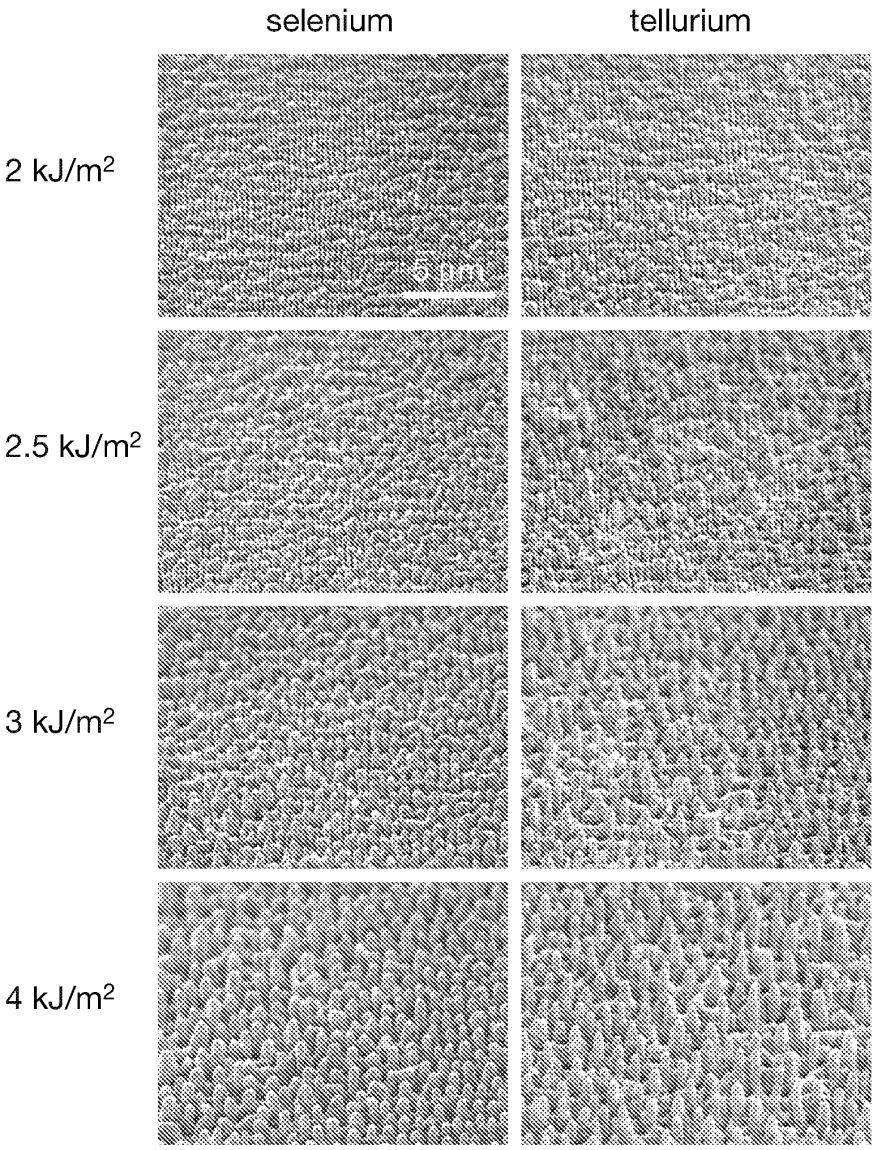


Figure 5.21: Scanning electron microscope images of selenium and tellurium-coated samples irradiated with fluences varying from 2–4 kJ/m^2 with 100 pulses/area in a background gas of 500 Torr of N_2. Images taken with samples at 45°.

SIONYX1403000043.0101

SAMSUNG EX. 1002 - 744/4148

5.4.6 Irradiating thin film silicon

In this section we present the results from irradiating thin films of silicon. The goal was to enhance the visible and infrared absorptance of silicon films to the same degree that is observed for femtosecond laser irradiated silicon wafers. Thin films of silicon were grown by two different methods: electron beam heating evaporation and hot-wire chemical vapor deposition (CVD).

Irradiating electron beam grown films

Several Si(100) wafers, *p*-type (ρ = 1–20 Ω-cm) were mechanically ground into powder and placed into a graphite crucible to be used as the source for electron beam heating evaporation in high vacuum. A film of silicon ($\sim$ 1.3μm thick) was grown on a clean glass microscope slide. The film was gray with a mirror finish.

The sample was loaded into the irradiation chamber, which was then evacuated and filled with 500 Torr of SF_6 gas. The laser was focused to a spot size of 150 μm. We varied the fluence and repetition rate of the laser in order to create a laser modified surface layer in the film and avoid completely ablating away the film. A fast mechanical shutter was used to vary the repetition rate of the laser. The sample was translated at a velocity of 1500 μm/s. Using the standard repetition rate of the laser (1000 Hz), Equation 5.5 can be used to determine that an average of 100 pulses/area hit the surface. Using a mechanical shutter frequency of 10 Hz and 20 Hz, the pulses/area can be reduced to 1 and 2 respectively.

The results are displayed in Figure 5.22. Based on the absorptance curve of the unirradiated film, we can determine that the silicon film is amorphous. Amorphous silicon's band gap (1.75 eV) is greater than crystalline silicon (1.12 eV) and its absorptance begins to decrease at smaller wavelengths of light ($<$ 700 nm). Growing an amorphous film is expected as our growth substrate is amorphous. Typically, growing a thin film of crystalline silicon

SIONYX1403000043.0102

SAMSUNG EX. 1002 - 745/4148

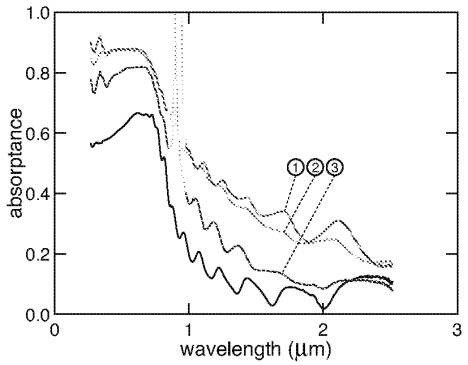


Figure 5.22: Absorptance spectra of femtosecond laser irradiated silicon films grown by electron beam heating evaporation. The laser conditions were: (1) 2 pulses/area at 4 kJ/m^2, (2) 1 pulse/area at 5 kJ/m^2, and (3) 1 pulse/area at 3 kJ/m^2. The dotted regions of the curves indicate a measurement anomaly near where the detector change occurred in the spectrophotometer. The bottom curve is the absorptance of the unirradiated film. The films are amorphous silicon and are initially 1.3 μm thick.

requires tailored experimental conditions such as substrate temperature and growth rate.

Based on the results we were able to increase the infrared absorptance by a factor of 2–3 times. Extremely low pulses/area were necessary in order to avoid destroying the film. The hills and valleys in the data are caused by thin film interference. The film thickness (1.3 μm) is on the order of the wavelength of the light and constructive and destructive interference occurs in the transmittance and reflectance signals in the near infrared range. These features should disappear when the light is incident at the same angle for transmittance and reflectance; some misalignment was present for all of our measurements.

Irradiating CVD grown films

Thin films of silicon were grown on 1 $\times$ 1 inch squares of glass by hot-wire chemical vapor deposition by the Atwater research group at the California Institute of Technology [120]. A tungsten wire is heated by resistive heating and brought in close proximity to

SIONYX1403000043.0103

SAMSUNG EX. 1002 - 746/4148

the substrate in a mixed atmosphere of silane (SiH_4) and hydrogen (H_2) gas. The films measured 2.1 μm thick using a profilometer.

The samples were loaded into the evaporation chamber which was evacuated and filled with 500 Torr of SF_6. The laser was focused to a spot size of 150 μm. The translation speed was fixed at 750 μm/s and the fluence, and number of pulses/area were varied in order to create an irradiated sample with the largest infrared absorptance.

An additional variable was used in this study to vary the pulses/area. The length of time that the fast mechanical shutter remained open was varied so that instead of a single pulse being delivered to the surface at the repetition rate of of the mechanical shutter, a burst of pulses could be delivered. Each time the shutter opens constitutes a single burst of pulses.

Figure 5.23, shows the results of irradiating 10 large areas of the film (6 mm $\times$ 8 mm) which were then analyzed with our spectrophotometer. Table 5.3 lists all the laser conditions that were attempted. Many conditions resulted in complete destruction of the film. The laser conditions used to make the samples in Figure 5.23 are indicated by the numbers 1–10.

To determine the pulses/area, Equation 5.5 is modified to accommodate the new variable pulses/burst, N_{burst}:

$$pulses/area = \frac{\nu d^{spot}}{v} \times N_{burst} \tag{5.6}$$

where ν is the repetition rate of the shutter (or laser when no shutter is used), d^{spot} is the diameter of the spot and v is the translation velocity of the sample.

Although the film was meant to be crystalline, we can see from the absorptance spectrum of the unirradiated film that it is also amorphous just like the film grown by electron beam evaporation. The CVD process used by the Atwater research group is usually

SIONYX1403000043.0104

SAMSUNG EX. 1002 - 747/4148

Sample No.	Fluence	Rep. rate	Pulses/burst	Pulses/area	Step size	Transparent
–	8 kJ/m^2	1000 Hz	1	200	50 μm	yes
–	7.5 kJ/m^2	25 Hz	10	50	50 μm	yes
–	7 kJ/m^2	25 Hz	10	50	50 μm	yes
–	7 kJ/m^2	25 Hz	5	25	50 μm	yes
–	7 kJ/m^2	25 Hz	3	15	50 μm	yes
–	6.5 kJ/m^2	20 Hz	5	20	50 μm	yes
–	6.5 kJ/m^2	15 Hz	4	12	50 μm	yes
–	6.5 kJ/m^2	10 Hz	4	8	50 μm	mostly
–	6 kJ/m^2	1000 Hz	1	200	50 μm	yes
–	6 kJ/m^2	20 Hz	5	20	50 μm	yes
–	6 kJ/m^2	15 Hz	4	12	50 μm	mostly
–	6 kJ/m^2	10 Hz	4	8	50 μm	barely
–	5.5 kJ/m^2	20 Hz	5	20	50 μm	yes
–	5.5 kJ/m^2	15 Hz	4	12	50 μm	barely
1	5.5 kJ/m^2	10 Hz	4	8	50 μm	no
–	5 kJ/m^2	20 Hz	5	20	50 μm	barely
2	5 kJ/m^2	15 Hz	4	12	50 μm	no
5	5 kJ/m^2	10 Hz	4	8	50 μm	no
3	4.5 kJ/m^2	20 Hz	5	20	50 μm	no
7	4.5 kJ/m^2	15 Hz	4	12	50 μm	no
8	4.5 kJ/m^2	10 Hz	4	8	50 μm	no
4	4 kJ/m^2	25 Hz	10	50	50 μm	no
6	4 kJ/m^2	20 Hz	5	20	75 μm	no
9	4 kJ/m^2	10 Hz	4	8	75 μm	no
10	4 kJ/m^2	10 Hz	2	4	75 μm	no

Table 5.3: Summary of laser conditions used in an attempt to create a laser modified surface layer on the CVD grown silicon film. The sample number refers to the number used in Figure 5.23. The comment under the column "Transparent" indicates whether visible light could be seen through the film using an optical microscope.

SIONYX1403000043.0105

SAMSUNG EX. 1002 - 748/4148

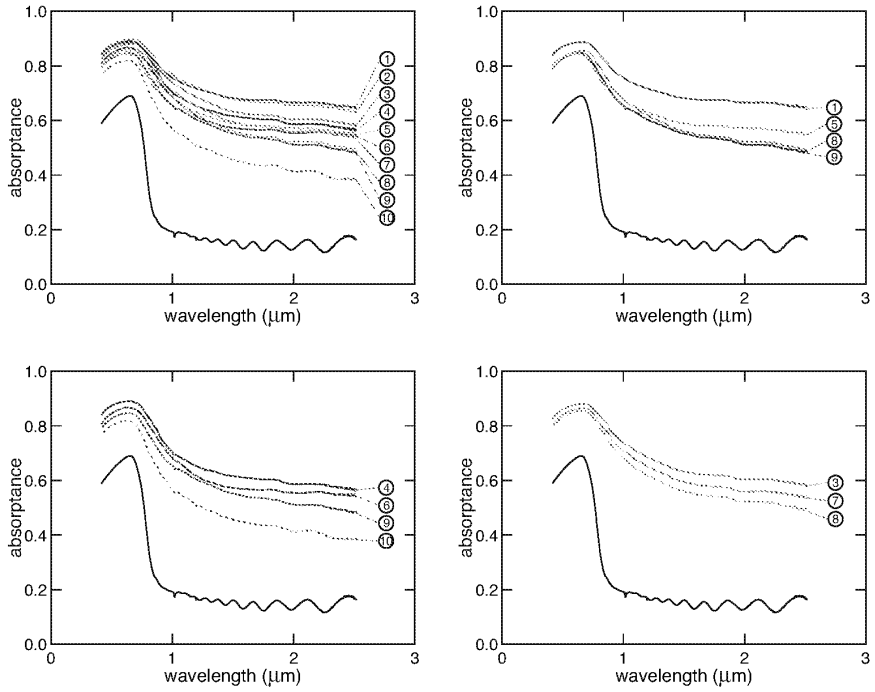


Figure 5.23: Absorptance spectra of femtosecond laser irradiated silicon films grown by hot-wire chemical vapor deposition. *Upper left:* Absorptance spectra of all ten samples. See Table 5.3 for the laser parameters. *Upper right:* Absorptance spectra for samples irradiated with 8 pulses/area at four different fluences. *Lower left and right:* Absorptance spectra for samples irradiated at 4 kJ/m^2 (*left*) and 4.5 kJ/m^2 (*right*) at varying pulses/area. The bottom curve in each graph is the absorptance of the unirradiated film. The films are amorphous silicon and are initially 2.1 μm thick.

used to grow films on glass slides that already have a thin crystalline silicon layer grown by other means. It is likely that the process had not been attempted on bare glass as in this case.

The conclusion of these two studies is that thin film silicon can be modified by the laser to bring about enhanced visible and infrared absorption. In both cases, the film was too thin to increase the absorptance to near unity although we come close in the 2.1-μm thick film. We believe that as more energy is deposited in the film, too much material is

SIONYX1403000043.0106

SAMSUNG EX. 1002 - 749/4148

removed and the resulting laser modified surface layer is not as thick as the typical layer that is formed with the irradiation of silicon wafers. We predict that with an additional 1–2 μm of material it will be possible to increase the absorptance of thin film silicon to the same level as has been observed in femtosecond laser irradiation of silicon wafers.

5.5 Summary discussion

In this chapter, we show that sulfur-doped femtosecond laser irradiated silicon behaves as a solar cell immediately after irradiation. The photovoltaic properties of short circuit current and open circuit voltage (and therefore efficiency) improve significantly with increased annealing temperature to a maximum at $T = 1075$ K. Further increasing the annealing temperature beyond this point, results in a degradation of solar cell performance. The low fill factor of ~ 0.37 remains relatively constant for all annealing temperatures.

We propose a model to explain the change in open circuit voltage, short circuit current and fill factor with annealing temperature. We speculate that the open circuit voltage rises as a result of an increase in the internal voltage barrier of the junction allowing for a larger voltage drop when the solar cell is operated in the open circuit condition. An increase in the internal voltage barrier is consistent with our previous work showing that annealing increases the free electron concentration in the laser modified surface [43].

The reason that the free electron carrier concentration increases with annealing temperature is still unknown. We do know that the maximum in open circuit voltage is obtained after an annealing temperature that is 200 K above the temperature at which the enhanced infrared absorptance is completely reduced to the value of intrinsic silicon (as seen in Chapter 4). This result might suggest that diffusion of the sulfur does not seem to be related to the increase in free carrier concentration, but this is not conclusive.

SIONYX1403000043.0107

SAMSUNG EX. 1002 - 750/4148

It is possible that a general healing of defects in the laser modified surface layer as a result of annealing causes the activation of trapped donor electrons contributed by those sulfur atoms that still remain in the grains. Although in Chapter 4 we propose that annealing causes diffusion of sulfur out of the grains, this does not suggest that all of the sulfur atoms will eventually leave with annealing. The concentration of sulfur would remain at least as high as the solid solubility of sulfur in silicon ($\sim 10^{15}/\text{cm}^3$, [87]) at the temperature of the highest anneal. This level of concentration could still provide a significant amount of donor electrons, keeping in mind that sulfur has two more valence electrons than silicon.

The increase in short circuit current with annealing temperature could be due to an increase in the width of the depletion region (as the internal voltage barrier increases), resulting in more free carriers excited inside the depletion region. Also an increase in short circuit current could be due to the general healing of defects in the portion of the laser modified surface layer contained in the depletion region.

We propose that the low fill factor exhibited after all annealing temperatures is a result of an extremely small diffusion length of free carriers that are generated outside of the depletion region. A small diffusion length of free carriers yields a photogenerated current that is highly dependent on the width of the depletion region (and therefore the applied voltage). As the applied voltage is increased in the forward bias direction, the depletion region will shrink and the photogenerated current will decrease, resulting in a low fill factor. Although we speculate that a general healing of defects occurs with annealing, this may only have a profound effect within the depletion region, where photogenerated carriers are driven by drift in addition to diffusion.

In addition to annealing temperature, we also report the effect of hydrogen dilution, surface morphology and etching time on the photovoltaic properties. We also show that

SIONYX1403000043.0108

SAMSUNG EX. 1002 - 751/4148

the visible and infrared absorptance of thin films of silicon can be enhanced by femtosecond laser irradiation. The creation of femtosecond laser irradiated thin film silicon solar cells is an exciting area of future work.

SIONYX1403000043.0109

SAMSUNG EX. 1002 - 752/4148

Chapter 6

Summary and future directions

We investigated a diverse range of scientific and engineering concepts in this thesis, including: laser ablation, phase transformations, diffusion, semiconductor doping, solid state physics and photovoltaics.

We studied the nucleation and growth of single crystal silicon nanoparticles and the formation of amorphous silicon generated in the superheated and pressurized material ejected from the silicon surface. We commented on the fundamental differences in particle formation after femtosecond laser ablation in a near atmosphere background gas versus vacuum. We also observed interesting structures of coagulated particles such as straight lines and bridges.

We investigated the enhanced absorption of visible and infrared light exhibited by the resulting femtosecond laser irradiated surface after doping with three different elements (sulfur, selenium and tellurium) in a comprehensive annealing study. Our analysis suggests the decrease in absorptance with heat treatments is due to the diffusion of the dopants within the nanometer-sized grains of the polycrystalline surface to the grain boundaries.

We incorporated femtosecond laser irradiated silicon into a device and measured its

SIONYX1403000043.0110

SAMSUNG EX. 1002 - 753/4148

photovoltaic properties as a function of various parameters such as: annealing temperature, laser fluence, background gas, surface morphology and chemical etching. In addition, we explored the concept of using thin films of silicon as the irradiation substrate and successfully enhanced the visible and infrared absorption of films of silicon with thicknesses ≤ 2 μm.

Although we have made good progress studying the properties of this new material, there remain many unanswered questions and exciting avenues of research to explore with femtosecond laser irradiated silicon. These avenues cross many fields including solid state devices, biological sensors, superhydrophobicity and more. We mention those here that are relevant to this thesis.

Research can be performed to further understand the structure of the laser modified surface and the nature of dopants and defects in the crystalline grains. Using low temperature studies, the electronic levels of the dopant and its configuration with the lattice could be probed. Changes in these levels could be correlated to various experimental parameters such as annealing temperature, dopant chemistry, laser fluence, and pulses/area.

Much work needs to be done to characterize the properties of the diode junction, specifically as a function of the initial doping of the wafer. Over the course of this research, we learned that it was difficult to reliably repeat many electronic measurements using different silicon wafers. Although the general behavior was similar, the results could vary greatly for different experimental parameters, specifically annealing. To understand this behavior, we recommend extensive characterization of the initial silicon wafer's resistivity and dopant concentration with greater precision than is provided by the manufacturer. These measurements can then be used to obtain repeatable diode junctions.

In addition to work with sulfur, the diode characteristics of silicon doped with other elements such as selenium, and tellurium could lead to even better results for photodetector and photovoltaic devices, specifically in the detection and absorption of infrared

SIONYX1403000043.0111

SAMSUNG EX. 1002 - 754/4148

light. Selenium- and tellurium-doped samples absorb more infrared light than sulfur-doped samples after the same heating treatment.

A final research area with great promise is the prospect of enhancing the efficiency of thin film silicon solar cells through incorporation of a femtosecond laser modified surface layer. The laser modified region can be used in a device as a single junction or stacked in a series in a multi-junction design. The laser modified region would be particularly suited for use as the bottom layer in a multi-junction device in order to absorb all light that penetrates the upper layers. In addition, due to the small diffusion length of excited carriers in femtosecond laser irradiated silicon, incorporating it into a *p-i-n* configuration similar to the design used for thin film silicon could result in a significant increase in photovoltaic efficiency.

SIONYX1403000043.0112

SAMSUNG EX. 1002 - 755/4148

Appendix A

Operation of a solar cell

In order for a material to convert light into electrical energy, it must satisfy two conditions. First, it needs to be able to absorb incident photons through the promotion of electrons to higher energy levels. Second, it must contain an internal electric field that accelerates the promoted electrons in a particular direction, resulting in an electrical current. For more detailed information on the operation of solar cells see references [112, 113, 116, 118, 119].

A.1 The photovoltaic cell in an electrical circuit

From the most basic point of view, a photovoltaic cell can be thought of as any device—when exposed to light—that causes current to flow in an electrical circuit with a given load resistance (*e.g.* wires plus a light bulb). An example electrical circuit is shown in Figure A.1. The voltage drop across the front and back contact and the current in the circuit can be measured with a voltmeter and ammeter respectively. As would be expected, the magnitude of the electrical current depends on the intensity of the incoming light. But, in addition, the current also depends on the load resistance of the circuit.

SIONYX1403000043.0113

SAMSUNG EX. 1002 - 756/4148

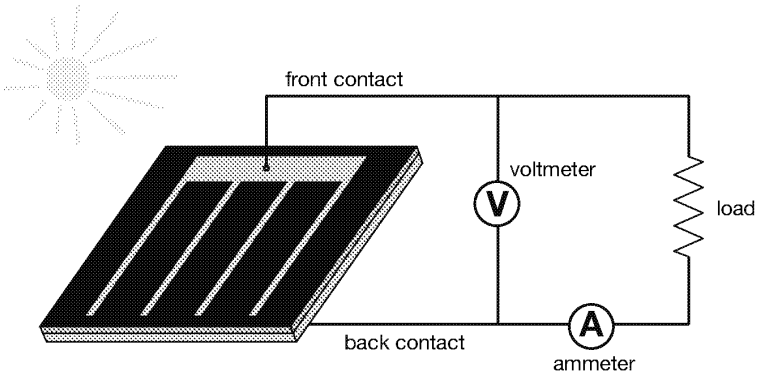


Figure A.1: A photovoltaic cell in a simple electrical circuit that allows the production of usable power.

For the following discussion, let us fix the intensity of the incoming light as T_l, and just vary the load resistance. If the resistance is infinite, the current will be zero. This is called the open circuit condition. In this case, the photons continue to generate pairs of electrons and holes within the photovoltaic material. The internal electric field separates the electrons and holes and accelerates them in opposite directions creating a voltage difference on either side of the photovoltaic cell. The magnitude of this voltage drop is called the open circuit voltage, V_{oc}. The open circuit voltage can change with the intensity of light, but for a given intensity, the voltage remains constant with time. The reason it remains constant, despite the fact that photons are continually absorbed, is that the generated electron-hole pairs recombine at a certain rate at defects and surfaces. Because of this, the open circuit voltage is a good measure for the quality of the photovoltaic cell—the higher the open circuit voltage, the more efficiently the cell can convert photons into electrical energy.

If the load resistance in the circuit shown in Figure A.1 is zero, then under a given intensity of light, the current that is generated will be at its maximum attainable value. Under these conditions the photovoltaic cell is said to be in its short circuit configuration

SIONYX1403000043.0114

SAMSUNG EX. 1002 - 757/4148

and the current is called the short circuit current, I_{sc}. Note that through $V = IR$, the voltage drop is also zero. The short circuit current is also limited by the recombination rate of the material and is a good measure of the quality of the photovoltaic cell. In order to maximize the efficiency of a photovoltaic cell, researchers and engineers attempt to maximize the open circuit voltage and short circuit current by removing recombination sites.

In between these two extremes—when there is a finite resistance in the circuit—the current and voltage are both less than their maximum values and are related to the load resistance through Ohms Law, $V = IR$. The power that is supplied as a result of the load resistance (*e.g.* the light bulb) is the product of the current and the voltage. For a higher load resistance, the voltage is increased but the current is decreased. For a lower load resistance, the voltage is decreased but the current is increased. Figure A.2 shows how the voltage and current of a circuit can vary as the load resistance is changed for a given amount of intensity of light. Rather than obtaining this curve by putting in various size resistors, the voltmeter, ammeter and resistor can all be replaced by a voltage/current source. By applying a voltage and measuring a current the same curve can be reproduced.

As can be seen from Figure A.2, there is a specific load resistance, that results in a certain current, I_{max}, and voltage, V_{max}, where the output power is a maximum. During the design of the circuit for photovoltaic cells the load resistance is specifically chosen to maximize the output power. The shape of the current-voltage curve, often called the I-V curve, greatly affects the resulting power output. To characterize the shape of the curve, researchers use a variable known as the fill factor, FF, which gives what fraction the maximum output power is of the product of the open circuit voltage and short circuit voltage.

$$FF = \frac{I_{max}V_{max}}{I_{sc}V_{oc}}. \tag{A.1}$$

SIONYX1403000043.0115

SAMSUNG EX. 1002 - 758/4148

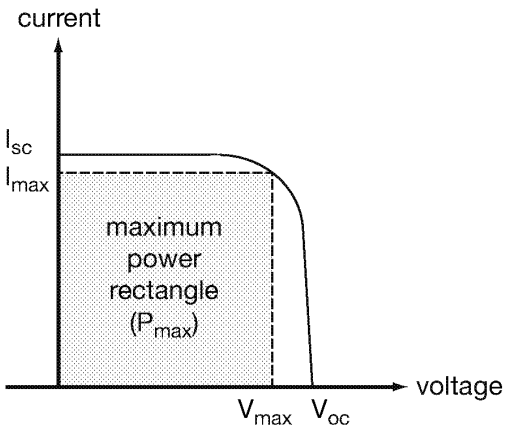


Figure A.2: The relationship between current and voltage in a photovoltaic cell

A typical fill factor is 0.8. The higher the fill factor, the better the solar cell, as this increases the maximum power output. The reason for the shape of the I-V curve will be discussed in subsequent sections.

With what we know already, it is possible to calculate the efficiency, η, of our photovoltaic cell. The efficiency is defined as the ratio of electrical power output to the power of the incident photons.

$$\eta = \frac{I_{max}V_{max}}{T_l A} \times 100\%, \tag{A.2}$$

Here T_l, is the intensity of the incoming light with the units of mW/cm^2, and A is the area of the photovoltaic cell in cm^2. Their product is the power of the incoming light, P_l. Combining Equations A.1 and A.2 we get,

$$\eta = \frac{(FF)I_{sc}V_{oc}}{P_l} \times 100\%. \tag{A.3}$$

This equation gives the efficiency using the variables, FF, V_{oc}, I_{sc}, which are used

SIONYX1403000043.0116

SAMSUNG EX. 1002 - 759/4148

to characterize a photovoltaic cell in research. These values can be obtained by measuring the *I-V* curve of the photovoltaic cell with a voltage source and ammeter. By varying voltage and measuring current, the load resistance is essentially varied from zero, at the highest current flow, I_{sc}, to infinity, at the highest voltage drop, V_{oc}. Maximizing the efficiency of a photovoltaic cell is the ultimate goal, as this maximizes the power output for a given intensity of incoming light. Efficiency values reported in research and industry are often for a solar intensity of air mass (AM) 1.5. This is the intensity of the sunlight on the earth after it passes through the atmosphere at 45°, which is roughly the average angle sunlight has over the course of the peak hours of the day. The intensity value for AM 1.5 is 100mW/cm^2. For a typical commercial silicon photovoltaic cell with properties $FF = 0.8$, $V_{oc} = 0.5$ V and $I_{sc} = 35$ mA/cm^2, the efficiency is 14%.

Now that we understand how a photovoltaic cell is treated in an electrical circuit let us take a closer look at the properties required by a material to be used as the active region in a photovoltaic cell.

A.2 Satisfying the two conditions required for a photovoltaic response

Whether a material satisfies the first condition, which requires that the material be able to absorb photons through electron promotion, depends on the energy of the incident light. For photovoltaic cells we are concerned specifically with the spectrum emitted by the Sun. The solar spectrum is shown in Figure A.3. As we can see in the graph, most of the photons coming from the sun are in the energy range of 1–4 eV. A material needs a band gap energy that is less than 4 eV in order to absorb these photons, otherwise there are no electron states available to accept the promoted electron during photon absorption. This requirement

SIONYX1403000043.0117

SAMSUNG EX. 1002 - 760/4148

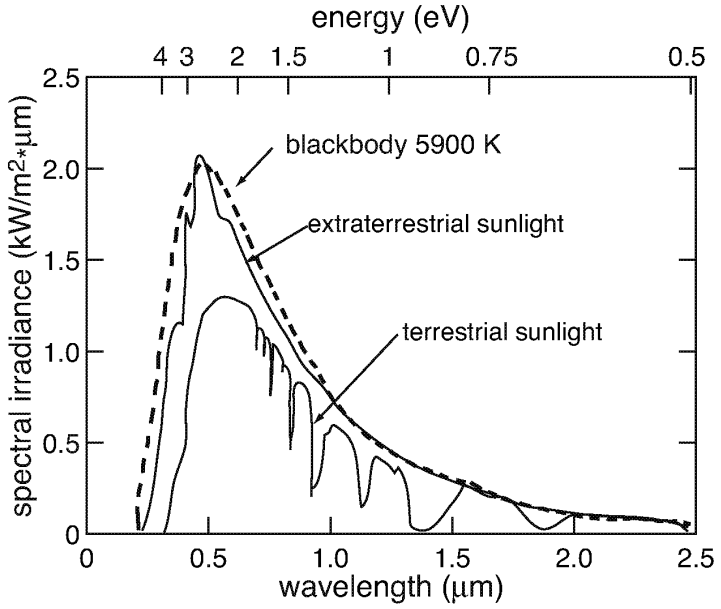


Figure A.3: Solar spectrum as it reaches earth in space (named AM 0) and after it passes through the earth's atmosphere at an angle of 45° to the surface (named AM 1.5). Dips in the intensity at specific wavelength are due to absorption by O_2, H_2O, and CO_2 in the atmosphere.

eliminates the use of insulators as a photovoltaic material, as the insulator/semiconductor transition is usually arbitrarily set at an energy band gap of 4 eV. However, in reality, the size of the band gap is even more limited. With a band gap energy of 3 eV the material would absorb less than half of the incoming photons. In order to maximize the number of photons absorbed and get the most electrical energy out of our solar cell, we should choose a material so its band gap has less energy than most of the incoming photons. This practical limit further narrows the material selection to materials with a band gap of less than ~ 2 eV.

The second condition, which requires that the material have an internal electric field, further limits the possible materials and contains most of the science of how a photo-

SIONYX1403000043.0118

SAMSUNG EX. 1002 - 761/4148

voltaic cell works. An all-metal photovoltaic cell is impossible as an internal electric field would never be stable. Even under an applied electric field, the electrons within a metal redistribute to counter the field so that the internal field is zero.

With the elimination of insulators and metals, we know that our photovoltaic cell must contain semiconductors in some way. In order to sustain an internal electric field, a stable charge gradient must be maintained in the material. The most common way to produce the internal electric field in all current photovoltaic cells is inside an inhomogeneous semiconductor or at the interface between two differently doped semiconductors with different band gaps.

A less common way to create the internal electric field is at the interface between certain metals and semiconductors, which, if chosen properly, create a field that allows current to flow in one direction but not the other. This is known as a Schottky barrier junction. The first solar cells made from selenium were Schottky barrier cells. While Shottky barrier cells are still under investigation today, they have never been made efficient enough or cheap enough to be used in a practical photovoltaic cell. All photovoltaic cells do indeed use metal/semiconductor interfaces as a part of their design to attach the active photovoltaic medium to a larger circuit with electrodes. However, the materials making up this interface are chosen so that the interface is considered an "ohmic contact," which contains no barrier to electron flow.

We will now discuss how the internal electric field is created.

A.3 Creating the internal electric field

The electric field is created by a spatial separation of charge inside solid material, which is stable and exists without the application of any external fields. It also exists

SIONYX1403000043.0119

SAMSUNG EX. 1002 - 762/4148

whether or not the material is exposed to light. In a single semiconductor material this field is generated by a doping gradient inside the material. The simplest form of this is the p-n junction from semiconductor physics. One side of the semiconductor contains n-type doping where the impurity atoms are donor atoms—which have one additional valence electron—and the opposing side contains p-type doping where the impurity atoms are acceptor atoms–which have one less valence electron and can easily accept a neighboring electron (i.e. a hole). The majority carriers in the n-type side are electrons and the majority carriers in the p-type side are holes. For a discussion on the nature of p-type and n-type semiconductors, please see reference [4], Chapter 29.

As an example let us take silicon. For silicon, boron is an acceptor atom and phosphorous is a donor atom. To make a p-n junction in silicon, typically boron is present in the silicon melt at a specific concentration and remains there as it crystallizes. Single crystalline, polycrystalline, amorphous and microcrystalline silicon can all be used to make solar cells. We will initially discuss single crystalline here and discuss the others in the Research section.

The single crystal of boron-doped silicon is sliced into thin wafers ~ 300 micrometers thick. Each wafer is exposed on one side to a heated phosphorous containing gas. The phosphorous atoms diffuse into the surface of the silicon resulting in a higher concentration than the boron. This creates a net n-type region where the majority carriers are electrons. This n-type region extends several micrometers into the surface. The p-n interface is a plane parallel to the wafer and several microns from the n-type side. By monitoring the conditions closely a uniform interface can be obtained.

For simplicity, in the following discussion we will consider an ideal p-n junction, which is one where the doping concentration changes abruptly in the silicon from n-type to p-type.

SIONYX1403000043.0120

SAMSUNG EX. 1002 - 763/4148

The mere presence of the varied concentration of impurity atoms is not enough to explain the electric field. Both the impurity atoms and the host atoms are electrically neutral. The electric field is generated by diffusion of majority carriers. With electrons as the majority carriers on the n-side and holes as the majority carriers on the p-side, a carrier concentration gradient is set up, which is the driving force for the diffusion. Those additional electrons on the n-side within a few 100 nm of the p-n interface diffuse from the n-side to the electron deficient p-side, where they recombine with holes in the hole-rich p-side. Let us look closely at the effect of this first step. The additional electrons in the n-side were provided by neutral phosphorous atoms. When the electrons diffuse in large numbers over 100 nm, they leave behind positive phosphorous ions. When these electrons recombine with holes on the p-side, this results in a region of depleted charge a few 100 nm into the p-side. In the region of depleted charge the carrier concentration is much lower than in the p-type and n-type material far from the interface.

Likewise the holes diffuse in the opposite direction from the p-side into the n-side. This leaves behind a several 100 nm thick region with negative boron ions and creates a charge depleted region several 100 nm into the n-side. The result of both of these effects is that a depleted region several 100 nm in length is formed on either side of the p-n interface, where the carrier concentration is very low. In addition, positive ions are left behind on the n-side of the p-n interface and negative ions are left on the p-side. The ions create an electric field which points from the n-side to the p-side as well as a voltage drop $\Delta\phi$ (from the n-side to the p-side) which are related through $E = -d\phi/dx$. This field exists without any applied voltage or field and without exposure to light. Figure A.4 summarizes how the depletion region forms an electric field.

It may be confusing why the diffusion of delocalized (conduction band) electrons or holes leaves behind charged ions, as this is never discussed under conditions of normal

SIONYX1403000043.0121

SAMSUNG EX. 1002 - 764/4148

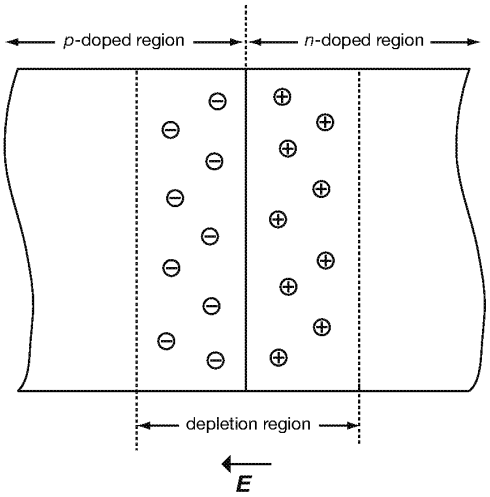


Figure A.4: The diffusion of majority carriers creates the depletion region. Positive phosphorous ions are left behind on the n-side and negative boron ions on the p-side.

current flow in a metal or semiconductor. The reason for this is that when the carriers are only being influenced by the electrostatic force of the underlying nuclei and core electrons, their spatial density is uniform everywhere. So they still cancel out the charge of the nuclei when averaged over volume. Even when current is flowing, as long as no charge is accumulating anywhere, the spatial density of the carriers will perfectly balance the charge of the nuclei resulting in no net electric fields. In the case of the p-n junction, there is an additional force acting on the carriers besides the electrostatic force. This additional force is a chemical potential gradient. The material will lower its free energy if the delocalized electrons on the n-side diffuse into the p-side (and vice-versa for holes). Now when the spatial density of the carriers is averaged over the volume of the depletion region their collective charge does not balance out the underlying nuclei. On the n-side of the depletion region there are not enough electrons to balance out the additional protons in the phosphorous atoms. The same is true for the holes on the p-side and therefore an

SIONYX1403000043.0122

SAMSUNG EX. 1002 - 765/4148

electric field is present.

The electric field that is generated perfectly balances the driving force for diffusion. If diffusion is not countered, all the additional electrons from the n-side would recombine with holes on the p-side. Let us look at this more closely. From the diffusion force, electrons want to flow from the electron-rich n-side to the p-side (and vice-versa for holes). These electrons and holes leave neutral atoms creating ions. The ions left behind generate an electric field, which applies a force on electrons so that they flow from the negatively charged boron ions on the p-side to the positively charged phosphrous ions on the n-side (the opposite occurs for holes). These two competing effects limit the depletion region to a certain size. At a certain point the energy gained by diffusion is perfectly balanced by the energy spent creating the electric field. The two important aspects of the depletion region are that it defines the spatial extent of the electric field and it is the region where the charge carriers are drastically reduced due to recombination.

Electron-hole pairs that are generated within the electric field through the absorption of photons or through thermal excitation will separate; the electrons will accelerate toward the positive phosphorous ions on the n-side and holes will accelerate toward the negative boron ions on the p-side. In a typical solar cell, the n-side faces the sun and finger-like metal electrodes are patterned on the surface to allow the maximum amount of sunlight through but still provide a metallic pathway for electron flow. Electrons flow toward the top of the solar cell, while holes flow in the opposite direction. The backside of the solar cell has a solid metal contact to complete the circuit.

Electron-hole pairs generated outside of the depletion region actually contribute most of the carriers to the photocurrent. This happens through diffusion of the photo-excited carriers to the edge of the depletion region where they are swept to the other side. This process contributes significantly to the resulting photocurrent as silicon, with

SIONYX1403000043.0123

SAMSUNG EX. 1002 - 766/4148

its indirect band gap, is not a strong absorber of light. In order to absorb enough of the incident photons, silicon wafers in solar cells need to be greater than 100 μm thick. They are typically 300 μm thick by convention as it is a good thickness for handling.

A.4 The *I-V* characteristics of the *p-n* junction

In this section we will discuss how the shape of the *I-V* curve shown in Figure A.2 comes about. We will start by defining a direction of positive current, j, across our solar cells *p-n* junction. To be consistent with most solid-state textbooks, we choose that positive current is current flowing from the *p*-side to the *n*-side, which we call the positive x-direction (note that holes flow with current and electrons against). We will see later that this actually results in the sun inducing a current in solar cells that is negative and researchers refer to the solar cell operating in the "4th quadrant" of the *I-V* curve, where current is negative and voltage is positive. The negative sign only indicates direction with respect to a reference system and has no other meaning.

With a direction of positive current, we can define the flow of holes and electrons across the *p-n* junction. We will use the symbol j for electrical current density and J for number current density after the fashion of reference [118], Chapter 29, so that,

$$j = j_h - j_e, \quad j_e = -eJ_e, \quad \text{and} \quad j_h = eJ_h. \tag{A.4}$$

Note that j_e is the portion of the electrical current density caused by the flow of electrons; this is why it contains a negative sign. Positive values of J_e and J_h indicate that the electrons or holes are flowing in the positive x-direction across the *p-n* junction (from *p* to *n*).

To better understand the competing forces of diffusion and the internal electric

SIONYX1403000043.0124

SAMSUNG EX. 1002 - 767/4148

field, we will name the flow of carriers depending on their direction. A flow of electrons from the p-side to the n-side under the force of the electric field is known as the electron generation current, J_e^{gen}. It is so named because there are very few conduction electrons on the p-side—they are the minority carriers—and any electrons that flow from the p-side to the n-side are likely generated by thermal excitation or photon absorption. As soon as they are generated and enter the depletion region they are swept to the other side by the electric field. Likewise, a flow of holes from the n-side to the p-side is called a hole generation current, J_h^{gen}, for the same reasons.

The flow of electrons from the n-side to the p-side, under the driving force of diffusion, is known as the electron recombination current, J_e^{rec}. It is so named because of what will happen when the electrons reach the hole-rich p-side; they will recombine. The electron recombination current has to fight the force of the internal electric field and therefore is temperature dependent. There is an energy barrier—stemming from the direction of the electric field and voltage difference $\Delta\phi$, (which are all caused by the formation of the depletion region)—that the electrons need to get over in order to pass from the n-side to the p-side. The probability that they will overcome this energy barrier follows the usual boltzmann distribution,

$$J_e^{rec} \propto \exp[-e(\Delta\phi)/kT]. \tag{A.5}$$

Where $e(\Delta\phi)$ is the energy required for an electron to flow down a voltage drop of $\Delta\phi$. Note that,

$$J_e = J_e^{gen} - J_e^{rec}, \quad \text{and} \quad J_h = J_h^{rec} - J_h^{gen}. \tag{A.6}$$

In the absence of an external applied voltage or light exposure, we have stated that the driving forces of diffusion and the electric field exactly cancel each other. In equation

SIONYX1403000043.0125

SAMSUNG EX. 1002 - 768/4148

form, this means that $J_e^{gen} = J_e^{rec}$ and $J_h^{rec} = J_h^{gen}$, which means that J_e and J_h are zero and the total current, j, is zero.

When an external voltage is applied or the solar cell is illuminated, this balance is disrupted and a non-zero current develops. First we will discuss what happens when an external voltage is applied, and then we will add light.

During normal operation of a solar cell there are no external applied voltages. However, during testing, applying a voltage to a solar cell is very useful as it simulates many different load resistances through the relationship $V = IR$. Refer to Figure A.5 for the state of the p-n junction with positive, negative and no applied voltage as you read the following discussion.

First we will define a positive applied voltage, V, as one that raises the p-side of the p-n junction with respect to the n-side. This effectively reduces the internal voltage drop from the n-side to the p-side and consequently reduces the internal electric field and shrinks the depletion region, as is seen in Figure A.5. The new voltage difference is

$$\Delta\phi = (\Delta\phi)_0 - V. \tag{A.7}$$

The subscript zero indicates that $(\Delta\phi)_0$ is the voltage drop when no external voltage is applied. The applied voltage is only felt at the depletion region because it is a region of high resistivity in series with low resistivity regions on either side. The depletion region shrinks because applying a positive voltage basically injects holes into the edge of the p-side and electrons in the edge of the n-side, shrinking the region where there are very little carriers. Likewise if a negative voltage is applied, the internal voltage drop from the n-side to the p-side will be increased and the depletion region will be increased as well.

The external voltage will have no effect on the electron or hole generation currents as these depend only on temperature, however it will affect the electron and hole recom-

SIONYX1403000043.0126

SAMSUNG EX. 1002 - 769/4148

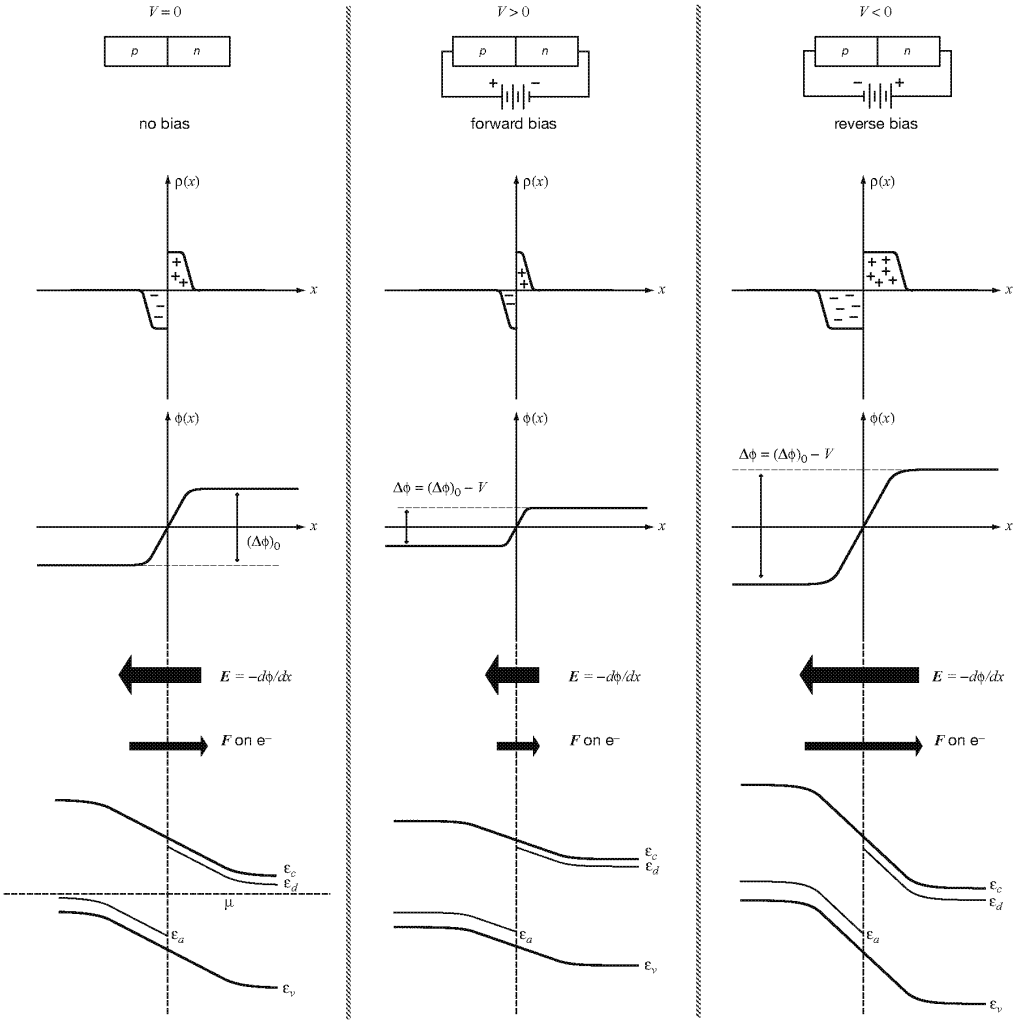


Figure A.5: Changes in spatial charge density, $\rho(x)$, internal voltage barrier, $\Delta\phi$, the electric field $\vec{E}$, the force on the electron $\vec{F}$, and the electronic band structure as the applied voltage, V, is varied from $V = 0$ (*left*), $V > 0$ (*middle*), and $V < 0$ (*right*).

SIONYX1403000043.0127

SAMSUNG EX. 1002 - 770/4148

bination rates which depend exponentially on the voltage difference from the n-side to the p-side as in Equation A.5. Let us write an explicit expression for the current as a function of applied voltage.

When $V = 0$, we know that $J_e^{gen} = (J_e^{rec})_{V=0}$ (the electric field and diffusion driving forces are balanced). Using Equations A.5 and A.7, we get,

$$J_e^{gen} \propto \exp[-e(\Delta\phi)_0/kT]. \tag{A.8}$$

Or this can be written explicitly as,

$$J_e^{gen} = A \exp[-e(\Delta\phi)_0/kT], \tag{A.9}$$

where A is the unknown proportionality constant. Like wise, J_e^{rec} can be written in the same manner,

$$J_e^{rec} = A \exp[-e\{(\Delta\phi)_0 - V\}/kT]. \tag{A.10}$$

By dividing Equation A.10 by Equation A.9 we get,

$$J_e^{rec} = J_e^{gen} \exp[eV/kT]. \tag{A.11}$$

Through the same argument the hole recombination current can be expressed as,

$$J_h^{rec} = J_h^{gen} \exp[eV/kT]. \tag{A.12}$$

By combining Equations A.11 and A.12 with A.6 and A.4 we get the current-voltage relationship,

$$j = e(J_e^{gen} + J_h^{gen})(\exp[eV/kT] - 1). \tag{A.13}$$

SIONYX1403000043.0128

SAMSUNG EX. 1002 - 771/4148

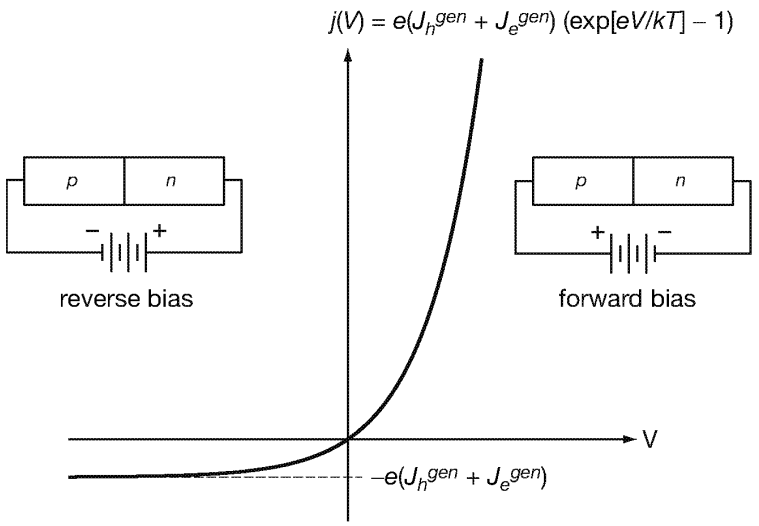


Figure A.6: Current-voltage relationship in an ideal p-n junction. A plot of Equation A.13.

Lets look at the limits: when $V = 0$, $j = 0$; when V is large and positive, current is exponential with voltage, $j \propto \exp[eV/kT]$; when V is large and negative, current is a small constant value, $j \cong -e(J_e^{gen} + J_h^{gen})$. This constant is known as the leakage current of the p-n junction. Equation A.13 is plotted in Figure A.6.

Let us evaluate Equation A.13 from the point of view of an electron. When $V = 0$, the same number of electrons are crossing the junction in both directions because the driving forces of diffusion and the electric field are perfectly balanced and thus there is no net current. When $V > 0$, the voltage difference and energy barrier are decreased and therefore the number of electrons crossing from the n-side to the p-side through thermal diffusion is increased (*i.e.* the electron recombination current is increased). The number of electrons passing from the p-side to the n-side as a result of the force of the electric field stays relatively constant as this is a function of temperature and not voltage (i.e. the electron generation current stays constant). This results in a net flux of electrons from the

SIONYX1403000043.0129

SAMSUNG EX. 1002 - 772/4148

n-side to the p-side and therefore we get a positive current (going from the p-side to the n-side in the positive x-direction) that increases exponentially with voltage.

When $V < 0$, the voltage drop and energy barrier increase. This reduces the number of electrons that can flow from the n-side to the p-side by way of thermal diffusion (i.e. the electron recombination current is decreased). The number of electrons flowing from the p-side to the n-side remains constant as explained above (i.e. the electron generation current remains constant). This results in a net electron flow from the p-side to the n-side and therefore the total electrical current in our coordinate system is negative. As voltage is increased to an extremely large negative value, the electrons flowing from the n-side to the p-side under thermal diffusion essentially stop because of the huge energy barrier in the way (i.e. the electric recombination current goes to zero). The total current then reaches a constant negative value because of the constant electron generation current that never stops. This exercise can be repeated with holes with the exact same result.

It may be a point of confusion as to why the generation current always remains constant even as the depletion region grows and shrinks with applied voltage per Figure A.5. This is because the vast majority of the electrons that get accelerated by the electric field come via thermal diffusion from the p-side (n-side for holes) material just outside the thin depletion region.

When the p-n junction is illuminated all the photoexcited electron-hole pairs separate because of the electric field and add to the generation currents. In this coordinate system, the effect of these extra carriers is to subtract a constant, j_{ph}, from Equation A.13 to get,

$$j = e(J_e^{gen} + J_h^{gen})(\exp[eV/BT] - 1) - j_{ph}. \tag{A.14}$$

The exponential curve is essentially lowered by the photocurrent, j_{ph}. The 4th

SIONYX1403000043.0130

SAMSUNG EX. 1002 - 773/4148

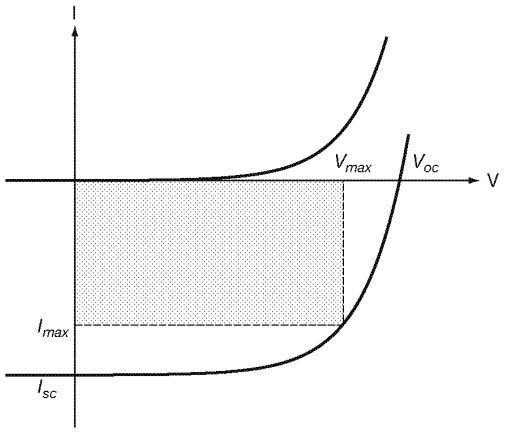


Figure A.7: I-V curve of an illuminated solar cell.

quadrant of the I-V graph is now being occupied. Figure A.7 shows the effect of the photocurrent on the I-V curve. Again, there is a certain voltage and current that will yield the most power as stated in Section A.1. Note that the photocurrent is not a function of the temperature or the voltage. The reason that the photocurrent is the same even though the size of the depletion region changes with applied voltage is the same as above. Most of the light excites carriers in the bulk p-type and n-type material. These carriers then find their way to the depletion region via thermal diffusion. The width of the depletion region does not have a large effect on this.

The equations in this section are based on an ideal p-n junction and describe its function through the use of charge balancing arguments. This method provides no estimate of the size of the prefactor $e(J_e^{gen} + J_h^{gen})$. To obtain this, a more detailed look needs to be taken involving the mobilities of electrons and holes. For this analysis see reference [118], chapter 29.

In addition, actual materials deviate from the I-V characteristics shown here due

SIONYX1403000043.0131

SAMSUNG EX. 1002 - 774/4148

to recombination at defects, surfaces and interfaces as well as other effects such as non-abrupt doping profiles.

A.5 The ideal material

Using the equations from the previous section and the known solar spectrum researchers have been able to determine the maximum efficiency that can be obtained as a function of the band gap energy of the material. The analysis provided by S.M. Sze in reference [119], results in the ideal material having a band gap of 1.35 eV and a maximum efficiency of 31%.

In reference [114], Equation A.14 is rearranged to solve for voltage with $j = 0$. An equation is obtained for the open circuit voltage of the solar cell. A semi-empirical formula is then used to relate the pre-exponential factor $e(J_e^{gen} + J_h^{gen})$ to the band gap of the material. This gives the open circuit voltage of the solar cell as a function of the materials band gap. Further analysis derives an equation for the fill factor and ultimately the efficiency as a function of the band gap energy of the material. The result is shown in Figure A.8, along with the band gap energy for several solar cell materials.

SIONYX1403000043.0132

SAMSUNG EX. 1002 - 775/4148

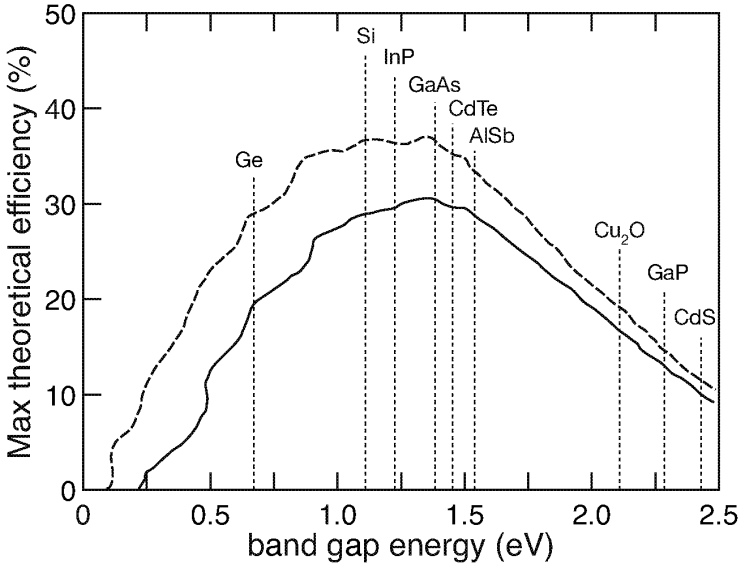


Figure A.8: Maximum theoretical efficiency as a function of band gap energy for AM 1.5 with the solar cell at 300 K at concentrations of 1 sun (solid line) and 1000 suns (dashed). The band gap of several solar cell materials are indicated. Data obtained from reference [119]

SIONYX1403000043.0133

SAMSUNG EX. 1002 - 776/4148

References

[1] P. L. Liu, R. Yen, N. Bloembergen, and R. T. Hodgson, "Picosecond laser-induced melting and resolidification morphology on Si," *Applied Physics Letters*, vol. 34, no. 12, pp. 864–866, 1979.

[2] J. M. Liu, R. Yen, E. P. Donovan, N. Bloembergen, and R. T. Hodgson, "Lack of importance of ambient gases on picosecond laser-induced phase-transitions of silicon," *Applied Physics Letters*, vol. 38, no. 8, pp. 617–619, 1981.

[3] J. M. Liu, R. Yen, H. Kurz, and N. Bloembergen, "Phase-transformation on and charged-particle emission from a silicon crystal-surface, induced by picosecond laser-pulses," *Applied Physics Letters*, vol. 39, no. 9, pp. 755–757, 1981.

[4] D. Y. Sheng, R. M. Walser, M. F. Becker, and J. G. Ambrose, "Heterogeneous nucleation of damage in crystalline silicon with picosecond 1.06-μm laser-pulses," *Applied Physics Letters*, vol. 39, no. 1, pp. 99–101, 1981.

[5] K. L. Merkle, H. Baumgart, R. H. Uebbing, and F. Phillipp, "Picosecond laser-pulse irradiation of crystalline silicon," *Applied Physics Letters*, vol. 40, no. 8, pp. 729–731, 1982.

[6] Y. I. Nissim, J. Sapriel, and J. L. Oudar, "Microprobe Raman analysis of picosecond laser annealed implanted silicon," *Applied Physics Letters*, vol. 42, no. 6, pp. 504–506, 1983.

[7] Y. Kanemitsu, I. Nakada, and H. Kuroda, "Picosecond laser-induced anomalous crystallization in amorphous-silicon," *Applied Physics Letters*, vol. 47, no. 9, pp. 939–941, 1985.

[8] W. K. Wang and F. Spaepen, "Face-centered-cubic Nb-Si solid-solutions produced by picosecond pulsed laser quenching," *Journal of Applied Physics*, vol. 58, no. 11, pp. 4477–4479, 1985.

SIONYX1403000043.0134

SAMSUNG EX. 1002 - 777/4148

[9] J. M. Liu, H. Kurz, and N. Bloembergen, "Picosecond time-resolved plasma and temperature-induced changes of reflectivity and transmission in silicon," *Applied Physics Letters*, vol. 41, no. 7, pp. 643–646, 1982.

[10] D. von der Linde and N. Fabricius, "Observation of an electronic plasma in picosecond laser annealing of silicon," *Applied Physics Letters*, vol. 41, no. 10, pp. 991–993, 1982.

[11] L. A. Lompre, J. M. Liu, H. Kurz, and N. Bloembergen, "Time-resolved temperature-measurement of picosecond laser irradiated silicon," *Applied Physics Letters*, vol. 43, no. 2, pp. 168–170, 1983.

[12] P. H. Bucksbaum and J. Bokor, "Rapid melting and regrowth velocities in silicon heated by ultraviolet picosecond laser-pulses," *Physical Review Letters*, vol. 53, no. 2, pp. 182–185, 1984.

[13] L. A. Lompre, J. M. Liu, H. Kurz, and N. Bloembergen, "Optical heating of electron-hole plasma in silicon by picosecond pulses," *Applied Physics Letters*, vol. 44, no. 1, pp. 3–5, 1984.

[14] H. M. Vandriel, L. A. Lompre, and N. Bloembergen, "Picosecond time-resolved reflectivity and transmission at 1.9 and 2.8-μm of laser-generated plasmas in silicon and germanium," *Applied Physics Letters*, vol. 44, no. 3, pp. 285–287, 1984.

[15] I. W. Boyd, S. C. Moss, T. F. Boggess, and A. L. Smirl, "Temporally resolved imaging of silicon surfaces melted with intense picosecond 1-μm laser-pulses," *Applied Physics Letters*, vol. 46, no. 4, pp. 366–368, 1985.

[16] C. V. Shank, R. Yen, and C. Hirlimann, "Time-resolved reflectivity measurements of femtosecond-optical-pulse induced phase-transitions in silicon," *Physical Review Letters*, vol. 50, no. 6, pp. 454–457, 1983.

[17] C. V. Shank, R. Yen, and C. Hirlimann, "Femtosecond-time-resolved surface structural dynamics of optically-excited silicon," *Physical Review Letters*, vol. 51, no. 10, pp. 900–902, 1983.

[18] H. W. K. Tom, G. D. Aumiller, and C. H. Britocruz, "Time-resolved study of laser-induced disorder of Si surfaces," *Physical Review Letters*, vol. 60, no. 14, pp. 1438–1441, 1988.

[19] K. Sokolowski-Tinten, J. Bialkowski, A. Cavalleri, D. von der Linde, A. Oparin, J. Meyer-ter Vehn, and S. I. Anisimov, "Transient states of matter during short pulse laser ablation," *Physical Review Letters*, vol. 81, no. 1, pp. 224–227, 1998.

SIONYX1403000043.0135

SAMSUNG EX. 1002 - 778/4148

[20] A. Cavalleri, K. Sokolowski-Tinten, J. Bialkowski, M. Schreiner, and D. von der Linde, "Femtosecond melting and ablation of semiconductors studied with time of flight mass spectroscopy," *Journal Of Applied Physics*, vol. 85, no. 6, pp. 3301–3309, 1999.

[21] D. von der Linde and K. Sokolowski-Tinten, "The physical mechanisms of short-pulse laser ablation," *Applied Surface Science*, vol. 154, pp. 1–10, 2000.

[22] T. E. Glover, "Hydrodynamics of particle formation following femtosecond laser ablation," *Journal Of The Optical Society Of America B-Optical Physics*, vol. 20, no. 1, pp. 125–131, 2003.

[23] J. R. Chelikowsky and M. L. Cohen, "Nonlocal pseudopotential calculations for electronic-structure of 11 diamond and zincblende semiconductors," *Physical Review B*, vol. 14, no. 2, pp. 556–582, 1976.

[24] M. A. Green and M. J. Keevers, "Optical-properties of intrinsic silicon at 300 K," *Progress in Photovoltaics*, vol. 3, no. 3, pp. 189–192, 1995.

[25] D. Hulin, M. Combescot, J. Bok, A. Migus, J. Y. Vinet, and A. Antonetti, "Energy-transfer during silicon irradiation by femtosecond laser-pulse," *Physical Review Letters*, vol. 52, no. 22, pp. 1998–2001, 1984.

[26] S. I. Kudryashov and V. I. Emel'yanov, "Band gap collapse and ultrafast "cold" melting of silicon during femtosecond laser pulse," *Journal of Experimental and Theoretical Physics Letters*, vol. 73, no. 5, pp. 228–231, 2001.

[27] K. Sokolowski-Tinten and D. von der Linde, "Generation of dense electron-hole plasmas in silicon," *Physical Review B*, vol. 61, no. 4, pp. 2643–2650, 2000.

[28] H. Dachraoui and W. Husinsky, "Thresholds of plasma formation in silicon identified by optimizing the ablation laser pulse form," *Physical Review Letters*, vol. 97, no. 10, 2006.

[29] K. Sokolowski-Tinten, J. Bialkowski, and D. Vonderlinde, "Ultrafast laser-induced order-disorder transitions in semiconductors," *Physical Review B*, vol. 51, no. 20, pp. 14186–14198, 1995.

[30] P. P. Pronko, P. A. VanRompay, C. Horvath, F. Loesel, T. Juhasz, X. Liu, and G. Mourou, "Avalanche ionization and dielectric breakdown in silicon with ultrafast laser pulses," *Physical Review B*, vol. 58, no. 5, pp. 2387–2390, 1998.

[31] P. Stampfli and K. H. Bennemann, "Theory for the laser-induced instability of

SIONYX1403000043.0136

SAMSUNG EX. 1002 - 779/4148

the diamond structure of Si, Ge and C," *Progress in Surface Science*, vol. 35, no. 1-4, pp. 161–164, 1990.

[32] P. Stampfli and K. H. Bennemann, "Theory for the instability of the diamond structure of Si, Ge, and C induced by a dense electron-hole plasma," *Physical Review B*, vol. 42, no. 11, pp. 7163–7173, 1990.

[33] P. Stampfli and K. H. Bennemann, "Dynamic theory of the laser-induced lattice instability of silicon," *Physical Review B*, vol. 46, no. 17, pp. 10686–10692, 1992.

[34] P. Stampfli and K. H. Bennemann, "Time-dependence of the laser-induced femtosecond lattice instability of Si and GaAs - role of longitudinal optical distortions," *Physical Review B*, vol. 49, no. 11, pp. 7299–7305, 1994.

[35] S. Amoruso, R. Bruzzese, N. Spinelli, R. Velotta, M. Vitiello, and X. Wang, "Emission of nanoparticles during ultrashort laser irradiation of silicon targets," *Europhysics Letters*, vol. 67, no. 3, pp. 404–410, 2004.

[36] T. E. Glover, G. D. Ackerman, R. W. Lee, and D. A. Young, "Probing particle synthesis during femtosecond laser ablation: initial phase transition kinetics," *Applied Physics B-Lasers And Optics*, vol. 78, no. 7-8, pp. 995–1000, 2004.

[37] P. M. Fauchet and A. E. Siegman, "Surface ripples on silicon and gallium-arsenide under picosecond laser illumination," *Applied Physics Letters*, vol. 40, no. 9, pp. 824–826, 1982.

[38] J. E. Sipe, J. F. Young, J. S. Preston, and H. M. Vandriel, "Laser-induced periodic surface-structure 1. theory," *Physical Review B*, vol. 27, no. 2, pp. 1141–1154, 1983.

[39] J. F. Young, J. S. Preston, H. M. Vandriel, and J. E. Sipe, "Laser-induced periodic surface-structure 2. experiments on Ge, Si, Al, and brass," *Physical Review B*, vol. 27, no. 2, pp. 1155–1172, 1983.

[40] J. F. Young, J. E. Sipe, and H. M. Vandriel, "Laser-induced periodic surface-structure 3. fluence regimes, the role of feedback, and details of the induced topography in germanium," *Physical Review B*, vol. 30, no. 4, pp. 2001–2015, 1984.

[41] H. M. Vandriel, J. E. Sipe, and J. F. Young, "Laser-induced coherent modulation of solid and liquid surfaces," *Journal of Luminescence*, vol. 30, no. 1-4, pp. 446–471, 1985.

SIONYX1403000043.0137

SAMSUNG EX. 1002 - 780/4148

[42] B. R. Tull, J. E. Carey, E. Mazur, J. McDonald, and S. M. Yalisove, "Surface morphologies of silicon surfaces after femtosecond laser irradiation," *Materials Research Society Bulletin*, vol. 31, pp. 626–633, 2006.

[43] J. E. Carey, *Femtosecond-laser Microstructuring of Silicon for Novel Optoelectronic Devices*. PhD thesis, Harvard University, 2004.

[44] T.-H. Her, R. J. Finlay, C. Wu, S. Deliwala, and E. Mazur, "Microstructuring of silicon with femtosecond laser pulses," *Applied Physics Letters*, vol. 73, pp. 1673–1675, 1998.

[45] T.-H. Her, R. J. Finlay, C. Wu, and E. Mazur, "Femtosecond laser-induced formation of spikes on silicon," *Applied Physics A-Materials Science and Processing*, vol. 70, pp. 383–385, 2000.

[46] C. H. Crouch, J. E. Carey, M. Shen, E. Mazur, and F. Y. Genin, "Infrared absorption by sulfur-doped silicon formed by femtosecond laser irradiation," *Applied Physics A-Materials Science and Processing*, vol. 79, pp. 1635–1641, 2004.

[47] C. H. Crouch, J. E. Carey, J. M. Warrender, M. J. Aziz, E. Mazur, and F. Y. Genin, "Comparison of structure and properties of femtosecond and nanosecond laser-structured silicon," *Applied Physics Letters*, vol. 84, pp. 1850–1852, 2004.

[48] R. J. Younkin, J. E. Carey, E. Mazur, J. A. Levinson, and C. M. Friend, "Infrared absorption by conical silicon microstructures made in a variety of background gases using femtosecond-laser pulses," *Journal of Applied Physics*, vol. 93, pp. 2626–2629, 2003.

[49] M. A. Sheehy, L. Winston, J. E. Carey, C. M. Friend, and E. Mazur, "The role of the background gas in the morphology and optical properties of laser-microstructured silicon," *Chemistry of Materials*, vol. 17, pp. 3582–3586, 2005.

[50] M. A. Sheehy, B. R. Tull, C. M. Friend, and E. Mazur, "Chalcogen doping of silicon via femtosecond laser irradiation," *Materials Science and Engineering B-Solid State Materials for Advanced Technology*, vol. 137, pp. 289–294, 2006.

[51] C. Wu, C. H. Crouch, L. Zhao, J. E. Carey, R. J. Younkin, J. A. Levinson, E. Mazur, R. M. Farrel, P. Gothoskar, and A. Karger, "Near-unity below-band gap absorption by microstructured silicon," *Applied Physics Letters*, vol. 78, pp. 1850–1852, 2001.

[52] J. E. Carey, C. H. Crouch, M. Shen, and E. Mazur, "Visible and near-infrared

SIONYX1403000043.0138

SAMSUNG EX. 1002 - 781/4148

responsivity of femtosecond-laser microstructured silicon photodiodes," *Optical Letters*, vol. 30, pp. 1773–1775, 2005.

[53] M. Shen, C. H. Crouch, J. E. Carey, R. J. Younkin, E. Mazur, M. A. Sheehy, and C. M. Friend, "Formation of regular arrays of silicon microspikes by femtosecond laser irradiation through a mask," *Applied Physics Letters*, vol. 82, pp. 1715–1717, 2003.

[54] C. Wu, C. H. Crouch, L. Zhao, and E. Mazur, "Visible luminescence from silicon surfaces microstructured in air," *Applied Physics Letters*, vol. 81, pp. 1999–2001, 2002.

[55] S. Deliwala, *Time-resolved studies of molecular dynamics using nano- and femtosecond laser pulses.* PhD thesis, Harvard University, 1995.

[56] R. J. Finlay, *Femtosecond-laser-induced reactions at surfaces.* PhD thesis, Harvard University, 1998.

[57] T.-H. Her, *Femtochemistry at gas/solid interfaces.* PhD thesis, Harvard University, 1998.

[58] A. V. Bulgakov, I. Ozerov, and W. Marine, "Silicon clusters produced by femtosecond laser ablation: non-thermal emission and gas-phase condensation," *Applied Physics A-Materials Science and Processing*, vol. 79, no. 4-6, pp. 1591–1594, 2004.

[59] D. B. Williams and C. B. Carter, *Transmission Electron Microscopy.* New York: Plenum Press, 1996.

[60] Y. Shao, F. Spaepen, and D. Turnbull, "An analysis of the formation of bulk amorphous silicon from the melt," *Metallurgical And Materials Transactions A-Physical Metallurgy And Materials Science*, vol. 29, no. 7, pp. 1825–1828, 1998.

[61] Y. W. Kim, H. M. Lin, and T. F. Kelly, "Amorphous solidification of pure metals in sub-micron spheres," *Acta Metallurgica*, vol. 37, no. 1, pp. 247–255, 1989.

[62] P. V. Evans, G. Devaud, T. F. Kelly, and Y. W. Kim, "Solidification of highly undercooled Si and Ge droplets," *Acta Metallurgica et Materialia*, vol. 38, no. 5, pp. 719–726, 1990.

[63] M. O. Thompson, J. W. Mayer, A. G. Cullis, H. C. Webber, N. G. Chew, J. M. Poate, and D. C. Jacobson, "Silicon melt, regrowth, and amorphization

SIONYX1403000043.0139

SAMSUNG EX. 1002 - 782/4148

velocities during pulsed laser irradiation," *Physical Review Letters*, vol. 50, no. 12, pp. 896–899, 1983.

[64] G. Devaud and D. Turnbull, "Undercooling of molten silicon," *Applied Physics Letters*, vol. 46, no. 9, pp. 844–845, 1985.

[65] C. G. Granqvist and R. A. Buhrman, "Ultrafine metal particles," *Journal Of Applied Physics*, vol. 47, no. 5, pp. 2200–2219, 1976.

[66] J. Soderlund, L. B. Kiss, G. A. Niklasson, and C. G. Granqvist, "Lognormal size distributions in particle growth processes without coagulation," *Physical Review Letters*, vol. 80, no. 11, pp. 2386–2388, 1998.

[67] L. B. Kiss, J. Soderlund, G. A. Niklasson, and C. G. Granqvist, "The real origin of lognormal size distributions of nanoparticles in vapor growth processes," *Nanostructured Materials*, vol. 12, no. 1-4, pp. 327–332, 1999.

[68] M. Wilkinson and B. Mehlig, "Caustics in turbulent aerosols," *Europhysics Letters*, vol. 71, no. 2, pp. 186–192, 2005.

[69] H. R. Vydyanath, W. J. Helm, J. S. Lorenzo, and S. T. Hoelke, "Development of selenium-doped silicon for 3–5 μm applications," *Infrared Physics*, vol. 19, no. 1, pp. 93–102, 1979.

[70] N. Sclar, "The effect of dopant diffusion vapor-pressure on the properties of sulfur and selenium doped silicon infrared detectors," *Journal of Applied Physics*, vol. 52, no. 8, pp. 5207–5217, 1981.

[71] Y. A. Astrov, L. M. Portsel, A. N. Lodygin, V. B. Shuman, and E. V. Beregulin, "Silicon doped with sulfur as a detector material for high speed infrared image converters," in *Gettering and Defect Engineering in Semiconductor Technology XI*, Solid State Phenomena 108-109, pp. 401–406, 2005.

[72] X. Zhang, M. Kleverman, and J. Olajos, "A photoluminescence study of selenium-diffused silicon," *Semiconductor Science and Technology*, vol. 14, no. 12, pp. 1076–1079, 1999.

[73] A. Henry, J. Svensson, E. Janzen, and B. Monemar, "New photoluminescence lines in selenium-doped silicon," *Materials Science and Engineering B-Solid State Materials for Advanced Technology*, vol. 4, no. 1-4, pp. 261–264, 1989.

[74] T. G. Brown and D. G. Hall, "Optical-emission at 1.32-μm from sulfur-doped crystalline silicon," *Applied Physics Letters*, vol. 49, no. 5, pp. 245–247, 1986.

SIONYX1403000043.0140

SAMSUNG EX. 1002 - 783/4148

[75] T. G. Brown, P. L. Bradfield, and D. G. Hall, "Concentration-dependence of optical-emission from sulfur-doped crystalline silicon," *Applied Physics Letters*, vol. 51, no. 20, pp. 1585–1587, 1987.

[76] M. A. Lourenco, M. Milosavljevic, S. Galata, M. S. A. Siddiqui, G. Shao, R. M. Gwilliam, and K. P. Homewood, "Silicon-based light emitting devices," *Vacuum*, vol. 78, no. 2-4, pp. 551–556, 2005.

[77] J. Bao, M. Tabbal, T. Kim, S. Charnvanichborikarn, J. S. Williams, M. J. Aziz, and F. Capasso, "Efficient point defect engineered Si light-emitting diode at 1.218 μm," *submitted to Applied Physics Letters.*

[78] M. Thiagarajan, K. Iyakutti, and E. Palaniyandi, "Electronic structure of chalcogen impurities in silicon," *Physica Status Solidi B-Basic Research*, vol. 205, no. 2, pp. 553–558, 1998.

[79] H. G. Grimmeiss, E. Janzen, H. Ennen, O. Schirmer, J. Schneider, R. Worner, C. Holm, E. Sirtl, and P. Wagner, "Tellurium donors in silicon," *Physical Review B*, vol. 24, no. 8, pp. 4571–4586, 1981.

[80] E. Janzen, R. Stedman, G. Grossmann, and H. G. Grimmeiss, "High-resolution studies of sulfur-related and selenium-related donor centers in silicon," *Physical Review B*, vol. 29, no. 4, pp. 1907–1918, 1984.

[81] E. Janzen, H. G. Grimmeiss, A. Lodding, and C. Deline, "Diffusion of tellurium dopant in silicon," *Journal of Applied Physics*, vol. 53, no. 11, pp. 7367–7371, 1982.

[82] R. G. Wilson, "Depth distributions of sulfur implanted into silicon as a function of ion energy, ion fluence, and anneal temperature," *Journal of Applied Physics*, vol. 55, no. 10, pp. 3490–3494, 1984.

[83] A. A. Taskin, B. A. Zaitsev, V. I. Obodnikov, and E. G. Tishkovskii, "Special features of spatial redistribution of selenium atoms implanted in silicon," *Semiconductors*, vol. 34, no. 3, pp. 312–318, 2000.

[84] F. Rollert, N. A. Stolwijk, and H. Mehrer, "Diffusion of S-35 into silicon using an elemental vapor source," *Applied Physics Letters*, vol. 63, no. 4, pp. 506–508, 1993.

[85] F. Rollert, N. A. Stolwijk, and H. Mehrer, "Diffusion of tellurium in silicon studied by the redistribution of an implanted source of radioactive Te-127," *Materials Science and Engineering B-Solid State Materials for Advanced Technology*, vol. 18, no. 2, pp. 107–114, 1993.

SIONYX1403000043.0141

SAMSUNG EX. 1002 - 784/4148

[86] P. L. Gruzin, S. V. Zemskii, A. D. Bulkin, and N. M. Makarov, "Diffusion of carbon and sulfur in phosphorus-doped silicon," *Soviet Physics Semiconductors-Ussr*, vol. 7, no. 9, pp. 1241–1241, 1974.

[87] R. O. Carlson, R. N. Hall, and E. M. Pell, "Sulfur in silicon," *Journal of Physics and Chemistry of Solids*, vol. 8, pp. 81–83, 1959.

[88] N. S. Zhdanovich and Y. I. Kozlov, "IR absorption and photoconductivity of silicon doped with sulfur or selenium," *Soviet Physics Semiconductors-USSR*, vol. 10, no. 10, pp. 1102–1104, 1976.

[89] H. R. Vydyanath, J. S. Lorenzo, and F. A. Kroger, "Defect pairing diffusion, and solubility studies in selenium-doped silicon," *Journal of Applied Physics*, vol. 49, no. 12, pp. 5928–5937, 1978.

[90] H. Stumpel, M. Vorderwulbecke, and J. Mimkes, "Diffusion of selenium and tellurium in silicon," *Applied Physics A-Materials Science and Processing*, vol. 46, no. 3, pp. 159–163, 1988.

[91] C. S. Kim and M. Sakata, "Diffusion-coefficient of selenium in silicon by sheet hall-coefficient measurements," *Japanese Journal of Applied Physics*, vol. 18, no. 2, pp. 247–254, 1979.

[92] H. G. Grimmeiss, E. Janzen, B. Skarstam, and A. Lodding, "Chemical-identification of deep energy-levels in Si-Se," *Journal of Applied Physics*, vol. 51, no. 12, pp. 6238–6242, 1980.

[93] C. W. White, S. R. Wilson, B. R. Appleton, and F. W. Young, "Supersaturated substitutional alloys formed by ion-implantation and pulsed laser annealing of group-III and group-V dopants in silicon," *Journal Of Applied Physics*, vol. 51, no. 1, pp. 738–749, 1980.

[94] E. M. Lawson, "Pulse-laser-induced supersaturation of indium and antimony in germanium," *Journal of Applied Physics*, vol. 53, no. 9, pp. 6459–6460, 1982.

[95] T. G. Kim, J. M. Warrender, and M. J. Aziz, "Strong sub-band-gap infrared absorption in silicon supersaturated with sulfur," *Applied Physics Letters*, vol. 88, no. 24, 2006.

[96] S. U. Campisano, G. Foti, P. Baeri, M. G. Grimaldi, and E. Rimini, "Solute trapping by moving interface in ion-implanted silicon," *Applied Physics Letters*, vol. 37, no. 8, pp. 719–722, 1980.

SIONYX1403000043.0142

SAMSUNG EX. 1002 - 785/4148

[97] M. J. Aziz, "Model for solute redistribution during rapid solidification," *Journal of Applied Physics*, vol. 53, no. 2, pp. 1158–1168, 1982.

[98] M. J. Aziz, J. Y. Tsao, M. O. Thompson, P. S. Peercy, and C. W. White, "Solute trapping - comparison of theory with experiment," *Physical Review Letters*, vol. 56, no. 23, pp. 2489–2492, 1986.

[99] J. A. Kittl, P. G. Sanders, M. J. Aziz, D. P. Brunco, and M. O. Thompson, "Complete experimental test of kinetic models for rapid alloy solidification," *Acta Materialia*, vol. 48, no. 20, pp. 4797–4811, 2000.

[100] U. M. Gosele, "Fast diffusion in semiconductors," *Annual Review of Materials Science*, vol. 18, pp. 257–282, 1988.

[101] H. Overhof, M. Scheffler, and C. M. Weinert, "Formation energies, electronic-structure, and hyperfine fields of chalcogen point-defects and defect pairs in silicon," *Physical Review B*, vol. 43, no. 15, pp. 12494–12506, 1991.

[102] Y. Mo, M. Z. Bazant, and E. Kaxiras, "Sulfur point defects in crystalline and amorphous silicon," *Physical Review B*, vol. 70, no. 20, 2004.

[103] F. Beeler, M. Scheffler, O. Jepsen, and O. Gunnarsson, "Identification of chalcogen point-defect sites in silicon by total-energy calculations," *Physical Review Letters*, vol. 54, no. 23, pp. 2525–2528, 1985.

[104] F. C. Frank and D. Turnbull, "Mechanism of diffusion of copper in germanium," *Physical Review*, vol. 104, no. 3, pp. 617–618, 1956.

[105] U. Gosele, W. Frank, and A. Seeger, "Mechanism and kinetics of the diffusion of gold in silicon," *Applied Physics*, vol. 23, no. 4, pp. 361–368, 1980.

[106] B. R. Tull, J. E. Carey, M. A. Sheehy, C. Friend, and E. Mazur, "Formation of silicon nanoparticles and web-like aggregates by femtosecond laser ablation in a background gas," *Applied Physics A-Materials Science and Processing*, vol. 83, no. 3, pp. 341–346, 2006.

[107] J. Crank, *The Mathematics of Diffusion*. Oxford: Clarendon Press, 1st ed., 1956.

[108] V. I. Emel'yanov and D. V. Babak, "Defect capture under rapid solidification of the melt induced by the action of femtosecond laser pulses and formation of periodic surface structures on a semiconductor surface," *Applied Physics A-Materials Science and Processing*, vol. 74, no. 6, pp. 797–805, 2002.

SIONYX1403000043.0143

SAMSUNG EX. 1002 - 786/4148

[109] H. J. Kim and C. V. Thompson, "Kinetic modeling of grain-growth in polycrystalline silicon films doped with phosphorus or boron," *Journal of the Electrochemical Society*, vol. 135, no. 9, pp. 2312–2319, 1988.

[110] Y. Wada and S. Nishimatsu, "Grain-growth mechanism of heavily phosphorus-implanted polycrystalline silicon," *Journal of the Electrochemical Society*, vol. 125, no. 9, pp. 1499–1504, 1978.

[111] R. Angelucci, M. Severi, and S. Solmi, "Effect of impurities on the grain-growth of chemical vapor-deposited polycrystalline silicon films," *Materials Chemistry and Physics*, vol. 9, no. 1-3, pp. 235–245, 1983.

[112] R. J. Komp, *Practical Photovoltaics, Electricity from Solar Cells*. Michigan: Aatec Publications, 3rd ed., 1995.

[113] M. D. Archer and R. Hill, *Clean Electricity from Photovoltaics*. London: Imperial College Press, 2001.

[114] A. V. Shah, R. Platz, and H. Keppner, "Thin-film silicon solar-cells - a review and selected trends," *Solar Energy Materials and Solar Cells*, vol. 38, no. 1-4, pp. 501–520, 1995.

[115] A. Shah, J. Meier, E. Vallat-Sauvain, N. Wyrsch, U. Kroll, C. Droz, and U. Graf, "Material and solar cell research in microcrystalline silicon," *Solar Energy Materials and Solar Cells*, vol. 78, no. 1-4, pp. 469–491, 2003.

[116] A. Goetzberger, J. Knobloch, and B. Voss, *Crystalline Silicon Solar Cells*. New York: John Wiley and Sons, 1998.

[117] S. Veprek and V. Marecek, "Preparation of thin layers of Ge and Si by chemical hydrogen plasma transport," *Solid-State Electronics*, vol. 11, no. 7, p. 683, 1968.

[118] N. W. Ashcroft and N. D. Mermin, *Solid State Physics*. Fortworth: Saunders College Publishing, 1976.

[119] S. M. Sze, *Physics of Semiconductor Devices*. Canada: John Wiley and Sons, Inc, 2nd ed., 1981.

[120] C. E. Richardson, Y. B. Park, and H. A. Atwater, "Surface evolution during crystalline silicon film growth by low-temperature hot-wire chemical vapor deposition on silicon substrates," *Physical Review B*, vol. 73, no. 24, 2006.

SIONYX1403000043.0144

SAMSUNG EX. 1002 - 787/4148

IEICE Electronics Express, Vol.1, No.18, 556–561

A high-sensitive digital photosensor using MOS interface-trap charge pumping

Akihiro Uehara,[a)] **Keiichiro Kagawa, Takashi Tokuda, Jun Ohta, and Masahiro Nunoshita**

Graduate School of Materials Science, Nara Institute of Science and Technology, 8916–5 Takayama, Ikoma, Nara 630–0101, Japan

a) a-akihir@ms.naist.jp

Abstract: A high-sensitive CMOS photosensor based on a pulse frequency modulation (PFM) scheme is presented. We propose and demonstrate the high-sensitive PFM photosensor, whose output frequency is proportionate to the incident light intensity, that utilizes MOS interface-trap charge pumping (ITCP) as a frequency-controlled ultra-low current. The proposed pixel sensor consists of only 4 transistors: a transistor as an ultra-low current source; a sense amplifier transistor; a selection transistor; and, a reset transistor. The prototype device is fabricated using 0.6-μm standard CMOS technology. High sensitivity $4.0 \times 10^5\,\mathrm{Hz}/(\mathrm{W \cdot m^{-2}})$, which is larger than two orders of magnitude compared to previous works, was obtained.

Keywords: PFM photosensor, retinal prosthesis, pixel-level ADC, charge pumping, interface-traps

Classification: Photonics devices, circuits, and systems

References

[1] J. Ohta, N. Yoshida, K. Kagawa, and M. Nunoshita, "Proposal of application of pulsed vision chip for retinal prosthesis," *Jpn. J. Appl. Phys.*, vol. 41, no. 4B, pp. 2322–2325, April 2002.

[2] A. Uehara, K. Kagawa, T. Tokuda, J. Ohta, and M. Nunoshita, "Back-illuminated pulse-frequency-modulated photosensor using silicon-on-sapphire technology developed for use as epi-retinal prosthesis device," *Electron. Lett.*, vol. 39, no. 15, pp. 1102–1104, July 2003.

[3] K. Kagawa, K. Isakari, T. Furuniya, A. Uehara, T. Tokuda, J. Ohta, and M. Nunoshita, "Pixel design of pulsed CMOS image sensor for retinal prosthesis with digital photosensitivity control," *Electron. Lett.*, vol. 39, no. 5, pp. 419–421, March 2003.

[4] D. Ziegler, P. Linderholm, M. Mazza, S. Ferazzutti, D. Bertrand, A. M. Ionescu, and Ph. Renaud, "An active microphotodiode array of oscillating pixels for retinal stimulation," *Sensor. Actuat. A*, vol. 110, pp. 11–17, 2004.

[5] J. S. Brugler and P. G. A. Jespers, "Charge pumping in MOS devices," *IEEE Trans. Electron Devices*, vol. 16, no. 3, pp. 297–302, March 1969.

© IEICE 2004

DOI: 10.1587/elex.1.556
Received November 01, 2004
Accepted December 08, 2004
Published December 25, 2004

SIONYX1403000043.0145

SAMSUNG EX. 1002 - 788/4148

[6] G. Groeseneken, H. E. Maes, N. Beltrán, and R. F. de Keersmaecker, "A reliable approach to charge-pumping measurements in MOS transistors," *IEEE Trans. Electron Devices*, vol. 31, no. 1, pp. 42–53, Jan. 1984.
[7] T. P. Chen, "Frequency-controlled low-level current source based on charge pumping," *Electron. Lett.*, vol. 27, no. 16, pp. 1046–1047, Aug. 2001.
[8] U. Ciliugiroglu, A. Becker-Gomez, and K. T. Veeder, "An evaluation of MOS interface-trap charge pump as an ultralow constant-current generator," *IEEE J. Solid-State Circuits*, vol. 38, no. 1, pp. 71–83, Jan. 2003.

1 Introduction

A photosensor based on a pulse frequency modulation (PFM) scheme is a suitable photosensor for retinal prosthetic devices [1]. Conventional PFM photosensors, however, have disadvantages such as low sensitivity, sensitivity fluctuation by the supply voltage, and a large circuit area [2, 3, 4].

In this letter, we propose a new PFM photosensor, light-to-frequency converter. Light-to-frequency conversion results from keeping a reverse voltage constant by charging the photodiode with a frequency-controlled current source. We applied the MOS interface-trap charge pumping (ITCP) current source for the conventional PFM photosensor to overcome the disadvantages previously mentioned. We report the experimental results of the prototype device, fabricated using 0.6-μm standard CMOS technology.

2 A new PFM photosensor by MOS ITCP

A conventional PFM photosensor (conceptual drawing and node voltages depicted in Fig. 1) is a self-reset photosensor where the output frequency is given by

$$f_{out} = K_{PFM} I_{PH} = \frac{I_{PH}}{C1 \cdot (V_R - V_T)}, \quad (1)$$

with K_{PFM}, I_{PH}, $C1$, V_R and V_T representing the sensitivity of PFM photosensor, photocurrent, junction capacitance of the photodiode, reset voltage, and threshold voltage of the CMOS logic inverter, respectively [1]. When the V_{PD} reaches V_T due to discharging of the $C1$ by the photocurrent, the photodiode is reset to the reset voltage V_R and one pulse is output.

The conventional PFM photosensor, however, has some important disadvantages: sensitivity is low because the amount of the injection charge per cycle Q_{inj} $(= C1 \cdot (V_R - V_T))$ is large ($\approx$ 10 fC) relative to the photocurrent, and the fluctuation of the sensitivity is quite large because the threshold voltage of the logic inverter is proportionate to the supply voltage.

A concrete approach to improve the conventional PFM photosensor is to realize a frequency-controlled, ultra-low current source within a limited circuit area. We make use of MOS ITCP to control the amount of Q_{inj}. The ultra-low current sources using this phenomenon have been reported [7, 8].

© IEICE 2004
DOI: 10.1587/elex.1.556
Received November 01, 2004
Accepted December 08, 2004
Published December 25, 2004

SIONYX1403000043.0146

SAMSUNG EX. 1002 - 789/4148

The ITCP, which was discovered in 1969 [4], is a transient recombination effect activated by cycling the Si-SiO_2 interface of a MOSFET between accumulation and inversion. For a brief explanation, the NMOS transistor, whose source and drain are both biased with voltage V_R, is considered. By pulsing the gate voltage V_G periodically, the mid-gap interface traps capture electrons that flow from the source and drain to form a channel in the inversion phase (Fig. 2 (a)) and are emptied in the accumulation phase by capturing holes that are supplied from the p-type substrate (Fig. 2 (b)). Acting as recombination centers, these traps transfer a net charge from the source to the p-type substrate and the net charge is given by

$$Q_{ss} = qD_{it}A\Delta E, \tag{2}$$

where q is the electron charge, A is the gate area, and D_{it} is the trap density per unit area per unit energy [6]. Assuming typical values, we can get an extremely small injection charge $Q_{ss} \approx 3.5$ aC (22 electrons per cycle) with the gate area of 0.5 μm × 2.5 μm [8].

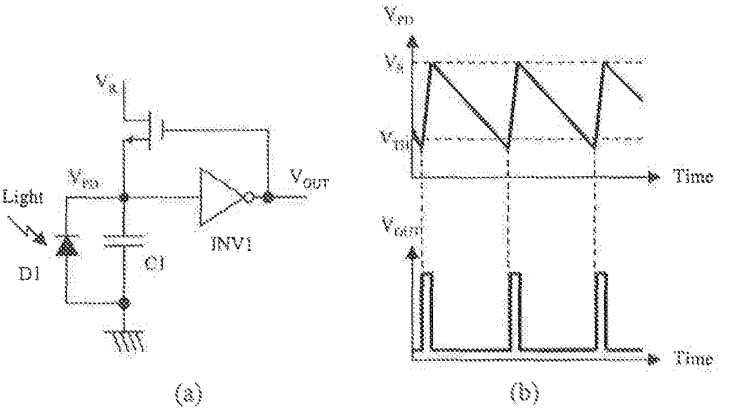


Fig. 1. (a) Schematic of conventional PFM photosensor. (b) Behavior of node voltages V_{PD} and V_{OUT}.

3 Design of a new PFM photosensor

A prototype four-transistor photosensor circuit is shown in Fig. 2 (d) with its transistor widths and lengths. The photodiode bias voltage V_{PD} is read out as a current I_{OUT} of the sense transistor $M2$ through the selection transistor $M4$. The MOS transistor $M1$ acts as an ultra-low current source as described previously. The voltage change of V_{PD} due to charge injection or clock feedthrough is suppressed by the additional MOS capacitor $C1$ of 1.2 pF.

The off-chip circuit controls the charge pumping frequency to keep V_{PD} in constant value V_R. We apply square pulses shown in Fig. 2 (c) to perform

© IEICE 2004
DOI: 10.1587/elex.1.556
Received November 01, 2004
Accepted December 08, 2004
Published December 25, 2004

SIONYX1403000043.0147

SAMSUNG EX. 1002 - 790/4148

charge pumping with the following conditions:

$$V_{TOP} > V_R + V_{TH}, \quad \text{(for inversion)} \tag{3}$$

and

$$V_{BASE} < V_{FB}, \quad \text{(for accumulation)} \tag{4}$$

where V_R, V_{TH}, V_{FB} is photodiode reset voltage, threshold voltage and flat-band voltage of M1, respectively.

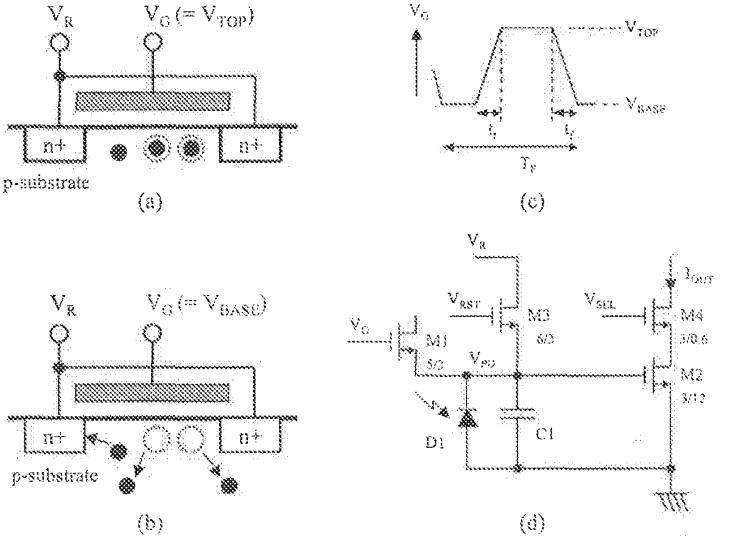


Fig. 2. (a) The interface traps are occupied by electrons when the NMOS is in the inversion phase. (b) The interface traps are emptied in the accumulation phase. (c) Square waveform applied to the gate to perform the charge pumping. (d) Schematic of the prototype device.

4 Experimental results and discussion

The device was fabricated using the 0.6-μm CMOS process with the circuit size being 40 μm × 43 μm. The n+/p-sub parasitic diode with junction area 17 μm^2 is used as the photodiode.

The measured result of the ITCP current (I_{cp}) dependence on the base voltage V_{BASE} is shown in Fig. 3 (a). The frequency, duty cycle, the V_{TOP}, and both the rising time and the falling time of the square waveform were 1 MHz, 50%, 3.0 V, and 12 nsec, respectively. The V_{BASE} was swept from −0.1 V to −0.6 V. The minimum value of the V_{BASE} was −0.6 V because of the existence of I/O protection diodes that are connected between the I/O pad and the substrate. The I_{cp} was calculated from the charging time of

© IEICE 2004
DOI: 10.1587/elex.1.556
Received November 01, 2004
Accepted December 08, 2004
Published December 25, 2004

SIONYX1403000043.0148

SAMSUNG EX. 1002 - 791/4148

the capacitance C1 from 1.0 V to 1.7 V with the assumption that the charge-pumping current is constant within that source and drain voltage range. The drain and source voltage of the transistor M1 were set to above 1.0 V for two reasons: 1) To drift back the mobile charge of the channel to source and drain when the gate voltage turns low [6]; and, 2) To decrease the voltage dependence of the MOS capacitance $C1$.

The measurements result shows that Q_{ss} ($= I_{cp}/f_{cp}$) was 1.4×10^{-16} C (875 electrons) per cycle when the V_{BASE} was -0.6 V. The saturation of the charge pumping current was not observed because the V_{BASE} was greater than the flat-band voltage. The calculated D_{it} with a typical energy range $\Delta E \approx 0.5$ eV is 1.2×10^{10} cm^{-2}, which is close to the previously reported value [8].

The relationship between the charge pumping frequency and the incident light intensity is shown in Fig. 3(b). When the V_{PD} was lower than 1.7 V,

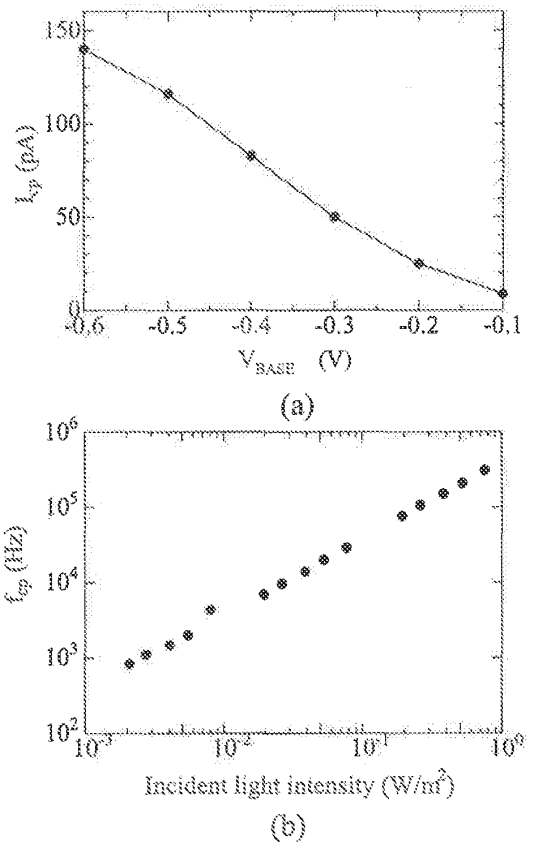


Fig. 3. Measurement results of the prototype device. (a) Relationship between the base voltage and the charge pumping current. (b) Relationship between the incident light intensity and the output frequency.

© IEICE 2004
DOI: 10.1587/elex.1.556
Received November 01, 2004
Accepted December 08, 2004
Published December 25, 2004

SIONYX1403000043.0149

SAMSUNG EX. 1002 - 792/4148

the off-chip circuit outputs square pulses with the same parameters that were used in the measurement of the ITCP current with V_{BASE} of −0.6 V. Monochromatic light with a wavelength of 630 nm was used as a light source. Various neutral density filters were introduced into the light path in order to achieve different light intensities.

The measured sensitivity, linearity, and dynamic range are 4.0×10^6 Hz $/(\mathrm{W \cdot m^{-2}})$, 6.3%, and 30 dB, respectively. The amount of injection charge by the ITCP was estimated about 90 aC (580 electrons) per cycle. High sensitivity, which is larger than two orders of magnitude, in comparison to the previous works, was obtained [2, 3, 4]. The photocurrent of M2 and dark current of the D1 limited the upper and lower limits of the detectable light intensity, respectively.

5 Conclusions

We propose a new four-transistor type CMOS active pixel sensor with an in-pixel analog-to-digital conversion (ADC). We describe and demonstrate the high-sensitive PFM photosensor that utilizes MOS interface-traps as a frequency-controlled ultra-low current, although the fraction of the geometric components to the ITCP current is not clear in this work[6].

The prototype device has been fabricated using the 0.6-μm CMOS process. We investigated the gate voltage dependence of the ITCP current. The measured sensitivity, linearity, and dynamic range are 4.0×10^6 Hz/$(\mathrm{W \cdot m^{-2}})$, 6.3%, and 30 dB, respectively. High sensitivity, which is larger than two orders of magnitude, compared to previous works, was obtained [2, 3].

The proposed PFM photosensor, which is able to be fabricated using standard CMOS process, is a novel four-transistor type pixel circuit leading toward the next generation of CMOS image sensor for its in-pixel ADC capability and high sensitivity.

Acknowledgments

This work is supported by NEDO (The New Energy and Industrial Technology Development Organization) and Health and Labor Sciences Research Grants, Japan.

© IEICE 2004
DOI: 10.1587/elex.1.556
Received November 01, 2004
Accepted December 08, 2004
Published December 25, 2004

SIONYX1403000043.0150

SAMSUNG EX. 1002 - 793/4148

C29

Depth distributions of sulfur implanted into silicon as a function of ion energy, ion fluence, and anneal temperature

R. G. Wilson
Hughes Research Laboratories, Malibu, California 90265

(Received 18 January 1983; accepted for publication 24 January 1984)

Depth distributions for sulfur (S) implanted in (100) and (111) silicon (Si) measured by secondary ion mass spectrometry are reported for S ion energies from 40 to 600 keV and ion fluences from 4×10^{12} to 4×10^{16} cm^{-2}. The results of Pearson IV fits are tabulated for the energy and fluence series; the range parameters given are peak depth (R_m) and $\mu(R_p)$, $\sigma(\Delta R_p)$, γ_1, β_2, and β_2' for both the peak of the distribution and the full curve (including the influence of the channeling tail). The S densities are measured from a maximum of 10^{21} down to $<10^{15}$ cm^{-3} where the detection limit is probably caused by background oxygen (mass 32). Sulfur profiles are shown for annealing temperatures from 100 to 950 °C in (100) and (111) Si orientations. Sulfur is retained in the region of damage for densities above about 10^{18} cm^{-3}, until an annealing temperature of 900 or 950 °C is reached, when the S is largely rejected from the Si crystal; the remaining S density is $<10^{15}$ cm^{-3}, in agreement with solid solubility.

PACS numbers: 61.70.Tm, 61.70.Wp, 66.30.Jt, 81.40.Ef

INTRODUCTION

Prior studies of S in Si have been primarily concerned with measuring the energy levels of S in the Si crystal. This work is reviewed by Koyama *et al.*[1] They and Fahrner and Goetzberger[2] used ion implantation into the Si. They used thermal processing to remove most of the associated damage and to diffuse the S into the Si. The solid solubility of S in Si is given as $<10^{15}$ cm^{-3} at 1000 °C by Trumbore.[3] Koyama *et al.*[1] support the interpretation of Fahrner and Goetzberger[2] that signals in transient capacitance and thermally stimulated current measurements attributed to S following 500 °C annealing of implanted S in Si arise from S atoms involved in damage complexes and not from S atoms in thermal equilibrium with the Si lattice. Our results show that for these ion energies and fluences, S remains in the as-implanted depth distribution at 500 °C and does not redistribute until an annealing temperature of 700 °C is reached. In the temperature range from 700 to 900 °C, some S is complexed with damage in the unannealed defect-rich transition layer between the more heavily implant-damaged region and the underlying crystalline Si. Some S is rejected from the Si lattice during annealing or regrowth as the S density approaches the solid solubility quoted by Trumbore,[3] but which cannot occur until the damage (defect complexes) is annealed. This final annealing occurs at about 950 °C, at which temperature most of the S has been rejected from the Si crystal (to the surface) and the S density is less than about 10^{15} cm^{-3}, in agreement with the solid solubility.

EXPERIMENTAL TECHNIQUES

The implants were all made at room temperature using mostly ^{32}S, although ^{34}S was implanted in several cases to compare with ^{32}S. Depth distributions of ^{34}S and ^{32}S agreed in the several cases studied. The (100) Si samples were oriented during implantation with a 7° tilt about an axis from which a [110] plane was rotated 18°. The ion energies are accurate to within about 2%. The depth distributions were measured by secondary ion mass spectrometry (SIMS) using a Cs ion beam and negative ion spectrometry. The background-subtracted detection sensitivities for ^{32}S and ^{34}S were about the same, so no advantage was to be gained by using the less abundant isotope ^{34}S. The detection limit is probably caused by the presence of oxygen in the sputtering ambient and hence on the Si surface. The SIMS sensitivity for S is high using a Cs ion beam and the resulting high counting statistics contributed to the good background-subtracted detection sensitivities, which were below 10^{15} cm^{3} in some cases. The background S density was about 10^{15} cm^{-3} or slightly lower. Densities were determined by setting the integral of the depth distribution equal to the ion fluence, known to within about 5%. The depth scales were determined by measuring the SIMS crater depths by surface profilometry (Dektak), estimated to be accurate to within about ± 7%. Crater shapes were generally good; in a few poorer cases the SIMS measurements were repeated. The SIMS measurements were enhanced by fairly rapid depth profiling (sputtering), about 10 nm/s. Implantation current densities varied from 0.02 to 0.5 μA/cm^2. The 0.5 μA/cm^2 current density was used only for the 4.0×10^{16} cm^{-2} fluence.

RESULTS AND DISCUSSIONS

In this work, we report implanted depth distributions for S in Si for ion energies of 40, 75, 150, 300, 450, and 600 keV at 4.0×10^{13} cm^{-2} fluence (Fig. 1) and for ion fluences of 4.0×10^{12}, 4.0×10^{13}, 4.0×10^{14}, 4.0×10^{15}, and 4.0×10^{16} cm^{-2} at 300 keV (Fig. 2). We have performed Pearson IV fits to these depth distributions and the results are given in Table I. The range parameters are R_m (the peak depth), and the four Pearson IV moments, $\mu(R_p)$, $\sigma(\Delta R_p$ or straggle), γ_1 (skewness), and β_2 (kurtosis). The relative kurtosis β_2' is also given[4] to show how much fourth moment exists in the profiles. Pearson IV fits are made for the peaks of the profiles, which are representative of the physics of stopping of S in Si and are more useful for modeling calculations such as Lind-

 0021-8979/84/103490-05$02.40 © 1984 American Institute of Physics

Downloaded 06 May 2008 to 146.186.238.1. Redistribution subject to AIP license or copyright; see http://jap.aip.org/jap/copyright.jsp

SIONYX1403000043.0151

SAMSUNG EX. 1002 - 794/4148

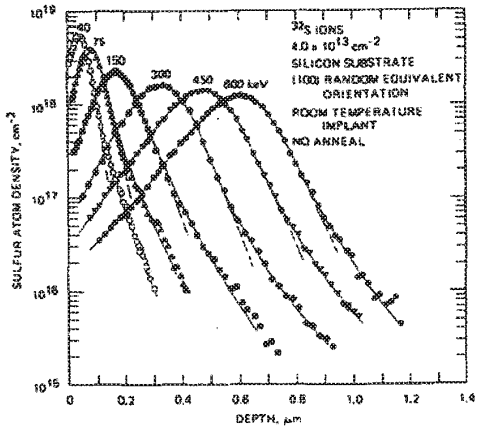


FIG. 1. Implanted sulfur depth distributions (by SIMS) *in silicon* for six ion energies at 4.0×10^{13} cm^{-2} ion fluence.

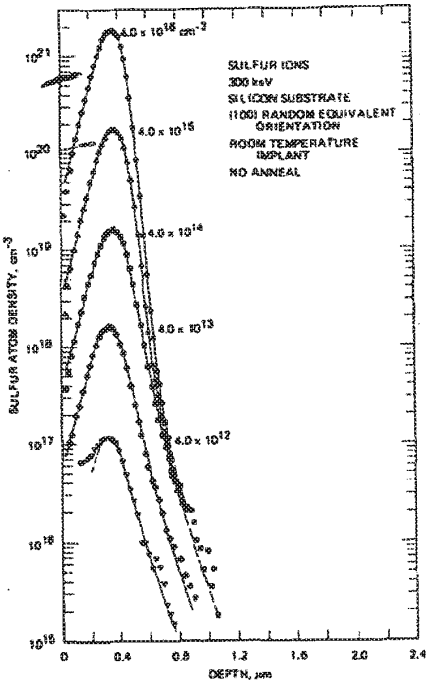


FIG. 2. Implanted sulfur depth distributions in silicon for five ion fluences at 300-keV ion energy.

hard, Scharff, and Schiøtt (LSS), and also for the full implanted profiles which include the significant channeling effect on the deep sides of the profiles. These latter moments are representative of the actual room temperature implanted depth distributions that are created by implantation. These two Pearson IV fits are shown in Fig. 1 by the dashed and solid curves, respectively. The experimental values of the range and range straggle are compared with the corresponding LSS values calculated by Gibbons *et al.*[5] in Table II. The range parameters, R_m, R_p or μ, and ΔR_p or σ, are plotted as a function of ion energy in Fig. 3. ΔR_p or σ is seen to be equal to R_p at about 40 keV and extrapolation to lower energy would predict that ΔR_p is greater than R_p. Unity slope is indicated in Fig. 3 and shows that the slopes of the R_m and R_p (peak) curves are unity at about 150 keV. The data for R_p

TABLE I. Range parameters and Pearson IV moments.

Ion energy (keV)	R_m, (μm)	N_{max} (cm^{-3})	R_p, μ (μm)	$\Delta R_p, \sigma$ (μm)	γ_1	β_2	β_2'
			Peak of distribution				
40	0.040	5.3{18}	0.036	0.047	−0.70	~100	~100
75	0.078	3.9{18}	0.081	0.050	−0.28	5.8	2.6
150	0.173	2.2{18}	0.169	0.092	−0.32	23	20
300	0.330	1.6{18}	0.313	0.117	−0.62	6.1	2.2
450	0.474	1.4{18}	0.444	0.156	−1.49	30	23
600	0.607	1.2{18}	0.569	0.169	−1.73	34	26
			Full profile, including deep-side tail				
40	0.040	5.6{18}	0.052	0.044	2.70	∞	∞
75	0.076	3.9{18}	0.090	0.060	2.40	∞	∞
150	0.173	2.3{18}	0.178	0.096	0.52	∞	∞
300	0.327	1.6{18}	0.314	0.133	−0.96	∞	∞
450	0.473	1.4{18}	0.447	0.162	−1.61	∞	∞
600	0.608	1.2{18}	0.575	0.173	−1.93	∞	∞
Fluence cm^{-2}			300-keV fluence series				
4{13}	0.330	1.6{18}	0.313	0.116	−0.62	6.1	2.2
4{14}	0.355	1.6{19}	0.337	0.114	−0.61	5.8	2.0
4{15}	0.367	1.75{20}	0.338	0.102	−0.88	5.3	0.6
4{16}	0.357	1.87{21}	0.326	0.099	−1.01	5.9	0.8

Downloaded 06 May 2008 to 146.186.238.1. Redistribution subject to AIP license or copyright; see http://jap.aip.org/jap/copyright.jsp

SIONYX1403000043.0152

SAMSUNG EX. 1002 - 795/4148

(full curve) form a straight line with a slope of 0.89, in correspondence with data we have measured for other ions in Si. Skewness is plotted as a function of ion energy in Fig. 4, for both the peak and full profile data. It is observed that the data are similar for energies above about 300 keV and quite different for lower energies, the result of channeling at the lower energies. A maximum in the value of γ_1 occurs at about 100 keV.

The values of the third moment or skewness of the S in Si profiles as determined from Pearson IV fitting to the experimental data are surprisingly large negative values for this ion-substrate combination. S and Si have similar atomic numbers, 16 and 14, respectively, and theory predicts small values of third moment for similar values of atomic numbers. The value of the third moment also varies with ion energy more than theory would predict (see Fig. 3). The experimental values of third and fourth moment given here may aid in future modeling efforts for implanted profiles—an area that deserves more study but that need experimental data. Another area that may deserve more study is suggested by the observation that experimental values of ΔR_p or σ are from 1.5 to 3 times the LSS values calculated by Gibbons *et al.*[5] (see Table II). In contrast, the experimental and calculated values for R_p or μ agree within 4%–20% over the factor of 15 in ion energy, which is very good.

The depth distribution measured for 300-keV S implanted into (100) and (111) Si at 4.0×10^{13} cm^{-2} and annealed at temperatures from 200 to 950 °C are shown in Figs. 5 and 6, respectively. The annealing data are similar for the two orientations, although some small differences exist. No redistribution of S occurs until a temperature between 650 and 700 °C is reached. Then the S appears to complex with detect clusters and "decorates" the damage as that damage is annealed.[6] This damage begins as two regions and then at 800 or 850 °C, becomes primarily one accumulation of defects at about 0.4 μm in (100) Si and at about 0.5 μm in (111) Si (for 300-keV implant energy). By 950 °C the damage has largely annealed (for 4×10^{13} cm^{-2} ion fluence) and the S atoms have been rejected from the Si crystal to the surface. The density is below 10^{15} cm^{-3} after the SIMS profile recovers from the high surface density of S (extending to about 0.05 μm). There is no indication of diffusion of S into the Si lattice for any temperature up to 950 °C above 10^{15} cm^{-3}, the probable solid solubility limit under these conditions. A measurement made for 1000 °C anneal temperature, but not shown, did indicate possible diffusion above 10^{15} cm^{-3}. At low anneal temperatures, the S atoms leave the Si lattice at densities above 10^{15} cm^{-3} on the deep side of the as-implanted depth distribution and appear to migrate to the defects in the implantation-damaged regions within the first 0.5 μm from the surface.

A consistent contrast is seen in Fig. 7 for a 4.0×10^{15} cm^{-2} sulfur ion fluence implanted into (111) float zone silicon. For this one hundred times greater fluence (compared with Figs. 5 and 6), which is greater than the amorphization fluence for 300-keV S in Si, the sulfur atoms are retained in the amorphized zone of the Si (0.5 μm thick) for all annealing temperatures from 200 to 950 °C. Essentially no change in the sulfur depth distribution occurs until an annealing temperature of 600 °C is reached. Between 600 and 700 °C, the S profile redistributes; the sulfur atoms are rejected from the Si

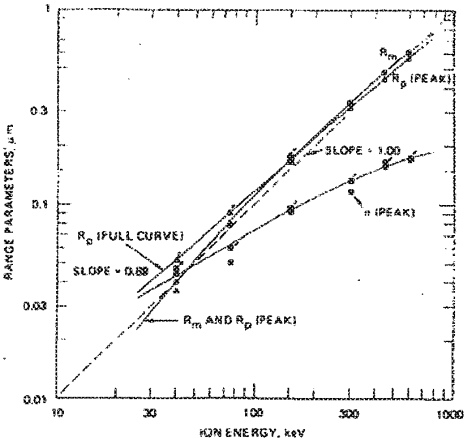


FIG. 3. Range parameters as a function of ion energy for sulfur implanted in silicon at 4.0×10^{13} cm^{-2} ion fluence.

TABLE II. Comparison between calculated and experimental range parameters.

Ion energy (keV)	LSS calculations[5] R_p (μm)	ΔR_p (μm)	Experimental Pearson IV values R_p (μm)	ΔR_p (μm)
40	0.046	0.015	0.036	0.047
75	0.086	0.026	0.081	0.050
150	0.176	0.046	0.169	0.092
300	0.360	0.077	0.313	0.117
450	0.542	0.101	0.444	0.156
600	0.710	0.118	0.569	0.169

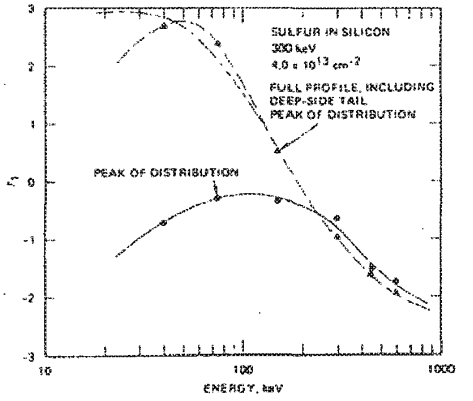


FIG. 4. Skewness (third moment) as a function of ion energy for sulfur implanted in silicon at 4.0×10^{13} cm^{-2} ion fluence.

Downloaded 06 May 2008 to 146.186.238.1. Redistribution subject to AIP license or copyright; see http://jap.aip.org/jap/copyright.jsp

SIONYX1403000043.0153

SAMSUNG EX. 1002 - 796/4148

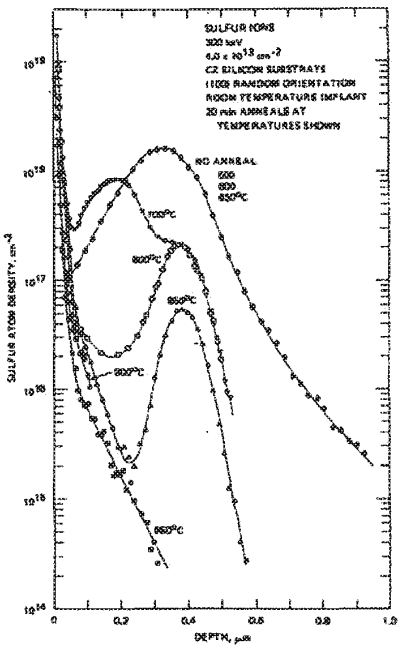


FIG. 5. Implanted sulfur depth distributions in (100) silicon as a function of annealing temperature for 300-keV ion energy and 4.0×10^{13} cm^{-2} ion fluence.

crystal at depths deeper than the amorphized layer (0.5 μm). At the amorphous-to-crystalline interface between 0.50 and 0.55 μm, the S atom density decreases by nearly one order of magnitude for each 100 °C increase in annealing temperature. A narrow peak occurs in the S profile in this transition interface region, remaining even after a 950 °C anneal, at which time the sulfur density is still about 10^{17} cm^{-3}, more than one hundred times the solid solubility. The peak of the sulfur depth distribution remains unaffected until an annealing temperature of 900 °C is reached, then a sharpening of the peaks occurs and some migration of sulfur atoms toward the Si surface occurs. Both of these effects are further enhanced after a 950 °C anneal. Apparently the implant damage is not annealed even for 950 °C annealing temperature and the sulfur atoms remain complexed with the residual defect clusters under these conditions at more than five orders of magnitude above the solid solubility, whereas for the lower fluence condition of Figs. 5 and 6, the sulfur has been rejected from the Si crystal. The sulfur atoms are retained only on the shallow side of the sharp interface at 0.5 μm, while they decrease in the 0.05-μm-wide interface region, probably in direct proportion to the annealing of defect complexes.

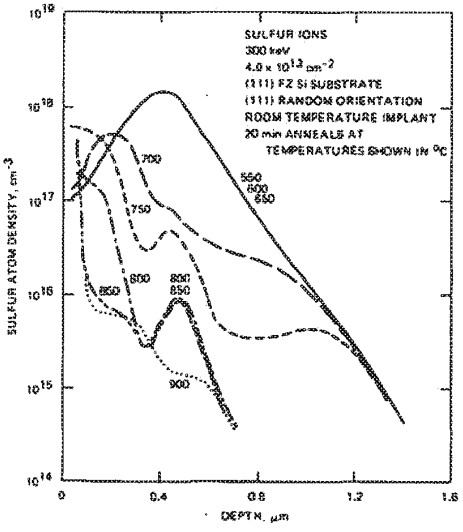


FIG. 6. Implanted sulfur depth distributions in (111) silicon as a function of annealing temperature for 300-keV ion energy and 4.0×10^{13} cm^{-2} ion fluence.

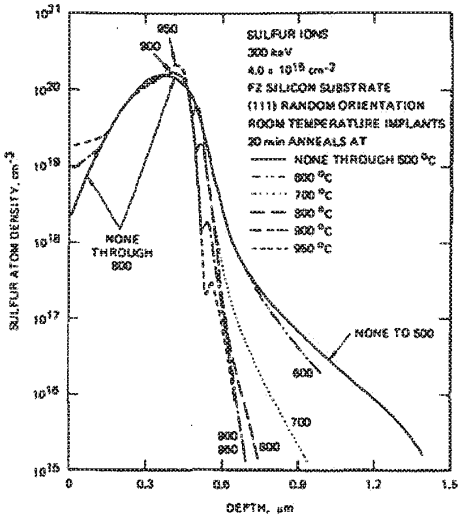


FIG. 7. Implanted sulfur depth distributions in (111) silicon as a function of annealing temperature for 300-keV ion energy and 4.0×10^{15} cm^{-2} ion fluence.

Because significant redistribution was seen in the profiles for 700 and 800 °C annealing temperatures in Figs. 5 and 6, we annealed all five orders of magnitude of fluence at these two temperatures in (100) Si. The results indicate that the implanted S is retained with slight redistribution from the as-implanted profile for the three highest fluences. Discontinuities in the depth distributions are exhibited for the two highest fluences at the probably amorphous/crystalline interface at about 0.5 μm, and it appears that crystal regrowth at 800 °C following amorphization at 4.0×10^{15} and 4.0×10^{16} cm^{-2} either does not regrow in the presence of the high S densities shown ($>10^{20}$ cm^{-3}) or incorporates the high densities of S atoms as precipitates in the regrown layer, in contrast to the results shown in more detail for the 4.0×10^{15} cm^{-2} fluence in Figs. 5 and 6.

Downloaded 06 May 2008 to 146.186.238.1. Redistribution subject to AIP license or copyright; see http://jap.aip.org/jap/copyright.jsp

SIONYX1403000043.0154

SAMSUNG EX. 1002 - 797/4148

ACKNOWLEDGMENTS

We wish to thank D. M. Jamba for making the implantations and the staff of Evans and Associates for the SIMS data. The portion of this work that involved redistribution in association with defect complexes was partially funded by DARPA through the Office of Naval Research.

[1] R. Y. Koyama, W. E. Phillips, D. R. Myers, Y. M. Liu, and H. B. Dietrich, Solid State Electron. 21, 953 (1978).
[2] W. Fahrner and A. Goetzberger, Appl. Phys. Lett. 21, 329 (1972).
[3] F. A. Trumbore, Bell Syst. Tech. J. 39, 205 (1960).
[4] R. G. Wilson, Radiat. Eff. 46, 141 (1980).
[5] J. F. Gibbons, W. S. Johnson, and S. W. Mylroie, *Projected Range Statistics Semiconductors and Related Materials* (Halstead, Wiley, New York, 1975).
[6] R. G. Wilson, D. K. Sadana, T. W. Sigmon, and C. A. Evans, Jr., Appl. Phys. Lett. 43, 549 (1983).

Downloaded 06 May 2008 to 146.186.238.1. Redistribution subject to AIP license or copyright; see http://jap.aip.org/jap/copyright.jsp

SIONYX1403000043.0155

SAMSUNG EX. 1002 - 798/4148

ELSEVIER Solar Energy Materials and Solar Cells 46 (1997) 239–248

Solar Energy Materials and Solar Cells

Reactive ion etching (RIE) as a method for texturing polycrystalline silicon solar cells

S. Winderbaum[a,*], O. Reinhold[b], F. Yun[c]

[a] *University of South Australia, School of Applied Physics, Adelaide, SA, Australia*
[b] *Microengineering Section, SES, Defence Science and Technology Organisation, Salisbury, SA, Australia*
[c] *University of New South Wales, Centre for PV Devices and Systems, Sydney, NSW, Australia*

Received 11 December 1996

Abstract

Reactive ion etching (RIE) has been applied and developed as a method for texturing polycrystalline silicon solar cells. Two structures (microgrooves and pyramids) were produced in this work. Reflectivity measurements between 400–1200 nm show an overall reflectance of 5.6% for pyramid and 7.9% for groove structures. These results are better than those using wet anisotropic etch techniques on single-crystal silicon. RIE texturing was performed on cast polycrystalline silicon and produced better reflection control than standard TiO_2 antireflection coatings. RIE texturing also changes the incidence angle of light into the silicon, this improves the response for long wavelengths which can be utilised in thin film, polycrystalline or amorphous silicon solar cells.

Keywords: Texturing; Polysilicon; Polycrystalline silicon; Reactive Ion Etching; Reflectivity

1. Introduction

Texturing has been used to reduce surface reflection for different materials, enabling multiple reflections to occur on the surface before light is reflected back to the atmosphere. It also has the side benefit of increasing the optical path of light in the bulk of the material, because of the change in the angle of incidence after multiple reflections occurred on the surface.

* Corresponding author. Email: saul.winderbaum@unisa.edu.au

0927-0248/97/$17.00 © 1997 Elsevier Science B.V. All rights reserved
PII S0927-0248(97)00011-1

SIONYX1403000043.0156

SAMSUNG EX. 1002 - 799/4148

Different techniques and schemes such as, sandblasting [1], mechanical grooving [2, 3], wet chemical etch [4], laser sculpturing and plasma etching [5] have been used to texture the surface of single and polycrystalline silicon.

One of the characteristics of all these methods is that they use either chemical- or physical-etching mechanisms to produce the desired pattern. This imposes limitations such as features geometry or selectivty of the process depending on which mechanism is chosen.

Among these techniques, wet chemical etching is the most highly developed and widely used. The most common application of this etching technique exposes the $\langle 1\,1\,1 \rangle$ planes in a $\langle 1\,0\,0 \rangle$ single-crystal silicon, leaving behind randomly distributed square base pyramids with a slope angle of 54.7°.

More sophisticated applications use photolithography masks which produce inverted pyramids [6], microgrooves and tilted pyramids [7, 8]. These texture schemes ensure a double bounce on the surface of the cell before light is reflected back to the atmosphere, reducing reflection levels to an order of 10%.

Reactive ion etching (RIE) is a dry etching process in which a substrate is etched by a combination of chemical and physical interactions between the reactant gas and the substrate. The etch rate and sidewall slope can be controlled by adjusting the chemical and physical parameters in the etching equipment [9–11]. RIE combines the selectivity of chemical processes and the directionality of physical processes.

2. Rie texturing

The RIE equipment used in these experiments was a Vacutech parallel-plate system. The lower electrode is powered by a 13.56 MHz-RF generator coupled through an automatic tuning network.

Each electrode is 200 mm in diameter and the distance between them is 23 mm. The RF electrodes are made of anodised aluminium. The chamber volume is 13 l and the system is pumped by a 350 l/min turbomolecular pump backed by a mechanical rotary vane pump. The base pressure before each run was less than 5×10^{-6} Torr.

A two-level factorial design of experiments was used to find the main and interaction effects governing etch rate and sidewall slope [12, 13]. Even though the RIE process performance is influenced by interaction effects between different factors, such as, oxygen content, power density, pressure and loading, at a chosen set of etching parameters, the slope of the texturing can be controlled by each one of them, i.e. the oxygen content in the etching gas mixture (Fig. 1).

The silicon substrate was covered with a 400 nm layer of thermal SiO_2 which was masked using a photoresist mask. The etch process consisted of two consecutive plasmas, first CHF_3, to etch the silicon dioxide and second SF_6/O_2, to etch the silicon. The silicon-etch process uses the remaining SiO_2 as the etch mask.

The selectivity achieved between silicon dioxide etch mask (masking material) and silicon for a slope of 70° was approximately 1 : 10. The application of this process using a photoresist mask of lines 3 μm width and 2 μm clear gap, produced a texture pattern of grooves with 72° slope and groove depth of 5 μm as shown in Fig. 2.

SIONYX1403000043.0157

SAMSUNG EX. 1002 - 800/4148

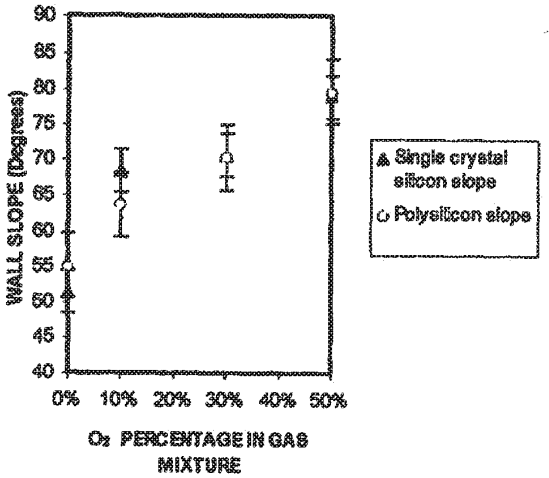


Fig. 1. Sidewall slope dependency on O_2 percentage in gas mixture, @ 100 W RF power and fixed SF_6 flow of 25 sccm for single as well as for polycrystalline silicon.

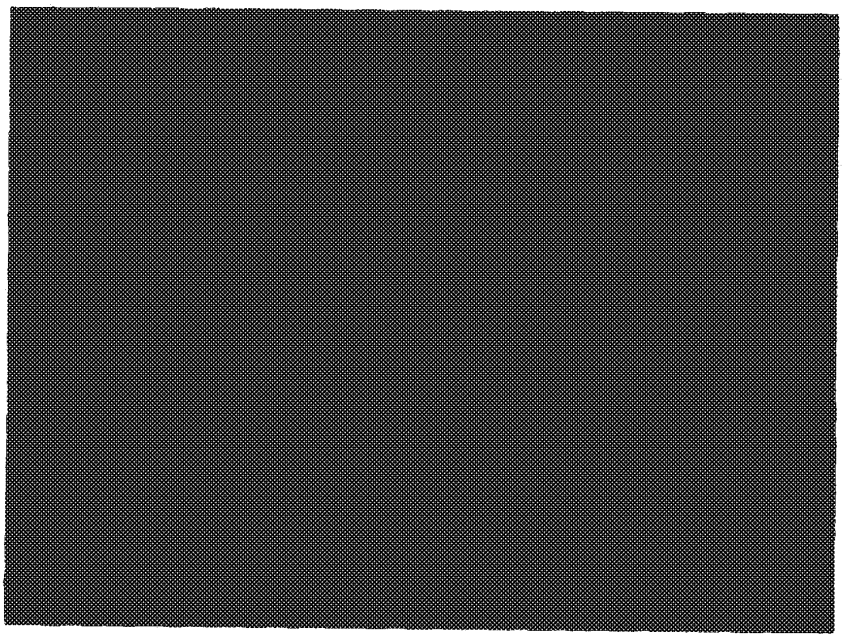


Fig. 2. SEM cross section of oxide masked microgrooves.

SIONYX1403000043.0158

SAMSUNG EX. 1002 - 801/4148

3. Results and discussion

Reflectivity measurements were performed on the textured substrates using a Cary-5 spectrophotometer and the results are shown in Fig. 3. An overall reflectivity for this texture of about 17% shows that double bouncing on the surface is not achieved for the incoming light. This is possibly due to the combination of rounded and shallow bottom of the grooves.

Textured and non-textured substrates (only chemically polished) were processed in to PESC solar cells and the average electrical results are shown in Table 1. From the results in Table 1, it can be seen that fill factor and open circuit voltage are deteriorated

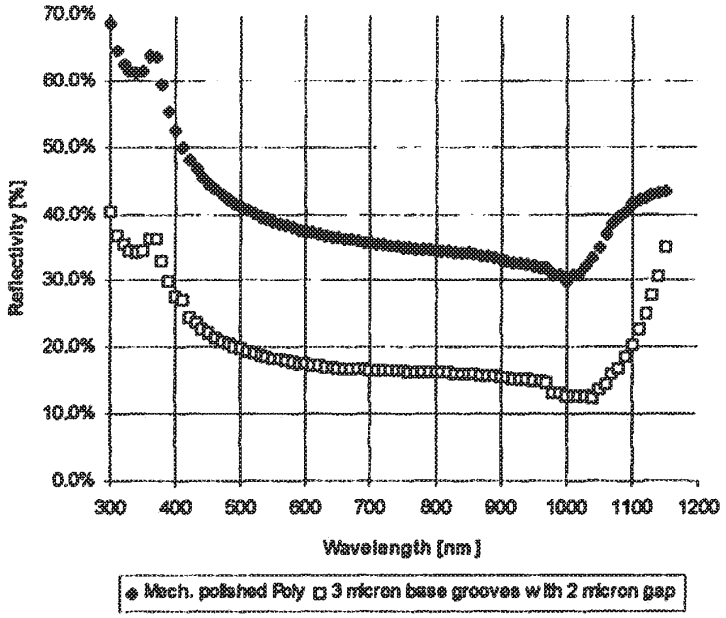


Fig. 3. Reflectivity measurement of 3 μm base RIE grooves.

Table 1
Chemically polished and (oxide mask)RIE textured cells

	Chemically polished	RIE textured	Change
Voc	0.5577	0.5406	− 3%
Jsc	0.0215	0.0279	+ 29%
Eff	9.07	10.17	+ 12%
FF	0.7521	0.6729	− 11.7%

SIONYX1403000043.0159

SAMSUNG EX. 1002 - 802/4148

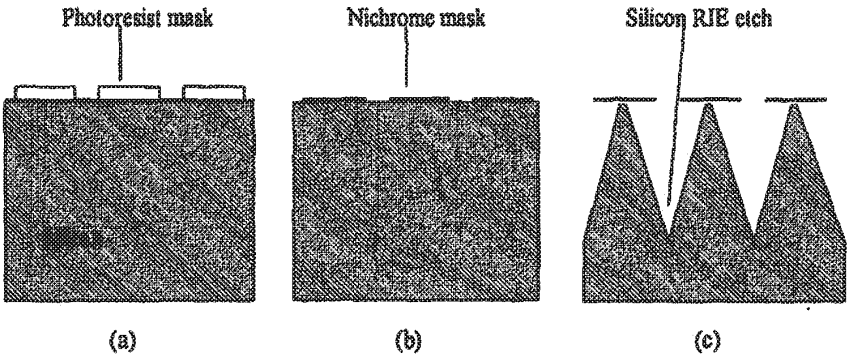


Fig. 4. Schematics of a cross section for the masking and RIE process.

Table 2
Non-optimised textured and reference cells masked with sputtered metal

	Chemically polished	RIE textured	Change
Voc	0.5604	0.5635	± 0%
Jsc	0.0190	0.0247	+ 30%
Eff	8.09	9.89	+ 22%
FF	0.7583	0.7107	− 6.6%

for the textured cells while short circuit current showed a good improvement, consistent with the reduction in surface reflectivity.

The reason for the deterioration of the voltage output in the textured cells was assumed to be originated in the high-temperature oxidation process used to mask the substrates before the RIE step. The options of changing this process were a PECVD oxidation process at 300°C instead of 1200°C, or a sputtered metal mask at room temperature.

The metal mask option was preferred because of the lower temperature involved, the better adhesion of photoresist to it and the almost infinite RIE selectivity compared to silicon.

A schematics of the masking and etching process is shown in Fig. 4.

The first application of this new masking process resulted in shallow and more perpendicular slopes than required for solar cell application.

The reason of this change in performance resides in the so-called 'loading effect', which was affected by the change in masking material, i.e., silicon dioxide offered a load to the reactant gases while the nichrome layer did not.

An SEM view of the patterns obtained by this new procedure is shown in Figs. 5 and 6 . As may be seen from those micrographs, the pattern has relatively large flat areas which deteriorates the effectivness of the texturing.

RIE textured cells (pyramids and grooves) were produced using this masking technique, from chemically polished cells were produced as a reference and the results of both are shown in Table 2

SIONYX1403000043.0160

SAMSUNG EX. 1002 - 803/4148

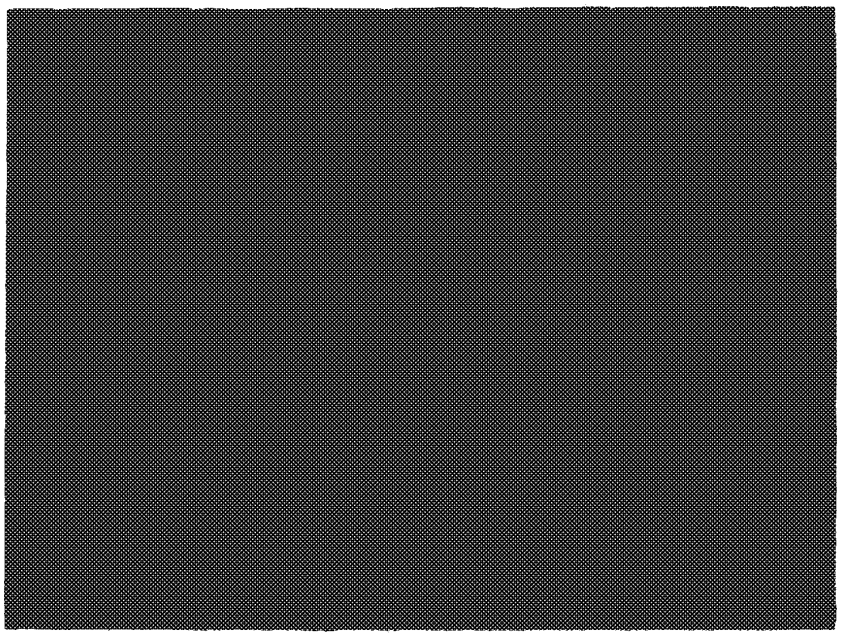


Fig. 5. Metal mask 5 μm base grooves.

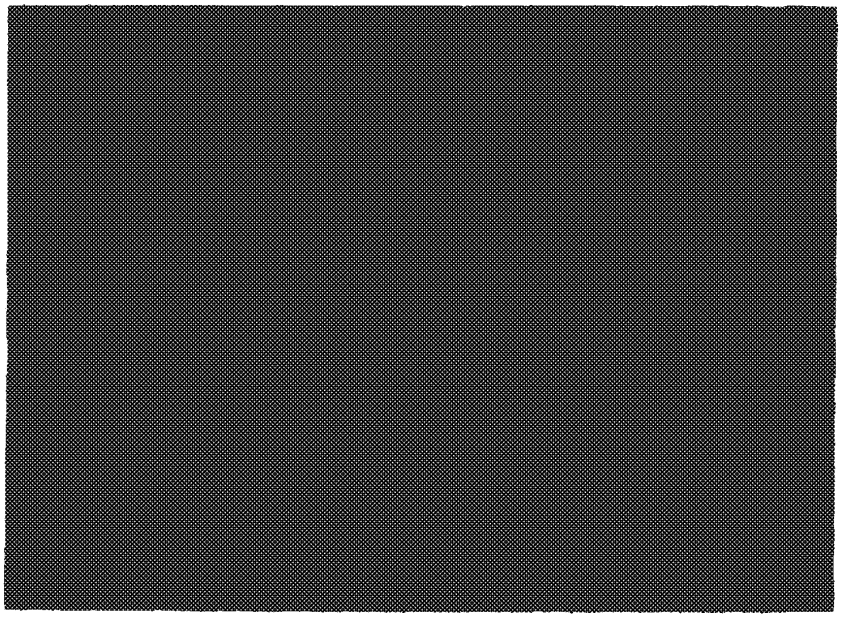


Fig. 6. Metal mask 5 μm base pyramids.

SIONYX1403000043.0161

SAMSUNG EX. 1002 - 804/4148



Fig. 7. SEM cross section of RIE microgrooves.

Table 3
Average reflectivity of RIE-textured surfaces, TiO_2 on polysilicon and bare polysilicon

RIE grooves	RIE pyramids	Bare polysilicon	Solarex TiO_2
7.9%	5.6%	34.1%	15.8%

As expected from our assumptions, two improvements are noticed from Table 2 when compared with the results from Table 1, first, there is no deterioration in open circuit voltage and second, the fill-factor reduction is smaller with the nichrome mask. Optimisation of the etching parameters for maximum optical absorbance (no flat areas), was obtained by rising the process pressure from 20 to 60 mTorr. 5 μm wide lines of nichrome with 2 μm gaps were used to produce the grooves (Fig. 7) and 5 μm × 5 μm squares of nichrome on a 7 μm grid were used to produce the pyramids (Fig. 8).

The results of reflectivity measurements for the optimised RIE texturing process shown in Table 3 and Fig. 9 clearly show that, for the RIE pyramids almost all the incoming light is experiencing a triple bounce at the substrate surface, providing excellent reflection control and greater prospects of further improvements in short-circuit current. As can be seen from Fig. 9, RIE textured surfaces have a much lower reflectivity than the standard TiO_2 antireflection coating.

SIONYX1403000043.0162

SAMSUNG EX. 1002 - 805/4148

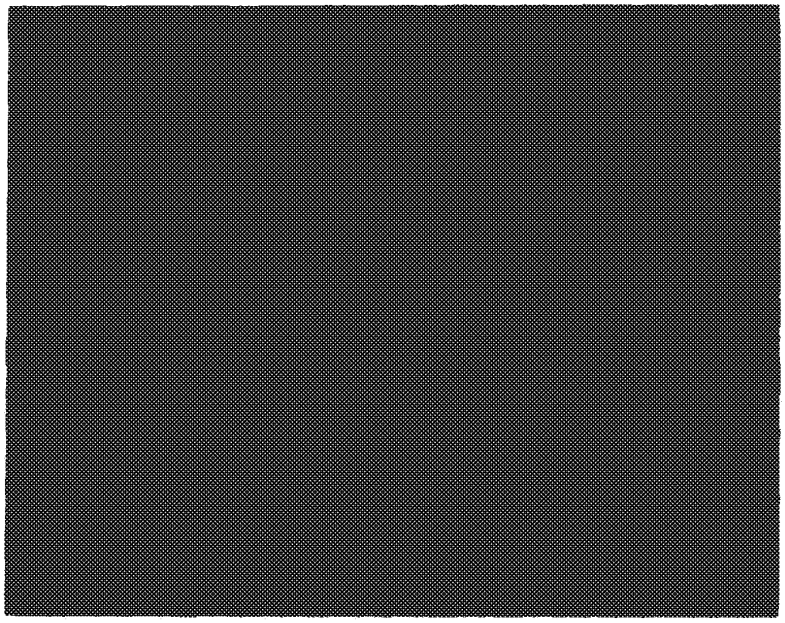


Fig. 8. SEM cross section of RIE pyramids.

A simulated calculation was performed using Sunrays [14] predicting the combination of microgroove texturing with a silicon nitride single-layer AR coating. The results of this calculation are shown in Fig. 10 and they predict zero reflection from 500 to 1000 nm, a result worth checking in the future work.

4. Conclusions

RIE has been developed succesfully as a method to texture polycrystalline silicon in an homogeneous way, independently of the grain orientation on the surface.

Reflectivity results obtained by this method surpass any previous results on polysilicon solar cells.

The final version of this novel method, now needs to be implemented in the production of photovoltaic cells to evaluate electrical performance of the RIE textured cells in comparison with the standard chemically or mechanically polished polysilicon solar cells. Simulated reflectivity calculations for the combination of this texturing method and a silicon nitride single-layer AR coating forecast zero reflelction between 500–1000 nm.

SIONYX1403000043.0163

SAMSUNG EX. 1002 - 806/4148

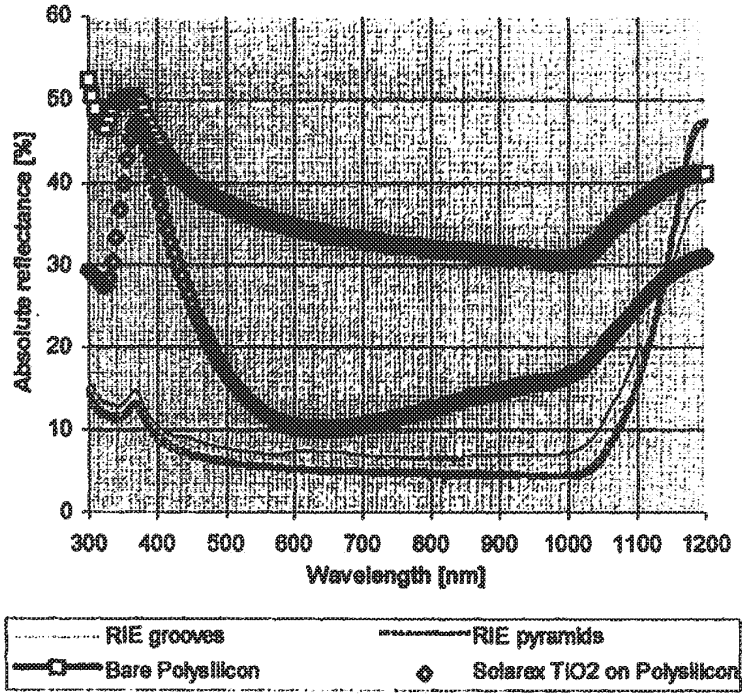


Fig. 9. Reflectivity measurements of bare polysilicon, TiO_2 on polysilicon and RIE microgrooves and pyramids.

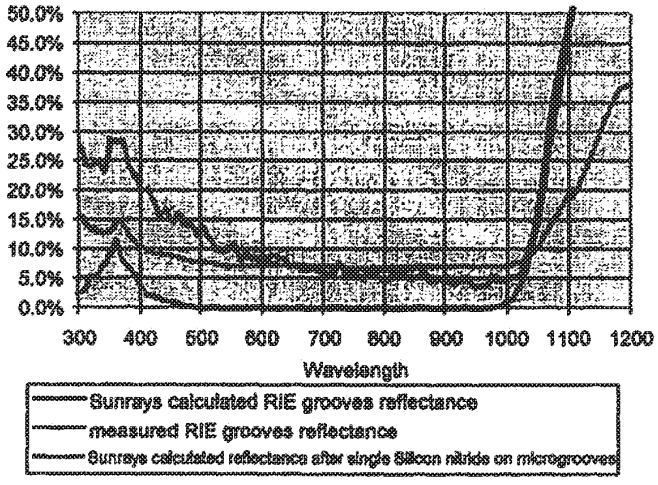


Fig. 10. Simulation of microgrooves combined with silicon-nitride AR coating.

SIONYX1403000043.0164

SAMSUNG EX. 1002 - 807/4148

Acknowledgements

The authors would like to thank the staff of the Microengineering Section of Scientific and Engineering Services at DSTO for the mask preparation, RIE processing and SEM pictures and to David Thorp from the Centre of Photovoltaic devices and Systems, UNSW, for the reflectivity measurements.

This work was supported by a South Australia State Energy Research Advisory Committee (SENRAC) grant and a University of South Australia Postgraduate Research Award (APRA).

References

[1] A.E.St. John, U.S. patent No. 3 487 223.
[2] H. Nakaya et al, Solar Energy Mater, Solar Cells 34 (1994) 219.
[3] R. Brendel, 0-7803-1220-1/93, IEEE, 1993, (1993) 252.
[4] P Campbell., Ph.D. Thesis, University of New South Wales, June 1989.
[5] S. Narayanan, Ph.D. Thesis, UNSW, ch. 5, 1989.
[6] A.W. Smith, A. Rohatgi, Solar Energy Mater. Solar Cells 29 (1993) 37.
[7] P. Campbell, M.A. Green, J. Appl. Phys. 62 (1) (1987) 243.
[8] P. Campbell, et al., 20th IEEE Photovoltaic Specialists Conf., September 1988.
[9] J.W. Coburn, Vacuum 34 (1984) 157.
[10] U.S. Tandom, B.D. Pant, Vacuum 42 (1991) 837.
[11] H. Jansen et al., J. Microelectronic Eng. 27 (1995) 475.
[12] S. Winderbaum, et al, Proc. of Microelectronics 95, Adelaide, Australia (1995) pp. 147–152.
[13] G.E.P. Box, W.G. Hunter, J.S. Hunter, in: Statistics for Experimenters, Wiley, New York, 1978, p. 1.
[14] R. Brendel, Sunrays 1.3, MPI-FKF D-70569 Stuttgart, Germany.

SIONYX1403000043.0165

SAMSUNG EX. 1002 - 808/4148

C22

BLACK SILICON: A NEW LIGHT ABSORBER

Claudia Wu
Tsing-Hua Her
Eric Mazur
Harvard University

APS Centennial Meeting
23 March 1999

SAMSUNG EX. 1002 - 809/4148

Introduction

SIONYX1403000043.0167

Introduction

Introduction

SAMSUNG EX. 1002 - 812/4148

Introduction

SAMSUNG EX. 1002 - 813/4148

Outline

- Conditions for formation

SAMSUNG EX. 1002 - 814/4148

Outline

- Conditions for formation
- Mechanism

SIONYX1403000043.0172

SAMSUNG EX. 1002 - 815/4148

Outline

- Conditions for formation
- Mechanism
- Light absorption

SIONYX1403000043.0173

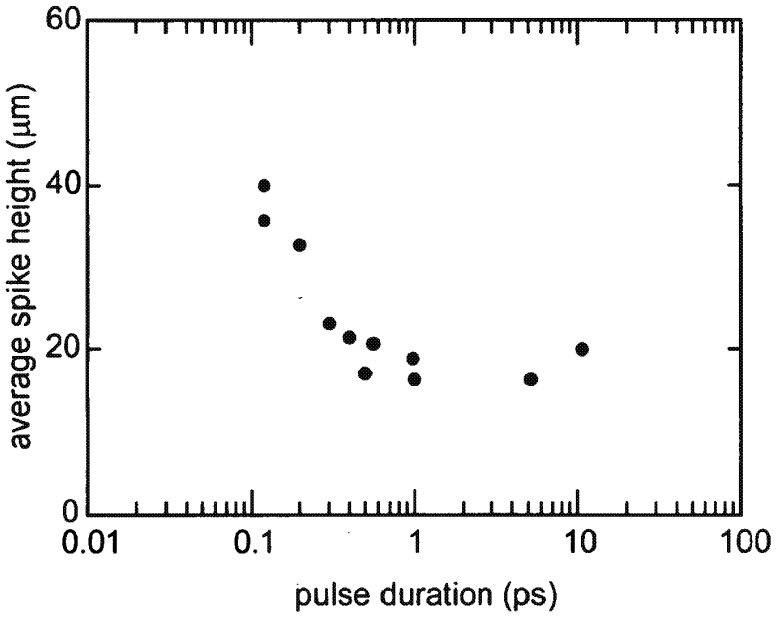
SAMSUNG EX. 1002 - 816/4148

Conditions for formation

Conditions for formation
average spike height (μm)
0
20
40
60
0
5
10
15
incident fluence (kJ/m2)

Conditions for formation

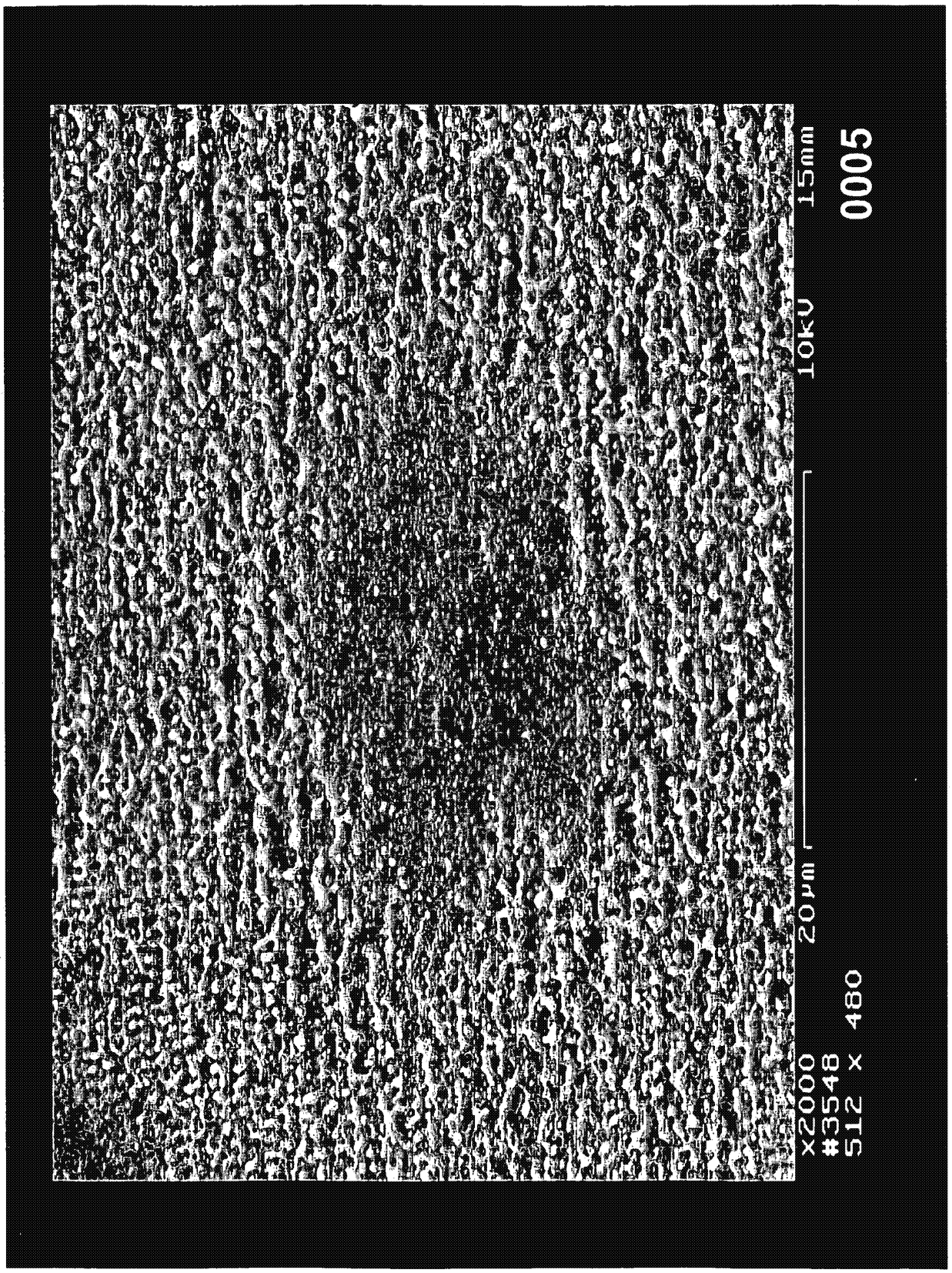
pulse duration dependence



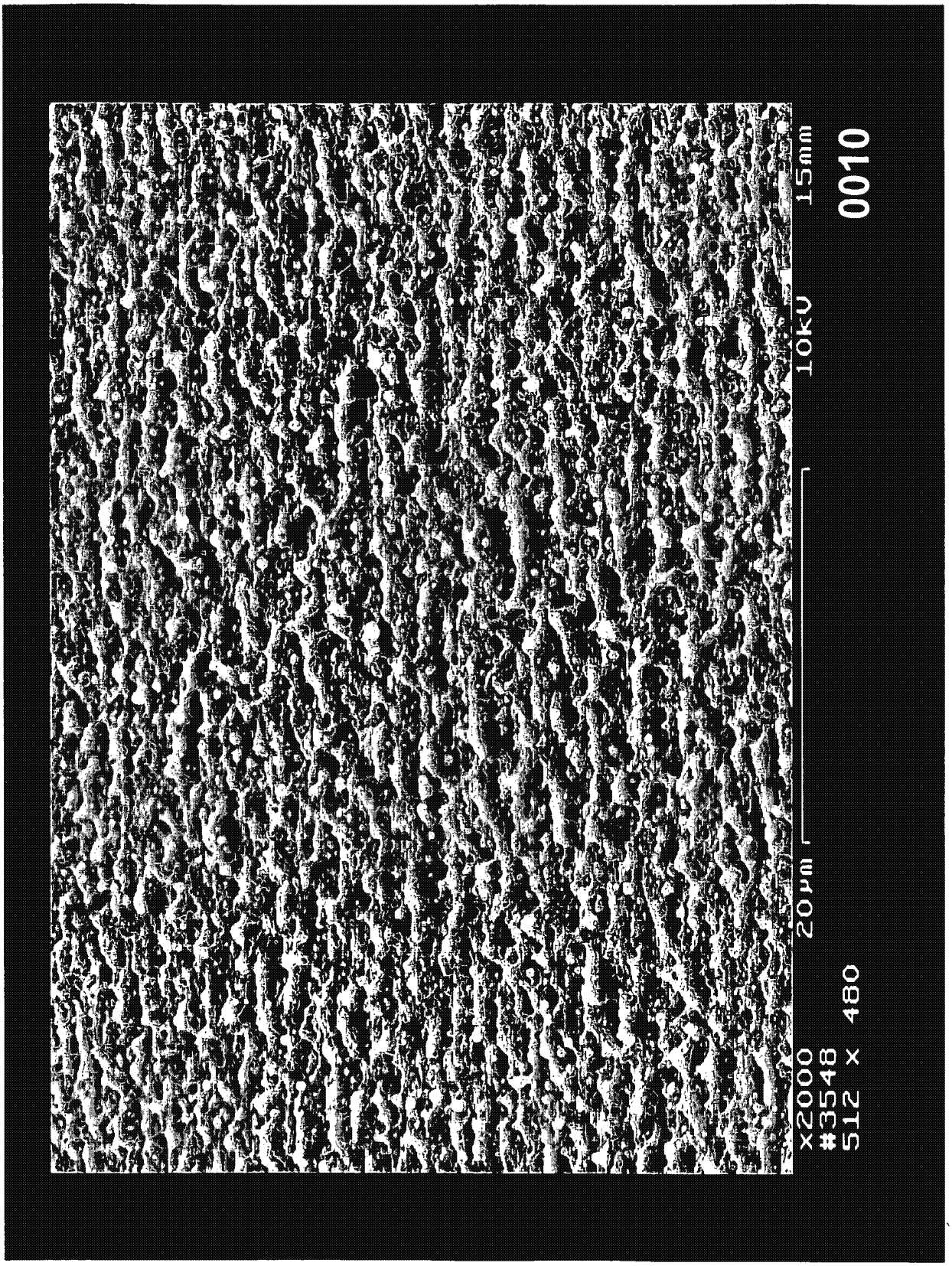
SAMSUNG EX. 1002 - 819/4148
SIONYX1403000044.0001

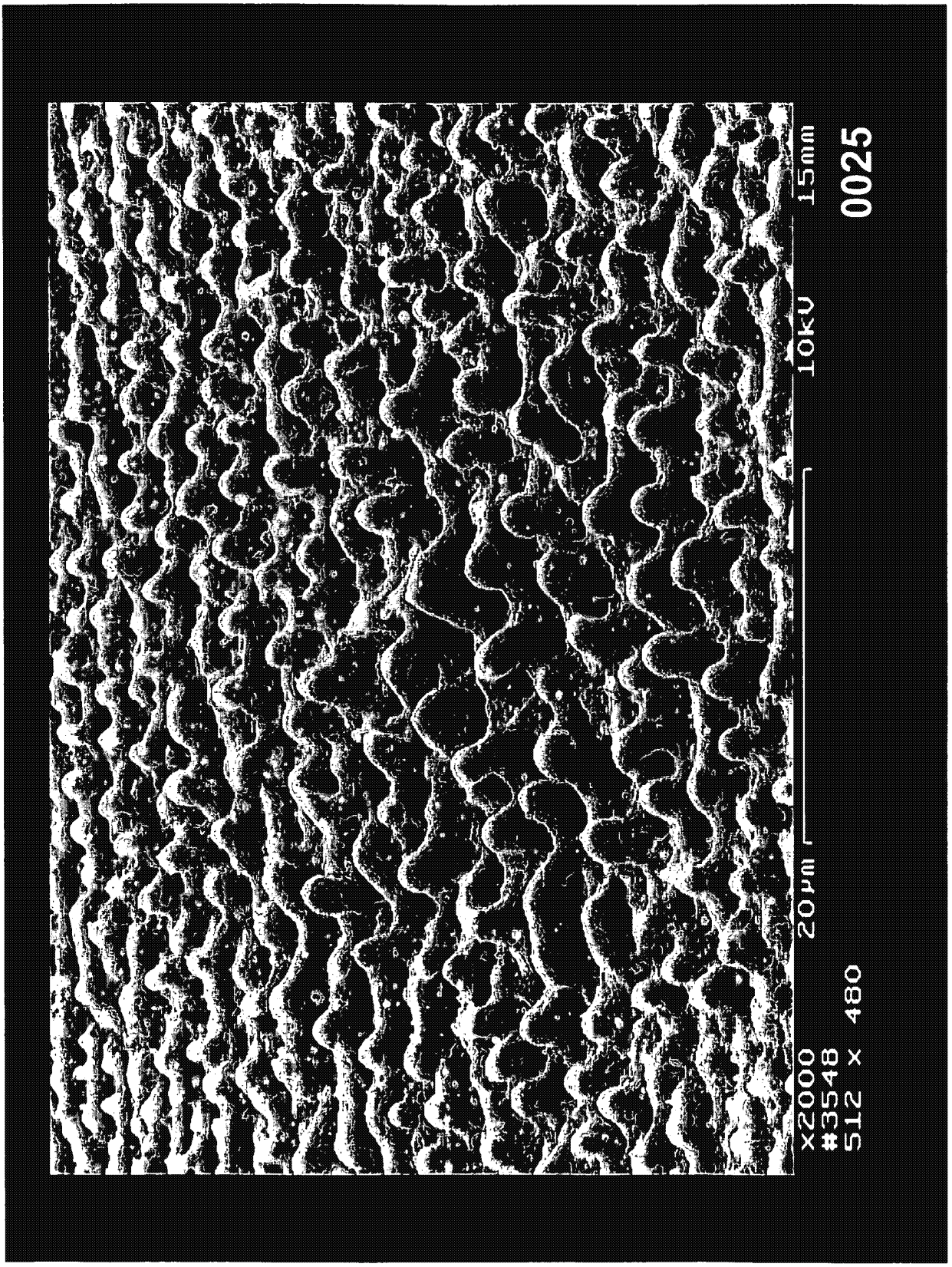
SAMSUNG EX. 1002 - 820/4148

SIONYX1403000044.0003



SIONYX1403000044.0004

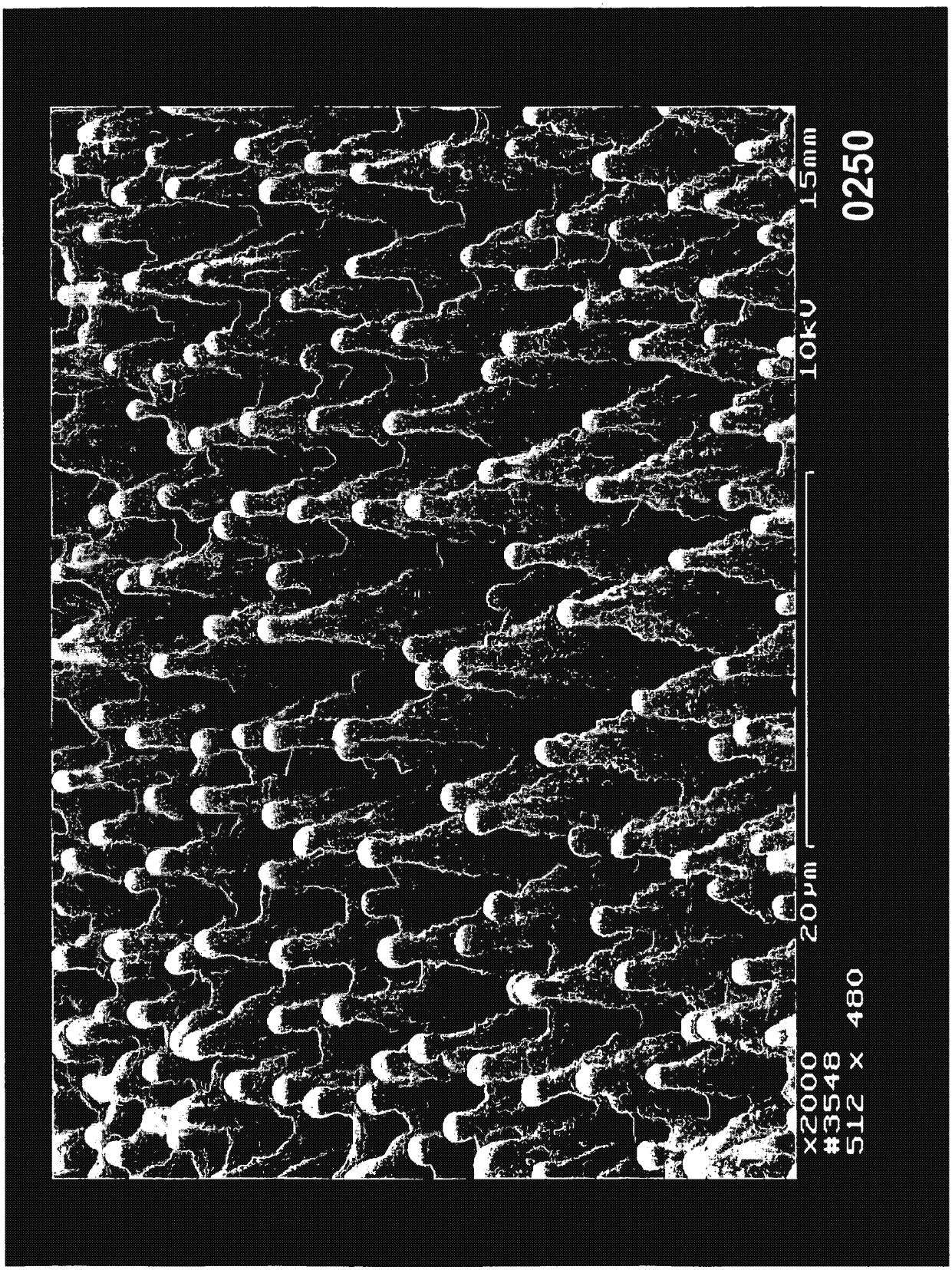

x2000
#3548
512 x 480
20µm
10kV
15mm
0010


0025
15mm
10kV
20µm
X2000
#3548
512 X 480

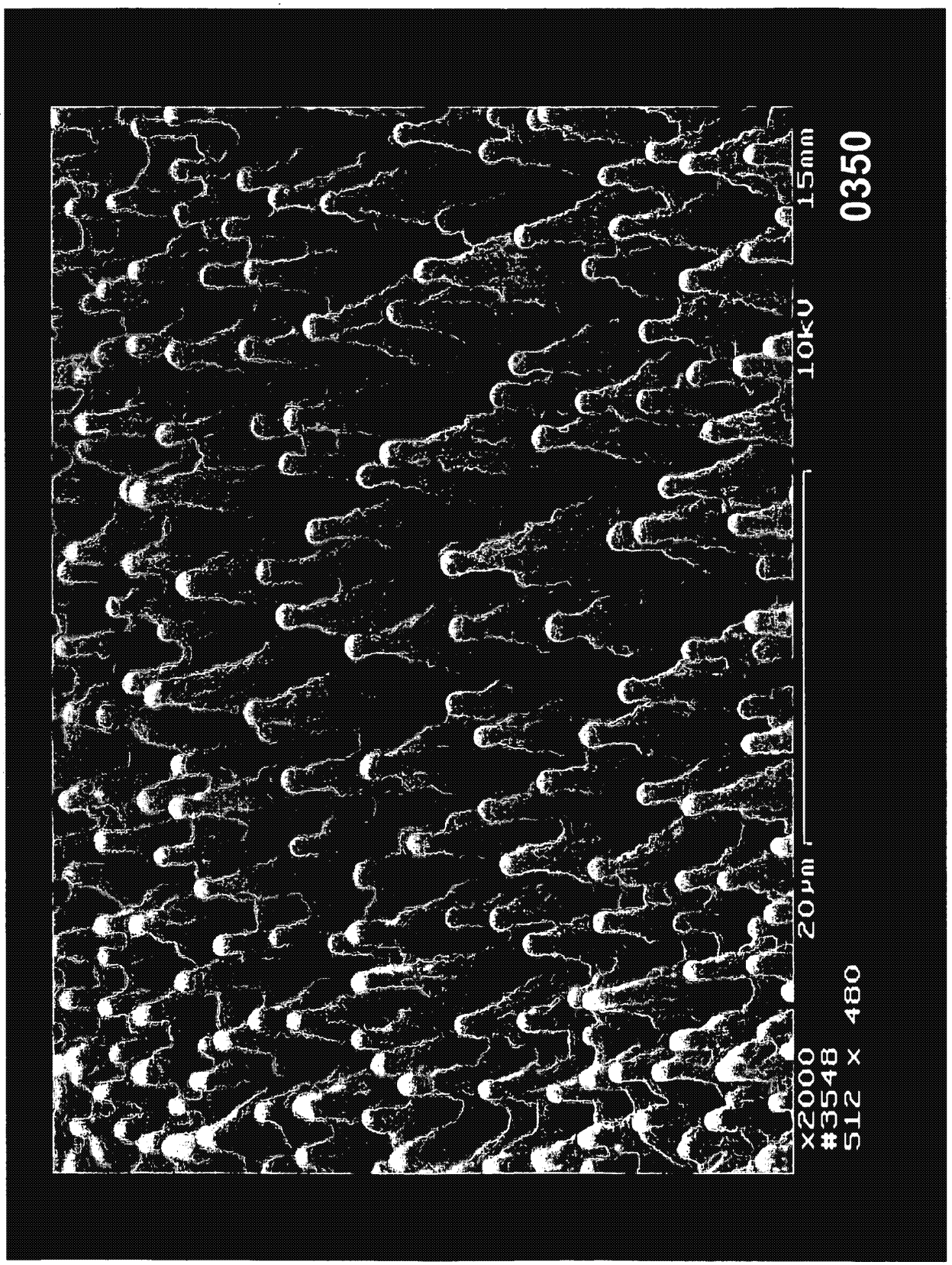
X2000
#3548
512 X 480
20µm
10kV
15mm
0050

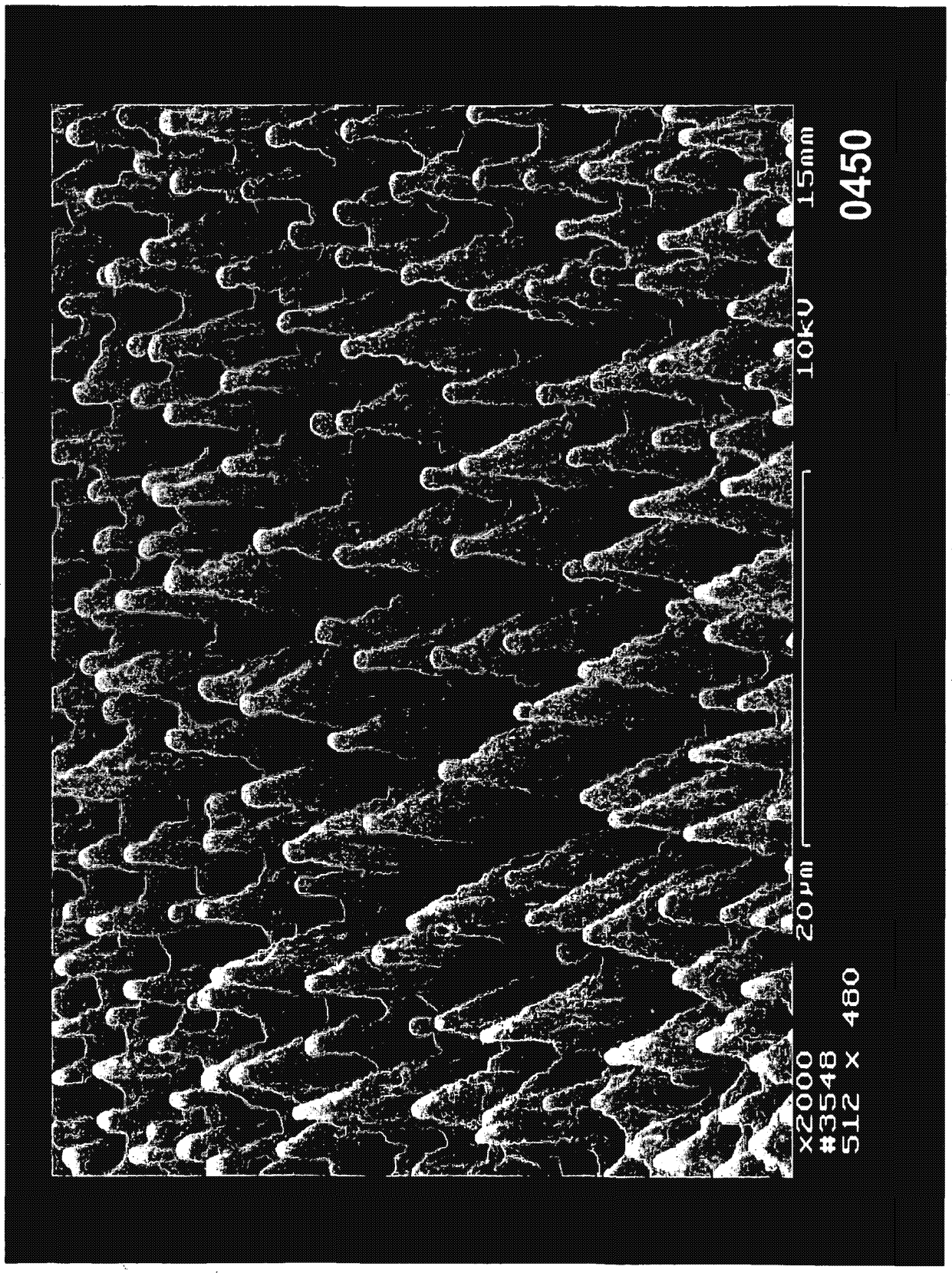
x2000
#3548
512 x 480
20µm
10kV
15mm
0075

X2000
#3548
512 x 480
20µm
10kV
15mm
0125

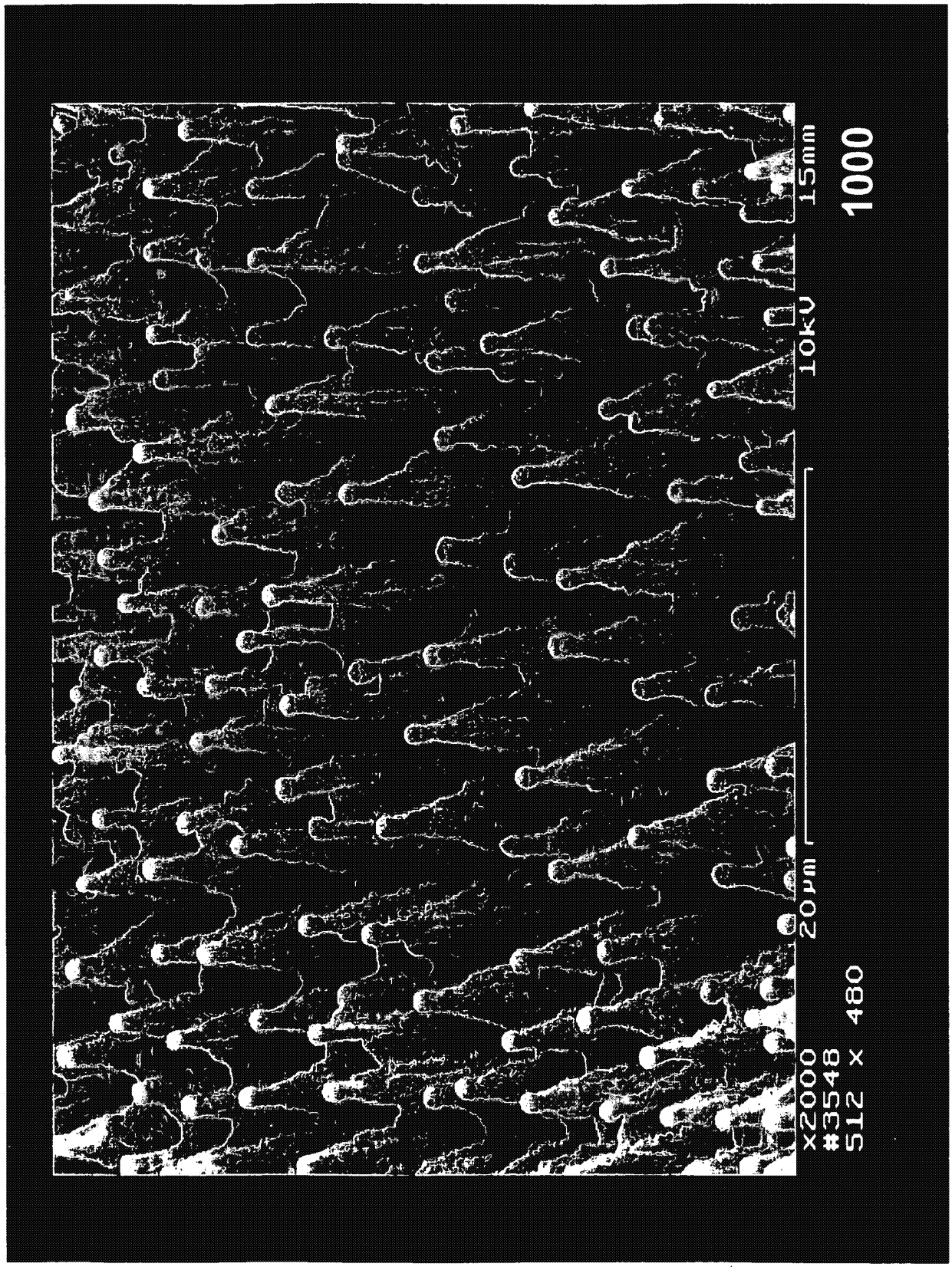


SIONYX1403000044.0010


x2000
#3548
512 x 480
20µm
10kV
15mm
0350



SAMSUNG EX. 1002 - 830/4148

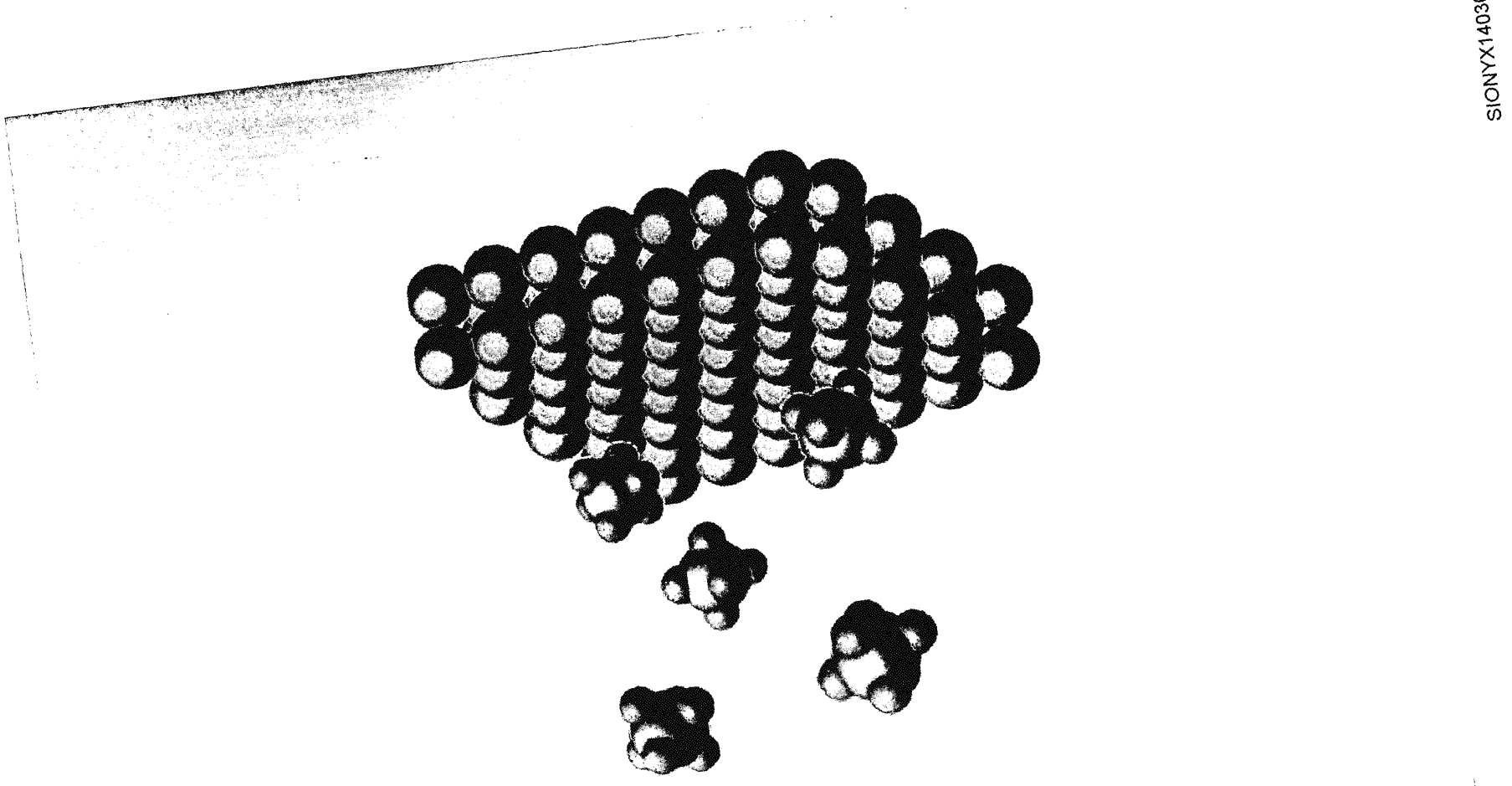

X2000
#3548
512 X 480
20µm
10kV
15mm
1000

Mechanism

SAMSUNG EX. 1002 - 832/4148

Mechanism

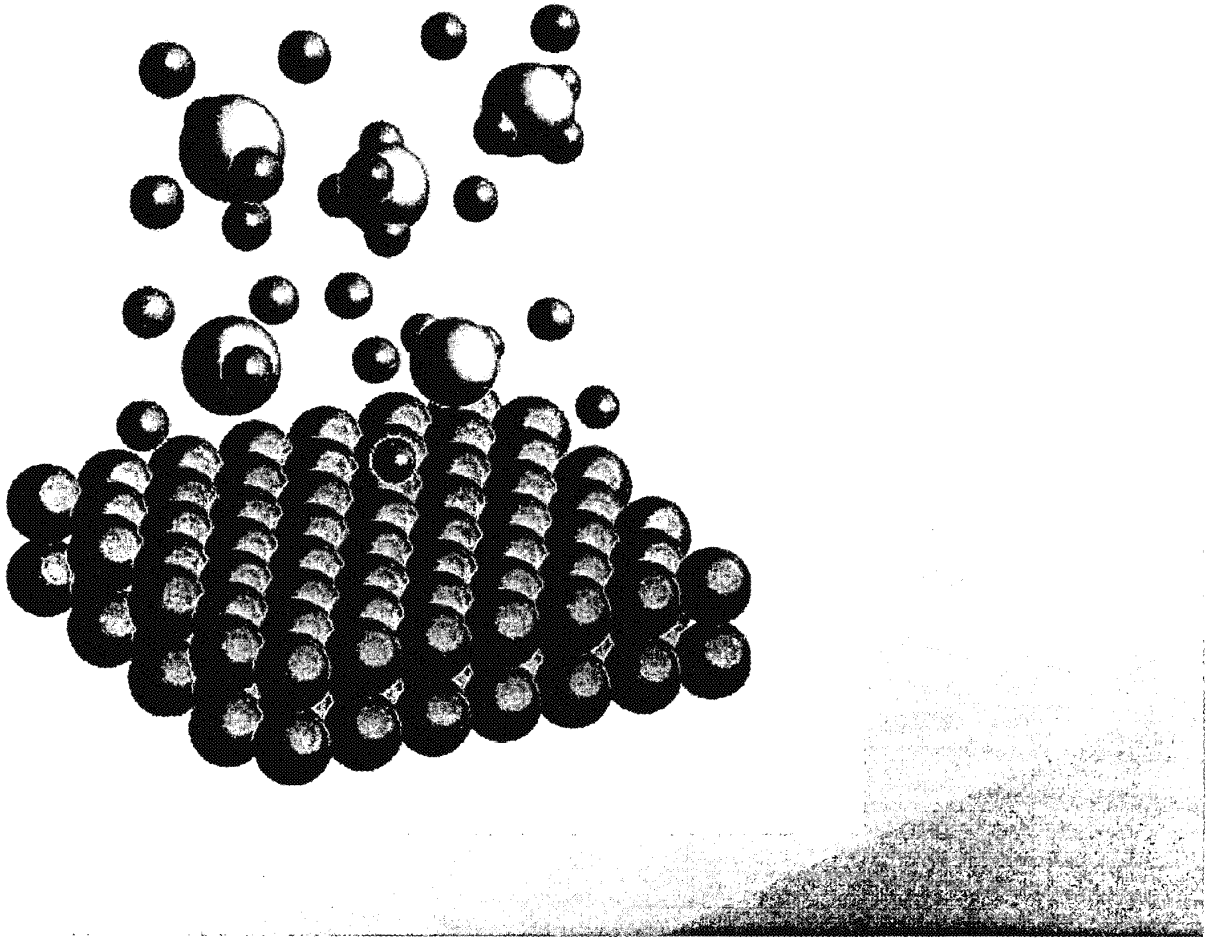
SIONYX1403000044.0016



Mechanism

SAMSUNG EX. 1002 - 834/4148

Mechanism



SAMSUNG EX. 1002 - 835/4148

Mechanism

SAMSUNG EX. 1002 - 836/4148

Mechanism

Light absorption

Light absorption

	normal Si	black Si
400 nm	0.52	
600 nm	0.60	
800 nm	0.67	

SIONYX1403000044.0021

SAMSUNG EX. 1002 - 839/4148

Light absorption

	normal Si	black Si
400 nm	0.52	1.00
600 nm	0.60	0.96
800 nm	0.67	0.80



SIONYX1403000044.0022

SAMSUNG EX. 1002 - 840/4148

Summary

- Novel technique for producing spikes
- Unity light absorption
- Luminescence?
- Field emission?

SAMSUNG EX. 1002 - 841/4148

SAMSUNG EX. 1002 - 842/4148

SAMSUNG EX. 1002 - 843/4148

GERMANIUM
10kV 15mm
5µm
X5000
#3554
512 x 480

C23

Femtosecond laser-gas-solid interactions

A thesis presented
by

Claudia Wu

to
The Department of Physics
in partial fulfillment of the requirements
for the degree of
Doctor of Philosophy
in the subject of

Physics

Harvard University
Cambridge, Massachusetts
August 2000

SIONYX1403000044.0027

SAMSUNG EX. 1002 - 845/4148

©2000 Claudia Wu
All rights reserved

SAMSUNG EX. 1002 - 846/4148

I want to dedicate this to my beloved parents *Dr. Hua-Chau* and *Pai-Ho Wu*.

SIONYX1403000044.0029

SAMSUNG EX. 1002 - 847/4148

Thesis advisor: Prof. Eric Mazur Claudia Wu

Femtosecond laser-gas-solid interactions

Abstract

This dissertation discusses two sets of experiments. The first set of experiments investigates the interaction of femtosecond laser pulses with silicon in the environment of a halogen-containing gas. We find that upon irradiation, sharp spikes are formed on the surface. Spike formation strongly depends on the laser and gas conditions. The spikes are crystalline and contain a high density of both structural and chemical defects. The spikes are very strong light absorbers and exhibit absorption exceeding $A > 0.9$ for ultraviolet (0.25 μm) to near-infrared (2.5 μm) wavelengths. Spiked avalanche photodiodes show a more than threefold increase in quantum efficiency upon illumination with 1.06 μm and 1.31 μm radiation . Unlike ordinary silicon, microstructured silicon luminesces strongly in the visible. The photoluminescence intensity and peak wavelength depend on the laser conditions used to produce the luminescent surfaces.

In the second set of experiments, we study the oxidation of CO from $CO/O_2/Pt(111)$ using femtosecond laser pulses. We observe a nonlinear dependence of both the CO-oxidation and O_2-desorption yields on the laser fluence. The yields depend strongly on the laser wavelength. Nonthermal electrons must play an important role in the excitation mechanism leading to desorption of O_2 and production of CO_2. Oxidation of CO from $CO/O_2/Pt(111)$ induced with femtosecond laser pulses most likely proceeds via the formation of an intermediate CO_3^* complex.

SIONYX1403000044.0030

SAMSUNG EX. 1002 - 848/4148

Acknowledgements

I was very fortunate when Professor Eric Mazur accepted me into his research group as a doctoral student. Eric is an outstanding advisor. Besides supervising his students on research and science, he puts a lot of effort into making graduate school fun. I have learned a tremendous amount from him, not just in science, but also about interpersonal values and skills that will be invaluable in my professional life. I thank him for his constant support and for always having an open ear for the many issues that a graduate student encounters besides research.

When I first spoke with Eric, he described his group as a small family. He did not exaggerate. Indeed, I joined a group of truly wonderful people. The Mazur group is famous for having a rich life outside the lab. I especially enjoyed our numerous group trips ranging from adventurous (at least to me) rock climbing trips to excursions to Tanglewood, which traditionally ended with a barbecue at Eric's house. There I liked playing the piano on several occasions.

During graduate school I worked with a number of exceptional people. Tsing-Hua Her and Richard Finlay taught me the essentials of lab work with patience and dedication. Catherine Crouch was a terrific partner on the "Black Silicon" project. I also thank her for reading and commenting on my thesis. Li Zhao was my buddy in lab, who stayed up with me at night to work on the experiment. Catherine, Li, and I were joined by Jim Carey, who learned all about the project in an astonishing short period of time. Besides my coworkers, it has been a great pleasure to work in the company of other members of the Mazur group: There is no doubt that Chris Schaffer was my angel in lab as a lab-mate and as a friend. He was tremendously helpful, always up for a chat, and has a marvelous sense of humor. Jon Ashcom with his sardonic wit was always a great joy to see and talk to, Albert Kim was my German buddy in lab, Nozomi Nishimura offered warmth and many smiles, Chris Roeser was never short of sharp remarks, Nan Shen was the quiet, dignified anker of our group, and Rebecca Younkin a resource of good suggestions for my research. Among the former group members I enjoyed many interesting conversations with André Brodeur, Paul Callan, Eli Glezer, Arieh Feder, and Li Huang.

Professor Cynthia Friend has been my role model as an extraordinary woman in science. I started working with her early on in my graduate career and learned a lot from her. I was always very impressed by her multi-faceted talents. I would like to thank Professor Mike Aziz for stepping in as committee member for my thesis defense and for offering help whenever needed. I also thank the Cusanuswerk in Germany for their belief

SIONYX1403000044.0031

SAMSUNG EX. 1002 - 849/4148

in my talent and for their fellowship that supported me during my graduate studies. At Harvard I was privileged to meet many wonderful friends with whom I am sharing endless memories. I wish that these people will always remain part of my life. I feel deep gratitude for my parents Hua-Chau and Pai-Ho, my sisters Kana and Anette, and my best friend Joe Oswald for their continuing support and love, without which I would not have achieved my study goals and be where I am today.

SIONYX1403000044.0032

SAMSUNG EX. 1002 - 850/4148

Citations to Previously Published Work

Some results described in this thesis have been previously published:

1. R.J. Finlay, T.-H. Her, C. Wu, and E. Mazur, *Chem. Phys. Lett.* **274**, 499–504 (1997).

2. T.-H. Her, R.J. Finaly, C.Wu, and E. Mazur, *J. Chem. Phys.* **108**, 8595–8598 (1998).

SIONYX1403000044.0033

SAMSUNG EX. 1002 - 851/4148

Contents

Dedication . . . iii
Abstract . . . iv
Acknowledgements . . . v
Citations to Previously Published Work . . . vii
Table of Contents . . . viii
List of Figures . . . xi

1 Introduction **1**
1.1 General overview . . . 1
1.2 Content and organization . . . 1

2 Formation of silicon microspikes with femtosecond laser pulses **3**
2.1 Introduction . . . 3
2.2 Experimental procedure . . . 5
2.3 Formation conditions . . . 7
2.3.1 Spike evolution . . . 7
2.3.2 Effects of laser and gas parameters . . . 7
2.3.3 Other materials . . . 12
2.4 Structural and chemical analysis . . . 12
2.4.1 Chemical analysis . . . 13
2.4.2 Structural properties . . . 18
2.4.3 Summary . . . 21
2.5 Formation mechanisms . . . 22
2.5.1 Femtosecond laser-solid interactions: Fundamental processes . . . 22
2.5.2 Formation mechanisms of laser cones . . . 30
2.5.3 Gas effects: Laser-induced chemical etching . . . 32
2.5.4 Discussion . . . 35

3 Optical Properties of Spiked Silicon **37**
3.1 Introduction . . . 37
3.2 Theoretical considerations . . . 38
3.3 Reflectance, transmittance, and absorptance in spiked silicon . . . 43
3.3.1 Measurement of optical properties . . . 43
3.3.2 Results . . . 46

SIONYX1403000044.0034

SAMSUNG EX. 1002 - 852/4148

3.4 Light absorption in spiked silicon 46
3.4.1 Increase in light absorption through surface structuring 46
3.4.2 Below-band gap absorption 49
3.5 Discussion 59
3.6 Applications 60

4 Photocurrent measurements **61**
4.1 Introduction 61
4.2 Charge carrier generation and recombination in silicon 63
4.3 Device design and fabrication 64
4.3.1 Device fabrication 67
4.3.2 Passivation 69
4.4 Photocurrent measurements 70
4.4.1 Experimental setup 70
4.4.2 Results 72
4.4.3 Effects of hydrogenation 74
4.5 Below-bandgap photocurrent from microstructured avalanche photodiodes . 77
4.5.1 Avalanche photodiodes (APD) 77
4.5.2 Increase in below-band gap quantum efficiency of microstructured APDs 78
4.6 Discussion 79

5 Visible photoluminescence of silicon laser-structured in air **81**
5.1 Introduction 81
5.2 Technological importance of luminescent silicon 82
5.3 Experiment 84
5.3.1 Fabrication of luminescent silicon samples 84
5.3.2 Photoluminescence measurements 85
5.4 Results 86
5.4.1 Series A: Effects of laser fluence 86
5.4.2 Series B: Effects of laser shot number 90
5.4.3 Series C: Effects of annealing 91
5.5 Discussion 93
5.5.1 Laser-induced formation of luminescent SiO_x 93
5.5.2 Origin of luminescence (series C) 95
5.6 Applications 97

6 Femtochemistry of CO and O_2 on Pt(111) **98**
6.1 Introduction 98
6.2 Photo-excitation at adsorbate-metal surfaces 99
6.3 Photochemistry of $CO/O_2/Pt(111)$ 102
6.3.1 Background 102
6.3.2 Linear photochemistry 104
6.3.3 Femtochemistry of $CO/O_2/Pt(111)$ 108
6.4 Reaction Pathways to CO_2-Formation from $CO/O_2/Pt(111)$ 113

SIONYX1403000044.0035

SAMSUNG EX. 1002 - 853/4148

7 Conclusion **126**
7.1 Formation of silicon microspikes with femtosecond laser pulses 126
7.2 Femtochemistry of $CO/O_2/Pt(111)$ 127

Bibliography **128**

SIONYX1403000044.0036

SAMSUNG EX. 1002 - 854/4148

List of Figures

2.1 (*a*) Spiked silicon surface as seen under the scanning electron microscope (SEM) at an angle of 45°, (*b*) closeup view of silicon spikes. 4
2.2 Experimental set-up for microstructuring silicon. 6
2.3 Silicon surface after (*a*) 0 pulses, (*b*) 1 pulse, (*c*) 5 pulses, (*d*) 10 pulses, (*e*) 25 pulses, (*f*) 50 pulses, (*g*) 150 pulses, (*h*) 300 pulses, (*i*) 450 pulses, (*j*) 1000 pulses, (*k*) 1500 pulses, and (*l*) sideview of cleaved spiked silicon chip as seen under the scanning electron microscope at a 45° view. 9
2.4 Comparison of structures formed in (*a*) SF_6 and (*b*) vacuum as seen under the SEM at a 45° view. 10
2.5 (*a*) Surface after irradiation with 500 laser pulses. The spike separation (and spike height) varies across the illuminated surface area due to the nonuniform laser energy beam profile. (*b*) Spike height as a function of laser fluence. [1] 11
2.6 Spike separation as a function of pulse duration. [1] 12
2.7 Structures made on (*a*) Ge and (*b*) InP. On germanium spikes are formed which are smaller and exhibit more protrusions on the sidewalls than those made in SF_6. No spikes are formed in InP or GaAs. 13
2.8 XPS spectra of (*a*) ordinary silicon and (*b*) spiked silicon. 14
2.9 (*a*) RBS spectrum of spiked silicon before the HF etch. The RBS spectrum of ordinary silicon is shown as well. (*b*) RBS spectrum after the HF etch. The oxygen signal disappeared and the spectrum is indistinguishable from that of ordinary silicon. 16
2.10 Masses collected by the mass spectrometer from spiked silicon after the HF-etch using SIMS. 17
2.11 SIMS spectra of spiked silicon as a function of sputtering time after an HF etch. 18
2.12 Schematic showing ion channeling spectra of (*a*) crystalline material, (*b*) amorphous or randomly oriented polycrystalline material, (*c*) crystalline material with a high density of chemical or structural defects. After Feldman. [2] 19
2.13 Ion channeling spectra of randomly aligned silicon, channeled spiked silicon, and channeled single-crystalline silicon. 20
2.14 Schematic of electronic excitation in a semiconductor by laser pulses: (*a*) single-photon excitation, (*b*) multi-photon excitation, (*c*) free carrier-absorption, (*d*) impact ionization. 23

SIONYX1403000044.0037

SAMSUNG EX. 1002 - 855/4148

2.15 Timescales of the energy distribution processes. 23
2.16 Depth-dependence of temperature increase in silicon upon irradiation of a single 100 fs, 0.5 kJ/m^2 laser pulse. 25
2.17 (*a*) Thermal and nonthermal phase transformations take place at different fluences. (*b*) Nonthermal processes are induced with subpicosecond laser pulses of 10 kJ/m^2 fluence, whereas picosecond laser pulses of the same fluence induce thermal processes. 29
2.18 Cone formation in ion sputtering seeded by a protective pit. Material is eroded around the pit. 31
2.19 Light is reflected off a protrusion which leads to enhanced light absorption and material removal at the sidewalls of the protrusion. 32
2.20 Schematic of material removal through laser-assisted etching. (1) A silicon surface is exposed to femtosecond laser pulses in the atmosphere of SF_6. (2) Fluorine radicals are created via photodissociation of the SF_6molecules. (3) The radicals react with silicon and form SiF_x compounds. (4) SiF_x compounds are desorbed by the laser, volatile species (such as SiF_4) leave the surface. 34

3.1 Photograph of black silicon patch. 37
3.2 Reflectance of ordinary crystalline silicon as determined by literature values for n and k [3] as (*a*) function of wavelength at 45° incidence angle and (*b*) incident angle for 800 nm light. 42
3.3 Diffusively reflected light is collected in an integrating sphere. 44
3.4 SEM images of three spiked surfaces with (*a*) 1-2 μm, (*b*) 4-7 μm, (*c*) 10-12 μm spike height. 45
3.5 Reflectance and transmittance of the three spiked surfaces and ordinary silicon. 47
3.6 Absorptance of the three spiked surfaces and ordinary silicon. 48
3.7 Schematic showing light trapping through multiple reflections. 48
3.8 Phonon-assisted photon absorption in silicon. 50
3.9 Sulfur energy levels in silicon. Values are shown in eV. After Janzen *et al.* [4] 52
3.10 SIMS spectra before and after vacuum anneal. 53
3.11 Reflectance and transmittance of spiked silicon after vacuum anneal for 3 hours at 1210 K. 54
3.12 Absorptance of spiked silicon before and after vacuum anneal for 3 hours at 1210 K. 55
3.13 XP spectra of spiked silicon before and after vacuum anneal. 56
3.14 Spiked silicon surface (*a*), (*b*) before and (*c*), (*d*) after vacuum anneal as seen under the SEM using a magnification of (*a*), (*c*) x 10 000 and (*b*), (*d*) x 100 000. 58
3.15 Ion channeling spectra taken from the spiked silicon sample before and after vacuum anneal of 3 hours at 1210 K. For comparison, the spectrum of the randomly aligned sample is shown as well. 59

4.1 (*a*) Generation of an electron-hole pair upon absorption of a photon, (*b*) band-to-band recombination, and (*c*) recombination via a trap. 64

SIONYX1403000044.0038

SAMSUNG EX. 1002 - 856/4148

4.2 (*a*) Photograph of the MSM device used for measuring photocurrent, (*b*) Schematic side view of the device. 65
4.3 Band diagram in a Schottky barrier (*a*) in thermal equilibrium, (*b*) with forward biasing, (*c*) with reverse biasing. 66
4.4 Band diagram in an MSM device: The side connected to the positive voltage terminal experiences a forward bias, whereas the side connected to the negative terminal a reverse bias. Switching the biasing produces a mirror image of the energy bands. 67
4.5 Schematic showing the photolithographic steps for making the front grid electrode: (*a*) Photoresist is deposited onto the sample, (*b*) The sample is illuminated with UV light under a gridded mask, only the photoresist under the transparent part of the mask is exposed to the light. The exposed photoresist washes away in the developer. (*c*) Metal is evaporated onto the sample, (*d*) The metal that was deposited onto the undeveloped photoresist washes away with acetone, leaving a gridded metal pattern behind. 68
4.6 Schematic of hydrogenation setup. 70
4.7 Circuit diagram of photocurrent measurements. 71
4.8 Schematic of the photocurrent measurement setup. 71
4.9 Photocurrent as a function of sample bias upon illumination of the flat part (solid line) and upon illumination of the spiked part (dashed line) of the device. 73
4.10 Increase in photocurrent as a function of hydrogenation time. The values are shown for forward biasing the front diode. 75
4.11 Comparison of photocurrent obtained by illuminating spiked silicon and by illuminating flat silicon of sample B: (*a*) before hydrogenation, (*b*) after 7 hours of hydrogenation, and (*c*) after 19 hours of hydrogenation. 76
4.12 Spiked surface (*a*) before and (*b*) after 7 hours of hydrogenation. After exposure to the hydrogen plasma the spikes have been sharpened and thinned. 77
4.13 Quantum efficiency of a 1x1 mm^2 APD pixel as a function of illumination wavelength. [5] 78
4.14 APD signal from illuminating the spiked and the flat parts of the device respectively with 1.31 μm light. Data were taken in collaboration with Radiation Monitoring Devices. [5] 79

5.1 Experimental set-up for measuring photoluminescence. 85
5.2 Surfaces made with laser pulses of fluence (*a*) 2.5 kJ/m^2, (*b*) 5 kJ/m^2, 10 kJ/m^2, and (*d*) 30 kJ/m^2, as seen under the scanning electron microscope at a 45° view. 87
5.3 (*a*) Photoluminescence of samples made with laser pulses of fluence 2.5 kJ/m^2, 5.0 kJ/m^2, 10.0 kJ/m^2, and 30.0 kJ/m^2, (*b*) RBS spectra of the surfaces showing increasing oxygen content in the samples with increasing laser fluence used to produce the samples. 88
5.4 (*a*) Computer simulation of RBS spectrum of surface made with 30 kJ/m^2, (*b*) photoluminescence intensity as a function of measured surface oxygen concentration. Normalization of the photoluminescence intensity is made to the sample produced at $F = 2.5$ kJ/m^2. 89

SIONYX1403000044.0039

SAMSUNG EX. 1002 - 857/4148

5.5 Photoluminescence of samples made with different laser shot number/unit surface area (series B). (*a*) Sample made with 50 μm/s and 2 scans, (*b*) 50 μm/s and a single scan, (*c*) 100 μm/s and two scans, and (*d*) 100 μm/s and a single scan. 90
5.6 (*a*) Photoluminescence of series C_2 without annealing after 0.5 hour, 1 hour, and 3 hours of vacuum annealing at 1300 K, (*b*) comparison of the photoluminescence spectra of series C_2 and series C_1 after 3 hours of annealing. . . 92
5.7 Photoluminescence of the sample from series A without anneal and after 5 hours anneal. 93
5.8 Surface of the sample from series A (*a*) before and (*b*) after 5 hours anneal as seen under the scanning electron microscope. 93

6.1 Nascent electron distribution after photoexcitation with photons of energy $\hbar\omega$. The density of states (DOS) is shifted by an energy $\hbar\omega$. E_f denotes the Fermi level and E_v the vacuum level. After Zhou and White [6] 100
6.2 Calculated electron and lattice temperatures in platinum following 100 fs, 32 μJ/mm^2, 800 nm laser pulses. Shown as well is the profile of the laser pulse. [7] 101
6.3 (*a*) TPD spectrum of $^{18}O_2$/Pt(111) showing mass 36 amu ($^{18}O_2$), (*b*) TPRS of $C^{18}O/^{18}O_2$/Pt(111) showing mass 48 amu ($C^{18}O_2$). 103
6.4 (*a*) O_2-desorption yield as a function of laser fluence, (*b*) CO_2-yield and O_2-yield as a function of laser wavelength. Note that the scales are different for figure a and figure b. After Mieher. [8] 105
6.5 Schematic of adsorbate-metal excitation in the DIET model. (1) An excited adsorbate-substrate complex makes a vertical transition from the ground state potential (PES 1) to an excited state potential (PES 2). (2) It moves towards the minimum on the PES 2 and acquires kinetic energy. (3) After a certain time, the adsorbate-substrate complex returns to PES 1. 107
6.6 Schematic of the experimental apparatus used in the femtochemistry experiments. 109
6.7 (*a*) O_2 and (*b*) CO_2 yields as a function of laser fluence using 267 nm, 400 nm, and 800 nm light as the excitation wavelength. 110
6.8 Schematic diagram of the excitation and de-excitation cycles in DIMET. Shown are two cycles. The first excitation path is depicted using filled arrows, the second excitation cycle is depicted using hollow arrows. After the first excitation cycle the adsorbate-substrate complex starts out vibrationally excited. 113

SIONYX1403000044.0040

SAMSUNG EX. 1002 - 858/4148

Chapter 1

Introduction

1.1 General overview

Femtosecond laser pulses open up unique opportunities for both research and application. Not only do they allow us to view ultrafast phenomena such as chemical reactions or phase transitions in real time with unprecedented time resolution, but they are also high power energy sources capable of delivering intensities exceeding TW/cm^2. When femtosecond laser pulses interact with matter, the intense and ultrafast excitation creates conditions unattainable through other means. In a solid, electronic temperatures of several thousand Kelvin in a cold atomic lattice are achieved. Under these highly nonequilibrium conditions, novel phenomena can occur. If the deposited energy exceeds the damage threshold of the solid, surface structuring results. Modification of materials using femtosecond laser pulses produces structures via novel mechanisms of surface damage.

If a gas is adsorbed on the surface of the solid, the highly excited substrate can lead to unique excitation and reaction pathways which can be observed, for example, through very high desorption and reaction yields.

1.2 Content and organization

This thesis investigates the interactions of femtosecond laser pulses in two systems, the first a gas/solid system and the second an adsorbate/solid system. In the first set of experiments we investigate the surface modification caused by irradiating a silicon surface with femtosecond laser pulses. We find that sharp spikes form when the irradiation takes

SIONYX1403000044.0041

SAMSUNG EX. 1002 - 859/4148

place in an environment of sulfur hexafluoride or chlorine. Chapter 2 investigates the spike formation conditions as well as the spikes' structural properties and chemical composition. A discussion of possible formation mechanisms follows.

In Chapter 3 we study the optical properties of spiked surfaces. These surfaces absorb nearly all incident light across the visible spectrum and therefore appear black to the eye. We measure both specular and diffuse reflectance and transmittance, which reveals, besides near-perfect absorption of ultraviolet and visible light, equally strong absorption of below-band gap radiation. Experiments are conducted to investigate the cause of the strong absorption in the spiked surface.

Spiked surfaces would greatly enhance the efficiency of ordinary silicon photovoltaics if the light absorption generates photocarriers available for conduction. Chapter 4 compares the photocurrent produced in spiked silicon devices to those produced in ordinary flat silicon devices. We examine the effects of surface and bulk passivation through hydrogenation and photocurrent production. Avalanche photodiodes are structured and tested for response to below-band gap radiation.

Chapter 5 studies the photoluminescence of silicon surfaces laser-structured in air rather than a halogenated gas. The photoluminescence is measured from surfaces made under different laser conditions. Annealing experiments are performed to investigate the origin of the luminescence.

In the second set of experiments presented in this thesis (Chapter 6), we study the oxidation of CO from $CO/O_2/Pt(111)$ using femtosecond laser pulses. High intensity laser pulses produce highly excited electrons in the underlying metal substrate. These electrons can induce photochemistry substantially different from that induced with low-intensity light sources. The experiments investigate both the excitation and reaction pathways leading to formation of CO_2 using femtosecond laser pulses.

SIONYX1403000044.0042

SAMSUNG EX. 1002 - 860/4148

Chapter 2

Formation of silicon microspikes with femtosecond laser pulses

2.1 Introduction

Laser-induced damage of solids has been of scientific and technological interest since the development of the laser. [9] The absorption of energetic photons by a solid can lead to a permanent modification of the surface by causing melting and resolidification, vaporization, or ablation of material. The possibility of materials processing using both continous and pulsed lasers has long been recognized. Today, laser annealing, sputtering, welding and cutting are important areas of research and application.

The damage produced in a solid by laser pulses has been studied for a wide range of materials including metals [10, 11], semiconductors [9, 12] and dielectrics. [13] In silicon, cumulative irradiation with laser pulses produces random damage patterns as well as regular surface structures. Periodic patterns in the form of ripples (known as laser-induced periodic surface structures (LIPSS)) has attracted much interest and has been studied by several groups. [12, 9, 14, 15, 16] Another phenomenon, first observed on Al_2O_3 and then also in silicon, is the formation of conical features under laser irradiation. These laser-induced cones were studied in the mid 1980s, mainly on various alloys in association with laser sputtering of materials.[1] The first laser-induced cones in silicon were reported by Rothenberg

[1]The formation of laser cones was initially encountered as a problem for pulsed laser deposition: structuring of the target material upon cumulative laser irradiation causes an alteration of the deposition rate and thus prevents a precise control over the deposited film thickness.

SIONYX1403000044.0043

SAMSUNG EX. 1002 - 861/4148

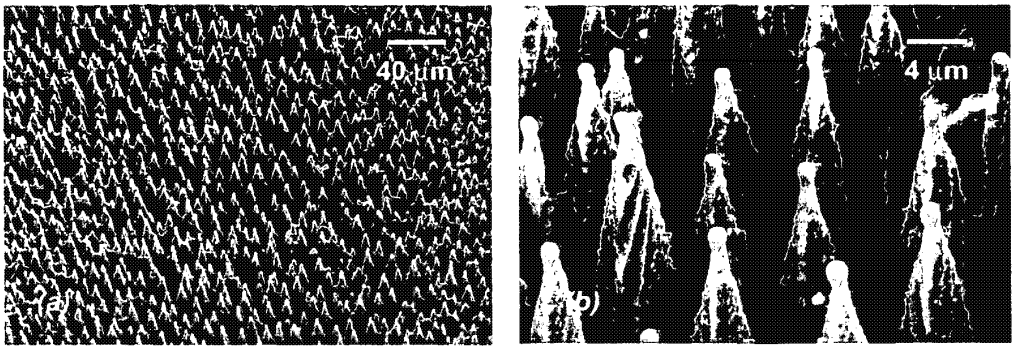


Figure 2.1: (*a*) Spiked silicon surface as seen under the scanning electron microscope (SEM) at an angle of 45°, (*b*) closeup view of silicon spikes.

and Kelly [17], who produced micron-sized irregular cones protruding above the surface using nanosecond UV laser pulses. Columnar structures in silicon were also reported using femtosecond laser pulses. [18, 19]

Whereas material modification using pico- and nanosecond laser pulses has matured to an important area of study over the last 20 years, femtosecond laser pulses have been considered only fairly recently for materials processing. Advantages of femtosecond laser pulses over picosecond and nanosecond pulses for micromachining have been demonstrated by a number of groups. [10, 20] The processes by which femtosecond laser pulses interact with the solid surface differ considerably from those of the interactions with picosecond or longer pulses. In particular, nonthermal, ultrafast phase transformations can occur on a timescale much faster than thermal processes. [21, 22, 23, 24] The use of femtosecond laser pulses thus leads to new phenomena and mechanisms of surface damage and structuring. As a fairly young field of study, the modification of solids with femtosecond laser pulses is not yet well understood.

We recently observed the formation of sharp, micron-sized spikes after a silicon surface was irradiated with hundreds of femtosecond laser pulses in an atmosphere of either SF_6 or Cl_2. These sharp spikes differ remarkably from the cones and columnar structures previously reported. The spikes exhibit a sharp tip with a subtended angle of less than 20° and show some homogeneity in their distribution. The spikes' characteristics depend on laser and gas conditions. They can be several tens of microns tall and the tip-to-tip

SIONYX1403000044.0044

SAMSUNG EX. 1002 - 862/4148

separation is several microns. Similar spikes have now also been reported by Pedraza *et al.* [25] using nanosecond pulses in an SF_6 environment. However, while exhibiting similar morphology, these spikes are produced above the silicon surface, suggesting a different formation mechanism.

This chapter is divided into two parts and is organized as follows. In the first part I provide details on the experimental setup (Sec. 2.2), discuss formation conditions (Sec. 2.3), and describe the spikes' structural and chemical composition (Sec. 2.4). In the second part I associate these results with possible mechanisms of spike production (Sec. 2.5).

2.2 Experimental procedure

Single-crystal silicon wafers were cleaned in a 10-minute ultrasonic trichlorethylene bath followed by a 10-minute ultrasonic acetone bath followed by a 10-minute ultrasonic methanol bath.[2] The samples were mounted on a motorized and computer-controlled two-axis translation stage inside a vacuum chamber. The vacuum chamber was pumped out with a corrosion-resistant pump (Edwards model 18) to a pressure of 10^{-3} Torr. We then backfilled the chamber with a selected gas. The pressure was monitored with a corrosion-resistant MKS capacitance-voltage transducer.

We use a regeneratively amplified Ti:sapphire laser system described elsewhere [26, 7, 27] to produce 100-femtosecond laser pulses of 800 nm wavelength at a rate of 1 kHz. The pulse energy is varied by a waveplate-polarizer combination and by the use of neutral density filters. The pulse duration is controlled by changing the distance of the gratings in the compressor after the amplification stage. The laser beam is focused with a 0.15 m focal-length lens onto the sample and is incident normal to the sample surface. The lens is mounted on a micrometer translation stage to allow different focal spotsizes to be produced on the sample. The spotsize of the nearly Gaussian laser beam is measured with a Cohu CCD camera. Typical spotsizes used in the experiments vary between 100 and 200 μm. The sample is also illuminated with the white light of a fiber lamp and imaged with magnification by a Sony CCD camera in order to monitor *in situ* the surface damage made by the laser. The experimental apparatus is depicted in Fig. 2.2.

The wafers are structured by two methods. One method is to raster the laser beam over the sample by translating the sample while it is exposed to the laser pulses. The

[2]Spikes are also produced on wafers that don't undergo the complete cleaning cycle.

SIONYX1403000044.0045

SAMSUNG EX. 1002 - 863/4148

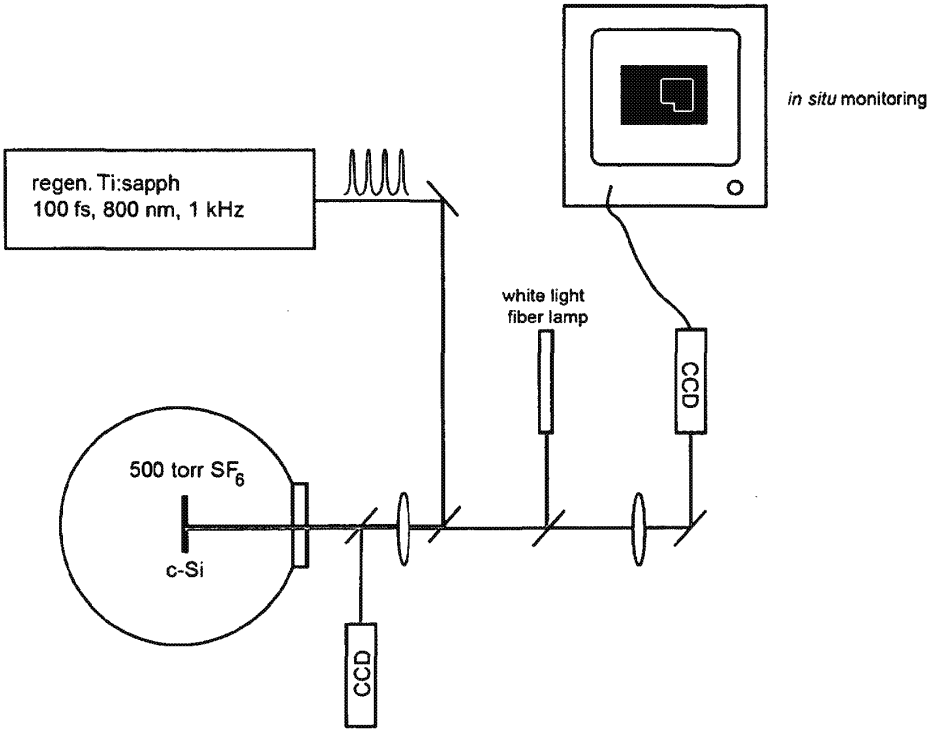


Figure 2.2: Experimental set-up for microstructuring silicon.

SIONYX1403000044.0046

SAMSUNG EX. 1002 - 864/4148

scanning velocity is adjusted according to the laser beam size at the sample. This method is used to produce spikes over patches larger than the spot size. The second method is to irradiate a single spot on the wafer without moving the sample. The number of laser pulses is controlled by a mechanical shutter, whose opening and closing times are synchronized with the laser pulses. The second method allows precise control over the number of laser pulses to which the surface is exposed.

2.3 Formation conditions

2.3.1 Spike evolution

The spikes form gradually over hundreds of laser pulses. The series of SEM pictures in Fig. 2.3 shows how the spikes develop successively as the number of laser pulses increases using 100-fs laser pulses of 10 kJ/m^2 fluence. The sample was irradiated in 500 torr of SF_6.[3] After a single laser pulse, point-like defects are observed (*b*). After 5 pulses a grain-like structure emerges (*c*). After 10 pulses we observe a rippled structure (*d*) , which forms segregated protrusions after 25 pulses (*e*). At this point the final distribution of spikes is determined. The protrusions develop into sharp spikes after several hundred laser pulses ($f - j$). The spikes become thinner until after a few thousand laser shots the spikes are destroyed and a crater is left behind. (*k*) shows the surface after 1500 laser pulses. A crater is visible in the center, the remaining spikes are thinned. A cutaway view of the spiked surface (*l*) shows that the spikes are not created by piling up material on the surface, but rather by removing material around the spikes.

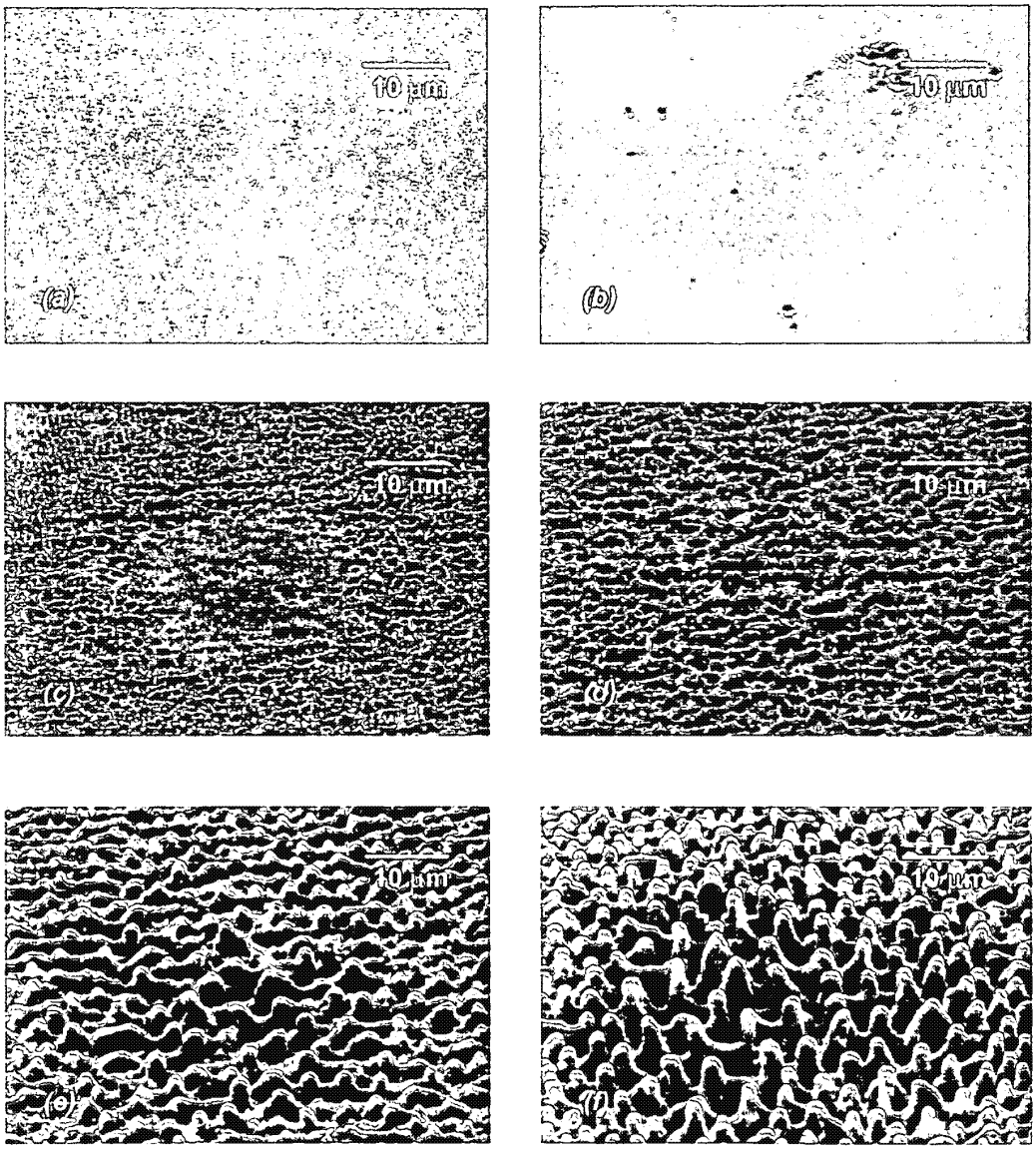
2.3.2 Effects of laser and gas parameters

Gas dependence

The presence and the nature of the gas is crucial to spike formation. Of the environments we tried, sharp spikes were only formed in SF_6 and Cl_2. Structures form in vacuum, nitrogen, helium, or argon, but they are blunt and irregular. Figure 2.4 compares the surface made in SF_6 with that made in vacuum using the same fluence ($F = 10$ kJ/m^2).

SIONYX1403000044.0047

SAMSUNG EX. 1002 - 865/4148



SIONYX1403000044.0048

SAMSUNG EX. 1002 - 866/4148

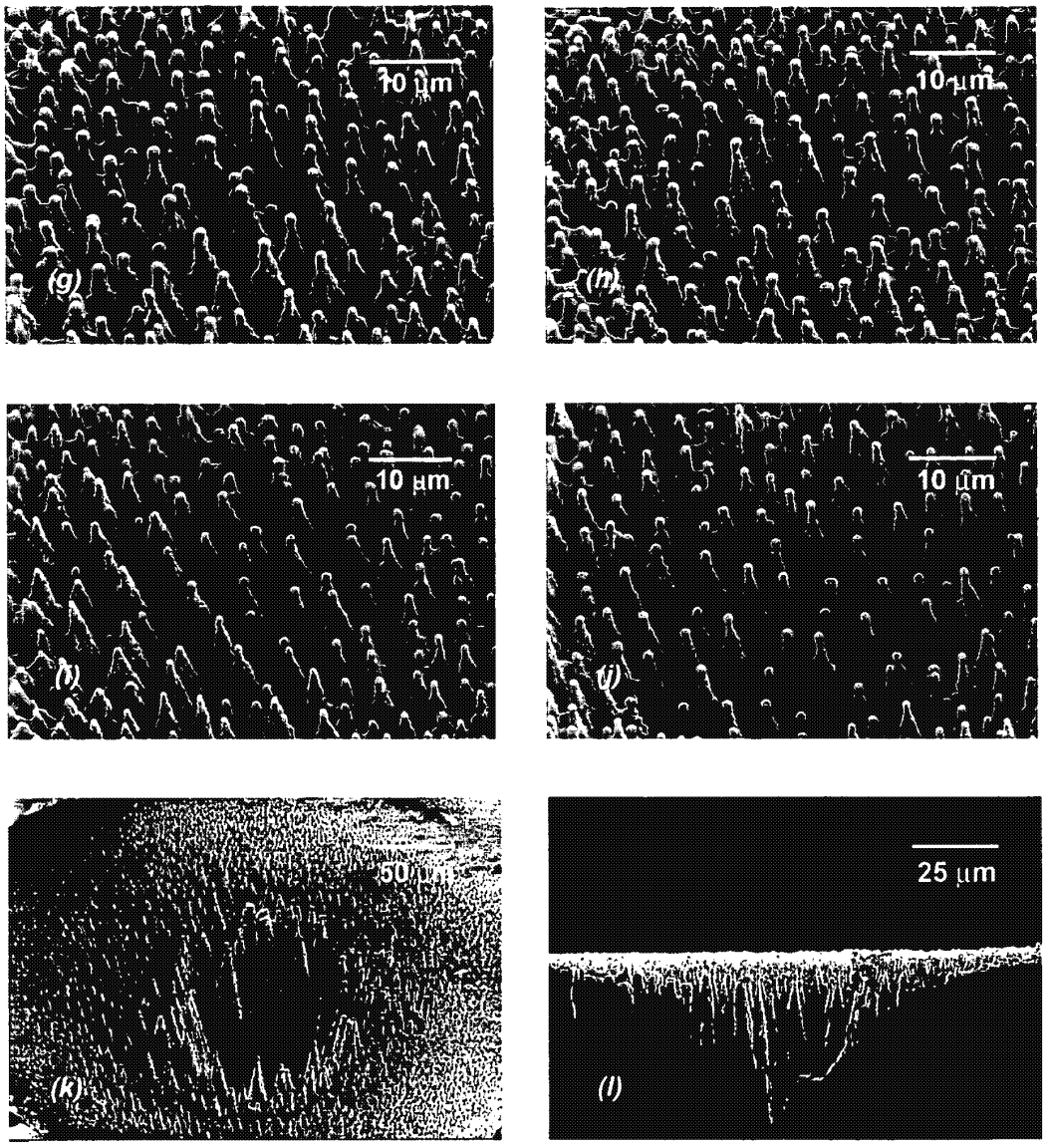


Figure 2.3: Silicon surface after (*a*) 0 pulses, (*b*) 1 pulse, (*c*) 5 pulses, (*d*) 10 pulses, (*e*) 25 pulses, (*f*) 50 pulses, (*g*) 150 pulses, (*h*) 300 pulses, (*i*) 450 pulses, (*j*) 1000 pulses, (*k*) 1500 pulses, and (*l*) sideview of cleaved spiked silicon chip as seen under the scanning electron microscope at a 45° view.

SIONYX1403000044.0049

SAMSUNG EX. 1002 - 867/4148

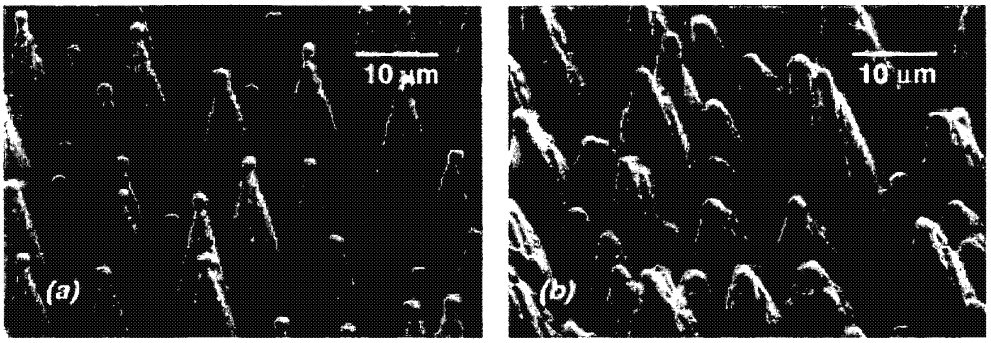


Figure 2.4: Comparison of structures formed in (*a*) SF_6 and (*b*) vacuum as seen under the SEM at a 45° view.

Fluence dependence

Spike formation is strongly dependent on the laser fluence. Under irradiating the silicon surface with 500 pulses, the fluence threshold for spike formation is roughly 5 kJ/m^2. With increasing fluence, the spike height increases nonlinearly. Figure 2.5a shows an SEM image of the surface after irradiation with 500 pulses using a fluence of 10 kJ/m^2. Since the fluence distribution in the laser beam is nonuniform (Gaussian), the spike height varies across the illuminated surface spot. In the center, where the fluence is the highest, the tallest spikes are formed. At the edge, merely a rippled structure is observed. Figure 2.5b shows the average spike separation d as a function of laser fluence. The spike height h scales nonlinearly with the spike separation d according to $h \propto d^{2.4\pm0.1}$. [1]

In Sec. 2.5.1, I will discuss processes that may cause such a fluence dependence.

Pulse duration dependence

The spike height is also strongly dependent on the laser pulse duration. Figure 2.6 shows the average spikes separation as a function of laser pulse duration (fluence (F = 10 kJ/m^2) and shot number (500 pulses) are constant). There seem to be two different regimes. For pulses durations of 0.1 ps - 1 ps there is a rapid decrease of the spike separation (and hence the spike height) with increase in pulse duration. For pulse durations of 1 ps and longer, the structure separation (and spike height) remains about constant. The two different regimes may indicate two different formation mechanisms. The pulse duration is

[3]Other fluences and other pulse durations were not studied.

SIONYX1403000044.0050

SAMSUNG EX. 1002 - 868/4148

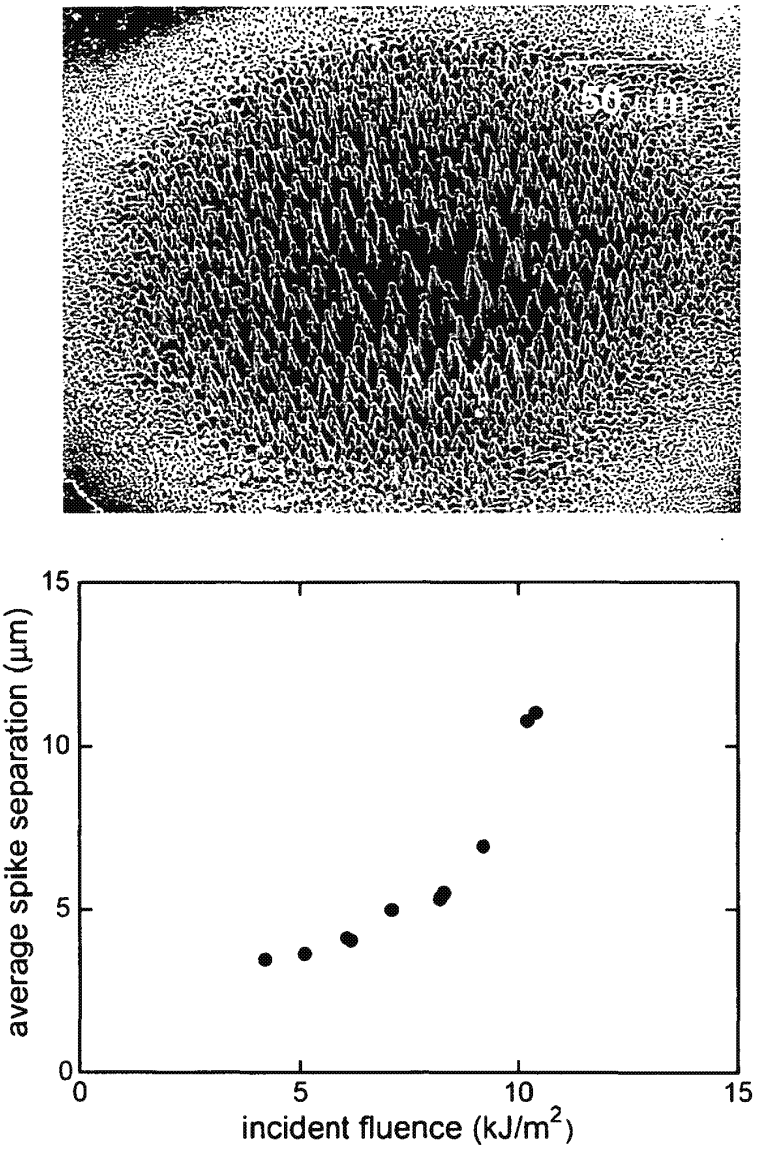


Figure 2.5: (*a*) Surface after irradiation with 500 laser pulses. The spike separation (and spike height) varies across the illuminated surface area due to the nonuniform laser energy beam profile. (*b*) Spike height as a function of laser fluence. [1]

SIONYX1403000044.0051

SAMSUNG EX. 1002 - 869/4148

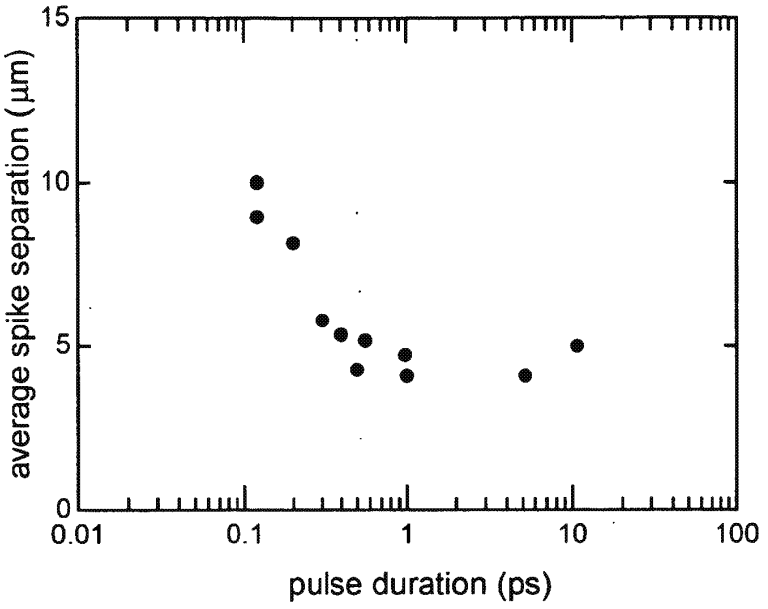


Figure 2.6: Spike separation as a function of pulse duration. [1]

discussed in Sec. 3.7.

2.3.3 Other materials

Besides silicon, spikes are also formed in germanium. Figure 2.7 shows a germanium surface after irradiation with 500 shots of 100 fs laser pulses at 10 kJ/m^2 fluence in 500 torr of SF_6. The structures formed in germanium are smaller and the sidewalls are covered with more spherical structures than the spikes made in silicon. Sharp spikes are not observed on III-V materials such as GaAs or InP. On these materials blunt and irregular structures are formed, which resemble those produced in vacuum.

2.4 Structural and chemical analysis

We performed several measurements to determine the structural properties and the chemical composition of the spikes. The spiked silicon surfaces on which all measurements were carried out, were produced by irradiating an undoped (float-zone) c-Si wafer

SIONYX1403000044.0052

SAMSUNG EX. 1002 - 870/4148

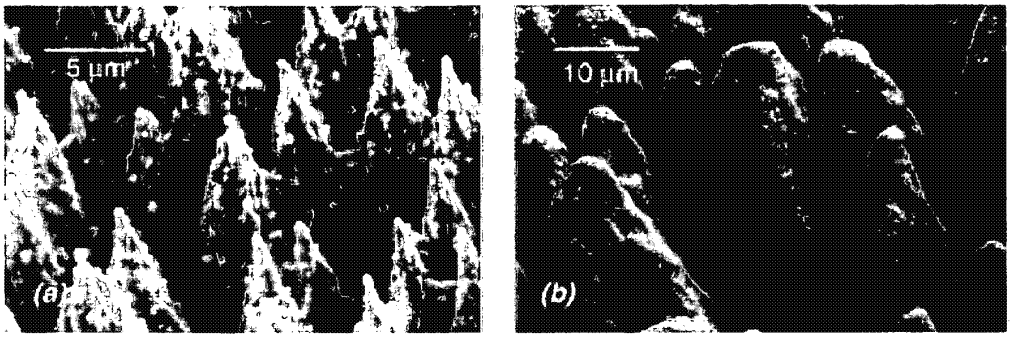


Figure 2.7: Structures made on (*a*) Ge and (*b*) InP. On germanium spikes are formed which are smaller and exhibit more protrusions on the sidewalls than those made in SF_6. No spikes are formed in InP or GaAs.

($\rho = 800 - 1000\,\Omega\,\mathrm{cm}$) in 500 torr of SF_6 with laser pulses of 100 fs duration and 11 kJ/m^2 fluence, a scan velocity of 200 μm/s, and a spotsize of 150 μm. These conditions generate spikes of about 10-12 μm in height.

2.4.1 Chemical analysis

The spikes' chemical composition was determined by X-ray Photoelectron Spectroscopy (XPS), Secondary Ion Mass Spectrometry (SIMS), and Rutherford Backscattering Spectrometry (RBS).

XPS

XPS is a surface analysis technique that probes the surface region to a depth of < 2 nm. It can detect about 1% of a monolayer of atoms. [28] In XPS highly energetic photons ($E > 1$ keV) from a monochromatic x-ray source remove core electrons from the target material. The chemical composition is determined by measuring the kinetic energy of the electrons (E_{kin}), which is related to the binding energy of the core electrons (E_b) according to:

$$E_{kin} = \hbar\omega - E_b$$

XPS was performed using a SurfaceScience model SSX-100 XPS spectrometer. Figure 2.8 shows the XPS spectra for ordinary (untreated) silicon and spiked silicon. Besides silicon, there is oxygen and carbon present in both samples. A native oxide layer, typically 1-10 nm

SIONYX1403000044.0053

SAMSUNG EX. 1002 - 871/4148

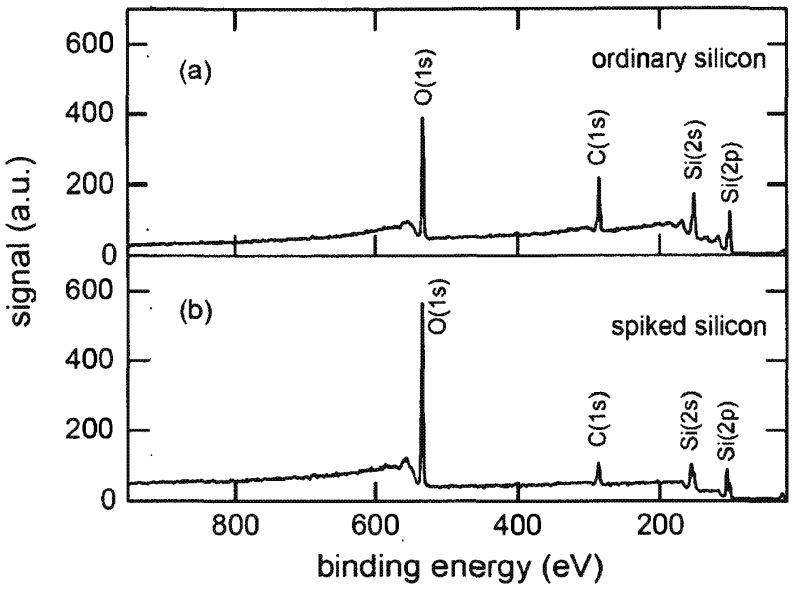


Figure 2.8: XPS spectra of (*a*) ordinary silicon and (*b*) spiked silicon.

thick, forms on a silicon surface. Table 2.1 summarizes the chemical composition for both ordinary and spiked silicon.

	Si(2s)	C(1s)	O(1s)
Ordinary (untreated) Si	33.35%	35.87%	30.77%
Spiked Si	31.50%	19.75%	48.75%

Table 2.1: Chemical surface composition of ordinary and spiked silicon as determined by XPS.

RBS

RBS probes the chemical composition depth profile of solids up to a depth of about 1 μm. In RBS, the target material is exposed to a beam of energetic alpha particles ($^4He^+$ ions of MeV energy) and the alpha particles backscattered into a specific solid angle are detected by a nuclear particle detector. The detector's output is voltage pulses, whose heights are proportional to the incident particle energies. A pulse height multichannel analyzer sorts the incoming voltage pulses by height into channels. An RBS spectrum

SIONYX1403000044.0054

SAMSUNG EX. 1002 - 872/4148

therefore shows the detected signal as a function of channel number, which corresponds to the energy of the backscattered alpha particles (an increasing channel number corresponds to increasing backscattered energy). The energy resolution (FWHM) of the system used is 22 keV and the depth resolution roughly 30 nm. The alpha particles had an energy of 2 MeV. Figure 2.9a shows the RBS spectra obtained from spiked silicon and ordinary silicon. The spiked surface contains a substantial amount of oxygen, which is indicated both by the oxygen peak in the spectrum and the decrease in the silicon signal at the surface. Silicon atoms are apparently replaced by oxygen atoms.

After etching the sample in ammonium-buffered hydrogen fluoride for about 5 minutes, the oxygen signal disappears and the RBS spectrum is indistinguishable from that of ordinary, flat silicon as shown in Fig. 2.9b. The RBS spectra are free of fluroine or sulfur. However, due to the insensitivity of RBS to lighter elements (such as sulfur, fluorine, or oxygen) as well as the S/N ratio of the RBS apparatus, fluorine, sulfur and oxygen can only be detected if the concentration exceeds 5-10%. Therefore, we conclude that if fluorine, sulfur, or oxygen is present in the spiked surface, their concentrations must be below the detection limit of a few percent.

SIMS

A more precise chemical analysis can be obtained using SIMS. In SIMS, the target material is sputtered off with energetic ions. The ablated material is detected and analyzed in a mass spectrometer. SIMS can detect elements to a level of 10^{-6}. [28] Therefore, SIMS is much more sensitive than RBS or XPS. However, SIMS capability of performing chemical analysis is restricted by the fact, that a distinction between different clusters of atoms having the same mass (or clusters of light atoms and a heavy element having the same mass) cannot been made. In addition, it is difficult to determine absolute concentrations of elements, because sputtering yields vary from element to element, depend on both the primary and secondary ion energies as well as the chemical environment in which SIMS is performed. [29] In contrast, XPS intensities are directly proportional to the adsorbate concentration. SIMS analysis was performed on a Physical Electronics 6650 Quadrupole instrument. The primary ions were 6 keV Cs^+ ions and the system base pressure was 1.4×10^{-4} Torr. A 30 nA beam with a 50 μm diameter was rastered at 30° and 60° off-normal incidence over an 800 μm x 800 μm area. Secondary ions were accepted from the

SIONYX1403000044.0055

SAMSUNG EX. 1002 - 873/4148

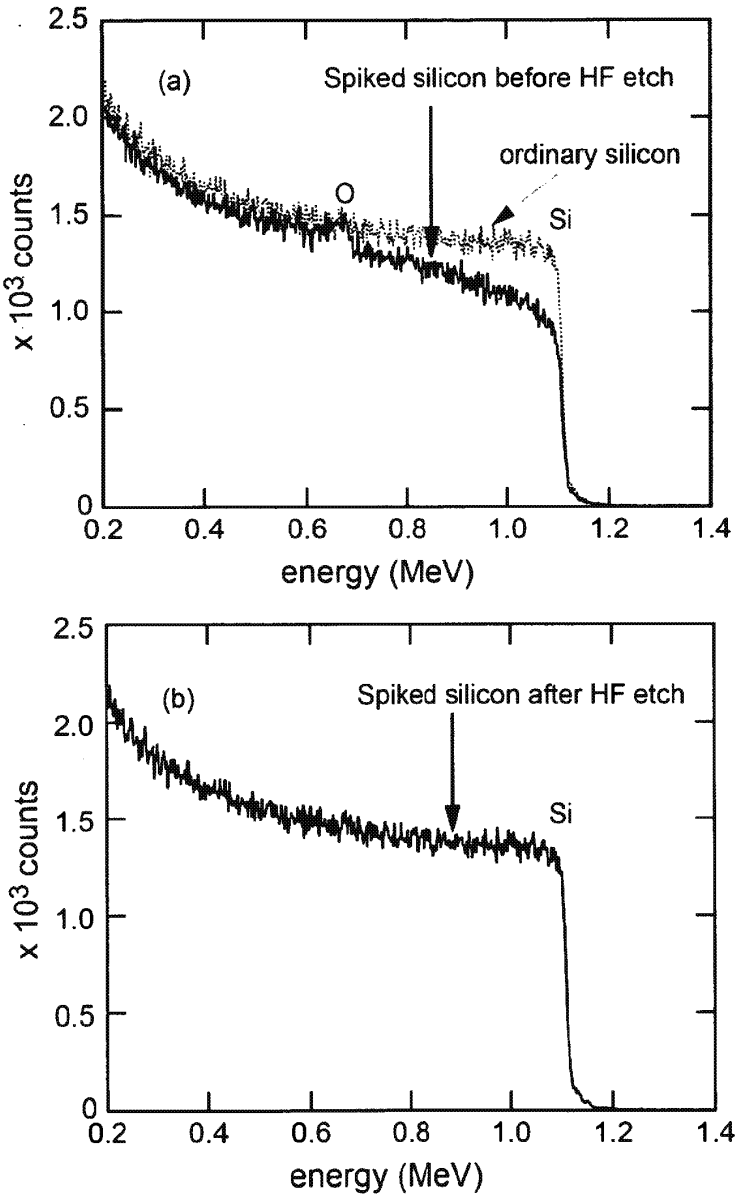


Figure 2.9: (*a*) RBS spectrum of spiked silicon before the HF etch. The RBS spectrum of ordinary silicon is shown as well. (*b*) RBS spectrum after the HF etch. The oxygen signal disappeared and the spectrum is indistinguishable from that of ordinary silicon.

SIONYX1403000044.0056

SAMSUNG EX. 1002 - 874/4148

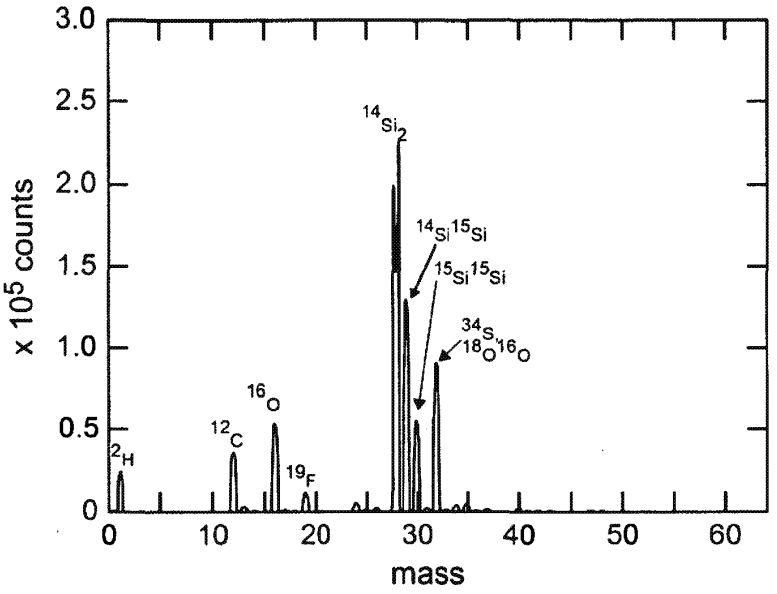


Figure 2.10: Masses collected by the mass spectrometer from spiked silicon after the HF-etch using SIMS.

center 15% of the crater area. Figure 2.10 shows the SIMS spectrum of spiked silicon. The spectrum was taken by sputtering the surface while performing a mass spectrometer scan. The data were collected over a time span of 5 minutes, while detecting each mass for 3 seconds. Besides carbon and oxygen, there is a substantial amount of fluorine (mass 19) in the sample. Figure 2.11 shows the depth profiles of various masses of an HF-etched spiked sample. The spectra were taken by setting the mass spectrometer to a specific mass and then recording the yields as a function of sputtering time.[4]

The oxygen concentration of the HF etched sample is comparable to that of the native oxide layer of ordinary, flat silicon. Noteworthy are the very high concentrations of sulfur and fluorine in the spiked sample. The concentration of sulfur is on the order of 1 part in 10^3 and the concentration of fluorine is on the order of 1 part in 10^6 using relative sensitivity factors given in Wilson *et al.* [30] The sulfur and fluorine contents both decrease with depth. The presence of sulfur and fluorine may be indicative of dissociation of SF_6

[4]Time to depth conversion under the above conditions would be 0.4 nm/s for flat silicon. For spiked silicon, however, the time to depth conversion is not known.

SIONYX1403000044.0057

SAMSUNG EX. 1002 - 875/4148

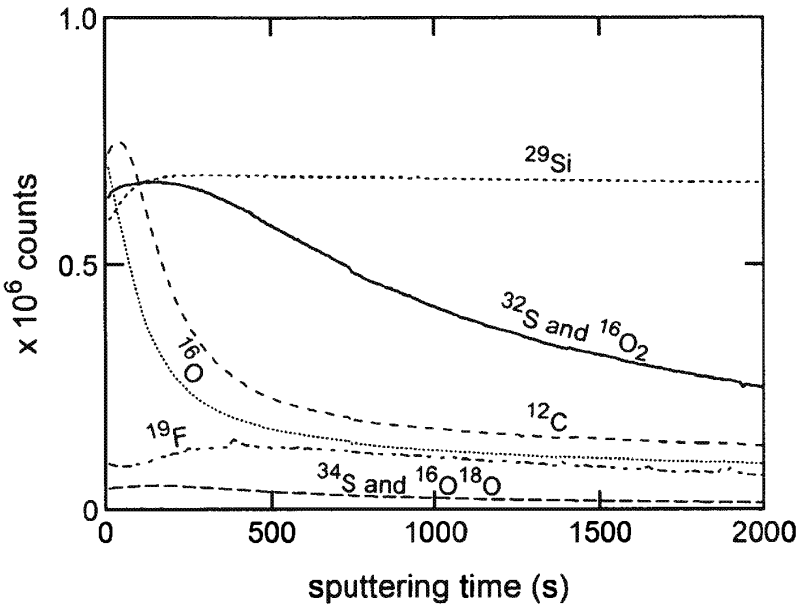


Figure 2.11: SIMS spectra of spiked silicon as a function of sputtering time after an HF etch.

during spike formation which is discussed in Sec. 2.5.3.

2.4.2 Structural properties

The structural properties of spiked silicon were investigated by ion channeling and Kikuchi diffraction (electron backscattering).

Ion channeling

Rutherford Backscattering Spectrometry with high-energy ions is referred to as ion channeling when the incident ion beam is aligned with a major symmetry axis of the target crystal. In ion channeling of single crystals, some of the incident ions scatter off the surface atoms leading to a surface peak in the spectrum. The ions that don't scatter traverse the crystal undisturbed until they scatter off a chemical or structural impurity. Since there is no scattering signal from the host atoms below the surface, ion channeling exhibits a reduced background signal and is much more sensitive to impurities and defects than RBS. [2]

SIONYX1403000044.0058

SAMSUNG EX. 1002 - 876/4148

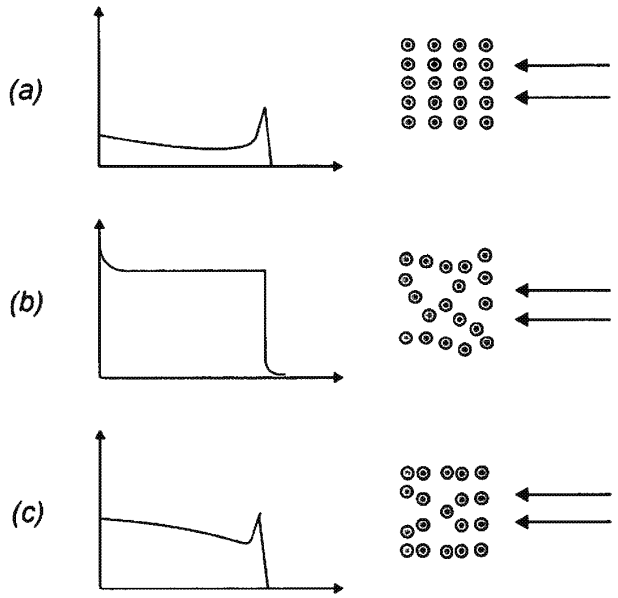


Figure 2.12: Schematic showing ion channeling spectra of (*a*) crystalline material, (*b*) amorphous or randomly oriented polycrystalline material, (*c*) crystalline material with a high density of chemical or structural defects. After Feldman. [2]

Therefore, it allows structural studies in addition to composition depth profiling. Within the limits of the depth resolution (here 30 nm), it can distinguish between crystalline, amorphous, and highly defective material. For each of these cases, the ion channeling spectra exhibits characteristic features. Figure 2.12 shows schematics of the ion channeling spectra for three different cases:

a) The spectrum of a properly aligned, single-crystalline target material exhibits a surface peak, which is followed by a reduced background signal.

b) Amorphous and polycrystalline material[5] show the same spectrum as a randomly aligned (non-channeled) crystalline material. The ions scatter off the host atoms, which produces a high background signal.

c) Crystalline material that is highly defective exhibits a spectrum that lies between that of amorphous and crystalline material. Defects give rise to dechanneling, which produces an elevated background signal.

[5]The crystallites are randomly oriented.

SIONYX1403000044.0059

SAMSUNG EX. 1002 - 877/4148

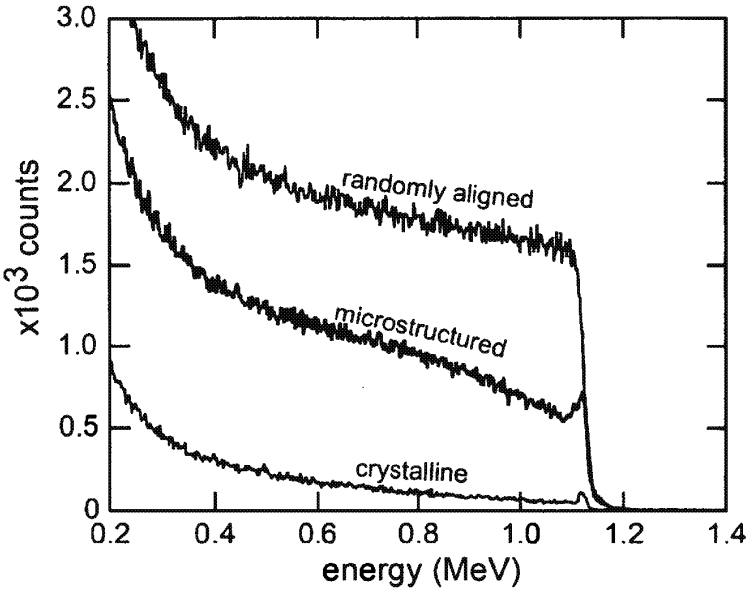


Figure 2.13: Ion channeling spectra of randomly aligned silicon, channeled spiked silicon, and channeled single-crystalline silicon.

Figure 2.13 shows the ion channeling spectrum obtained from randomly aligned silicon, channeled spiked silicon, and channeled single-crystal silicon. The channeling spectrum of spiked silicon lies between that of randomly aligned and channeled single crystalline silicon. It exhibits a clear surface peak which is followed by a reduced scattering signal. The spectrum suggests that the spikes are crystalline within the depth resolution of the measurement. The elevated background indicates a large number of structural defects in the crystal.

Kikuchi diffraction (electron backscattering)

In Kikuchi diffraction, electrons are scattered off the target material. If the material is crystalline, the diffraction of the backscattered electrons leads to the formation of distinctive lines (Kikuchi lines). From those lines, crystallographic information, such as the crystal face, can be obtained. Less pronounced lines are formed if the crystalline surface is defected or exhibits chemical impurities. Kikuchi diffraction can be used to distinguish

SIONYX1403000044.0060

SAMSUNG EX. 1002 - 878/4148

between amorphous and crystalline structure, but cannot yield information about the level of defects on the surface.

Unlike ion channeling, Kikuchi diffraction is surface-sensitive and bulk-insensitive, because it uses low-energy electons, which have a small penetration depth (< 1 nm). Therefore, it is a complementary measurement to ion channeling, which cannot yield structural information about the first few tens of nm due to the limited depth resolution. The same Kikuchi lines are formed on ordinary and spiked surfaces. There is no variation in the line pattern as the electron beam is scanned across the entire spiked sample. The electron backscattering data confirm that the spiked surface is of crystalline nature and that it possesses the same crystallographic face as that of the flat, untreated surface.

2.4.3 Summary

The main results obtained are:

1. Spikes are formed gradually over hundreds of femtosecond laser pulses in an environment of several hundred torr of SF_6.

2. Spike formation is strongly dependent on the laser and gas conditions. Spike height increases with increasing fluence and decreases with increasing pulse duration. No spikes are formed in air, vacuum, helium, nitrogen, or argon.

3. Spikes also form on germanium, but not on Cu, GaAs or InP.

4. The spikes contain high concentrations of sulfur (one part in 10^3) and fluorine (one part in 10^5).

5. The spikes are of crystalline nature, but contain many structural defects.

SIONYX1403000044.0061

SAMSUNG EX. 1002 - 879/4148

2.5 Formation mechanisms

How do the silicon spikes actually form? What formation mechanism can explain the presented results? When intense laser pulses interact with solid matter, the surface can undergo melting, evaporation, ablation, and resolidification. An interplay of several of these processes is likely involved in forming silicon spikes. Furthermore, interactions of subpicosecond laser pulses with a solid surface introduce unique phenomena of surface modifications. These interactions have to be considered in spike formation. The formation mechanism is further complicated by the presence of the gas, which is a necessary condition for forming sharp and tall spikes. A formation mechanism therefore has to include the interaction of the laser pulses with both the surface and the gas as well as the interaction of the surface and the gas.

I start with the interaction of subpicosecond pulses with solid matter and elaborate on the various physical processes occuring in different laser fluence regimes in Sec. 2.5.1. In Sec. 2.5.2 I discuss laser-induced cone formation in the absence of an ambient gas. The effects of the gas in the formation mechanism follows in Sec. 2.5.3. Finally, I combine the results of the last two sections and propose a possible mechanism for spike formation in Sec. 2.5.4.

2.5.1 Femtosecond laser-solid interactions: Fundamental processes

The initial interaction of laser pulses with a solid is the excitation of electrons. Upon photon absorption electrons are excited into higher-lying unoccupied states. The four basic processes of optical excitation in a solid are illustrated in Fig. 2.14. The electrons can undergo interband transitions by (*a*) single-photon excitation, (*b*) multiple photon-excitation or (*c*) intraband transitions by free-carrier excitation. Single-photon band-to-band excitation is the primary process whereas the latter two become increasingly significant with increasing laser intensities. If the carrier density in the conduction band is sufficient, some free carriers can acquire enough energy to create addditional conduction band electrons by (*d*) impact ionization. A highly excited electron in the conduction band relaxes by releasing some of its energy through promoting another electron from the valence band to the conduction band. This process increases the number of free carriers in the conduction band. If the laser intensity is high enough, multi-photon absorption and impact ionization can lead to optical breakdown, which produces a plasma. [31, 32]

SIONYX1403000044.0062

SAMSUNG EX. 1002 - 880/4148

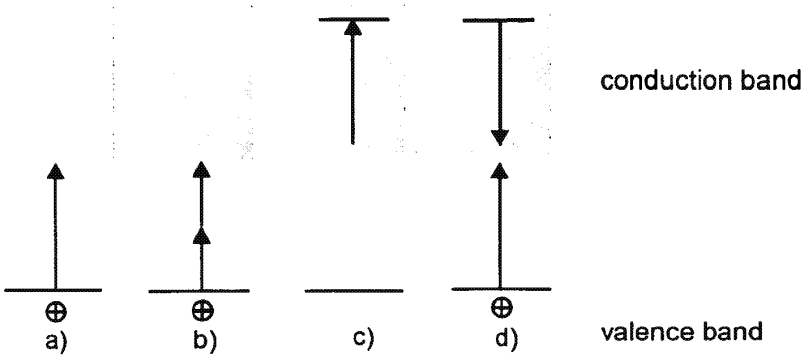


Figure 2.14: Schematic of electronic excitation in a semicondcutor by laser pulses: (*a*) single-photon excitation, (*b*) multi-photon excitation, (*c*) free carrier-absorption, (*d*) impact ionization.

The excited electrons relax and the deposited energy is redistributed through a number of processes on different timescales: Carrier-carrier scattering takes place on a time scale of about 10^{-13}s. [33] Relaxation via carrier-phonon scattering occurs on a time scale of $10^{-13} - 10^{-11}$s. [21, 34] After the phonons have reached equilibrium, the temperature of the solid is defined. Subsequent processes are of thermal nature. After phonon relaxation, redistribution of phonons, the diffusion of heat from the surface to the bulk, follows on the time scale of 10^{-11}s. [21] If the laser pulse intensity exceeds the melting threshold, melting occurs on the timescale of 10^{-11}s. Thermal ablation takes place on a timescale of 10^{-10}s. Figure 2.15 shows the timescales of the energy relaxation processes.

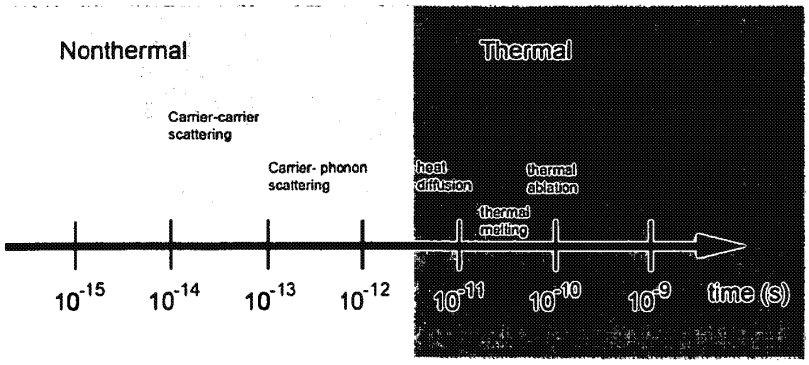


Figure 2.15: Timescales of the energy distribution processes.

SIONYX1403000044.0063

SAMSUNG EX. 1002 - 881/4148

Mechanisms leading to structural modifications using picosecond and longer laser pulses are thermal in nature, i.e., they take place on timescales longer than a picosecond.

In contrast, high-intensity femtosecond laser pulses open up physical and chemical processes considerably different from thermal processes. Nonthermal pathways can be accessed that take place on a timescale shorter than a picosecond, hence before thermal processes kick in. In particular, with high intensity subpicosecond laser pulses two novel ultrafast phase transitions can occur:

- Ultrafast solid-liquid transition

  Carrier densities in the conduction band exceeding $10^{22}/\text{cm}^3$ can be readily achieved. Stampfli and Bennemann [35, 36] showed that at these high carrier densities the lattice becomes unstable. Melting occurs in less than 1 ps. [21]

- Ultrafast solid-plasma transition

  If the laser fluence is high enough to induce optical breakdown, a plasma is formed. The ionized material is ablated rapidly with the expansion velocity of the plasma. [21] In semiconductors this ultrafast ablation occurs on a timescale of 5 - 10 ps which is faster than normal thermal ablation. [21]

There are four classes of interactions between subpicosecond laser pulses and silicon. Which of these interactions dominates, depends on the laser fluence. I discuss these interactions and their effects on spike formation in turn.

a) $F < 0.5$ kJ/m^2: Laser heating and cooling

Conventional laser heating and cooling with femtosecond laser pulses takes place at low fluences, that do not induce multiphoton absorption, evaporation, or plasma formation. In this fluence regime, the silicon surface is merely heated. No spikes are formed. Heating and cooling of silicon is not different from that with picosecond pulses [24] and is of thermal nature.

In laser heating two cases are distinguished [37], which lead to different light absorption profiles. $L = 2DIt_p$ here denotes the thermal diffusion length, with $D = \frac{\kappa}{C_v \rho}$, C_v =specific heat per unit mass, κ =thermal conductivity, ρ =density of mass, t_p =pulse duration, and I =laser intensity:

SIONYX1403000044.0064

SAMSUNG EX. 1002 - 882/4148

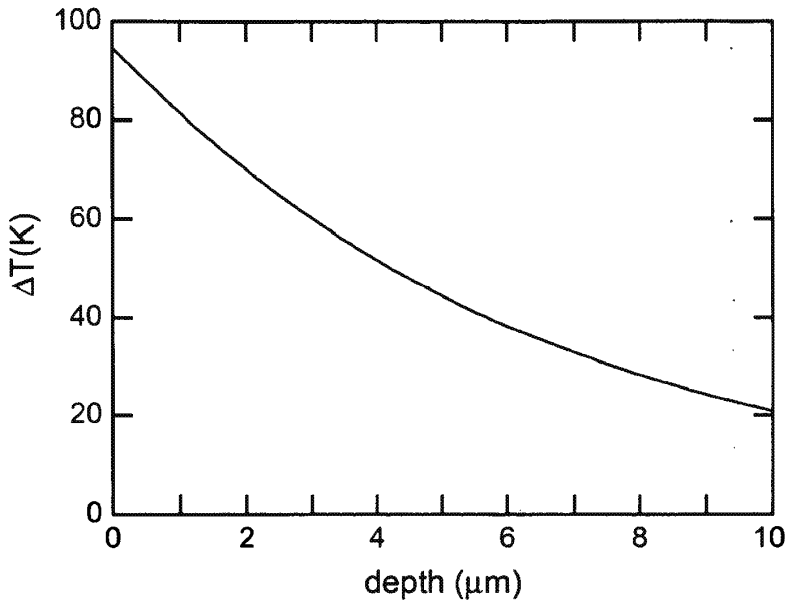


Figure 2.16: Depth-dependence of temperature increase in silicon upon irradiation of a single 100 fs, 0.5 kJ/m^2 laser pulse.

1. $\alpha 2DIt_p \gg 1$ For small absorption depths ($\alpha 2DIt_p \gg 1$), a layer of thickness $L = 2DIt_p$ is heated.

2. $\alpha 2DIt_p \ll 1$ For large absorption depths (α2DIt$_p \ll 1$) the temperature profile follows an exponential decay with a characteristic length α^{-1}.

The absorption depth of 800 nm light in silicon is $\alpha^{-1} = 11$ μm (using n and k as given by Palik [3]). The thermal diffusion coefficient is $D = 0.7\frac{\text{cm}^2}{\text{sec}}$. Therefore, the optical absorption depth is large compared to the thermal diffusion length. A temperature profile is created in the surface which follows:

$$\Delta T[z] = \frac{(1-R)\alpha I \exp(-\alpha z) t_p}{C_v \rho} \tag{2.1}$$

Figure 2.16 shows ΔT using a fluence of 0.5 kJ/m^2 and 100 fs laser pulses at 800 nm. The highest temperature reached in the surface is roughly 690 K (right at the surface), which is too low to cause thermal melting. The surface is heated, but remains undisturbed.

SIONYX1403000044.0065

SAMSUNG EX. 1002 - 883/4148

This is consistent with our observation, that no spikes are formed in this fluence regime.

1.5 kJ/m^2 < F < 2.25 kJ/m^2: Thermal melting

Sokolowski-Tinten *et al.* determined the fluence threshold for melting of silicon using femtosecond laser pulses to be $F > 1.5$ kJ/m^2. In this regime, multi-photon processes become increasingly important. Multi-photon absorption leads to a decrease in the absorption depth of the laser pulse.[6] The absorbed energy is distributed over a smaller volume, and a higher temperature is reached in the surface. The surface melts thermally and subsequently resolidifies. [21] In this regime, we do not observe spike formation.

b) 2.25 kJ/m^2 < F < 3.0 kJ/m^2: Ultrafast melting

When the intensity of the femtosecond laser pulses exceeds the melting threshold fluence by a factor of 1.5 [24, 21], an ultrafast solid-to-liquid transition occurs. This ultrafast melting is unique to the use of femtosecond laser pulses and is distinctively different from using ps pulses. Shank *et al.* [38] first observed that melting of silicon with intense femtosecond laser pulses occurs in less than 1 ps. Since then, ultrafast phase transformations in semiconductors have been observed and studied by a number of other groups. [39, 24, 40, 41, 42, 22] Ultrafast melting is caused by the excitation of a large number of electrons from the valence to the conduction band. This destabilizes the lattice and causes the silicon to melt on a timescale much shorter than required for thermal processes.[7] Theoretical work by Van Vechten [43] and Stampfli and Bennemann [35, 36, 44] showed that the lattice becomes unstable when the concentration of carriers in the conduction band exceeds $10^{22}/\text{cm}^{-3}$. This density is easily achieved with high-intensity femtosecond laser pulses. A density of this order of magnitude corresponds to 10% of the total number of valence electrons. Stampfli and Bennemann showed [36] that the diamond structure of silicon becomes unstable when more than 8% of the valence electrons are excited into the conduction band. The instability causes a rapid melting of the material.

Sokolowski-Tinten *et al.* [21] confirmed from optical reflectivity measurements, that these carrier densities are indeed reached for laser fluences exceeding 1.5 kJ/m^2.

[6] Nonlinear coefficients are added to the linear component of the absorption coefficient.
[7] This kind of melting is also termed electronic or cold melting.

SIONYX1403000044.0066

SAMSUNG EX. 1002 - 884/4148

No material evaporation or ablation is associated with ultrafast melting at these fluences. The silicon surface resolidifies.[21] No spikes are observed in this fluence regime.

c) $F > 3.2$ kJ/m^2: Ultrafast melting and ablation

In this regime, ultrafast melting is associated with ablation, which likely takes place via thermal mechanisms. [21, 45] Material is ablated in macroscopic clusters, which leave the surface in a plume. The single pulse ablation threshold for silicon was determined by von der Linde *et al.* [21] to be 3.2 kJ/m^2. We observe the same threshold for damage of the silicon surface. Silicon debris is deposited on the quartz window of the vacuum chamber in this fluence regime.

From the values of the latent heat for silicon (4.2 kJ/cm^{-3} solid-liquid and 32 kJ/cm^{-3} for the liquid-vapor transition) [46, 47] we can determine an upper limit for the ablated depth per pulse. For example, a fluence of 5 kJ/m^2 a pulse can melt and vaporize silicon to a maximum depth of 138 nm. If all the energy is not used for material removal, the depth is smaller.

At laser energies, that cause laser-ablation, very high lattice and electron temperatures are reached. Cavalleri *et al.* [23] showed that the surface temperature in this regime exceeds the melting temperature by several thousand degrees K. At the ablation threshold, the surface temperature is between 3000 and 4000 K. The electronic temperatures reached is $T > 11000$ K. [48] Ablation in this regime occurs on the order of several ps and is therefore thermal. Downer *et al.* [38] showed that using 5 kJ/m^2, 100 fs laser pulses, silicon is ejected after 10 ps initially in form of liquid droplets of molten silicon, which then atomize within 550 ps.

In the fluence regime $F > 3.2$ kJ/m^2, we observe spike formation. However, we obvserve white light emission, while the spikes are formed. The white light indicates the presence of a plasma, because the excitation of a plasma leads to emission of white light. Therefore, the ablation process may be associated with the generation of a plasma. This is discussed in the following section.

d) Plasma formation and ultrafast plasma ablation

If the fluence is high enough to cause optical breakdown, a plasma is formed. The fluence threshold reported for plasma formation in silicon varies. Whereas Sokolowski-

SIONYX1403000044.0067

SAMSUNG EX. 1002 - 885/4148

Tinten [23], reported plasma formation for fluences exceeding $F > 10$ kJ/m^2 (620 nm, 100 fs pulses), Pronko *et al.* observed plasma emission after single-pulse irradation at $F > 1.3$ kJ/m^2 (800 nm, 80 fs pulses). [48] We determined the threshold for single-pulse visible optical breakdown to be $F = 4.3$ kJ/m^2 (800 nm, 100 fs). The threshold was reduced with increasing number of laser shots. The threshold for plasma formation for a corrugated surface can be different from that of a flat surface, because of inhomogenous absorption due to scattering.

The processes leading to optical breakdown are not well understood. Several mechanisms have been proposed including avalanche ionization, multiphoton absorption, and tunneling ionization.

An interesting phenomenon associated with plasma formation is the possibility of an ultrafast solid-plasma transition (ultrafast plasma ablation) as reported by Sokolowski-Tinten *et al.* [21] If the pulses are short enough, that the expansion of the plasma is negligible during the duration of the pulse (which is the case for 100 fs and shorter laser pulses), a very fast ablation of the ionized material can lead to a direct transition from the solid to the plasma state. [21]

Processes involved in spike formation

From the foregoing discussion of femtosecond laser interactions with silicon, we conclude that spike formation is associated with ultrafast melting and laser ablation:

- Melting in the fluence regime in which we observe spike formation is ultrafast and nonthermal. This is also emphasized by the pulse duration measurements. For subpicosecond laser pulses at $F = 10$ kJ/m^2 the decrease in spike height with increasing pulse duration may indicate the transition from nonthermal processes to thermal processes.

- Spike formation is associated with laser ablation of silicon. Spikes are formed using laser fluences above the ablation threshold for silicon ($F > 3.2$ kJ/m^2). In addition, spike formation is accompanied by plasma formation; we observe white-light emission while the spikes are formed. Thus, the plasma may be associated with a direct ultrafast ablation process.

Figure 2.17a summarizes the processes involved in different fluence and pulse duration regimes. Ablation is not the sole process involved in forming spikes. In vacuum or gases

SIONYX1403000044.0068

SAMSUNG EX. 1002 - 886/4148

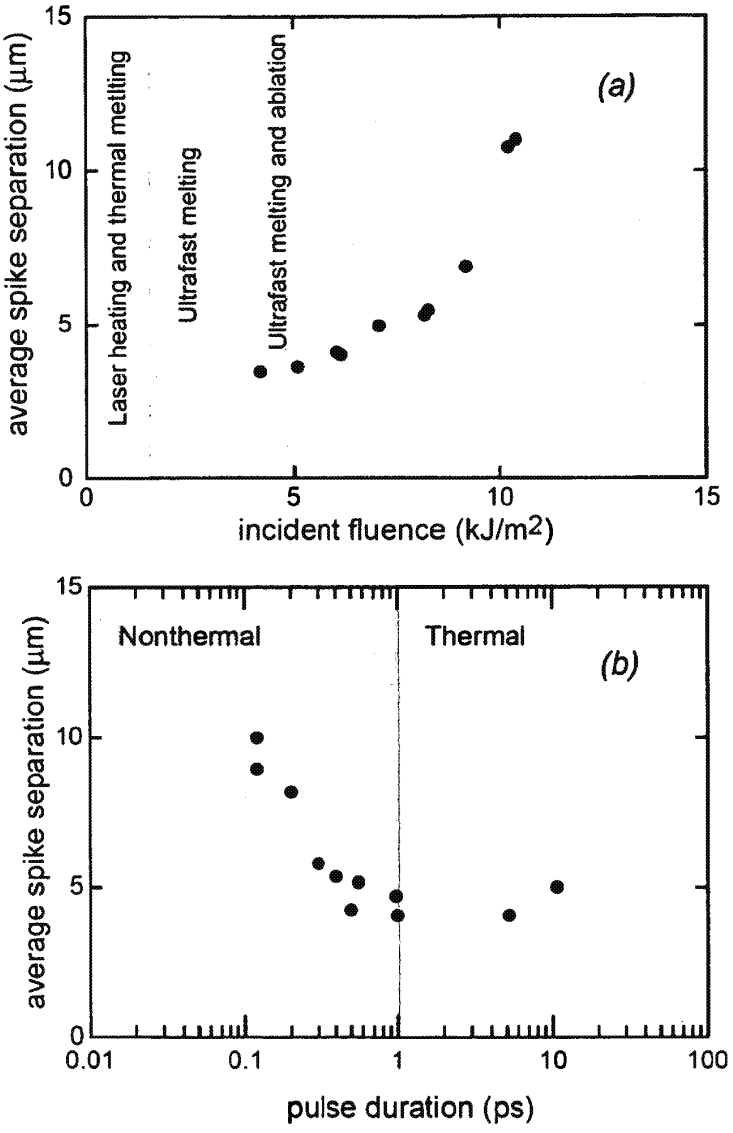


Figure 2.17: (*a*) Thermal and nonthermal phase transformations take place at different fluences. (*b*) Nonthermal processes are induced with subpicosecond laser pulses of 10 kJ/m^2 fluence, whereas picosecond laser pulses of the same fluence induce thermal processes.

SIONYX1403000044.0069

SAMSUNG EX. 1002 - 887/4148

that do not etch silicon, we observe not sharp spikes but blunt features. A chemical reaction involving the ambient gas must contribute to the formation of spikes. Therefore, the spikes are most likely produced by both laser ablation and laser-assisted chemical etching. The processes involved in laser-assisted chemical etching are treated separately in Sec. 2.5.3. First I discuss how conical structures are formed from material removal through cumulative irradiation of a surface with laser pulses.

2.5.2 Formation mechanisms of laser cones

Cones formed using nanosecond laser pulses, as well as the spikes we observe, exhibit many similarities to the cones known to form in ion sputtering: Conical structures are produced after cumulative exposure to irradiation of ions/photons, these structures form in the direction of the bombarding beams, and material is not piled up on the surface but instead removed, leaving a cone structure behind. Given these similarities, a number of authors have investigated whether laser cones produced with nanosecond laser pulses form in ways similar to sputter cones. [17, 49, 50, 51, 52, 53, 54] In the following I describe mechanisms by which cones are produced through a preferential material removal process. Despite the differences in forming laser cones in vacuum with nanosecond laser pulses and forming laser spikes with femtosecond laser pulses in the presence of a halogen-containing gas, the concept of preferential material erosion through cumulative photon irradiation may also be valid for the latter. The shorter pulse duration may result in a faster material removal rate through nonthermal processes and the gas may enhance material removal through laser-assisted chemical etching. I discuss both effects on spike formation in Sec. 2.5.4.

Sputter cones

In ion sputtering, cones are formed by preferential erosion of the surface. One model explains the beginning of sputter cones through the formation of aggregates of foreign atoms on the surface. These aggregates are introduced from a separate target. The clusters of foreign atoms are resistant to sputtering and therefore shield the underlying material from erosion. [55] Only material surrounding this protective pit is removed. As the bombardment progresses, sputter cones are formed. Figure 2.18 shows schematically how a cone is formed from an initial bump.

SIONYX1403000044.0070

SAMSUNG EX. 1002 - 888/4148

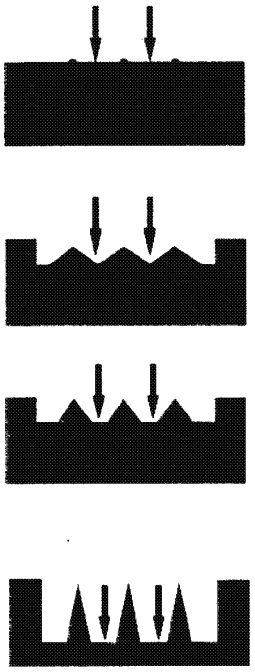


Figure 2.18: Cone formation in ion sputtering seeded by a protective pit. Material is eroded around the pit.

Laser cones

Applying this model to formation of cones using laser pulses, the presence of a protective cap is necessary to shield the underlying material from erosion. The question arises then as to how this protective mask is formed and of what it is composed of. One possibility is the redeposition of ablated material on the surface in form of clusters. [49, 50] It is also possible that the laser pulses create impurity-rich regions on the surface, which shield the underlying substrate from being eroded. [49]

The foregoing discussion explains laser cone formation in the absence of a gas. The presence of the gas complicates the formation process. As shown in Sec. 2.3.2, the gas plays an essential role in forming sharp spikes. The bluntness of structures formed in vacuum for example indicates that the gas contributes to sharpening the spikes. Given these observations, material removal must be at least partly due to chemical etching of silicon. Another possible effect of the gas, as suggested by Pedraza *et al.* [56] is deposition of silicon

SIONYX1403000044.0071

SAMSUNG EX. 1002 - 889/4148

onto the surface via chemical vapor deposition. The following section addresses possible effects of chemical etching on spike formation.

2.5.3 Gas effects: Laser-induced chemical etching

Chemical etching can be initiated or enhanced by laser excitation of the substrate, adsorbates on the surface, or species in the gas phase. Laser-chemical etching of a surface is associated with one or a combination of these excitations. SF_6 and Cl_2 are known etchants of silicon. Since all results presented in this thesis were obtained from spiked surfaces produced using SF_6 as the ambient gas, the discussion of the effects of laser-chemical etching on spike formation is limited to the etching of silicon with SF_6.

Si-SF_6

SF_6 is stable at 300 K and does not chemisorb on silicon. However, it can be physisorbed at 90 K or at a pressure of $P \geq 1$ Torr at room temperature. At 1 torr about 0.5 ML of SF_6 can be adsorbed on silicon. As the gas pressure is increased to 20 Torr, the surface coverage increases, but does not exceed 1 ML. [57]

Laser-induced etching of silicon with SF_6 can take place via a vibrationally or electronically excited molecule or a radical created by photodissociation. Plasma etching of silicon through dissociation of SF_6 creating reactive fluorine radicals in a radio frequency discharge chamber [58, 59] and by electron beams [60] is well known. Using high-fluence cw laser light from a CO_2 laser, Chuang *et al.* demonstrated that SF_6 can be dissociated through multi-photon absorption leading to etching of silicon. [61, 62] Raksi *et al.* showed gas-phase photodissociation of SF_6 producing fluorine radicals by intense femtosecond laser pulses at 800 nm. [63]

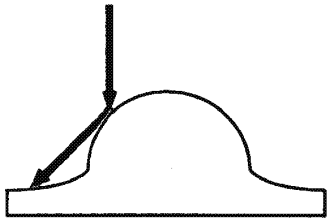


Figure 2.19: Light is reflected off a protrusion which leads to enhanced light absorption and material removal at the sidewalls of the protrusion.

SIONYX1403000044.0072

SAMSUNG EX. 1002 - 890/4148

Etching of silicon can also proceed via vibrationally excited SF_6 molecules. Chuang *et al.* [61] also showed that etching of silicon with SF_6 using a cw CO_2 laser can lead to the reaction of silicon with vibrationally excited SF_6 molecules.

Possible chemistry involved in spike formation

How the surface is etched by the gas during spike formation is unclear at this point. It is possible that chemical etching associated with spike formation is either due to excited molecules or photodissociated SF_6. The SIMS results show that the spikes contain high concentrations of sulfur and fluorine, which suggests a spikes formation mechanism involving dissociation of SF_6. It is likely that etching with SF_6 proceeds via formation of fluorine radicals.

Figure 2.20 shows a possible scenario of how etching of the surface via photodissociation of SF_6 may take place.

1. A silicon surface is exposed to femtosecond laser pulses in the atmosphere of SF_6.
2. Intense femtosecond laser pulses disrupt the molecules close to the surface, where the fluence is high (the laser light is focussed onto the surface). This creates reactive fluorine radicals.
3. The radicals react with (possibly liquid) silicon and form SiF_x compounds.
4. SiF_x compounds are desorbed by the laser, volatile species (such as SiF_4) leave the surface.

The aforementioned scenario explains the process of material removal via laser-assisted chemical etching. Given the fact that cones are produced in the absence of the gas, it is most likely, that the spikes are formed through a combination of both ablation and chemical etching of the surface. One possibility is that ablation produces structures, that are sharpened by the gas.

SIONYX1403000044.0073

SAMSUNG EX. 1002 - 891/4148

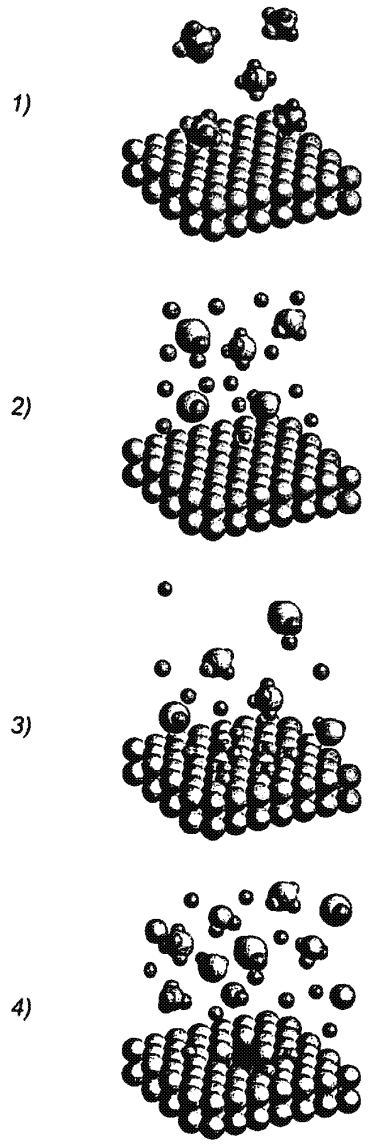


Figure 2.20: Schematic of material removal through laser-assisted etching. (1) A silicon surface is exposed to femtosecond laser pulses in the atmosphere of SF_6. (2) Fluorine radicals are created via photodissociation of the SF_6molecules. (3) The radicals react with silicon and form SiF_x compounds. (4) SiF_x compounds are desorbed by the laser, volatile species (such as SiF_4) leave the surface.

SIONYX1403000044.0074

SAMSUNG EX. 1002 - 892/4148

2.5.4 Discussion

The foregoing sections show how spikes or cones can be formed through preferential material erosion of a solid leaving a spiked surface behind. In forming silicon spikes, most likely both laser-assisted chemical etching and laser ablation are involved.

Whereas the concept of preferential material removal may be the same for forming spikes using femtosecond laser pulses in the presence of a halogen containg gas and forming cones using nanosecond laser pulses in vacuum, the actual mechanims could be considerably different. With high-intensity femtosecond laser pulses, nonthermal mechanisms of melting and ablation take place. These processes possibly lead to higher material removal rates than thermal processes. This is indicated by the results of the pulse duration measurements presented in Sec.2.3.2. As the pulse duration is increased from 0.1-1.0 ps, the spike height decreases by a factor of 2. Furthermore, using the same fluence, taller spikes are formed using femtosecond laser pulses and SF_6 than producing spikes using nanosecond laser pulses in vacuum. Whereas Rothenberg and Kelly [17] used a fluence of $F = 60$ kJ/m^2 to produce a structure height of tens of microns with nanosecond laser pulses, we observe spike heights of > 40 μm using a fluence of only 10 kJ/m^2.

The gas plays an essential role in forming sharp spikes. Without a gas that etches silicon, blunt irregular structures are formed. The addition of a plasma etchant such as SF_6 sharpens the structures and creates a more regular pattern. Therefore, the gas must be involved in sharpening the spikes. A comparison of the heights of structures made in vacuum to those made in SF_6 using the same laser fluence ($F = 10$ kJ/m^2) indicates that the etching does not lead to a significantly faster material removal rate, because the structure heights produced in the two environments are comparable.

Pedraza *et al.* [56] observed cones in silicon surrounded by microholes using ns laser pulses at 248 nm and a fluence of $F = 26$ kJ/m^2 and $F = 30$ kJ/m^2 respectively in an SF_6 environment. They suggest cone formation via an interplay between redeposition and etching/ablation of silicon which leads to deepening of the microholes and to the growth of the columnar structures. They attribute the growth of cones to the formation of silicon fluoride compounds SiF_2 and SiF_4, which are volatile at the transient temperatures reached during laser-heating. SiF_2 reacts with molten silicon at the tip and the sides of the columns and decompose according to

$$2SiF_2 \rightarrow SiF_4 + Si$$

SIONYX1403000044.0075

SAMSUNG EX. 1002 - 893/4148

The molten silicon is a catalyst to this reaction. Silicon is deposited on the column, which causes the columns to grow. As for formation of spikes using femtosecond laser pulses, we do not see evidence that the spikes grow via deposition of material. In contrast to the structures reported by Pedraza *et al.*, we do not observe growth of the structures to tens of μm height *above* the surface. Rather, the spikes seem to evolve from laser pulse to laser pulse via increasing material removal as observed by scanning electron microscopy of a cleaved spiked surface (see Fig. 2.3). Further investigation is needed to test if and to what extent different mechanisms are involved in spike formation using nanosecond versus femtosecond laser pulses.

SIONYX1403000044.0076

SAMSUNG EX. 1002 - 894/4148

Chapter 3

Optical Properties of Spiked Silicon

3.1 Introduction

Spiked silicon has astonishing light absorption properties. Grey silicon turns velvet black after irradiation with hundreds of femtosecond laser pulses in SF_6 or Cl_2. Inspired

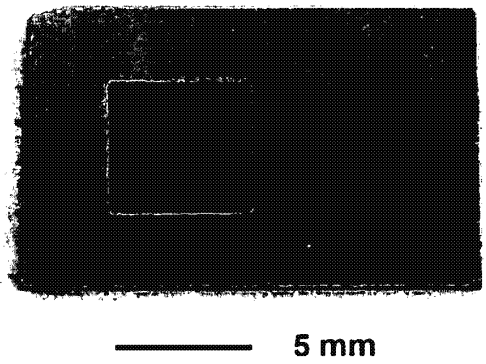


Figure 3.1: Photograph of black silicon patch.

SIONYX1403000044.0077

SAMSUNG EX. 1002 - 895/4148

by the black appearance of the irradiated silicon patch, we performed a detailed characterization of the optical properties of spiked silicon. Our results show that spiked silicon absorbs nearly all incident light from the near-UV to the mid-IR. Strong absorption is even observed in the THz regime. The below-bandgap absorption in spiked silicon is especially puzzling: In ordinary silicon, photon energies smaller than the band gap energy (1.12 eV at room temperature corresponding to 1.11 μm) are not absorbed but transmitted. In spiked silicon, there is no difference in the absorption of below or above bandgap photon energies. Reflection reduction by trapping of light in the corrugated, spiked surface may contribute to the near-unity light absorption of photons with energies greater than the bandgap, however it cannot fully account for the below-bandgap absorption.

We performed a series of experiments to investigate the striking light absorption of spiked silicon. In particular, we wished to answer the following questions:

- Is the band structure of spiked silicon different from that of ordinary silicon?
- Is the dramatic increase in light absorption, particularly below the band gap, associated with crystallographic or chemical changes?

The chapter is organized as follows: First I give a brief overview of the theoretical treatment of reflection and transmission in semiconductors (Sec. 3.2). Then I present our measurements of the optical properties of spiked silicon in Sec. 3.3. Sec. 3.4 elaborates on possible mechanisms for the increased light absorption of spiked silicon; Sec. 3.4.1 discusses the effect of multiple reflections and Sec. 3.4.2 the contributions of structural defects and impurities to below-bandgap absorption. Finally, in Sec. 3.6, I talk about applications of the near-unity light absorption in spiked silicon.

3.2 Theoretical considerations

Complex refractive index

When light impinges on a substrate, three processes can occur: Reflection, transmission, and absorption. In electromagnetic theory, the degree to which each of these processes occurs is determined by a material-dependent complex refractive index $\tilde{n} = n + ik$. The real part n is usually called the refractive index and relates the velocity of light in a

SIONYX1403000044.0078

SAMSUNG EX. 1002 - 896/4148

medium to that in vacuum.

$$v_{medium} = \frac{c}{n}$$

where c is the velocity of light in vacuum. The imaginary part k is called the extinction coefficient and is a measure of the absorption in the material. The absorption coefficient α of a medium is defined by

$$I(\vec{r}) = I(\vec{r_0}) \exp -\alpha\vec{r}$$

where

$$\alpha = \frac{4\pi\ k}{\lambda}$$

α^{-1} is the distance by which the incident flux has decreased to $1/e$ and is called skin or penetration depth. [64]

Fresnel equations

Reflectance (R), transmittance (T) and absorptance (A) are related through [65]:

$$R(\lambda) + T(\lambda) + A(\lambda) = 1 \tag{3.1}$$

Reflectance and transmittance are expressed through the complex refractive index $\tilde{n}$ by the Fresnel equations. The Fresnel coefficients for reflectance and transmittance at an interface can be derived from Maxwell's equations with certain boundary conditions. [64, 66] The reflectance and transmittance depend on the polarization and the angle of incidence of the light; different coefficients are obtained for p-polarized light (E-field in the plane of incidence) and s-polarized light (E-field perpendicular to the plane of incidence). For p-polarized light, the amplitude ratio of the reflected electric field (E_r) to the incident electric field (E_i) and the transmitted electric field (E_t) to the incident electric field is given by [66]

$$r_p = \frac{E_r}{E_i} = \frac{2\tilde{n}\tilde{n}'cos\Theta}{\frac{\mu}{\mu'}\tilde{n}'^2cos\Theta + \tilde{n}\sqrt{\tilde{n}'^2 - \tilde{n}^2sin^2\Theta}} \tag{3.2}$$

$$t_p = \frac{E_t}{E_i} = \frac{\frac{\mu}{\mu'}\tilde{n}'^2cos\Theta - \tilde{n}\sqrt{\tilde{n}'^2 - \tilde{n}^2sin^2\Theta}}{\frac{\mu}{\mu'}\tilde{n}'^2cos\Theta + \tilde{n}\sqrt{\tilde{n}'^2 - \tilde{n}^2sin^2\Theta}} \tag{3.3}$$

and for s-polarized light

SIONYX1403000044.0079

SAMSUNG EX. 1002 - 897/4148

$$r_s = \frac{E_r}{E_i} = \frac{2\tilde{n}cos\Theta}{\tilde{n}cos\Theta + \frac{\mu}{\mu'}\sqrt{\tilde{n}'^2 - \tilde{n}^2 sin^2\Theta}} \tag{3.4}$$

$$t_s = \frac{E_t}{E_i} = \frac{\tilde{n}cos\Theta - \frac{\mu}{\mu'}\sqrt{\tilde{n}'^2 - \tilde{n}^2 sin^2\Theta}}{\tilde{n}cos\Theta + \frac{\mu}{\mu'}\sqrt{\tilde{n}'^2 - \tilde{n}^2 sin^2\Theta}} \tag{3.5}$$

where μ is the permittivity, ϵ the dielectric constant (see following section), Θ the angle of incidence measured to the surface normal, and the prime denotes the specific quantity of the medium entered. For normal incidence, the equations for both p- and s-polarized light reduce to

$$\frac{E_r}{E_i} = \frac{2}{\sqrt{\frac{\mu\epsilon'}{\mu'\epsilon}} + 1} \rightarrow \frac{2\tilde{n}}{\tilde{n}' + \tilde{n}} \tag{3.6}$$

$$\frac{E_t}{E_i} = \frac{\sqrt{\frac{\mu\epsilon'}{\mu'\epsilon}} - 1}{\sqrt{\frac{\mu\epsilon'}{\mu'\epsilon}} + 1} \rightarrow \frac{\tilde{n}' - \tilde{n}}{\tilde{n}' + \tilde{n}} \tag{3.7}$$

Complex dielectric function

The complex dielectric function $\tilde{\epsilon}(\omega)$ (also referred to as dielectric constant for a specific wavelength), which relates the displacement field to the electric field in a medium is related to $\tilde{n}$ through

$$\tilde{n} = \sqrt{\epsilon} = [n + i\kappa]$$

where

$$\tilde{\epsilon} = \epsilon_1 + i\epsilon_2$$

and

$$\epsilon_1 = n^2 - \kappa^2$$

$$\epsilon_2 = 2n(\omega)\kappa(\omega)$$

An equation of the dielectric function (and hence the complex refractive index) can be derived using classical mechanics and electrodynamics. [1] Bound electrons in a semiconductor are treated as an ensemble of uncoupled harmonic oscillators. The complex dielectric

[1] Determining optical properties from classical mechanics and electrodynamics is a remarkably good approximation. [67]

SIONYX1403000044.0080

SAMSUNG EX. 1002 - 898/4148

function is determined by the coupling of these oscillators to the electromagnetic radiation field.

Electromagnetic radiation drives the electrons to oscillate at the frequency of the incident wave by the electric field $\vec{E}$. The oscillations give rise to a macroscopic polarization of the form:

$$\vec{P} = -Ne\vec{r} \tag{3.8}$$

where N is the number of electrons per unit volume. The motion of each bound electron can be modeled using the equation of motion for a classical, uncoupled, harmonically damped oscillator [68]:

$$(-m\omega^2 - i\omega\mathrm{m}\gamma + \mathrm{K})\vec{\mathrm{r}} = -\mathrm{e}\vec{\mathrm{E}} \tag{3.9}$$

where K is the effective force constant of the potential holding the electron to the atom, and γ is the damping constant. The polarization of an ensemble of N oscillators all driven in phase [2] can then be written as

$$\vec{P} = \frac{Ne^2}{-m\omega^2 - i\omega m\gamma + K}\vec{E} = \frac{\frac{Ne^2}{m}}{\omega_0^2 - \omega^2 - i\omega\gamma}\vec{E} \tag{3.10}$$

with ω_0 the resonance frequency. The displacement field is given by

$$\vec{D} = \epsilon_0\vec{E} + \vec{P} = \epsilon_0(1 + \frac{Ne^2}{m\epsilon_0}(\omega_0^2 - \omega^2 - i\omega\gamma)^{-1})\vec{E} \tag{3.11}$$

and the dielectric function

$$\epsilon_\omega(\omega) = (1 + \frac{Ne^2}{m\epsilon_0}(\omega_0^2 - \omega^2 - i\omega\gamma)^{-1}) = \chi(\omega) + 1 \tag{3.12}$$

This result if based on the assumption that all electrons are identically bound. To take into account electrons bound in different potentials, we sum the contributions to the dielectric function over the resonance frequencies ω_{oj} associated with the different potentials. Each frequency contributes to the weight f_j where $\sum_j f_j = Z$ (f_j is called the oscillator strength)

$$\epsilon(\omega) = 1 + \sum_j \frac{f_j}{\omega_{0j} - \omega^2 - i\omega\gamma_j} \tag{3.13}$$

Equation 3.13 is the Kramers-Heisenberg dielectric function, which has a real part and an imaginary part. From the expression for the dielectric function, we can see that different resonance frequencies and different oscillator strengths both influence the real and

[2] The oscillators are in phase because they are driven by the same force. This is valid when the wavelength is short.

SIONYX1403000044.0081

SAMSUNG EX. 1002 - 899/4148

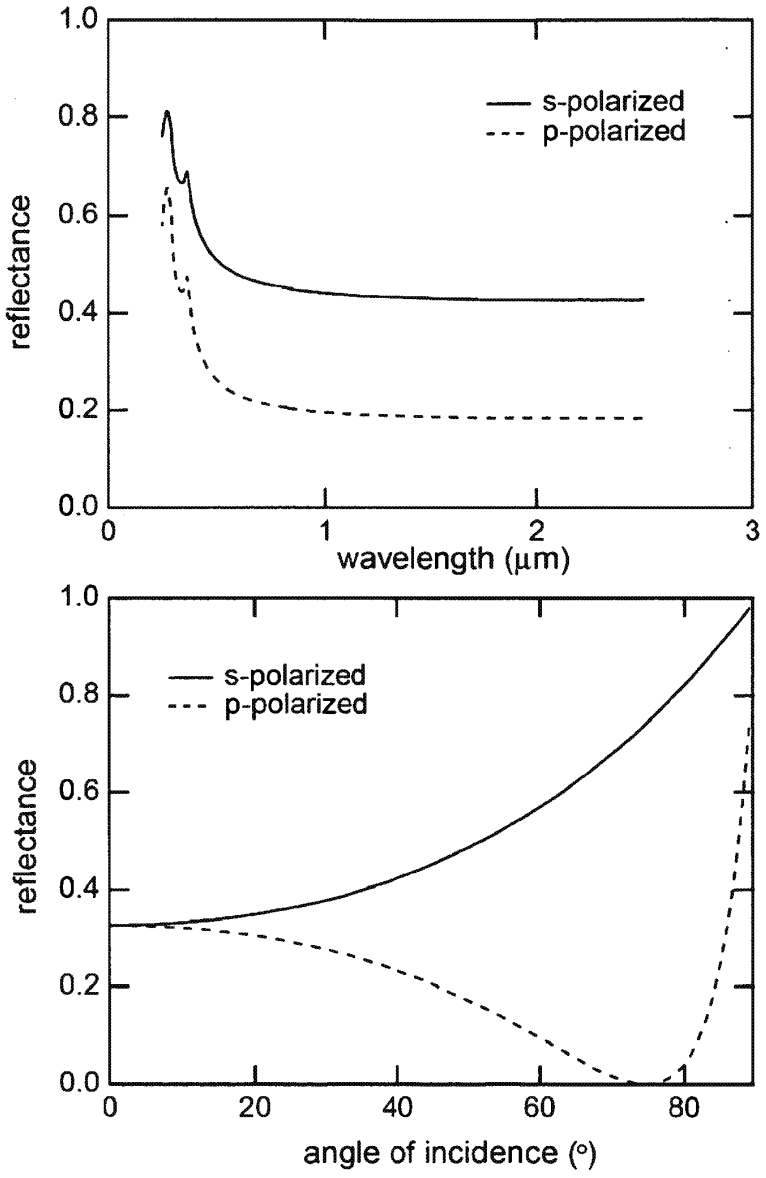


Figure 3.2: Reflectance of ordinary crystalline silicon as determined by literature values for n and k [3] as (a) function of wavelength at 45° incidence angle and (b) incident angle for 800 nm light.

SIONYX1403000044.0082

SAMSUNG EX. 1002 - 900/4148

the imaginary part and hence will change the complex refractive index. Thus, structural or chemical changes in the medium will alter the optical properties of a material. This is important to understand the light-absorption properties of spiked silicon.

Reflectance of ordinary crystalline silicon

Ordinary crystalline silicon is highly reflective across the electromagnetic spectrum. The refractive index and the extinction coefficients for silicon have been determined experimentally by transmittance and reflectance measurements by a number of groups and are summarized elsewhere. [3] The absorption of ordinary silicon changes abruptly and decreases to essentially zero for below-band gap energies (absorption edge). The refractive index n of silicon lies in the range $1.5 < n < 6.8$ for $0.25\ \mu\text{m} < \lambda < 1.0\ \mu\text{m}$. For below bandgap radiation down to THz frequencies, the refractive index varies little and is about $n \cong 3.4$. The reflectance of ordinary crystalline silicon for $0.25\ \mu\text{m} < \lambda < 2.5\ \mu\text{m}$ is shown in Fig. 3.2 as determined by literature values of n and k. [3]

3.3 Reflectance, transmittance, and absorptance in spiked silicon

3.3.1 Measurement of optical properties

Reflectance and transmittance of a material are usually measured directly, absorption is often inferred from transmission measurements corrected for reflection losses. The absorptance can be determined via the relationship given in equation 3.1. It is difficult to measure the optical properties for corrugated surfaces because of scattering, which enhances the diffusive component of the reflectance and transmittance. Different techniques are common to either single out the specular or diffuse component or to measure both at the same time. [65] A common way to measure reflectance and transmittance from a strongly scattering material is to use an integrating sphere. The integrating sphere allows simultaneous collection of both specularly reflected light and scattered light. Such a sphere is coated on the inside with a diffusively reflective material. A photodetector is positioned on the sphere. Light, that is reflected from the sample onto the walls of the sphere is diffusively scattered (averaged), before it hits the detector. The sphere is a diffuse reflector (Lambertian source), whose radiance does not depend on the viewing angle. Therefore,

SIONYX1403000044.0083

SAMSUNG EX. 1002 - 901/4148

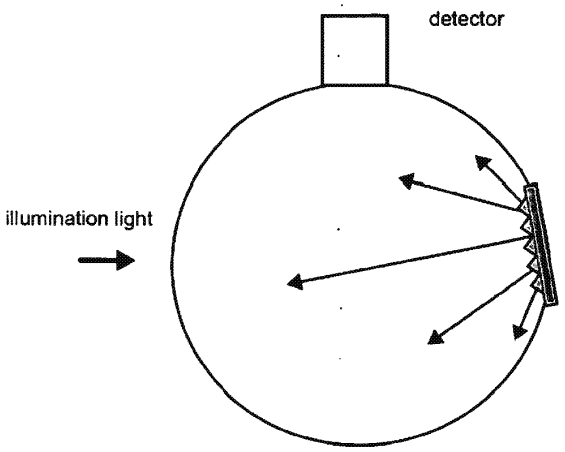


Figure 3.3: Diffusively reflected light is collected in an integrating sphere.

reflection from any point in the sphere onto the detector yields the same radiance. [69] The reflectance and transmittance of spiked silicon were measured from the near ultraviolet (0.25 μm) to the near infrared (2.5 μm) using a spectrophotometer (Hitachi Model U-440) equipped with an integrating sphere detector. The integrating sphere has an inner diameter of 60 mm and is coated with highly reflective barium sulfate. Light was incident on the sample at an angle of 10° to enable collection of specularly reflected as well as scattered light. The photodetector for ultraviolet and visible wavelengths was a R928 photomultiplier; near-infrared wavelengths were detected with a cooled PbS cell. An iodine tungsten lamp (0.35 μm – 2.5 μm) and a deuterium discharge tube (0.25 μm – 0.35 μm) provided illumination. The light was dispersed via a prism-diffraction grating double monochromator. The slit width used for all measurements was 6 nm. The light was focused onto the sample with a lens; the beam diameter at the sample was 0.2 x 0.8 cm.

Prior to the measurements, the apparatus was calibrated by measuring the reflectance and transmittance of a sub-white aluminum sulfide plate which served as a baseline. The actual data were then divided by this baseline.

We measured the reflectance and transmittance and determined the absorptance for three spiked surfaces with different spike heights. All sample were made from undoped Si(111) wafers with resistivity $\rho = 800 - 1200\ \Omega$cm. Sample fabrication conditions are summarized in Table 3.1.

SIONYX1403000044.0084

SAMSUNG EX. 1002 - 902/4148

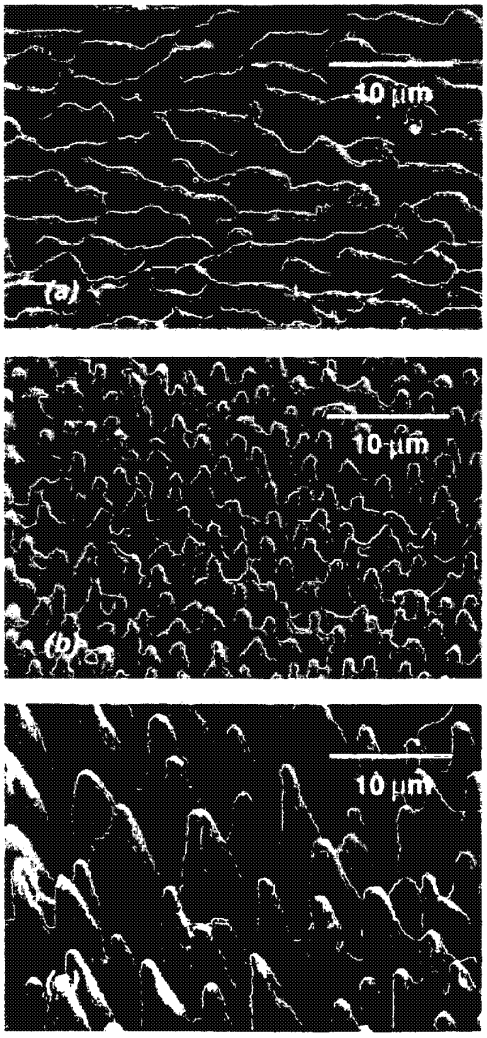


Figure 3.4: SEM images of three spiked surfaces with (*a*) 1-2 μm, (*b*) 4-7 μm, (*c*) 10-12 μm spike height.

SIONYX1403000044.0085

SAMSUNG EX. 1002 - 903/4148

Table 3.1: Sample fabrication conditions

	1-2μm	4-7 μm	10-12 μm
Laser fluence	2.98 kJ/m^2	5.69 kJ/m^2	11.06 kJ/m^2
Scan velocity	300 μm/s	300 μm/s	200 μm/s

Figure 3.4 shows the three surfaces as seen under the SEM.

3.3.2 Results

Figure 3.5 shows the measured reflectance and the transmittance of the three spiked surfaces and the flat, untreated surface; Fig. 3.6 depicts the calculated absorptance. For spiked silicon, R and T are dramatically less than for flat silicon. The taller the spikes, the less the reflectance and transmittance (and consequently the greater the absorptance). The absorptance is >0.9 for 500 nm–2500 nm for the sample with 10-12 μm spikes. However, the biggest change in the optical properties occurs on going from ordinary silicon to the sample with spikes only 1-2 μm tall.

3.4 Light absorption in spiked silicon

The light absorption of ordinary, crystalline silicon is limited by two factors:

1. Silicon is highly reflective across the electromagnetic spectrum due to its high index of refraction. Thus, a substantial amount of light incident on the surface is reflected and not absorbed.

2. Only radiation with energy greater than the bandgap energy can be absorbed. For wavelengths longer than 1.1 μm, any light that is not reflected is transmitted.

In the following section (Sec. 3.4.1) I elaborate on increasing light absorption through reflection reduction. The next section (Sec. 3.4.2) deals with producing below-bandgap absorption by introducing structural and chemical defects.

3.4.1 Increase in light absorption through surface structuring

It is well known that texturing of surfaces can enhance light absorption through reflection reduction. If the structures are on a scale large compared to the incident radiation, multiple reflections at the corrugated surface cause the radiation to be trapped,

SIONYX1403000044.0086

SAMSUNG EX. 1002 - 904/4148

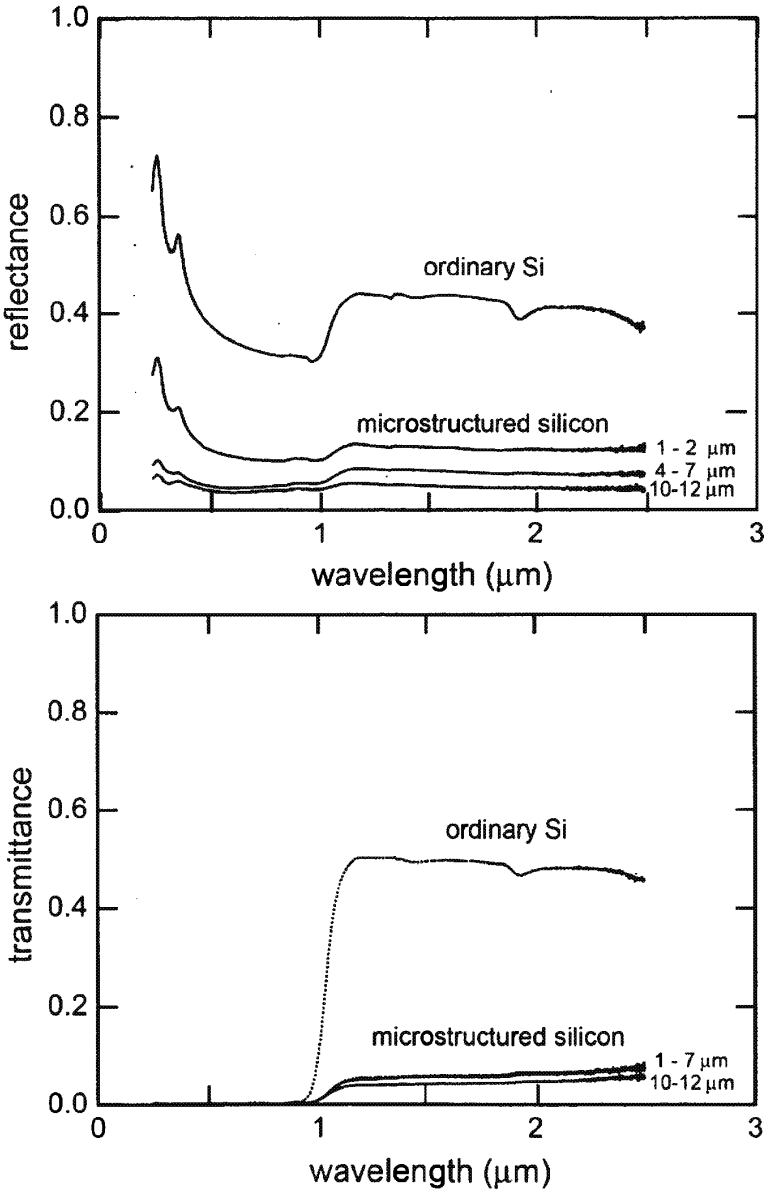


Figure 3.5: Reflectance and transmittance of the three spiked surfaces and ordinary silicon.

SIONYX1403000044.0087

SAMSUNG EX. 1002 - 905/4148

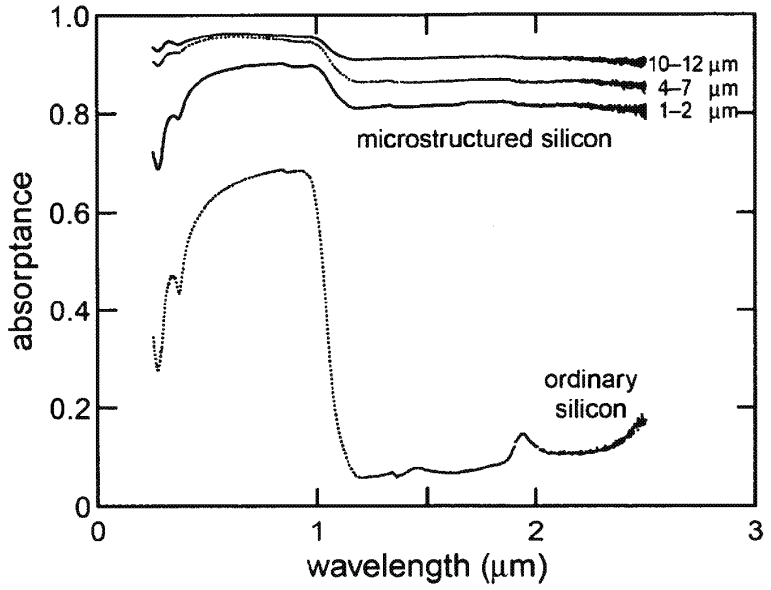


Figure 3.6: Absorptance of the three spiked surfaces and ordinary silicon.

hereby enhancing the absorption. This principle is employed in anechoic acoustic surfaces. Figure 3.7 shows schematically how radiation is trapped by multiple reflections both at the outer and inner walls of a surface structure. Structuring silicon on the micrometer scale

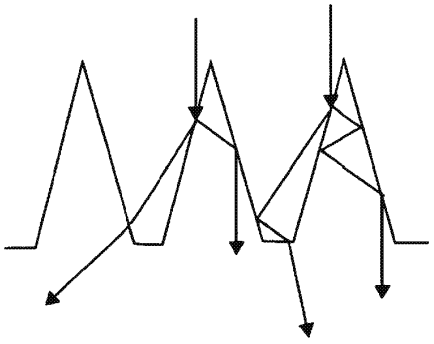


Figure 3.7: Schematic showing light trapping through multiple reflections.

thus reduces reflectance of visible and near-infrared light. One established technique for

SIONYX1403000044.0088

SAMSUNG EX. 1002 - 906/4148

structuring silicon on the micrometer scale is the generation of random pyramidal structured surfaces (known as RPSS) through anisotropic etching. [70] A significant reduction in reflectance to a few percent in the visible and to about 20% [3] in the infrared was reported using this method.

If the structures are on a scale small compared to the incident radiation, the light encounters essentially an unstructured medium. Structuring the surface on a scale much smaller than the wavelength of the incident light also reduces reflective losses, but by a different mechanism. The medium appears smooth but with a constant smooth variation in the index of refraction from that of the ambient medium to that of the reflecting surface. [71, 72] Effective medium theory is used to model the interaction of light with subwavelength structures.[4] Theoretical calculations show that maximum reduction of reflection is achieved when the ratio of the graded refractive layer thickness layer d to the wavelength of the incident light λ is at least $d/\lambda \leq 0.4$. [74] Nature has utilized this principle of reflection reduction on the cornea of certain moth eyes. [75] The corneal lens of these moths is covered with conical protuberances of 200 nm height and spacing. The submicron stuctures lead to a graded refractive index which reduces the reflection for visible and near-infrared light to essentially zero.

Submicron structuring of silicon has been done by reactive ion etching and anodic etching. Gittleman *et al.* [76] and Craighead *et al.* [77] showed that the reflectance of silicon in the visible could be reduced to almost zero by producing submicron structures on silicon, while there was a high reflectance above 1 μm in the infrared. A material with such absorptance properties was proposed as an effective solar absorber. Porous silicon has also been demonstrated to have reduced reflectance in the visible. [78, 79, 80]

However, multiple reflections cannot solely account for the observed absorptance in spiked silicon. Reduced reflection in the infrared would lead to increased transmittance in the infrared and not to increased absorption. Other mechanisms must be at work.

3.4.2 Below-band gap absorption

In a semiconductor, light can be absorbed when the energy $\hbar\omega$ of the incident photon is greater than the band gap energy of the material. The energy from the absorbed

[3] With the use of an antireflection coating the reflectance of these surfaces could be further reduced. The reported reflectance varied strongly across the wavelength range measured.

[4] Modelling this method of reflection reduction dates back to the work of Lord Rayleigh in 1880. [73]

SIONYX1403000044.0089

SAMSUNG EX. 1002 - 907/4148

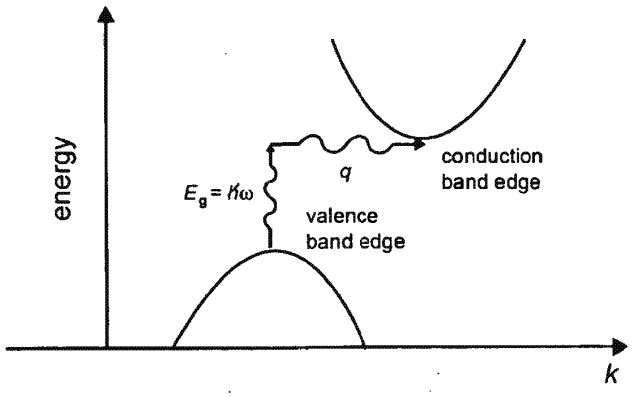


Figure 3.8: Phonon-assisted photon absorption in silicon.

photon promotes an electron from the valence band to the conduction band, leaving behind a hole in the valence band. In silicon, the minimum energy point of the conduction band and the maximum energy point of the valence band lie at different points in k-space (indirect gap). Therefore the absorption of photons is indirect: the promotion of an electron from the valence to the conduction band at energies near the indirect band gap requires simultaneously changing the electron momentum by absorption or emission of a phonon. The indirect band gap lies at 1.12 eV (corresponding to a wavelength of 1.11 μm) at 300 K. For energies exceeding 1.12 eV there is an abrupt absorption increase (absorption edge). (See Fig. 3.6) Photons with energies less than the band gap energy can not be absorbed by silicon, unless the photon flux is sufficiently great to produce multiphoton absorption. In view of the absorption of ordinary silicon, the observed strong infrared absorption in spiked silicon is very puzzling.

There are two ways to produce below-band gap absorption in ordinary silicon: by introducing impurity atoms or by changing the structural order. Deviations from periodicity in the crystal lattice can introduce electronic energy levels within the band gap. Transitions from or to these levels can occur which enable absorption of photons with subbandgap energies. Impurity atoms bind electrons with a different potential and thus can introduce states in the band gap. The following section discusses both of these possibilities in greater detail.

SIONYX1403000044.0090

SAMSUNG EX. 1002 - 908/4148

a) Subgap absorption through chemical changes

The presence of foreign atoms in a crystal alters the periodicity of a crystal lattice and thus can create absorbing states in the band gap. A distinction is made between impurity levels close to the valence or conduction band (shallow impurities) and those deep in the band gap (deep impurities). Foreign atoms with the same number of valence electrons as the host are referred to as isoelectronic impurities, whereas donor atoms have more, leading to extra electrons (n-doping), and acceptor atoms fewer, leading to a deficit of electrons (p-doping). [81] Typical dopants used in silicon are arsenic (group V) or boron (group III), for n-doped and p-doped silicon respectively. Highly doped silicon can absorb infrared radiation. We determined the absorptance of n-Si(111) with a resistivity of $\rho < 0.005\ \Omega\,\mathrm{cm}$ to be $0.7 < R < 0.8$ for the wavelength range of $1.0\ \mu\mathrm{m} < \lambda < 2.5\ \mu\mathrm{m}$. Since the samples used for the optical measurements presented in Sec. 3.3.2 were made by structuring undoped Si(111), there is no diffusion and redistribution of dopants, that could have formed an infrared-absorbing layer.

So, if impurities cause the absorption in spiked silicon, where do they come from and what kind of impurities are those? While the spikes are formed, impurities from the ambient environment are incorporated into the structures. As shown in Chapter 3, Sec. 2.4.1, the spikes are heavily sulfur-doped. It is likely, that the sulfur atoms embedded in the silicon are the infrared absorbing centers. Sulfur in the silicon spikes would be expected to introduce states in the band gap. Sulfur can be incorporated into silicon as atomic sulfur, as diatomic S_2 or sulfur-related complexes, either neutral (S^0) or singly ionized (S^+). These various forms of sulfur in silicon give rise to several different donor levels in silicon. The energy levels of sulfur in silicon have been measured by a number of groups. In particular, the midgap state at 0.614 eV has been studied by a variety of methods. [82, 83, 84, 85] Figure 3.9 depicts the energy levels as determined by Janzen *et al.* [4] The subscript denotes if the donor is atomic (no subscript), diatomic sulfur (2) or a sulfur-related complex (c). The superscript denotes if it is neutral (0) or singly ionized (+). (X) denotes that it is a sulfur-related complex, where only little information is available. Allowed transitions between the discrete levels cause peaks in the absorption spectra of sulfur in silicon in the infrared. We do not observe discrete absorption peaks. The high concentration of sulfur in the spikes, on the order of $10^{20}/\mathrm{cm}^3$, is high enough to form a band within the band gap instead of introducing discrete levels, [86] which could account for the featureless absorption.

SIONYX1403000044.0091

SAMSUNG EX. 1002 - 909/4148

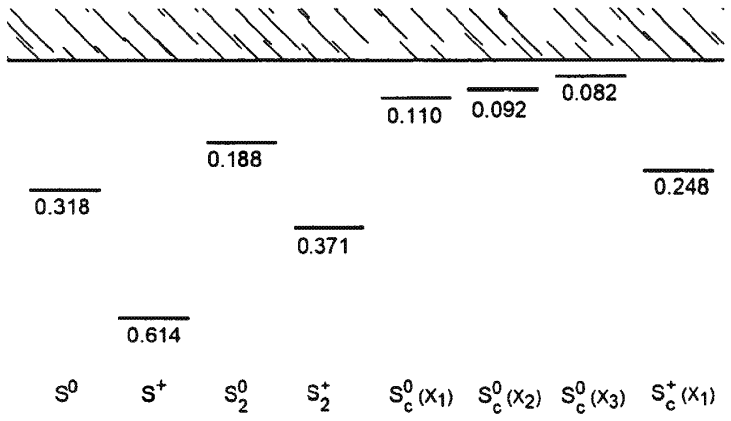


Figure 3.9: Sulfur energy levels in silicon. Values are shown in eV. After Janzen *et al.* [4]

In order to test if sulfur is responsible for the below-band gap absorption, we performed a vacuum anneal ($P = 10^{-7}$ Torr) at 1210 K for three hours on the sample with the 10-12 μm spike height. The anneal does not change the macroscopic morphology of the spikes. At this temperature, sulfur is ejected from the silicon lattice and can diffuse from the bulk into the surface region. [87] Wilson, who introduced sulfur into silicon by ion implantation, found that the sulfur remains at its lattice site for temperatures below 1000 K. Above 1000 K it starts to form complexes with the damages formed during the ion implantation. For temperatures exceeding 1200 K, the damages have annealed out and the sulfur diffuses to the surface. We performed SIMS and XPS of the surface before and after the anneal. Figure 3.10 compares the SIMS spectra before and after anneal at 1210 K. After anneal, the sulfur content is decreased compared to the sample before the anneal. XPS of the spiked surface after the anneal shows a small sulfur peak in the surface region, that was not present before the anneal. The sulfur peak in the XP spectrum may indicate that sulfur has diffused from the bulk to the surface region.

If sulfur atoms cause the below-band gap absorption, a change in the concentration of sulfur in the samples would affect the absorption properties. Figure 3.11 shows the measured reflectance and transmittance and Fig. 3.12 the calculated absorptance of the sample after the anneal.

SIONYX1403000044.0092

SAMSUNG EX. 1002 - 910/4148

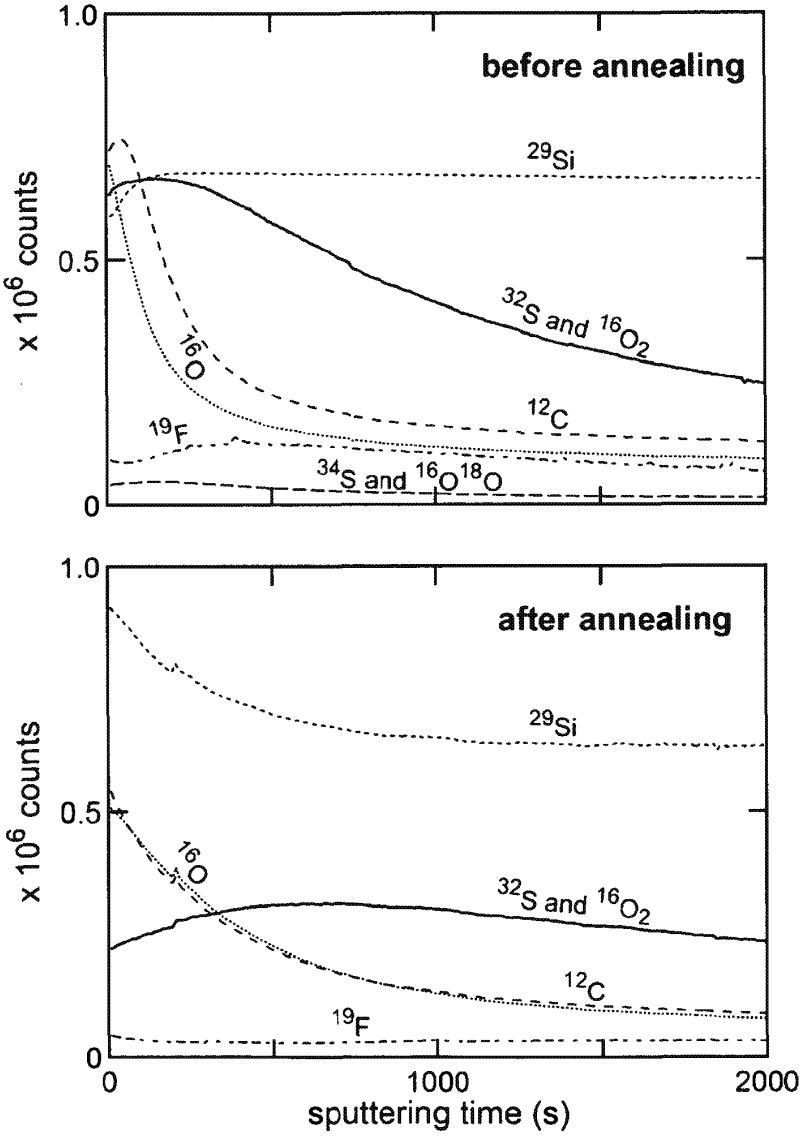


Figure 3.10: SIMS spectra before and after vacuum anneal.

SIONYX1403000044.0093

SAMSUNG EX. 1002 - 911/4148

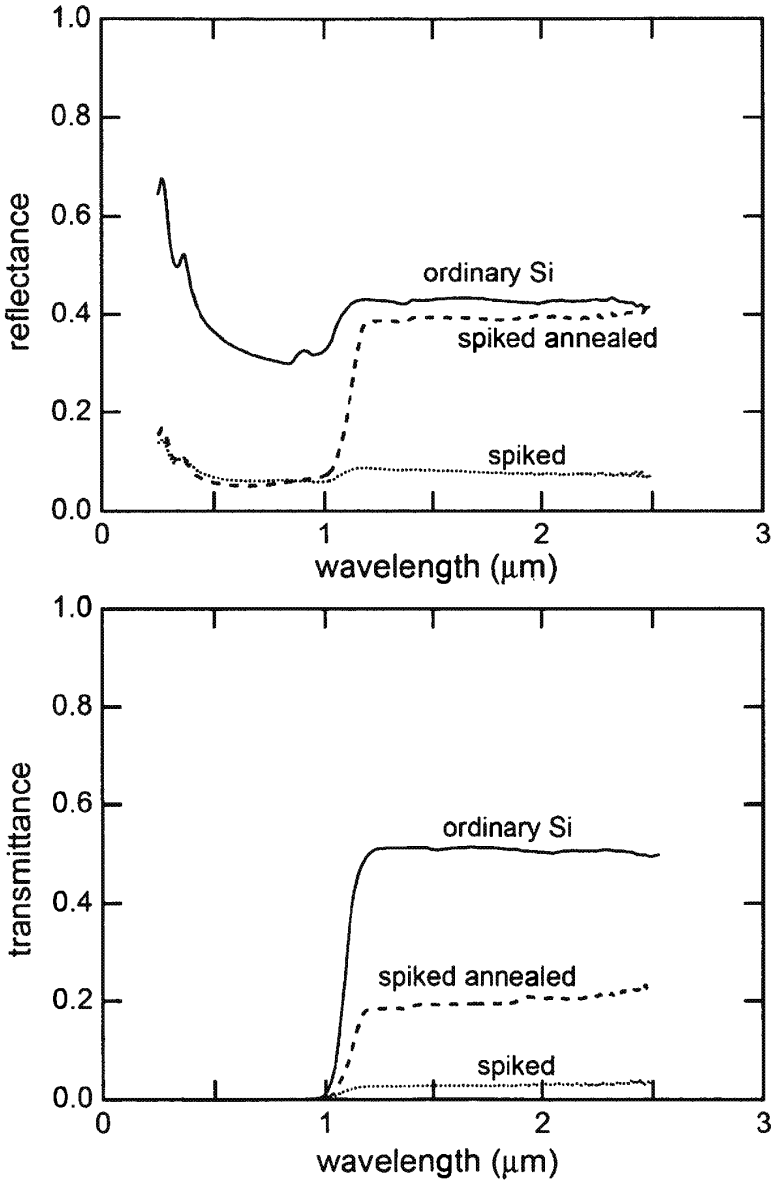


Figure 3.11: Reflectance and transmittance of spiked silicon after vacuum anneal for 3 hours at 1210 K.

SIONYX1403000044.0094

SAMSUNG EX. 1002 - 912/4148

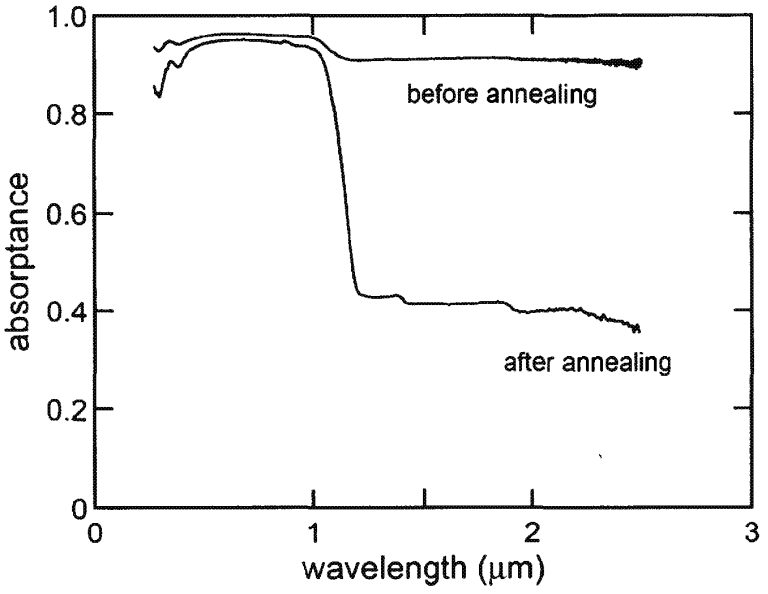


Figure 3.12: Absorptance of spiked silicon before and after vacuum anneal for 3 hours at 1210 K.

After the anneal, the optical properties of spiked silicon changed. The reflectance of below-band gap radiation returned to almost the values of that of flat silicon, while the reflectance of visible light remained nearly unchanged. The below-band gap transmittance increased to roughly T=0.2 over the measured wavelength range and the absorptance decreased by roughly a factor of 2. Like the reflectance, the values in the visible were almost unchanged by the anneal. SIMS and XPS of the sample after the vacuum anneal show that the chemical composition of the silicon spikes has changed.

The simultaneous decrease in absorptance and the sulfur concentration suggests that the subgap absorptance of spiked silicon is associated with the sulfur embedded in the silicon. Are chemical defects the sole cause for the absorptance? As shown, in Chapter 2, Sec. 2.4.2, the spikes contain a high number of defects. Do these defects contribute to the high absorption of below-band gap radiation? The next section addresses this question.

SIONYX1403000044.0095

SAMSUNG EX. 1002 - 913/4148

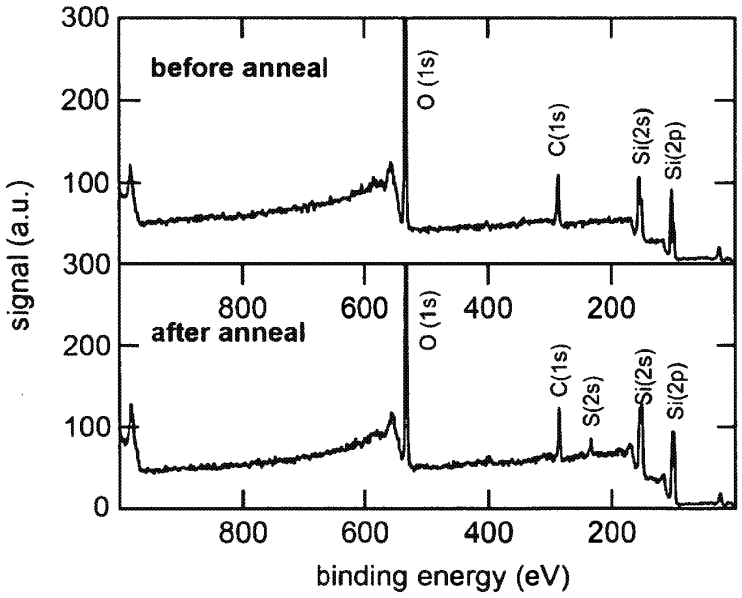


Figure 3.13: XP spectra of spiked silicon before and after vacuum anneal.

SIONYX1403000044.0096

SAMSUNG EX. 1002 - 914/4148

b) Subgap absorption through structural changes

Structural changes cause deviations from the periodic crystal lattice and can also introduce subgap states. Amorphous silicon (a-Si), polycrystalline silicon (poly-Si), and damaged/deformed silicon exhibit subgap absorptance. [88, 89, 90] In all cases, the presence of significant disorder broadens the abrupt band edge of crystalline silicon producing so-called band tails of localized states extending into the gap. Surface states are very close in energy to the band edge, whereas bulk defects produce states further in the tail. In amorphous silicon, the band tailing has an exponential-like dependence on photon energy and the band edge is known as the Urbach-edge. Depending on the amount of disorder, defect states can produce an absorptance as great as a few percent for wavelengths 1.1 μm $< \lambda <$ 2.5 μm. [88] Although the disorder is associated with subgap absorption, there is no agreement on what kind of defects are responsible for subgap absorption. Poly-Si and damaged silicon exhibit dangling bonds (untied silicon bonds) at grain boundaries, stacking faults, and other structural defects. While Jackson *et al.*[89, 90] suggested that subgap absorption in polycrystalline silicon stems from dangling bonds, Saeger and Lenahan [88, 91] could not find a correlation between the density of dangling bonds and subgap optical absorption. They proposed that absorption in damaged and polycrystalline silicon was probably due to electrons in strained or bent bonds, i.e. band-tail states.

Spiked silicon

Spiked silicon is not amorphous, but mainly crystalline with some disorder, as indicated by electron backscattering (Kikuchi diffraction) and ion channeling (Chapter 3, Sec. 2.4.2). To examine if structural changes cause the subgap absorption in spiked silicon we performed SEM and ion channeling on the sample after the anneal:

Annealing at 1100-1300 K can remove point defects (such as those resulting from sputtering). [92] At these temperatures, silicon atoms can move back into the lattice sites. However, annealing cannot remove line defects (such as grain boundaries, twinning, stacking faults etc.) or convert poly-crystalline into single-crystalline silicon.

As already discussed in the previous section, the annealing changes both the reflectance, transmittance and consequently the absorptance. Apparently, the infrared absorption is partially reversed by the anneal. Comparison of the surface before and after the anneal also reveals a change in the surface morphology: The anneal removed many of the

SIONYX1403000044.0097

SAMSUNG EX. 1002 - 915/4148

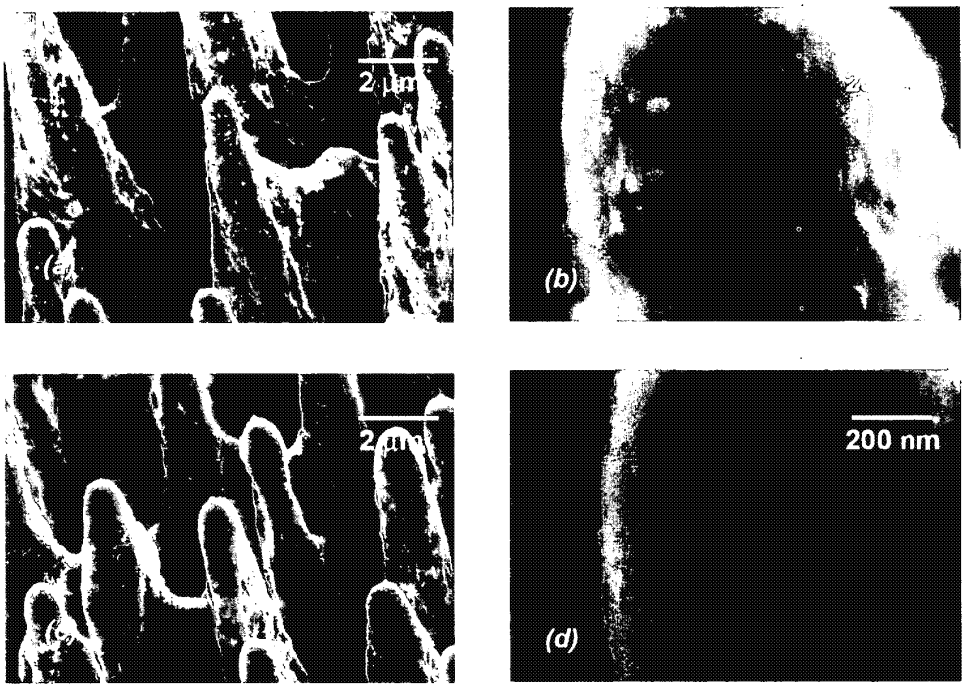


Figure 3.14: Spiked silicon surface (*a*), (*b*) before and (*c*), (*d*) after vacuum anneal as seen under the SEM using a magnification of (*a*), (*c*) x 10 000 and (*b*), (*d*) x 100 000.

nanometer spheres on the surface of the spikes. Figure 3.14 shows the surface before and after the anneal as seen under the SEM at different magnifications. Ion channeling before and after the treatment does not show a significant change in the background level. We attribute the elevated background in the channeling spectra to the presence of structural defects. Thus, the anneal does not produce a significant change in the amount of disorder in the spikes.

SIONYX1403000044.0098

SAMSUNG EX. 1002 - 916/4148

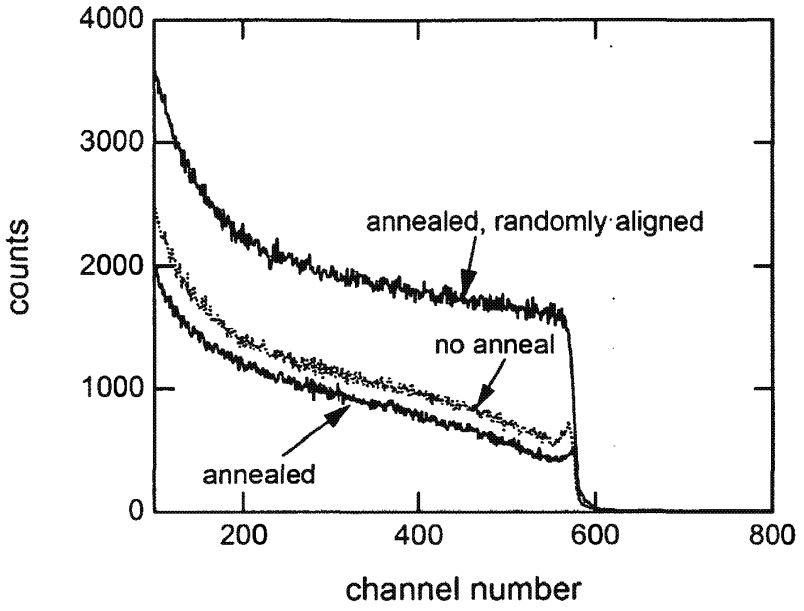


Figure 3.15: Ion channeling spectra taken from the spiked silicon sample before and after vacuum anneal of 3 hours at 1210 K. For comparison, the spectrum of the randomly aligned sample is shown as well.

3.5 Discussion

The increase in light absorption of spiked silicon over such wide wavelength range has not been previously achieved by other methods of modifying silicon. Especially puzzling is the near-unity below-band gap absorption.

While multiple reflections at the corrugated surface probably contribute to the increase in light absorption, they cannot solely account for the observed light absorption properties of spiked silicon. First, reduced reflectance of below-band gap radiation would lead to increased transmittance, but not to increased absorptance. Second, after annealing the reflectance of below-band gap radiation returns to nearly that of flat, ordinary silicon despite the fact that the macroscopic morphology of the spiked surface is unchanged by the anneal.

The increased absorptance must thus be associated with other changes in the silicon surface. Comparison of the SIMS spectra before and after the anneal shows a de-

SIONYX1403000044.0099

SAMSUNG EX. 1002 - 917/4148

creased sulfur content in the spikes after the anneal. Sulfur does exhibit subgap states. It is therefore possible that sulfur embedded in silicon cause the observed below-band gap light absorption.

How about structural changes? After the anneal, many of the nm-spheres on the spikes disappeared. Subgap states associated with these nm-structures could contribute to the observed below-band gap absorptance. However, it is unlikely that the density of the potrusions could cause such a dramatic change in the light absorption properties. Defects within the crystal lattice of the spikes can also not by the sole cause of near-unity light absorptance as shown by the small change in the ion channeling spectra after the anneal.

The most likely explanation for the near-unity absorption is therefore a combination of multiple reflections and states within the band gap of silicon. These subgap states likely stem mostly from impurities in silicon with some contributions from structural defects.

3.6 Applications

The high absorption of spiked silicon in the visible and especially in the infrared could have important technological applications. More than 95% of today's photovoltaics (such as solar cells and photodetectors) are made from silicon. Since silicon is highly reflective across the electromagnetic spectrum, additional treatments are made to reduce the reflection of the silicon surface such as depositing antireflective coatings or structuring the surface. Reducing reflection by producing spikes on a light-collecting surface is a very efficient method to reduce reflection of light in silicon, because the spiked surface exhibits near-zero reflection over a very broad wavelength range. If the increased light absorption leads to the production of photocarriers, spiked silcon could be used to improve the efficiency of existing photovoltaics.

Besides the high anti-reflective properties of spiked silicon, the near-unity light absorption of below-band gap radiation is of particular interest. Infrared detection is of great importance to many fields, such as telecommunications, remote sensing or space research. If the absorptance of below-band gap radiation creates photocarriers for conduction, spiked silicon could fundamentally change infrared detection technology.

SIONYX1403000044.0100

SAMSUNG EX. 1002 - 918/4148

Chapter 4

Photocurrent measurements

4.1 Introduction

Photovoltaic devices, such as solar cells and photodetectors, absorb light and in doing so convert energy from photons into electrical energy. The observed near-unity light absorption of spiked silicon surfaces has the potential to greatly enhance the effciency of these devices. The efficiency of photovoltaics is determined by the absorptance of the light-collecting surface and the ability of converting absorbed photons to charge carriers (quantum efficiency). However, enhanced light absorption alone is insufficient for enhancing quantum efficiency; the absorbed photons must create electron-hole pairs that are sufficiently long-lived to be collected.

Structuring the light-collecting surface of a photovoltaic device is a common technique to reduce reflection and enhance absorption. Grebel *et al.* showed that forming V-grooves with a laser on the surface of solar cells increased the light collection efficiency by 23 % compared to nonpatterned cells. [93] Hahn *et al.* also reported increased carrier collection efficiency in deeply V-textured solar cells. [94] Forming random pyramidal structured surfaces (known as RPSS) by anodic etching is also used to reduce the reflectivity of silicon surfaces. [70] Using porous silicon as the light absorbing material, Zhang *et al.* and Lee *et al.* [78, 79] reported a near unity quantum efficiency photodetector for the visible wavelength range.

One potential problem with patterning silicon surfaces for use in photovoltaics however, is that modifying the surface may introduce defects into the lattice. Chemical impurities may also be incorporated if the structuring is done in the presence of a gas rather

SIONYX1403000044.0101

SAMSUNG EX. 1002 - 919/4148

than in ultra-high vacuum. All such defects are potential recombination centers for electrons and holes, and their presence can drastically reduce the number of electrons available for conduction. A variety of methods are used to reduce the number of recombination centers. One source of traps, dangling silicon bonds, are commonly eliminated by surface and bulk passivation. At the surface, controlled oxidation is used to terminate the surface, whereas hydrogenation is used to tie up dangling bonds in the bulk. [95, 96, 97, 98] For devices in which only the surface is important, surface impurities can be removed by gettering, which introduces impurity sinks in the material. Impurities diffuse to these centers and are removed from the surface region of the wafer. [95]

The atomic structure of spiked silicon surfaces has crystalline order, but contains a high concentration of chemical and structural defects (as discussed in Chapter 2, Sec. 2.4.2) and the greatly enhanced surface area leads to a high density of surface states. These defect and surface states are likely to promote recombination of generated carriers. It is therefore not immediately obvious if the increased light absorption of spiked silicon could be used to increase the quantum efficiency of photovoltaic devices. In exploring the possibility of using spiked silicon for devices, we studied the following three experimental questions:

1. Does spiked silicon produce more photocurrent than ordinary, flat silicon?
2. Does subsequent passivation of the spiked surface increase photocurrent production?
3. Does the strong absorption of below-band gap radiation in spiked silion (see Chapter 3) lead to the generation of photocarriers?

The latter question is of particular interest to infrared detection technology. Given the fact that ordinary silicon practically does not absorb below-band gap radiation, silicon is not normally used to detect infared light. If spiked silicon produces photocarriers upon below-band gap radiation, it may be used to expand the wavelength range of existing silicon-based detectors. This would be especially important to the telecommunications industry, remote sensing, and detectors for the use in space, which rely heavily on the detection of infrared signals.

The first part of this chapter describes photocurrent measurements of spiked silicon upon white-light illumination and the effects of hydrogen passivation. In the second part, I desribe photocurrent measurements of spiked silicon upon illumination with below-band gap radiation, that were performed in collaboration with Radiation Monitoring Devices (RMD),

SIONYX1403000044.0102

SAMSUNG EX. 1002 - 920/4148

in Watertown, MA. The sections are organized as follows: I briefly introduce the processes of charge carrier generation and recombination in silicon in Sec. 4.2. Sec. 4.3 describes the design and fabrication of the device used for measuring photocurrent generated by white-light illumination. The white-light photocurrent measurement procedure, results, and the effects of hydrogenation are presented in Sec. 4.4. In Sec. 4.5, I present the results obtained from structuring avalanche photodiodes for detecting below-band gap radiation. Finally, I discuss the applicability of spiked silicon for photovoltaics in Sec. 4.6.

4.2 Charge carrier generation and recombination in silicon

Absorption of photons in a semiconductor can produce electron-hole pairs if the energy of the photons exceeds the band gap energy of the semiconductor: electrons from the valence band are promoted to the conduction band, leaving behind a hole in the valence band. Such photogenerated carriers recombine as the semiconductor returns to thermal equilibrium. Whether such photocarriers are useful for conduction depends on how quickly they recombine.

Recombination occurs via a variety of processes, either nonradiative or radiative. Nonradiative recombination takes place through several competing processes including the transfer of the energy to a phonon or another electron or hole (Auger process). Recombination of electron-hole pairs can also proceed radiatively by releasing the excess energy as a photon. The recombination can take place through band-to-band recombination (recombination of an electron in the conduction band and a hole in the valence band) or through trapping of an electron and a hole via states within the band gap. Deep defect levels (those that are close to the middle of the bandgap) are especially effective traps.[1] Dislocations or point defects produce deep levels within the gap. Some impurities, including sulfur, which is present in great abundance in spiked silicon produced in the presence of SF_6, also produce deep levels.

[1] The recombination rate U is given by [99]

$$U = \sigma v_{th} N_t \frac{pn - n_i^2}{n + p + 2n_i cosh(\frac{E_t - E_i}{kT})} \tag{4.1}$$

where σ is the electron and hole capture cross section (set equal here), v_{th} the carrier thermal velocity, N_t the trap density, E_t the trap energy level, E_i the Fermi level, and n_i the intrinsic carrier density. When E_t is close to the Fermi level E_i, the recombination rate is large.

SIONYX1403000044.0103

SAMSUNG EX. 1002 - 921/4148

Figure 4.1 depicts the generation and radiative recombination processes of electron-hole pairs in a semiconductor.

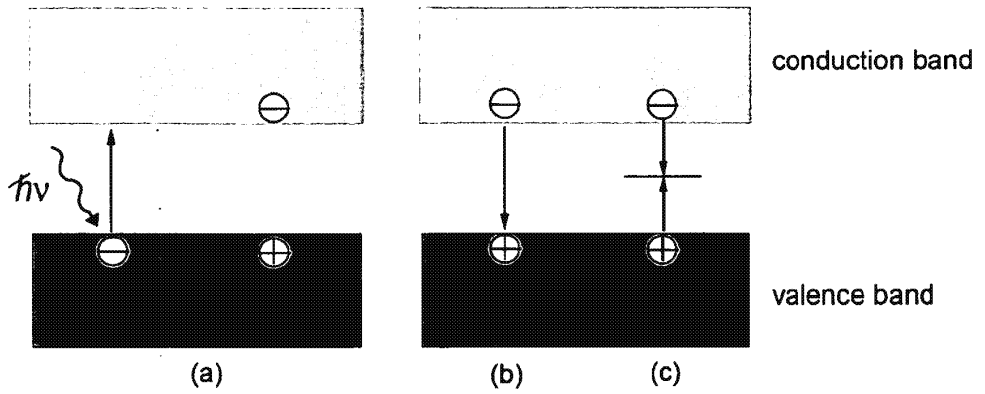


Figure 4.1: (*a*) Generation of an electron-hole pair upon absorption of a photon, (*b*) band-to-band recombination, and (*c*) recombination via a trap.

Because spiked surfaces contain a high density of defects (see Chapter 2.4), the presence of subgap states is likely to limit the usefulness of spiked silicon as made for photovoltaics. Minimizing defect recombination is therefore of special importance for the applicability of spiked silicon to photovoltaics.

4.3 Device design and fabrication

The device used to compare the photoconductance of spiked silicon to that of flat silicon was a partially spiked, metal-semiconductor-metal (MSM) Schottky barrier photodetector. Figure 4.2a shows a photograph of the MSM device, Figure 4.2b illustrates the sideview of the device schematically. The MSM sandwich design was chosen for simplicity of fabrication. A Schottky barrier between a metal and a semiconductor layer is created as follows: A potential barrier forms at the metal-semiconductor interface due to the difference in Fermi levels of the two materials. Such a potential barrier is similar to that of an abrupt *pn*-junction, for which the acceptor density of the *p*-semiconductor is much larger than the donor density of the *n*-semiconductor. In the case of an *n*-doped semiconductor in contact with a metal as in the device discussed here, electrons diffuse from the *n*-doped semiconductor to the metal, causing the bands of the semiconductor to bend upwards at the

SIONYX1403000044.0104

SAMSUNG EX. 1002 - 922/4148

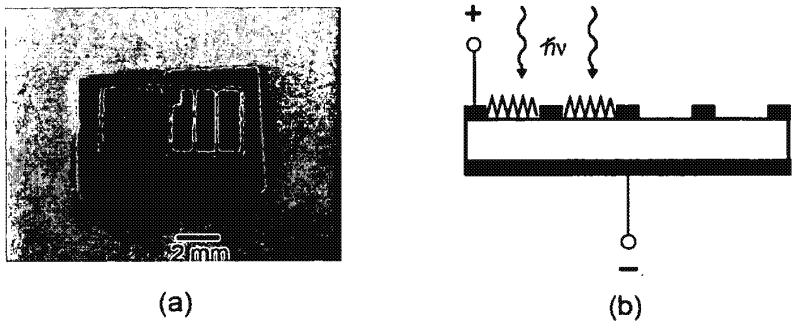


Figure 4.2: (*a*) Photograph of the MSM device used for measuring photocurrent, (*b*) Schematic side view of the device.

metal-semiconductor interface. Electron diffusion stops when the Fermi levels in the two materials meet at the interface. A depletion layer is formed near the metal-semiconductor interface, because the diffusion of electrons leave the semiconductor positively charged near the interface. Figure 4.3a shows the resulting energy bands in thermal equilibrium.

If a positive voltage bias is applied to the metal with respect to the semiconductor (forward bias), the potential difference between the semiconductor and the metal decreases and electrons can flow from the semiconductor into the metal more easily. If a negative voltage is applied (reverse bias), the potential difference increases and fewer electrons flow across the barrier. Figure 4.3 also depicts the energy-band diagram of a metal n-type semiconductor contact in (*b*) reverse and (*c*) forward bias (idealized).[2] W denotes the work function of the metal and χ the electron affinity of the semiconductor. The difference between both is the height of the Schottky barrier. An MSM device includes two Schottky barriers, one at the front semiconductor-electrode interface and one at the back interface. The device effectively consists of two diodes in series with opposite orientation. When a bias voltage is applied, the two diodes experience opposite biasing; if the two diodes are identical, reversing the bias has no effect on the behavior of the combination. Therefore, an MSM device with two identical Schottky barriers is not diodic but instead has a symmetric I-V characteristic. Asymmetries in the I-V characteristic of the device can also occur if the electrodes are not identical, for example, if they have different contact areas, which produces different contact resistances. Figure 4.4 depicts the energy bands of a symmetric

[2]For an unidealized case, surface states and a thin oxide layer need to be taken into account.

SIONYX1403000044.0105

SAMSUNG EX. 1002 - 923/4148

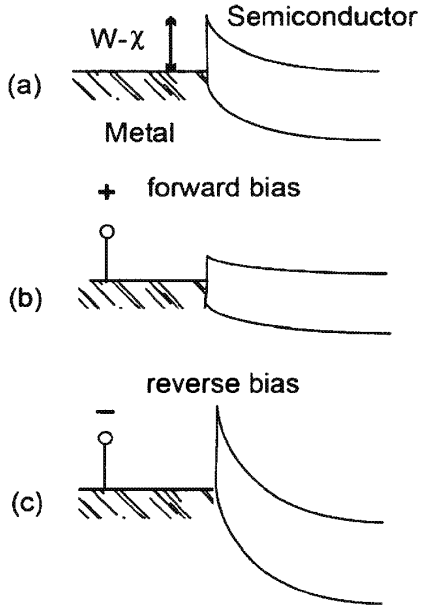


Figure 4.3: Band diagram in a Schottky barrier (*a*) in thermal equilibrium, (*b*) with forward biasing, (*c*) with reverse biasing.

SIONYX1403000044.0106

SAMSUNG EX. 1002 - 924/4148

MSM device under both biasing conditions.

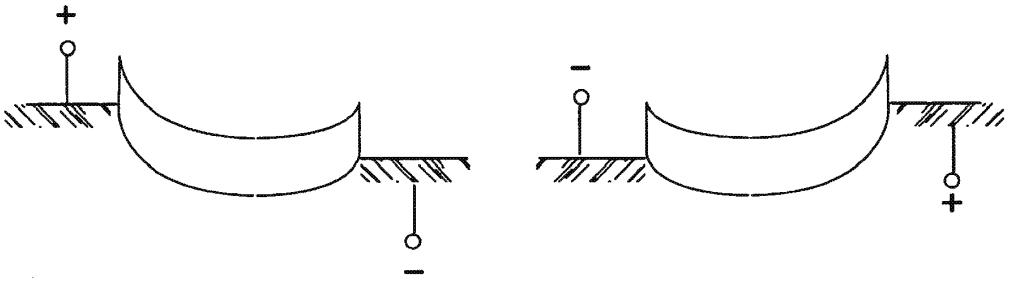


Figure 4.4: Band diagram in an MSM device: The side connected to the positive voltage terminal experiences a forward bias, whereas the side connected to the negative terminal a reverse bias. Switching the biasing produces a mirror image of the energy bands.

4.3.1 Device fabrication

The MSM device was made by evaporating electrodes on both sides of a 7 mm x 4 mm silicon chip (thickness 0.5 mm). The front electrode was patterned in a grid using standard photolithography. Silicon chips were cleaned in an ultrasonic trichlorethylene bath for 10 minutes, followed by a 10–minute ultrasonic acetone bath, followed by a by 10–minute ultrasonic methanol bath. A primer (Microposit primer Hexamethyldisilazane) followed by a 1–μm thick layer of photoresist (Microposit 1805) were deposited on the cleaned chip. Homogenous distribution of primer and resist was ensured by spinning the samples during deposition. The photoresist was then hardened by baking the samples on a hotplate for 3.5 minutes at 105 °C. Lithography was done by exposing the samples to UV light (350–450 nm) under a film mask with the gridded pattern for 60 s. After exposure the samples were bathed in a developer (Shipley microposit 351 mixed with water at a 1:5 ratio) and then rinsed with distilled water. The exposed photoresist washed away in the developer leaving a grid-shaped chip surface exposed. A 5-nm thick layer of chrome and a 80-nm thick layer of gold were then evaporated onto the chip in a thermal evaporator. [3] After evaporation the samples were bathed in acetone to remove the photoresist that was left on the surface. In this way the metal, that was deposited on the photoresist, is removed

[3]Gold is not evaporated directly onto silicon because it does not wet the surface evenly and diffuses readily into silicon; the chrome layer allows evaporation of a uniform layer of gold and serves as a barrier to diffusion between the gold and the silicon.

SIONYX1403000044.0107

SAMSUNG EX. 1002 - 925/4148

from the sample, leaving a metal grid behind. The back electrode, which covered the entire back surface of the chip, was also deposited in the thermal evaporator, and was also 5-nm Cr followed by 80-nm of Au. After deposition of the electrodes, one half of the front side of

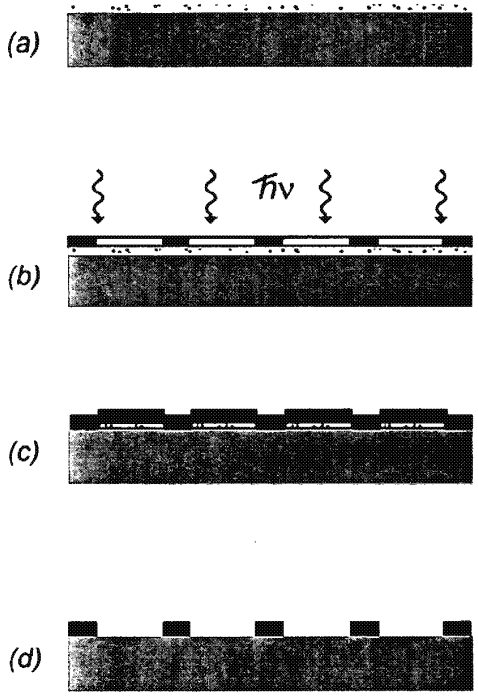


Figure 4.5: Schematic showing the photolithographic steps for making the front grid electrode: (*a*) Photoresist is deposited onto the sample, (*b*) The sample is illuminated with UV light under a gridded mask, only the photoresist under the transparent part of the mask is exposed to the light. The exposed photoresist washes away in the developer. (*c*) Metal is evaporated onto the sample, (*d*) The metal that was deposited onto the undeveloped photoresist washes away with acetone, leaving a gridded metal pattern behind.

the chip was structured with the laser to produce spikes and one half was left as ordinary silicon. Spike formation conditions, summarized in Table 4.1, were the same for all samples discussed in this chapter. Prior to filling in the SF_6, the chamber was pumped out with a turbo pump to a pressure of 10^{-6} Torr.

Electrical contacts to the electrodes were made via gold wires and a conducting paste (butyl cellosolve acetate).

SIONYX1403000044.0108

SAMSUNG EX. 1002 - 926/4148

Table 4.1: Conditions for spike generation

Crystal orientation	Resistivity	Fluence	Pulsewidth	Scan velocity	SF_6 pressure
n-Si(111)	500-600 Ω cm	11 kJ/m^2	100 fs	200 μm/s	900 Torr

4.3.2 Passivation

Structural defects and impurities reduce the lifetime of photogenerated carriers by trapping electron-hole pairs and promoting carrier recombination. It is likely that photocarriers in spiked silicon are very short-lived due to

- A thick oxide layer. (See Chapter 3, Sec. 2.4.1)
- High defect (structural and chemical) density in the spikes. (See Chapter 3, Sec. 2.4.2)
- Enhanced density of surface states due to increased surface area

To reduce the density of defects, we passivated the surface of the devices by etching the device with a 7:1 ammonium fluoride buffered oxide etch and by hydrogen bombardment. Etching with HF removes the oxide, and terminates the surface with hydrogen (ties up dangling bonds).[4] Hydrogenation decreases the defect density in polycrystalline silicon [96, 97, 98] and amorphous silicon films [100] by several orders of magnitude. The passivation of dangling bonds with hydrogen dramatically improves electronic quality of highly defected silicon, because recombination centers are removed.

We performed hydrogenation of our silicon devices in a radio frequency plasma hydrogenation chamber. Hydrogen was admitted to the chamber with a H_2 flow of 40 sccm. A radio frequency field with $f = 13.56$ MHz inductively produces a plasma of H^+ ions. The sample is heated during hydrogenation. A schematic of the hydrogenation setup is illustrated in Fig. 4.6.

[4] After a few hours the native oxide layer of several tens of nm, which is also present on flat silicon, grows back.

SIONYX1403000044.0109

SAMSUNG EX. 1002 - 927/4148

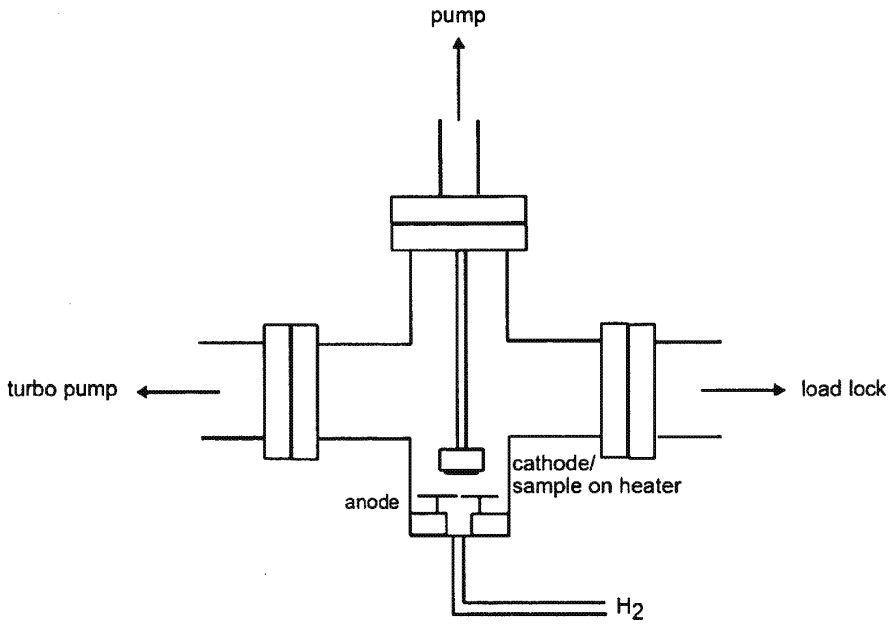


Figure 4.6: Schematic of hydrogenation setup.

4.4 Photocurrent measurements

4.4.1 Experimental setup

Photocurrent measurements were performed by measuring the voltage change across a sense resistor placed in series with the sample upon illumination of the device. The photodetector was illuminated with a white-light fiber lamp. The light was focussed with a 0.02 m focal length lens onto a pinhole. The pinhole was then imaged onto the sample such that an area of about 3 mm^2 was illuminated on the sample covering either the flat or the spiked part of the device. The circuit used to measure the photoccurrent is shown in Fig. 4.7. The sample was connected in series with a 10–Ω sense resistor and the variable voltage across the two was provided by a function generator, which delivered a voltage sweep from −2.5 V to +2.5 V at a 5–Hz period. The voltage change across the sense resistor upon illumination was measured and recorded with a digital oscilloscope. Figure 4.8 shows the experimental setup schematically.

SIONYX1403000044.0110

SAMSUNG EX. 1002 - 928/4148

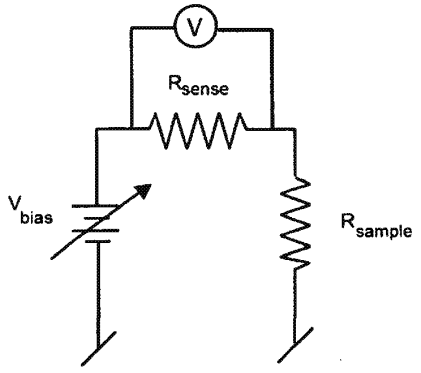


Figure 4.7: Circuit diagram of photocurrent measurements.

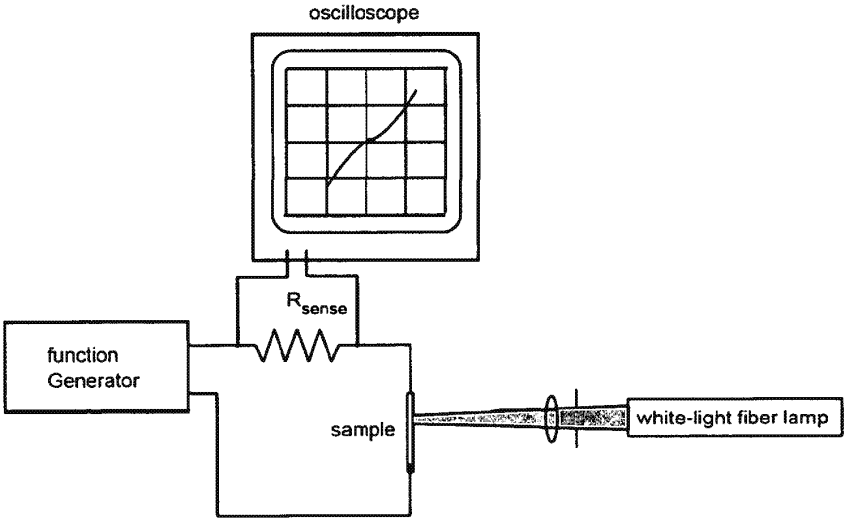


Figure 4.8: Schematic of the photocurrent measurement setup.

SIONYX1403000044.0111

SAMSUNG EX. 1002 - 929/4148

Measuring I-V characteristics with a sense resistor

Determining the photocurrent generated in the sample by measuring the voltage change across a sense resistor was more straightforward than measuring the voltage change across the sample, because unlike the sample resistance, the resistance of the sense resistor remains constant upon illumination of the sample. The current through the sample and the sense resistor, which are connected in series, is the same. The applied bias voltage is split between the two. The resistance of the sense resistor was chosen to be as small as possible in order to maximize the sample bias at a given bias voltage. A power resistor with $R = 10\ \Omega$ was used, which is able to dissipate the power in the circuit without changing resistance through heating. The I-V of the device is determined by:

$$I_{sample}(V_{sample}) = I_{sense}(V_{sample}) = \frac{V_{sense}(V_{sample})}{R_{sense}}$$

with the sample bias being

$$V_{sample} = V_{bias} - V_{sense}$$

4.4.2 Results

Prior to measuring the photocurrent of spiked silicon, the device was characterized by measuring its resistance at zero-bias. All devices had a resistance of about $R = 350 - 400\ \Omega$ in the absence of illumination.

Comparison of spiked silicon to flat silicon

The photocurrent of the device as a function of sample bias ($I_{spikes/flat}(V_{sample})$) was determined by subtracting the measured current at a given sample bias in the absence of illumination ($I_{dark}(V_{sample})$) from the current measured upon illumination of the spiked part and the flat part of the device respectively at that sample bias ($I_{light}(V_{sample})$).

$$\begin{aligned} I_{spikes/flat}(V_{sample}) &= I_{light}(V_{sample}) - I_{dark}(V_{sample}) \\ &= \frac{V_{sense,light}(V_{sample}) - V_{sense,dark}(V_{sample})}{R_{sense}} \end{aligned}$$

SIONYX1403000044.0112

SAMSUNG EX. 1002 - 930/4148

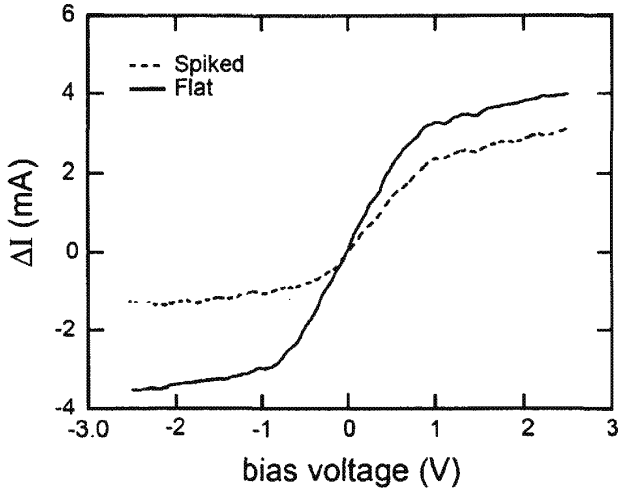


Figure 4.9: Photocurrent as a function of sample bias upon illumination of the flat part (solid line) and upon illumination of the spiked part (dashed line) of the device.

Figure 4.9 shows the I-V curves of the device upon illumination of the spiked part of the sample and upon illumination of the flat part of the sample. The I-V characteristics of the device reflects the presence of two Schottky barriers (one on the front side and one on the backside of the device) as discussed in Sec. 4.3. The response of the device is not perfectly symmetric, because the front grid and the back electrode are not equal (for example, the front electrode has a higher contact resistance than the back electrode because it has a smaller contact area.)

We determined the relative change in photocurrent $\frac{\Delta I}{I_{flat}}$ when illuminating the spiked part of the sample compared to that when illuminating the flat part at maximum sample bias according to

$$\frac{\Delta I_{spikes-flat}}{I_{flat}} = \frac{I_{spikes}(V_{sample,max.}) - I_{flat}(V_{sample,max.})}{I_{flat}(V_{sample,max.})}$$

Before hydrogenation, the device measures less photocurrent when illuminating the spiked part than when illuminating the flat part.

SIONYX1403000044.0113

SAMSUNG EX. 1002 - 931/4148

4.4.3 Effects of hydrogenation

The I-V characteristics changed significantly after hydrogenation. Results are reported for two samples which were processed under the same hydrogenation conditions. The power of the plasma was 30 W and the sample temperature during hydrogenation was 200°C. Both samples were hydrogenated multiple times. Table 4.2 summarizes the hydrogenation times and the resulting change in photocurrent, where t_h denotes the number of hydrogenation hours of one run and $t_{h-total}$ the total number of hydrogenation hours for the sample. After hydrogenation, the I-V characteristics of both devices became more asymmetric. The increasing asymmetry of the device with increasing hydrogenation is likely due to hydrogen diffusion into the electrode-semiconductor interface, which changes the contact resistance. If the front grid is forward biased, the increased contact resistance does not influence the flow of carriers much. However, if the front grid is reverse biased, the change in constant resistance reduces the flow of carriers, hence less photocurrent is detected. The change in photocurrent of the device generated by illuminating the spiked part compared to illuminating the flat part increased with hydrogenation time. For a hydrogenation time exceeding 30 hours, roughly 50% more photocurrent is produced when illuminating the spiked part of the device than when illuminating the flat part. The change in photocurrent also depends on the biasing direction. It is larger when the front electrode is connected to the positive voltage terminal (forward bias of front diode). The two samples show good agreement in $\frac{\Delta I}{I_{flat}}$ with hydrogenation time. In Fig. 4.10 the increase in photocurrent is plotted as a function of hydrogenation time.

Table 4.2: Effects of hydrogenation

Sample	t_h [hrs]	$t_{h-total}$[hrs]	$\frac{\Delta I_{rev.bias}}{I_{flat}}$	$\frac{\Delta I_{forw.bias}}{I_{flat}}$
A	0	0	-0.16	-0.60
A	4	4	-0.8	0.8
A	6.7	10.7	0.10	0.16
A	20	30.7	0.40	0.48
B	0	0	-0.17	-0.58
B	6.7	6.7	-0.4	0.14
B	12	19.7	0.17	0.31

Figure 4.11 shows the I-V curves for device B when the microstructured side of the device was illuminated and when the flat part is illuminated (a) before hydrogenation, (b) after 7 hours hydrogenation, and (c) after 19 hours of hydrogenation. Before hydrogenation

SIONYX1403000044.0114

SAMSUNG EX. 1002 - 932/4148

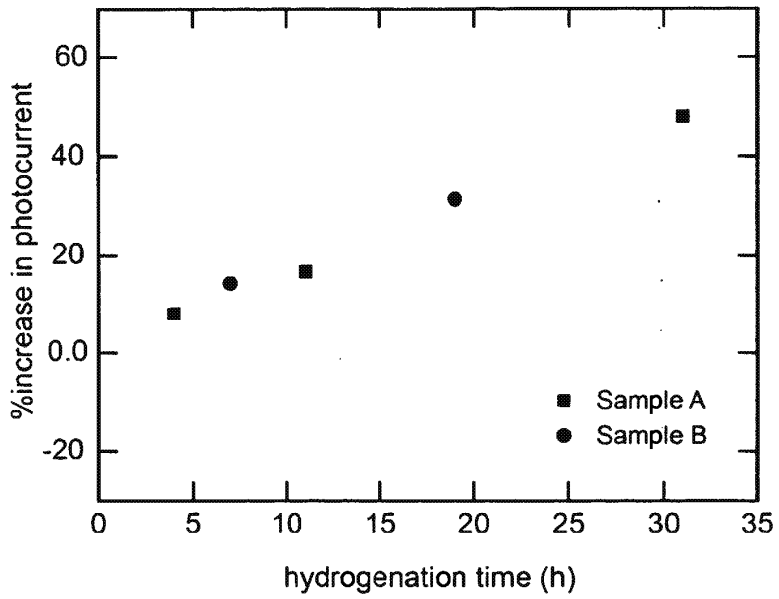


Figure 4.10: Increase in photocurrent as a function of hydrogenation time. The values are shown for forward biasing the front diode.

there is less than 20% measurable photocurrent produced in spiked silicon than in flat silicon when forward biasing the front diode. The hydrogenation changes the photocurrent upon illuminating the spiked part: After 7 hours of hydrogenation the photocurrent is about the same and after 19 hours there is an increase of about 30% when illuminating the spiked part of the sample than when illuminating the flat part in forward biasing the front diode. It is noteworthy that hydrogenation does modify the surface morphology. The spikes are sharpened and thinned by the treatment. The bombardment with a hydrogen plasma leaves a less regular structured surface behind. Figure 4.12 shows the surface of sample A after 30 hours of hydrogenation.

SIONYX1403000044.0115

SAMSUNG EX. 1002 - 933/4148

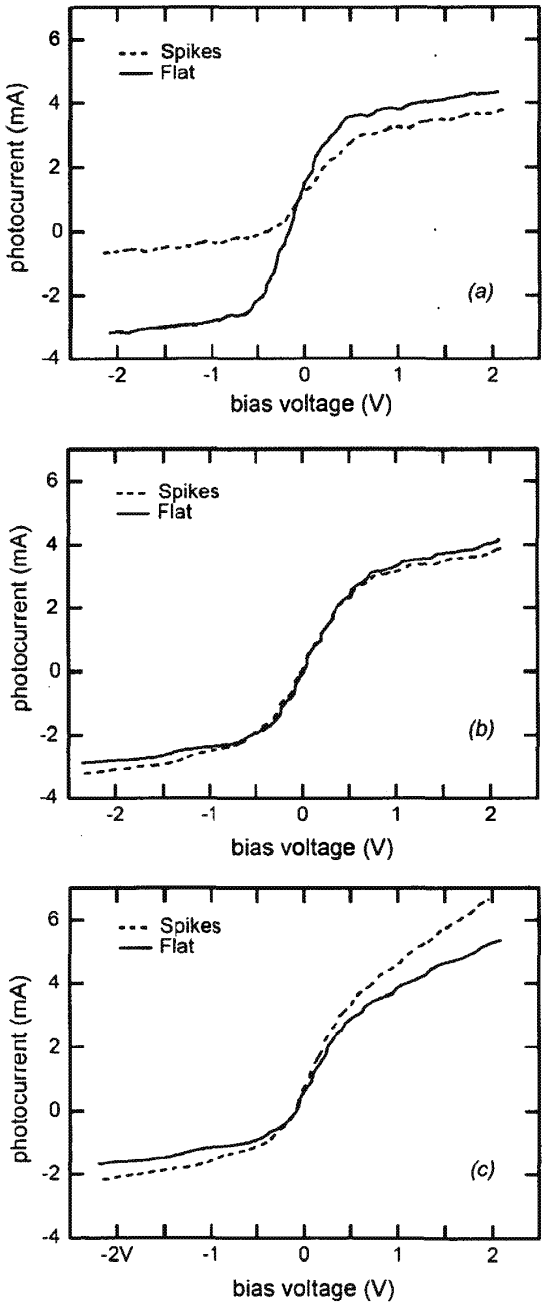


Figure 4.11: Comparison of photocurrent obtained by illuminating spiked silicon and by illuminating flat silicon of sample B: (*a*) before hydrogenation, (*b*) after 7 hours of hydrogenation, and (*c*) after 19 hours of hydrogenation.

SIONYX1403000044.0116

SAMSUNG EX. 1002 - 934/4148

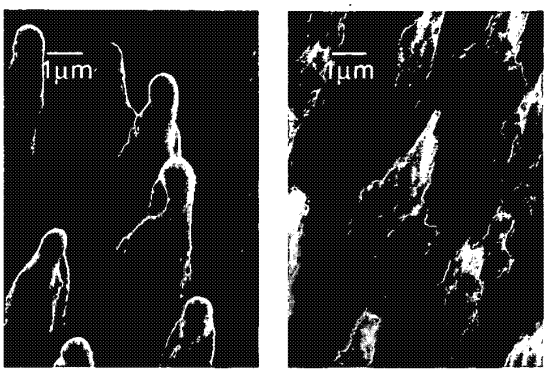


Figure 4.12: Spiked surface (*a*) before and (*b*) after 7 hours of hydrogenation. After exposure to the hydrogen plasma the spikes have been sharpened and thinned.

4.5 Below-bandgap photocurrent from microstructured avalanche photodiodes

4.5.1 Avalanche photodiodes (APD)

An APD is a strongly biased photodiode and is several orders of magnitudes more sensitive than ordinary photodetectors. In an APD, photocarriers produced by absorption of photons, are multiplied in an avalanche process [101]: A high reverse bias (typically > 1000 V) provides a strong electric field in the junction region. Photocarriers entering the region are accelerated in the high electric field. If the acquired energy is larger than the band gap energy, these carriers can create additional electron-hole pairs by impact ionization. The generated carriers can produce more carriers if the energy they acquire in the electric field is sufficient. The result is a cascade of carriers. Typically, one photon can create several thousand electron-hole pairs in an APD.

Quantum efficiency of ordinary APDs

The quantum efficiency of ordinary silicon avalanche photodiodes drops rapidly towards zero for wavelengths longer than 1 μm due to the absorption edge of silicon at 1.1 μm(see Chapter 4, Sec. 3.3). Figure 4.13 shows the quantum efficiency of a $1x1$ mm^2 APD pixel fabricated by Radiation Monitoring Devices [5] as a function of illumination wavelength. At 1.06 μm, the quantum effciency is 22 % and drops quickly to below 1 % for

SIONYX1403000044.0117

SAMSUNG EX. 1002 - 935/4148

longer wavelengths.

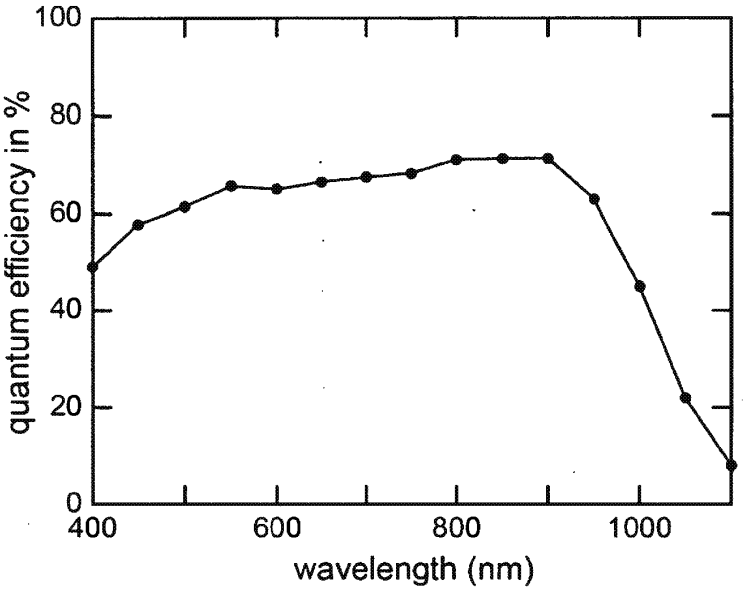


Figure 4.13: Quantum efficiency of a 1x1 mm^2 APD pixel as a function of illumination wavelength. [5]

4.5.2 Increase in below-band gap quantum efficiency of microstructured APDs

In collaboration with Radiation Monitoring Devices, spikes were produced on the light-collecting surface of a silicon avalanche photodiode (APD). The APDs were specially designed to test below-band gap photocurrent from the spiked surface. The APDs were not passivated neither by hydrogenation nor by oxide stripping. We microstructured one half (1x2 mm) of the light-collecting surface and left half unstructured. The response of the device was measured upon illumination with light from a pulsed Nd:YAG laser (1.06 μm) and with light from a 1.31 μm laser diode (continous wave, chopped at 100 Hz) of the microstructured and flat parts respectively. The laser beam was focussed with a 0.05 m focal length lens onto the sample such that an area of < 0.2 mm^2 was illuminated. The light was chopped via triggering of the laser diode with a TTL wave produced with a function generator.

SIONYX1403000044.0118

SAMSUNG EX. 1002 - 936/4148

The structured APDs show a more than threefold increase in quantum efficiency of radiation at 1.06 μm and 1.31 μm. Figure 4.14 compares the response of the device to irradiation to 1.31 μm upon illumination of the flat and spiked parts respectively.

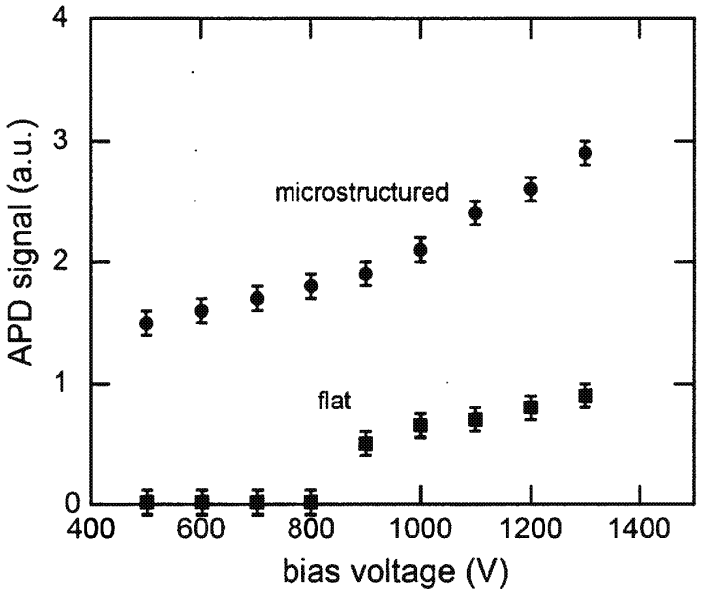


Figure 4.14: APD signal from illuminating the spiked and the flat parts of the device respectively with 1.31 μm light. Data were taken in collaboration with Radiation Monitoring Devices. [5]

4.6 Discussion

Effects of hydrogenation

The results presented in this chapter confirm that spiked silicon contains a high density of defects: Despite the higher absorptance of spiked silicon than that of flat silicon, there is less photocurrent from illuminating the spiked part than when illuminating the flat part of the photodetector in an unpassivated device. The defects that cause recombination of electrons and holes, could be associated with dangling bonds, because hydrogenation, which ties up dangling bonds, changes the photovoltaic characteristics of spiked silicon drastically; the photocurrent measurements after hydrogenation of the device show that hydrogenation

SIONYX1403000044.0119

SAMSUNG EX. 1002 - 937/4148

of the spiked surface for several hours causes an increase in the measured photocurrent as high as 48% when comparing illuminating the spiked part to the flat part. Therefore, spiked silicon can exhibit a strong increase in quantum efficiency of converting light into electric current after hydrogenation of the surface for several hours. It is noteworthy, that hydrogenation also changes the surface structure; the tall silicon spikes are transformed into much thinner and sharper spikes.

Detection of below-band gap radiation

Especially interesting is the response of the spiked APDs to below-band gap radation. Despite the strong recombination of electron-hole pairs in spiked silicon, the structured APDs show a more than threefold increase in quantum efficiency for detecting light of both 1.06 μm and 1.31 μm wavelength. These results indicate, that spiked silicon can detect below-band gap radiation and therefore may be used to extend the wavelength range of existing photovoltaic devices. Further improvements and optimization of the quantum efficiency need to be made in order to verify the application of spiked silicon for infrared detection. The results at 1.06 μm and 1.31 μm, however, are promising and may lead the way to a revolutionary new technology to produce silicon photodetectors for the infrared. Of special importance would be the integration of silicon photodetectors for the infrared into existing microelectronics. The high density of both structural and chemical defects could lead to high-speed devices, because recombination of generated carriers can significantly shorten the electrical signal. Time-resolved measurements are needed to measure the lifetime of excited carriers in spiked silicon.

SIONYX1403000044.0120

SAMSUNG EX. 1002 - 938/4148

Chapter 5

Visible photoluminescence of silicon laser-structured in air

5.1 Introduction

Does the strong light absorption and the recombination of generated carriers in spiked silicon lead to enhanced light-emission? Inspired by this question, we tested the spiked surfaces for luminescence (the radiative recombination of electron-hole pairs) in the visible and the infrared. The spikes do not show any enhanced luminescence in the near-infrared (1.0 μm $< \lambda <$ 1.7 μm) except for the 1.12 μm luminescence peak of untreated, crystalline silicon at room temperature. However, unlike untreated silicon, spiked silicon luminesces strongly in the visible, easily seen by eye. The peak wavelength and the intensity of the luminescence depend on the laser conditions used to structure the surface. When we irradiate silicon in air rather than in SF_6, which also produces a textured, however not spiked surface (see Chapter 2, Sec. 2.3.3), we observe a similar, but greatly enhanced luminescence from the patterned surface. Given the strong luminescence from these surfaces, we studied photoluminescence of silicon laser-irradiated in air.

The chapter is organized as follows: I first elaborate on the importance of luminescent silicon to technology and introduce substochiometric silicon dioxide, SiO_x with $x < 2$, as a luminescent form of silicon in Sec. 5.2. In Sec. 5.3 I describe the conditions for producing luminescent samples with femtosecond laser pulses and the experimental procedure for measuring photoluminescence. Sec. 5.4 presents the results of the photoluminescence mea-

SIONYX1403000044.0121

SAMSUNG EX. 1002 - 939/4148

surements. In Sec. 5.5 I discuss these results and propose mechanisms for the luminescence. Finally, I briefly comment on applications of laser-structured silicon in Sec. 5.6.

5.2 Technological importance of luminescent silicon

Silicon is the material of choice for most microelectronic applications and is at the heart of today's information and communication technology. Despite being a superior material for electronic applications, it is not of comparable importance for optical and electro-optical applications, [102] because silicon is a very poor light emitter. The emission of a photon results from radiative recombination of electrons and holes; energy and momentum must be conserved in this process. Since the band gap of silicon is indirect, electrons and holes are located at different positions in the Brillouin zone and therefore photon emission is only possible with the simultaneous absorption or emission of a phonon. Light emission in silicon is therefore a higher-order process. Since electron-hole pairs combine via a number of competing channels (see Chapter 4, Sec. 4.2), radiative recombination in silicon is much less efficient than in a direct-band gap semiconductor such as GaAs.[1]

However, the integration of optical and electronic components on a single silicon wafer would be highly desirable. Many attempts have been made to improve silicon's light emission efficiency through strategies such as band gap engineering (altering the bandgap through zone folding in superlattices) or defect engineering (introduction of isoelectronic defects into silicon, which confine electrons and holes to a small volume, hereby decreasing the nonradiative recombination to zero). [15] In some cases light-emission efficiencies of up to 10 % have been achieved by these methods. In 1990, Canham's [103] discovery of light-emission from porous silicon, a mesh of nanometer-sized silicon pores, led to an explosion of interest and intensive research. The use of porous silicon posed a number of problems for practical applications, however: Porous silicon is fragile and highly reactive, oxidizing spontaneously in air. In addition, the light emission is unstable and degrades with time. As a result, it is now commonly agreed that porous silicon is not a suitable material for electro-optic applications.

[1] Silicon's light-emission efficiency is an order of 10^{-5} smaller than that of GaAs, which is the main material used in light-emitting semiconductor devices.

SIONYX1403000044.0122

SAMSUNG EX. 1002 - 940/4148

Luminescence from SiO_x

Recently, another light-emitting silicon-based material has begun to generate considerable interest. Substochiometric silicon dioxide, SiO_x with $x < 2$, consists of silicon nanocrystals embedded in SiO_2. It exhibits light emission properties similar to porous silicon, but is chemically stable and much less fragile. The luminescence characteristics depend on the sample preparation conditions and the luminescence bands range throughout the visible spectrum. The origin of the luminescence in SiO_x is not yet clear. Possibilities include point-like defects [104, 105], extended defects [106], radiative decay of self-trapped excitons [107], quantum confinement within silicon nanoclusters [104], and recombination near the $Si_{nc} - SiO_2$ interface. [106]

There are several methods by which luminescent SiO_x can be produced: implantation of Si^+ into silica [108, 109], implantation of oxygen into silicon [110, 111], plasma-enhanced chemical vapor deposition [112, 113, 114], and co-sputtering of oxygen and silicon. [115, 116] Laser-induced formation of porous SiO_x by irradiation of single-crystal silicon in air with ns laser pulses at 532 nm has been reported by Dimova-Malinovska *et al.* [117] Laser-induced formation of luminescent silicon has significant advantages over ion implantation, sputtering, or CVD, because the laser permits precise patterning of luminescent areas without the need for masks.

Silicon oxidizes spontaneously in air to form a thin native oxide layer of 1-10 nm thickness. Oxidation proceeds via direct reaction of oxygen atoms or molecules with the surface atoms or simply through diffusion. Surface oxidation of silicon upon laser irradiation in an oxygen-rich atmosphere is a well-known phenomenon. [118, 119, 120, 121] Irradiation can enhance diffusion of oxygen into the silicon substrate and enhance oxidation by raising the surface temperature (and perhaps melting) or, if the laser fluence exceeds the breakdown threshold of the ambient atmosphere, creates a plasma which excites reactants. Oxide layers of up to more than 1 μm thickness have been reported using laser-enhanced oxidation of silicon surfaces. [118]

The luminescence we observe is most likely from SiO_x produced by the laser (see Sec. 5.5.1). The luminescence disappears when the surfaces are dipped in HF, which removes oxidized silicon. We observe no luminescence when silicon is structured in vacuum.

SIONYX1403000044.0123

SAMSUNG EX. 1002 - 941/4148

5.3 Experiment

5.3.1 Fabrication of luminescent silicon samples

Microstructured, luminescent silicon was made in similar fashion to spiked silicon. Si(111) samples of resistivity $\rho = 800 - 1200\ \Omega$ cm were cleaned in a 10-minute trichlorethylene bath, followed by a 10-minute ultrasonic acetone bath, followed by a 10-minute ultrasonic methanol bath. The samples were placed on the computer-controlled translation stage in the vacuum chamber described in Chapter 2, Sec. 2.2. Patches of microstructured silicon were made by translating the sample while illuminating it with the laser beam. We used 100-fs laser pulses at 800 nm at a repetition rate of 1 kHz to pattern the samples in air. After patterning, the samples were viewed under the scanning electron microscope and analyzed with Rutherford Backscattering Spectrometry. Three series of samples were produced (series A, series B, series C) under the following conditions:

- Series A: Variation of laser fluence

  In series A, 4 samples were patterned using fluences of 2.5 kJ/m^2, 5 kJ/m^2, 10 kJ/m^2, and 30 kJ/m^2 respectively. The laser scan speed was 50 μm/s.

- Series B: Variation of number of laser shots

  In series B, the average number of laser shots per unit area was changed by varying the sample translation velocity and the number of scans over the samples. The average number of laser shots per unit area decreases with increasing scanning speed and increases with increasing number of scans.[2] Two samples were produced with a single scan using a laser spotsize of 100 μm and a scan velocity of 100 μm/s ($n_{av} = 1000$) and 50 μm/s ($n_{av} = 2000$) respectively. Two more samples were made by scanning over the sample twice using the same laser spot size with a scan velocity of 50 μm/s ($n_{av} = 4000$) and 100 μm/s ($n_{av} = 2000$) respectively. For all samples the fluence used was 2.5 kJ/m^2.

[2]The average number of laser pulses per unit surface area is roughly

$$n_{av} = \frac{S}{v} f N$$

where S is the laser spotsize, v the scan velocity, f the repetition rate of the laser and N the number of scans.

SIONYX1403000044.0124

SAMSUNG EX. 1002 - 942/4148

- Series C: Annealing

  In series C, two sets of samples were patterned using a scan velocity of 100 μm/s. Four of these samples were produced using a fluence of 7.5 kJ/m^2 (series C_1) and 4 samples were produced using a fluence of 15 kJ/m^2 (series C_2). After patterning, one sample of each set was annealed at 1300 K in vacuum ($P = 10^{-7}$ Torr) for 30 minutes, 60 minutes, and 3 hours respectively. The remaining two samples were not annealed and served as reference samples. In addition, the sample from series A made with a fluence of 30 kJ/m^2 and a scan speed of 50 μm/s was annealed for 5 hours at 1300 K.

5.3.2 Photoluminescence measurements

Photoluminescence measurements in the visible were carried out using a Spectra Physics 171 cw Ar ion laser (50-mW power) as the excitation source. An Oriel interference filter singled out the 488 nm line from the laser. The photoluminescence was measured from 500 nm–800 nm. A homemade stepper motor enabled a 0.6 nm resolution. The luminescence and the scattered light was dispersed in a double monochromator spectrometer (Spex model 1400) and measured with a thermo-electrically cooled GaAs photomultiplier tube (RCA C31034-A02) using a Princeton Applied Research discriminator (model 1121) and photon counter (model 1109). All data were taken at room temperature in air. The setup used to measure visible luminescence is illustrated in Fig. 5.1.

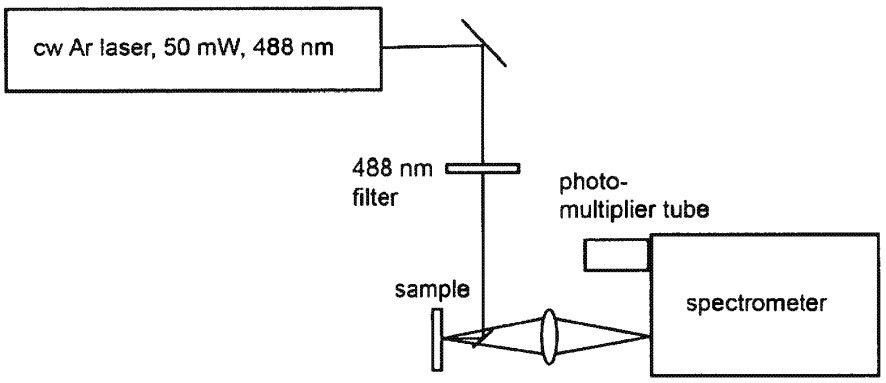


Figure 5.1: Experimental set-up for measuring photoluminescence.

SIONYX1403000044.0125

SAMSUNG EX. 1002 - 943/4148

5.4 Results

5.4.1 Series A: Effects of laser fluence

Figures 5.2a-e show the series A samples as seen under the SEM at a 45° angle. As the fluence used to structure the surface increases from 2.5 kJ/m^2 to 30 kJ/m^2, the surface morphology changes from a rippled structure to cones. Noteworthy here is that the structures are covered with many nanometer-scale particles (hereafter "nanoparticles"). These particles could be silicon aggregates produced during material removal of the surface and then redeposited.

Figure 5.3a shows the photoluminescence of the samples from series A. We observe a green luminescence band centered at around 560 nm. The photoluminescence intensity increases with increasing laser fluence while the peak wavelength does not vary.

Rutherford Backscattering Spectrometry reveals that the oxygen content of the samples increases with increasing laser fluence; the RBS spectra for the four samples appear in Fig. 5.3b. The increase in oxygen content is indicated both by the growth of the oxygen peak and the decrease of the silicon signal (which includes both the silicon surface and the background signal). Simulation of the RBS spectra with the program RUMP [122] shows that the oxygen concentration decreases with depth. Figure 5.4a shows the fit for the sample made with 30 kJ/m^2 fluence. The fit was produced using a layered profile with a decrease in oxygen concentration with increasing depth. The profile details of this simulation are given in Table 5.1. Column 2 shows the atomic ratio of oxygen to silicon in the layers. Plotting the photoluminescence intensity versus surface oxygen concentration of the four samples made with different laser fluence, yields a linear dependence of the luminescence

Table 5.1: Fit profile details for sample made with 30 kJ/m^2 fluence. All layers have a thickness of 300 nm.

Layer No.	O/Si
1	0.81
2	0.66
3	0.53
4	0.42
5	0.33
6	0.28
7	0.21
8	0.11

SIONYX1403000044.0126

SAMSUNG EX. 1002 - 944/4148

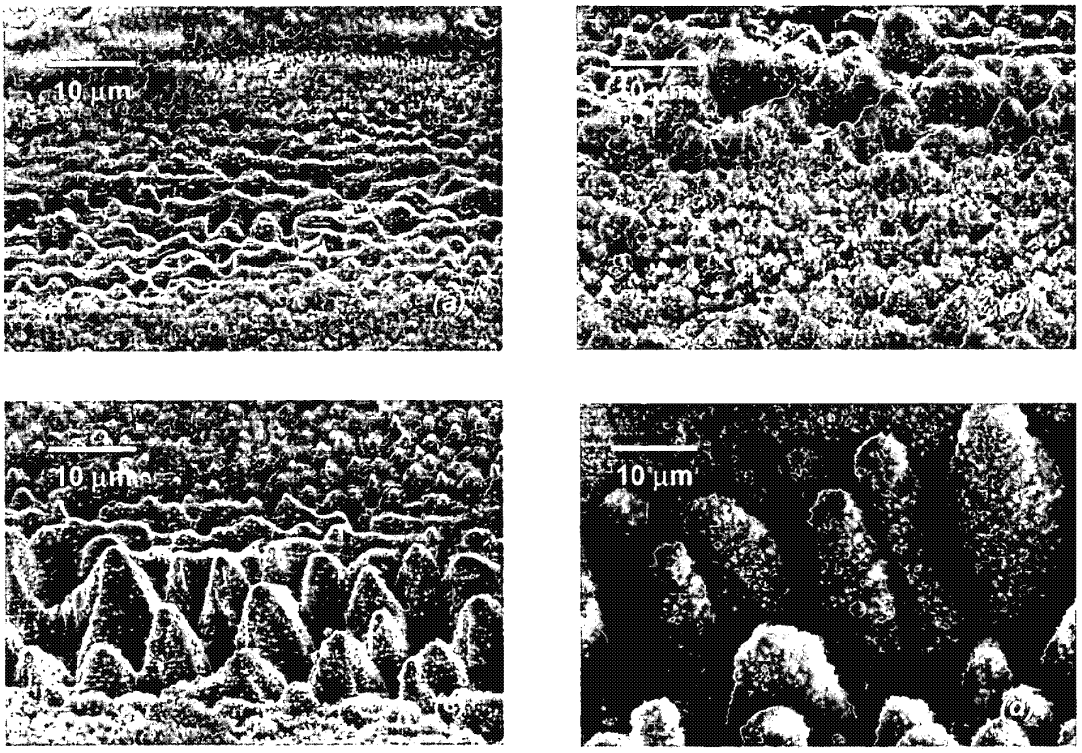


Figure 5.2: Surfaces made with laser pulses of fluence (*a*) 2.5 kJ/m^2, (*b*) 5 kJ/m^2, 10 kJ/m^2, and (*d*) 30 kJ/m^2, as seen under the scanning electron microscope at a 45° view.

SIONYX1403000044.0127

SAMSUNG EX. 1002 - 945/4148

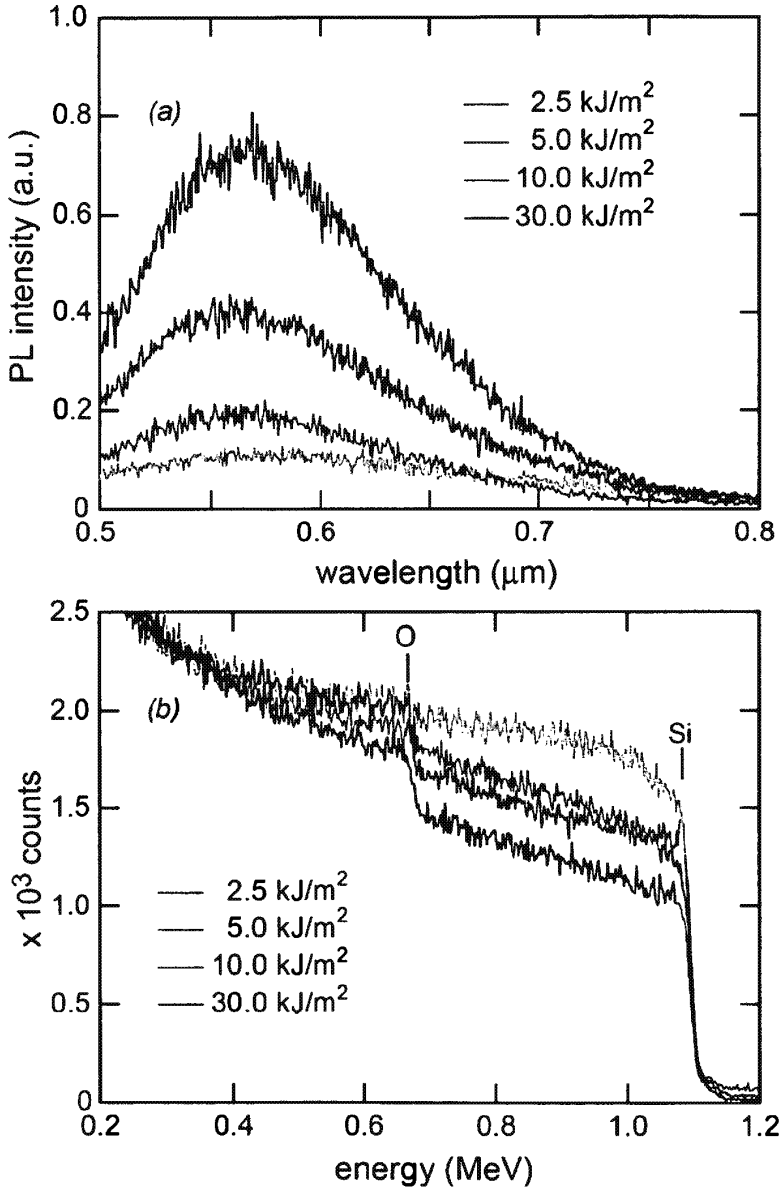


Figure 5.3: (*a*) Photoluminescence of samples made with laser pulses of fluence 2.5 kJ/m^2, 5.0 kJ/m^2, 10.0 kJ/m^2, and 30.0 kJ/m^2, (*b*) RBS spectra of the surfaces showing increasing oxygen content in the samples with increasing laser fluence used to produce the samples.

SIONYX1403000044.0128

SAMSUNG EX. 1002 - 946/4148

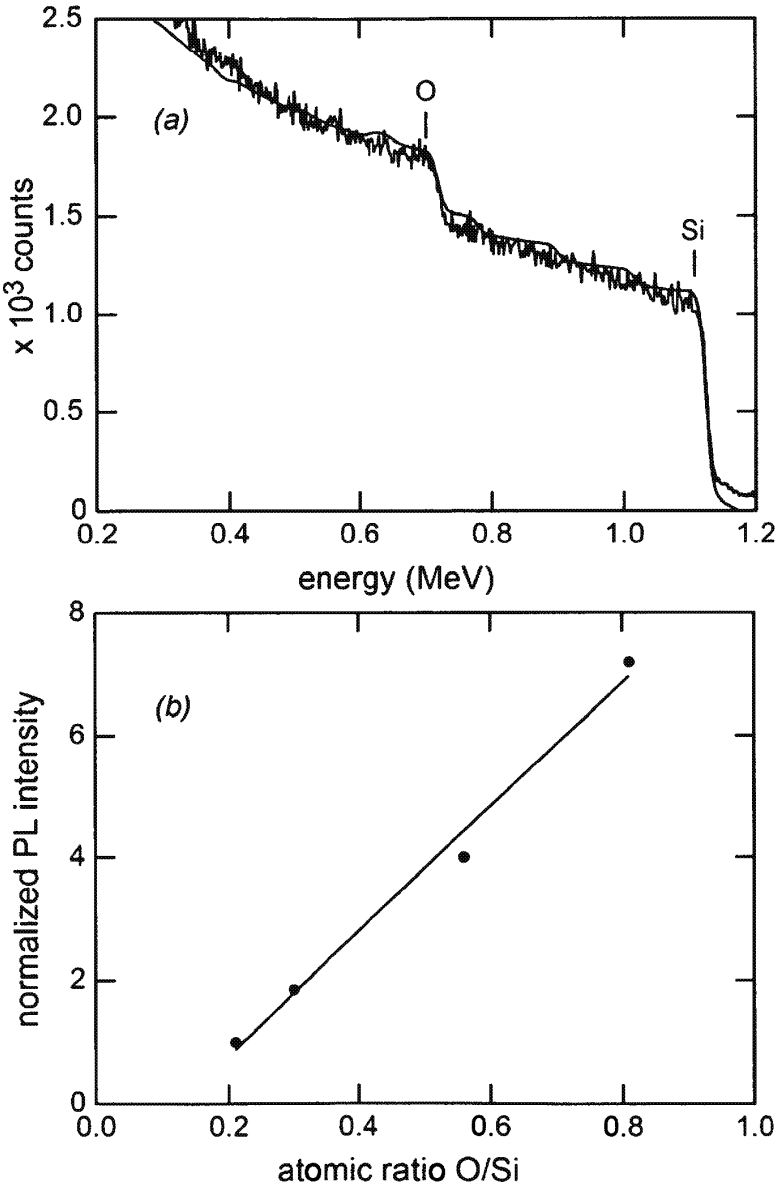


Figure 5.4: (*a*) Computer simulation of RBS spectrum of surface made with 30 kJ/m^2, (*b*) photoluminescence intensity as a function of measured surface oxygen concentration. Normalization of the photoluminescence intensity is made to the sample produced at $F = 2.5$ kJ/m^2.

SIONYX1403000044.0129

SAMSUNG EX. 1002 - 947/4148

intensity on surface oxygen content. Figure 5.4b shows the photoluminescence intensity of the four samples (normalized to that of the 2.5 kJ/m^2 sample) versus surface oxygen concentration.

5.4.2 Series B: Effects of laser shot number

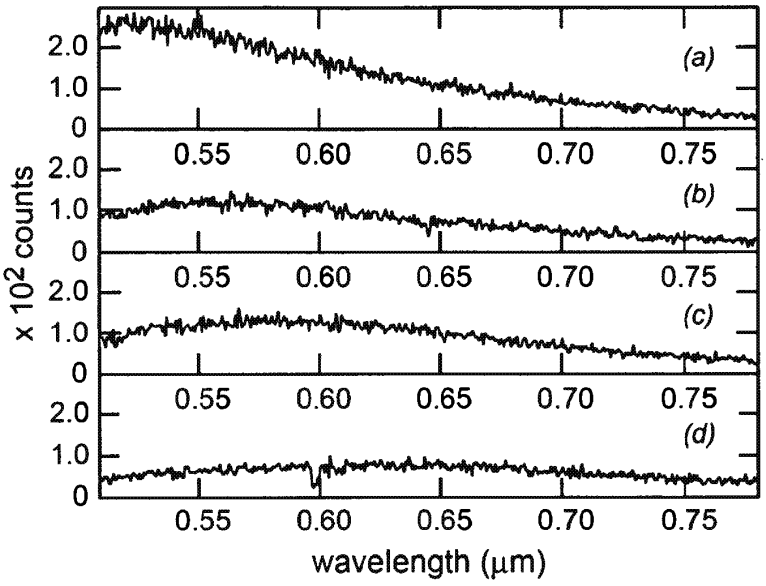


Figure 5.5: Photoluminescence of samples made with different laser shot number/unit surface area (series B). (*a*) Sample made with 50 μm/s and 2 scans, (*b*) 50 μm/s and a single scan, (*c*) 100 μm/s and two scans, and (*d*) 100 μm/s and a single scan.

Figure 5.5 shows the photoluminescence obtained from the samples made with different numbers of laser shots per unit surface area. The laser peak wavelength blue-shifts with increasing exposure to laser pulses. The photoluminescence peak wavelength is 520 nm using a velocity of 50 μm/s and scanning twice over the samples, 540 nm using the same velocity and a single scan, 560 nm using a velocity of 100 μm/s and two scans, 630 nm using a velocity of 100 μm/s and a single scan.

SIONYX1403000044.0130

SAMSUNG EX. 1002 - 948/4148

5.4.3 Series C: Effects of annealing

Annealing changes the photoluminescence spectra drastically. Figure 5.6a shows the photoluminescence spectra of series C_2 (F=15 kJ/m^2) before annealing and after annealing for 0.5 hour, 1 hour, and 3 hours in 1300 K respectively. Prior to annealing, the spectrum exhibits a red band centered at 630 nm and no green band is visible. Three changes occur in the photoluminescence spectrum with increasing annealing time:

1. The photoluminescence intensity increases.
2. The red peak shifts to longer wavelengths.
3. A green luminescence peak appears and grows.

Figure 5.6b compares the photoluminescence of the samples made with F= 7.5 kJ/m^2 and F=15 kJ/m^2 after 3 hours anneal. The luminescence intensity of the sample made with F= 7.5 kJ/m^2 is lower than that made with F= 15 kJ/m^2, as is expected from the fluence dependence results of series A. This is unchanged by the anneal.

Unlike the samples from series C, the sample from series A exhibits a green band centered at 560 nm and no peak in the red before annealing. Figure 5.7a shows the photoluminescence after 5 hours of annealing in vacuum at 1300 K. The annealing increases the photoluminescence intensity of the green band by a factor of 4. This time, a red band appears upon annealing. Scanning electron microscopy of both series A and series C samples reveals that most of the nanoparticles are removed after annealing, leaving a much smoother surface. Figure 5.8 shows the surface of the sample from series A before and after 5 hours anneal.

SIONYX1403000044.0131

SAMSUNG EX. 1002 - 949/4148

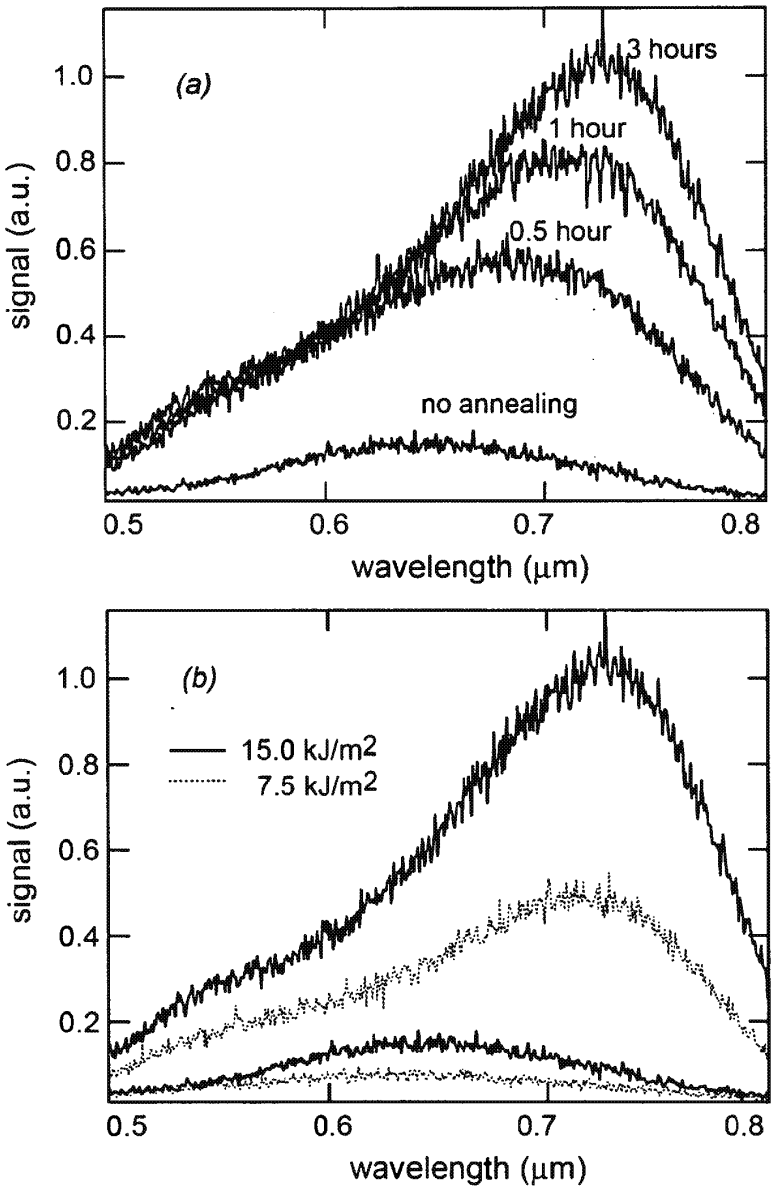


Figure 5.6: (*a*) Photoluminescence of series C_2 without annealing after 0.5 hour, 1 hour, and 3 hours of vacuum annealing at 1300 K, (*b*) comparison of the photoluminescence spectra of series C_2 and series C_1 after 3 hours of annealing.

SIONYX1403000044.0132

SAMSUNG EX. 1002 - 950/4148

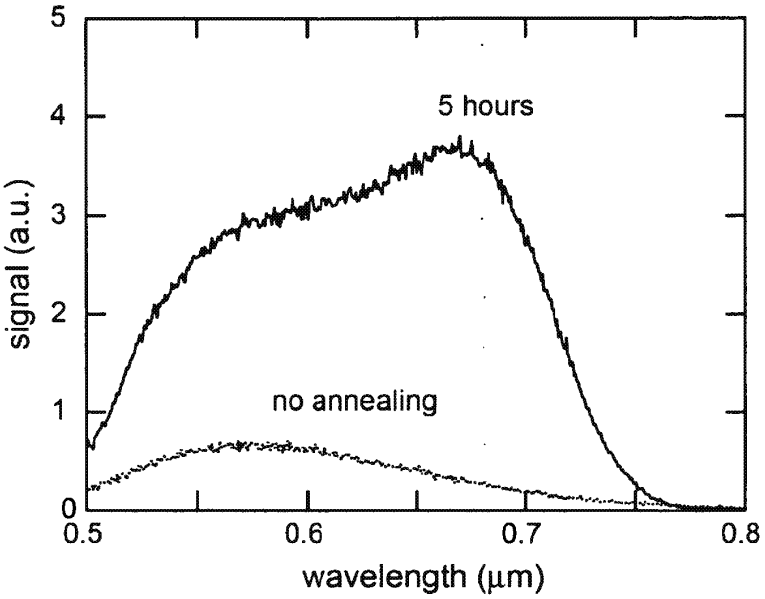


Figure 5.7: Photoluminescence of the sample from series A without anneal and after 5 hours anneal.

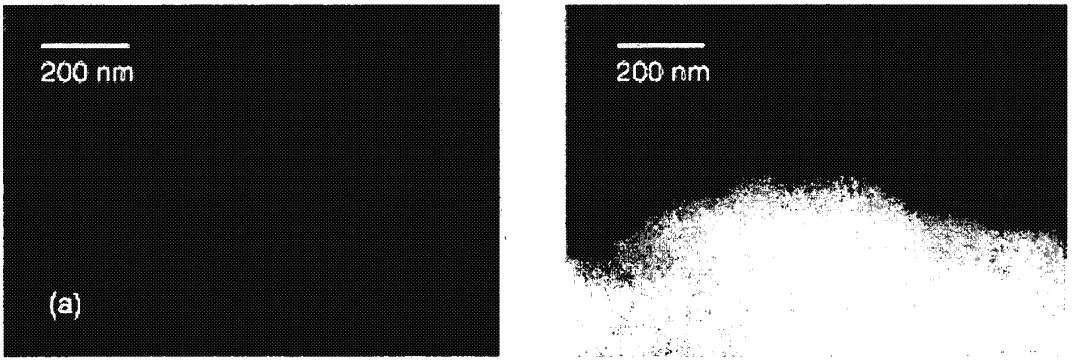


Figure 5.8: Surface of the sample from series A (*a*) before and (*b*) after 5 hours anneal as seen under the scanning electron microscope.

5.5 Discussion

5.5.1 Laser-induced formation of luminescent SiO_x

We created luminescent silicon by structuring the silicon surface in air with femtosecond laser pulses. The observed photoluminescence most likely stems from SiO_x layers

SIONYX1403000044.0133

SAMSUNG EX. 1002 - 951/4148

for the following reasons:

- The photoluminescence intensity increases with the oxygen content of the samples.
- The luminescence disappears after etching the samples in HF, which removes most of the oxidized surface layers.
- There is no visible luminescence when the surface is structured in vacuum ($P = 10^{-4}\ Torr$).

Though quantum confinement could also give rise to photoluminescence, we find that the photoluminescence is not necessarily associated with the surface nanoparticles found on the surface prior to annealing. After annealing, the photoluminescence intensity is enhanced, while many of the nanoparticles disappeared.

The luminescence characteristics of the SiO_x layer depend on the laser parameters used for structuring the surface.

Increase of oxygen content with increasing laser fluence (series A)

As shown by RBS, increasing the laser fluence increases the oxygen content in the samples. This may be associated with the fact that a higher fluence causes a greater increase in the surface temperature and a larger melt depth upon laser irradiation, because more energy is deposited in the surface during the duration of the laser pulse. The diffusion coefficient of oxygen in liquid silicon increases by six orders of magnitudes compared to that of solid silicon. [118] Therefore, with higher laser fluence, a thicker layer can be oxidized. The linear increase of the photoluminescence intensity with the oxygen content indicates that doubling the number of oxygen sites doubles the number of luminescence centers.

Shift of peak wavelength with number of laser shots (series B)

The number of laser shots per unit surface area to which the surface is exposed, is related to the oxidation time. In conventional thermal oxidation, the surface first oxidizes by forming SiO_x, which then gradually evolves into SiO_2 with increasing oxidation time. [123, 124] We observe a blue-shift of the photoluminescence peak with increasing number of laser shots. In comparison to thermal oxidation, the observed shift of the peak wavelength may be due to a changing stochiometry of SiO_2 with increasing number of laser pulses.

SIONYX1403000044.0134

SAMSUNG EX. 1002 - 952/4148

5.5.2 Origin of luminescence (series C)

Green luminescence band

A green-yellow photoluminescence band has been observed from SiO_x layers produced by plasma-enhanced chemical vapor deposition [104, 125] or implantation of Si^+ into layers of SiO_2. [106, 105] However, depending on the formation conditions of SiO_x, different luminescence characteristics are observed. Likewise, different explanations are given for the origin of the green luminescence band including point defects associated with oxygen vacancies or interstitials [105, 104] or extended defects in form of silicon chains [106] in the silica matrix.

The luminescence behavior of the green band that we observe from laser-structured silicon produced in series A resembles very much that of SiO_x produced by implantation of SiO_x into silica films as reported by Ghislotti *et al.* [106]: The photoluminescence is centered at 560 nm and its intensity increases upon annealing with longer anneal durations, while the peak wavelength remains unchanged. Ghislotti *et al.* associated the green luminescence band with luminescence from extended defects (such as chains of silicon atoms) in the SiO_2 matrix. The increase of the luminescence intensity upon annealing was explained by the removal of nonradiative recombination sites, which increases the probability for radiative recombination.

Luminescence from point-like defects such as oxygen vacancies or interstitials in laser-structured silicon is unlikely, because annealing at a temperature of 1300 K would remove those defects. Rather, the observed photoluminescence from laser-structured silicon increases in intensity with annealing. This suggests that either the number of radiative sites increases or the number of nonradiative sites decreases with annealing. A decrease of nonradiative sites at the boundaries of silicon chains, as suggested by Ghislotti *et al.*, would be consistent with the luminescence charactersitics that we observe.

Red luminescence band

A red luminescence peak from SiO_x films has been observed by several groups. [106, 105, 104, 125, 126] However, depending on the conditions under which the SiO_x was formed, some groups observe a red peak only after annealing, while others observe it from as-grown samples. In addition, a redshift of the peak wavelength with increasing temperature was reported by several groups [104, 109], while others do not observe a shift upon annealing.

SIONYX1403000044.0135

SAMSUNG EX. 1002 - 953/4148

[106, 105] The different luminescence characteristics of the red band suggest that more than one mechanism causes SiO_x to luminesce in the red.

We observe a red band from the samples as-made in series C (made at a scan velocity of 100 μm). The peak wavelength of the red band shifts to longer wavelength with increasing annealing time.

The luminescence of the red band likely stems from nanoclusters within the SiO_x matrix. The annealing behavior of the red band when annealing the samples from series C can be explained as follows:

The conditions under which the samples were produced may have created a SiO_x layer which consists partially of non-oxidized silicon islands. SiO_x becomes unstable when annealed at temperatures at 1000 K or above. [106] Silicon atoms diffuse within the SiO_x-matrix and can either increase the size of existing silicon clusters or form new ones. With increasing annealing time, the size of the clusters increases. This process is called "Ostwald ripening". [112, 104, 106] The shift of the red band towards longer wavelengths indicates, that the red luminescence is associated with luminescence from quantum confined silicon nanoclusters within the SiO_x layer. Quantum confinement causes a change in the band gap energy due to the confinement of atoms and molecules to nanometer-sized structures. [102] The smaller the volume to which the structures are confined is, the bigger the increase in band gap. Annealing causes the structures to grow in size by "Ostwald ripening". Thus, if luminescence is due to quantum-confined species, annealing would cause a redshift of the luminescence peak wavelength. Our results are therefore consistent with attributing the red luminescence band to quantum confined structures. Luminescence from quantum-confined structures could also explain the appearance of the red luminescence peak when annealing the sample from series A (made at a scan velocity of 50 μm/s). The slower scan speed (and therefore the increased number of laser shots) may have led to a complete oxidization of the surface, not leaving any silicon islands. The lack of silicon nanoclusters may explain the absence of a red luminescence peak. Upon annealing, silicon diffuses within the SiO_x to form silicon nanoclusters, which may give rise to the appearance of the red luminescence shoulder.

The increase in luminescence intensity with annealing could be due to the fact that oxygen evaporates from the silicon surface as the sample is annealed at 1300 K. I propose that as more and more oxygen leaves the surface, more silicon clusters are formed, which gives rise to the increased luminescence intensity.

SIONYX1403000044.0136

SAMSUNG EX. 1002 - 954/4148

5.6 Applications

An important aspect of producing luminescent SiO_x with a laser is its potential for technological applications. Unlike other methods, it offers the possibility of precise, localized patterning of silicon chips without the use of masks or multi-step processing. In comparison to porous silicon, laser-structured silicon is mechanically and chemically stable. In addition, the luminescence can be controlled with the laser parameters: The luminescence intensity depends on the laser fluence and the peak wavelength on the number of laser shots per unit surface area.

Further research is needed to quantify quantum efficiency and material longevity. Finally, laser-structured silicon should be tested for electroluminescence, which would make this material all the more useful for electro-optic applications.

SIONYX1403000044.0137

SAMSUNG EX. 1002 - 955/4148

Chapter 6

Femtochemistry of CO and O_2 on Pt(111)

6.1 Introduction

The catalytic oxidation of CO from $CO/O_2/Pt(111)$ has been investigated for many decades, dating back to the work by Langmuir in 1922. [127, 128] Since it is a relatively simple reaction involving only a few reaction steps, it is a model reaction for the study of fundamental surface kinetics. In particular, the research has been driven by interest in this catalytic reaction because of its applications in the reduction of pollution. [127] Prior to 1989, most of the work investigated the formation of CO_2 from coadsorbed oxygen and carbon monoxide on platinum under thermal activation. [127, 129, 130] A few studies were also carried out investigating CO-oxidation from either adsorbed oxygen with CO-molecules supplied from the gas phase [131] or adsorbed CO under irradiation with an atomic oxygen beam. [132]

In 1989 Mieher and Ho [8] observed the formation of CO_2 from $CO/O_2/Pt(111)$ induced by UV light from an arc lamp. It was the first demonstration of a light-induced bimolecular reaction at a solid surface. Since then, several groups have studied the photochemistry of $CO/O_2/Pt(111)$ with continuous light from an arc lamp [133], nanosecond laser pulses [134, 135], and femtosecond laser pulses. [135, 136, 137]

Investigations of light-induced CO-oxidation from $CO/O_2/Pt(111)$ have focused on two major topics. One subject of interest is the excitation pathway leading to CO-

SIONYX1403000044.0138

SAMSUNG EX. 1002 - 956/4148

photo-oxidation. Illumination with intense femtosecond laser pulses creates highly excited electrons in the substrate. Once these electrons thermalize, their temperature can exceed several thousand Kelvin. The strongly excited electrons, both non-thermalized and thermalized, can induce chemistry that can differ considerably from that induced by low-intensity light sources.

Another subject of interest is the reaction pathway leading to CO_2 production from $CO/O_2/Pt(111)$. There is currently some debate about how CO_2 is formed. Oxidation of CO could proceed by dissociation of the oxygen molecule and subsequent reaction of CO with an oxygen atom. Another possibility is the formation of CO_2 by reaction of CO with an excited O_2 molecule via the formation of a transient CO_3-complex.

This chapter presents and discusses the results of surface photochemistry of carbon monoxide and oxygen coadsorbed on platinum induced by femtosecond laser pulses. In the first part of the chapter I discuss the excitation pathways leading to CO_2 production. I briefly describe the response of the substrate to photoexcitation in Sec. 6.2. In Sec. 6.3.2 I provide the results of the photochemistry of $CO/O_2/Pt(111)$ induced with low-intensity light sources. This is followed by the presentation of our work on photochemistry induced with femtosecond laser pulses in Sec. 6.3.3. In the final part of this chapter, Sec. 6.4, results of experiments are presented that investigate two possible reaction pathways to light-induced CO_2 production.

6.2 Photo-excitation at adsorbate-metal surfaces

When an adsorbate-metal system is irradiated with light, energy from the photons may be transferred to the adsorbate-metal system through direct excitation of the adsorbate or through electronic excitation of the substrate. Light absorption in the substrate leads to the generation of excited carriers, which can interact with the adsorbate inducing desorption, dissociation, or reaction with other adsorbates at the surface.

When light is incident on a metal, it is partially reflected and partially absorbed. Since in metals there is no energy gap between the valence and conduction bands, there is no minimum photon energy required for absorption (unlike for light absorption in semiconductors as discussed in Chapter 3). Upon photon absorption, an electron is excited into a higher-lying unoccupied level. Assuming that one photon excites a single electron and excluding multiphoton absorption, the initial density of states (DOS) is shifted by an

SIONYX1403000044.0139

SAMSUNG EX. 1002 - 957/4148

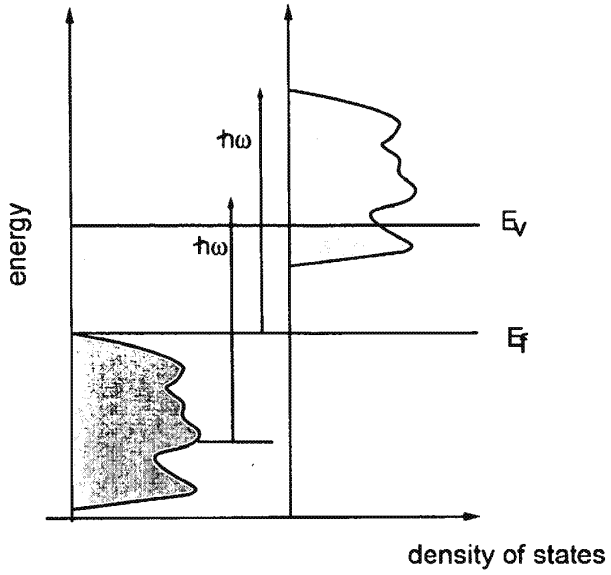


Figure 6.1: Nascent electron distribution after photoexcitation with photons of energy $\hbar\omega$. The density of states (DOS) is shifted by an energy $\hbar\omega$. E_f denotes the Fermi level and E_v the vacuum level. After Zhou and White [6]

amount of energy $E = \hbar\omega$ (the photon energy) if the transition probability is proportional to the DOS. [6] Figure 6.1 shows the excitation of electrons upon absorption of photons by the substrate. If the photon energy is larger than the surface work function, electrons can leave the metal. When the photon energy is lower than the surface work function, excited electrons remain in the metal and scatter off each other, relaxing to thermal equilibrium in $10^{-13} - 10^{-12}$s. [33, 138] Once they thermalize, they have a well-defined Fermi temperature T_f. The excited electrons (either non-thermalized or thermalized) can excite the adsorbate and induce photoprocesses. Excitation with non-thermalized electrons leads to photoprocesses for which the yields depend on the photon energy, because different photon energies cause a different shift of the density of states. Chemistry that is induced by thermalized electrons will depend only on the total energy absorbed and thus be photon-energy independent.

Besides equilibrating with each other through scattering, the electrons also scatter off phonons. The equilibration with the lattice is reached after several ps. [139] The response of a metal to subpicosecond laser pulses can be described by a set of coupled diffusion

SIONYX1403000044.0140

SAMSUNG EX. 1002 - 958/4148

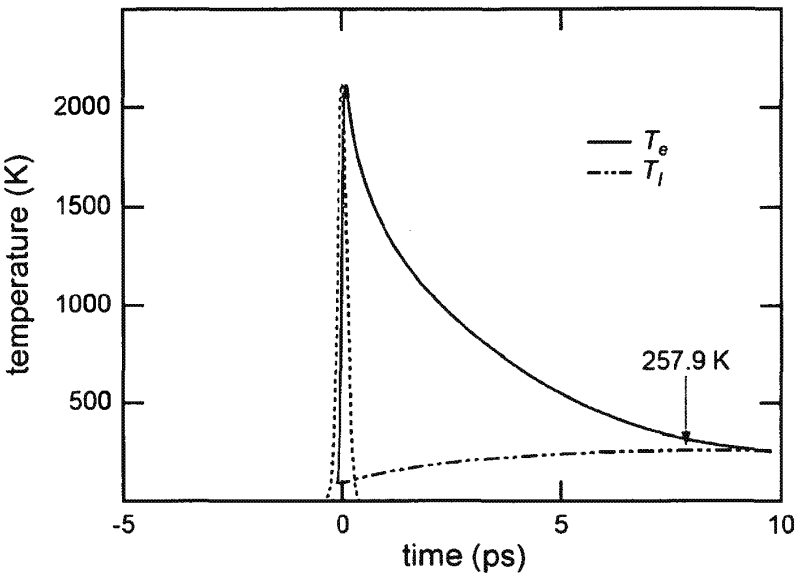


Figure 6.2: Calculated electron and lattice temperatures in platinum following 100 fs, 32 μJ/mm^2, 800 nm laser pulses. Shown as well is the profile of the laser pulse. [7]

equations. The temperature of the electrons and the temperature of the lattice evolve according to:

$$C_e(T_e)\frac{\partial T_e}{\partial t} = \kappa(T_e)\frac{\partial^2 T_e}{\partial x^2} - g(T_e - T_l) + A(x,t) \quad (6.1)$$

$$C_l(T_l)\frac{\partial T_l}{\partial t} = g(T_e - T_l) \quad (6.2)$$

where A(x,t) denotes the energy deposited by the laser, C_e and C_l the heat capacities of the electrons and the lattice, and g the coupling coefficient between electrons and phonons. [139] The electronic temperature reached with illumination of subpicosecond laser pulses is several thousand Kelvin, whereas the lattice remains much colder. These very high electronic temperatures, unique to excitation of the metal with subpicosecond laser pulses, open up new adsorbate-metal excitation and reaction pathways. [140] Figure 6.2 shows the evolution of the electronic and lattice temperatures following excitation with 800 nm laser pulses having a fluence of 32 μJ/mm^2. The initial temperature of the sample is 90 K. [7] It is important to note that this model assumes the electrons equilibrate with each other instantaneously (that they have a well-defined temperature at all times). However, as mentioned above, this is not really accurate. The absorption of photons initially creates

SIONYX1403000045.0001

SAMSUNG EX. 1002 - 959/4148

a non-thermalized electron distribution, which relaxes in a finite time. Therefore, this model is inaccurate for the time before the electrons have thermalized with each other (approximately the first 0.5 ps).

6.3 Photochemistry of $CO/O_2/Pt(111)$

6.3.1 Background

Carbon monoxide and oxygen coadsorbed on platinum have been well characterized using thermal desorption, vibrational spectroscopy (electron energy loss spectroscopy (EELS) and infrared reflection-absorption spectroscopy (IRAS)), and low energy electron diffraction (LEED). A summary can be found, for example, in reference [27].

Thermal Chemistry of $CO/O_2/Pt(111)$

Desorption of O_2 and formation of CO_2 from $CO/O_2/Pt(111)$ have been widely investigated using temperature programmed desorption (TPD) and temperature programmed reaction spectroscopy (TPRS). [129, 130, 141, 131, 142] In both TPD and TPRS, the substrate is heated at a constant rate while the species in the chamber are recorded with a mass spectrometer. In TPD, molecules desorb from the surface upon heating; in TPRS the adsorbates react to form new products prior to desorption.

We performed TPD for $CO/Pt(111)$ and $O_2/Pt(111)$ and TPRS for $CO/O_2/Pt(111)$ in order to calibrate and measure adsorbate coverages as well as to verify the cleanliness of our platinum sample.[1] Figure 6.3a shows the TPD spectrum of $^{18}O_2$ from $^{18}O_2/Pt(111)$. The sample was dosed with $^{18}O_2$ to distinguish the signal from the background $^{16}O_2$. The first peak in the spectrum at T = 145 K, denoted α $-O_2$, is due to desorption of molecular oxygen. At this temperature dissociation also takes place and competes with desorption. [143] At T = 700 K, the dissociated oxygen atoms recombine and desorb giving rise to the broad β–O_2peak. Figure 6.3b shows the TPRS spectrum of $C^{18}O_2$ from $C^{18}O/^{18}O_2/Pt(111)$. The sample was first dosed with $^{18}O_2$ and then with $C^{18}O$. There are three peaks in the TPRS spectrum. The first peak (α CO_2) occurs at 145 K and is likely due to the reaction of CO with unequilibrated atomic oxygen. [142] The temperature of the peak coincides with the temperature at which molecular oxygen dissociates on the

[1] cleanliness of the platinum sample was further confirmed by performing LEED and Auger measurements.

SIONYX1403000045.0002

SAMSUNG EX. 1002 - 960/4148

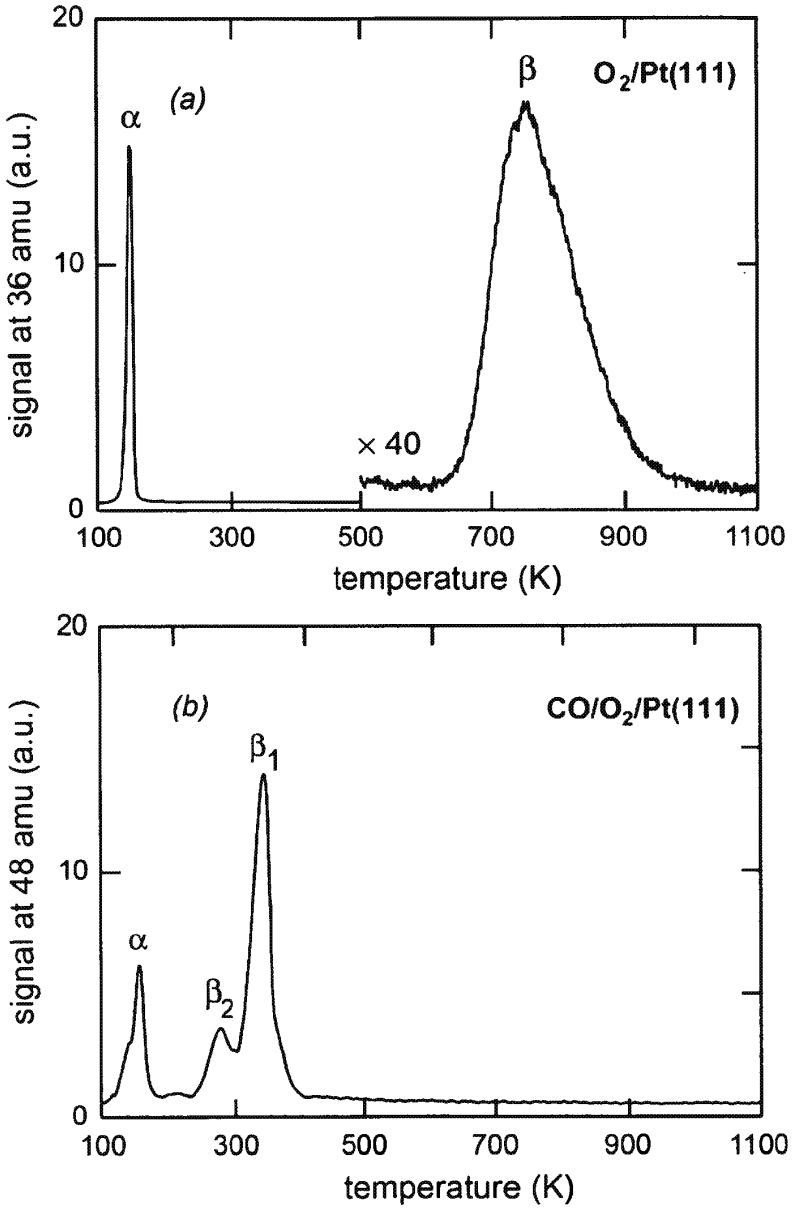


Figure 6.3: (*a*) TPD spectrum of $^{18}O_2$/Pt(111) showing mass 36 amu ($^{18}O_2$), (*b*) TPRS of $C^{18}O/^{18}O_2$/Pt(111) showing mass 48 amu ($C^{18}O_2$).

SIONYX1403000045.0003

SAMSUNG EX. 1002 - 961/4148

platinum surface. When the sample is dosed with atomic oxygen, there is no α–CO_2 peak. This agrees with the α–CO_2 stemming from the reaction of CO with unequilibrated oxygen atoms (the oxygen atoms on the surface are equilibrated if the sample is dosed with atomic oxygen). The two other peaks occur at 250 K (β_2–CO_2) and 330 K (β_1–CO_2). They are both due to CO reacting with atomic oxygen that is equilibrated with the surface. Allers *et al.* concluded that the β_2–CO_2 peak is due to reaction proceeding in dense O+CO layers or boundaries, while the β_1–CO_2 peak likely stems from CO oxidation at the boundaries of oxygen islands. [142]

6.3.2 Linear photochemistry

Desorption of O_2 and CO-oxidation from $CO/O_2/Pt(111)$ can be induced with continous light and nanosecond laser pulses. The yields of the photoprocesses exhibit a characteristic linear dependence on laser fluence. Therefore, the chemistry induced with low-level light sources is termed linear photochemistry. In the following I discuss linear photochemistry of $O_2/Pt(111)$ and $CO/O_2/Pt(111)$ and then compare the results to the photochemistry induced with high-intensity subpicosecond laser pulses in the next section.

O_2-Desorption

Photodesorption of O_2 from $O_2/Pt(111)$ and $CO/O_2/Pt(111)$ using continous light or nanosecond laser pulses has been studied by several groups. [8, 133, 125, 134, 135] Figure 6.4a shows the O_2 yields obtained from irradiation of $O_2/Pt(111)$ using 240 nm light as found by Mieher *et al.* The figure shows the characteristic linear dependence of the desorption yield on laser fluence ($Y = F^p$ with $p = 0.97 \pm 0.03$). The wavelength dependence of the O_2 yield on fluence is shown in Fig. 6.4b; no desorption was observed for wavelengths longer than 500 nm and the yield dropped sharply with increasing wavelength. A similar wavelength dependence of the O_2- desorption yield was also found by Zhu *et al.* [125]

CO-Oxidation

Photo-induced CO-oxidation with low-intensity light sources was investigated using continous light [8, 133] and nanosecond laser pulses. [134, 135] A linear dependence of the yield on fluence was also observed for CO_2 production from $CO/O_2/Pt(111)$. Mieher *et al.* found the same wavelength dependence as for O_2 desorption. The wavelength depen-

SIONYX1403000045.0004

SAMSUNG EX. 1002 - 962/4148

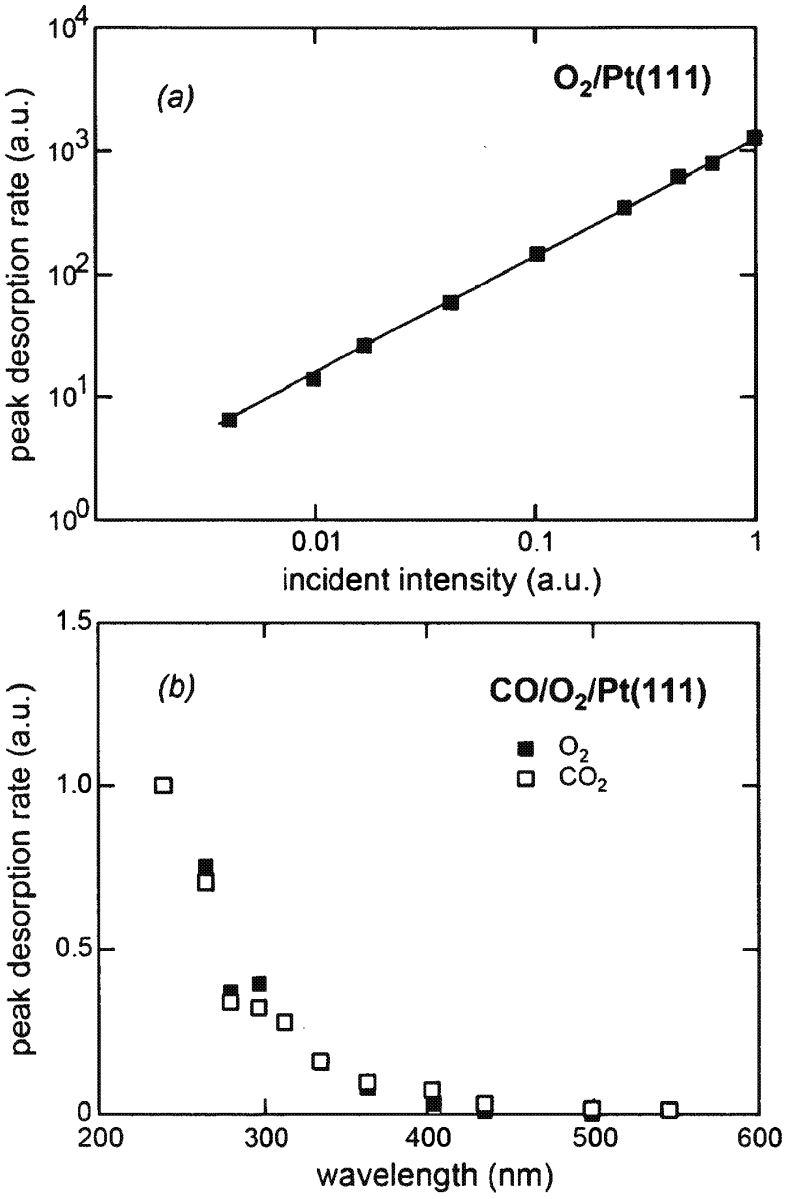


Figure 6.4: (*a*) O_2-desorption yield as a function of laser fluence, (*b*) CO_2-yield and O_2-yield as a function of laser wavelength. Note that the scales are different for figure a and figure b. After Mieher. [8]

SIONYX1403000045.0005

SAMSUNG EX. 1002 - 963/4148

dence of CO-oxidation is also shown in Fig. 6.4b. The ratio of O_2yield to CO_2 production for 240 nm - 400 nm was found to be 2.5 ± 0.5. Photo-oxidation with nanosecond pulses also exhibits a linear dependence of the yield on laser fluence ($p = 1.01 \pm 0.05$) and the same cross section for CO_2 production as that for O_2 desorption at 620 nm. [135]

Mechanisms of O_2Desorption and CO_2Production

The results of linear photochemistry can be accounted for by a model that was introduced by Menzel, Gomer and Redhead. [144, 145] The model associates photoinduced processes with electronic excitation of the adsorbate-substrate complex; desorption is induced by electronic transitions (DIET). The electronic transition can be either direct (intra-adsorbate) or indirect (substrate-mediated).

In direct excitation, electronic transitions into normally vacant orbitals lead to excitation of the adsorbate. The electronic excitation causes the adsorbate atom or molecule to move and to acquire vibrational or translational energy. The wavelength dependence is explained through the difference in the acquired electronic energy. Mieher *et al.* observed the same dependence on photon energy for O_2 -desorption as the electronic EELS spectrum of O_2/Pt(111). They concluded that the photoexcitation mechanisms leading to desorption and reaction are due to direct electronic excitation of O_2. They attributed the desorption and dissociation of adsorbed O_2 molecules to excitation of electrons into the π_b or $3\sigma_u$ molecular orbitals. [8]

In indirect excitation, photo-excited carriers (hot electrons) that are produced in the near surface region inelastically scatter off the adsorbed molecule. [146] The scattered electron leaves a fraction of its energy with the adsorbate before it returns to the substrate. The acquired energy is used for desorption, dissociation, or reaction with other adsorbates. The transfer of substrate electronic energy to the adsorbate occurs in the following steps, illustrated in figure 6.5:

1. An excited substrate electron makes a transition into an unoccupied adsorbate level, thereby attaching itself to the adsorbate. A temporary negative ion forms. The adsorbate-substrate complex makes a vertical transition from the ground state potential energy surface (PES 1) to an excited potential energy surface (PES 2).

2. The adsorbate-substrate complex moves towards the minimum on the PES 2, which is associated with a decrease in the nuclear distance between the adsorbate and the

SIONYX1403000045.0006

SAMSUNG EX. 1002 - 964/4148

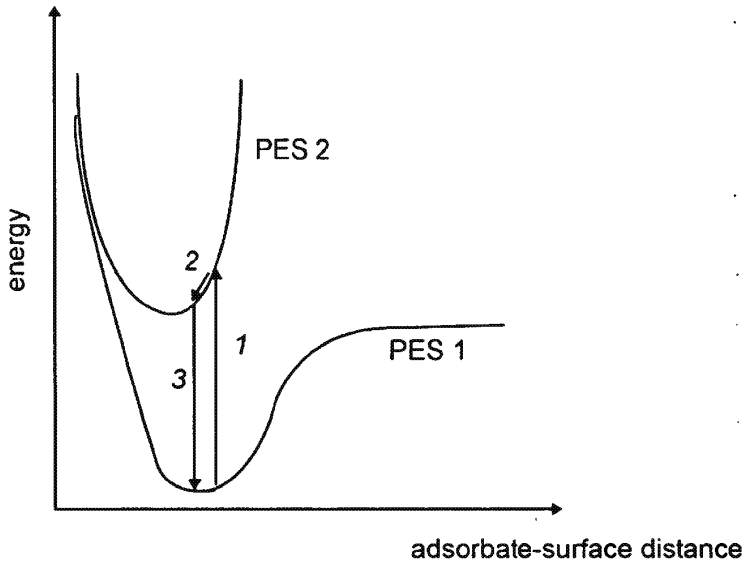


Figure 6.5: Schematic of adsorbate-metal excitation in the DIET model. (1) An excited adsorbate-substrate complex makes a vertical transition from the ground state potential (PES 1) to an excited state potential (PES 2). (2) It moves towards the minimum on the PES 2 and acquires kinetic energy. (3) After a certain time, the adsorbate-substrate complex returns to PES 1.

substrate molecule. This decrease in internuclear distance is caused by the attraction of the negative ion to its image charge at the surface. At the same time, as the potential energy decreases, the kinetic energy of the adsorbate-substrate complex increases.

3. After a certain time τ, the adsorbate-substrate complex returns to the ground potential energy surface (the electron detaches from the adsorbate and returns to the substrate).

If the adsorbate-substrate complex remains long enough on PES 2, the gain in kinetic energy may be sufficient for desorption, dissociation, or reaction with other adsorbates. If the energy acquired during τ is not sufficient, the adsorbate remains vibrationally excited. The vibrational energy is eventually dissipated to heat.

The DIET model predicts the following dependence of the yields in linear photochemistry:

SIONYX1403000045.0007

SAMSUNG EX. 1002 - 965/4148

- Linear dependence of yield on fluence The number of electrons available for adsorbate excitation is directly proportional to the number of photo-excited substrate electrons, which is in turn directly proportional to the incident number of photons.

- Wavelength dependence of yield

  Nonthermalized electrons are responsible for the excitation of the adsorbate. A different photon energy corresponds to a different shift of the DOS in the band structure (see Sec.6.2). The nascent electron distribution created by higher energy photons has a greater energy overlap with the adsorbate affinity level, therefore the desorption cross section increases with photon energy.

Substrate-mediated desorption and reaction via subvacuum level substrate electrons was favored by Kao *et al.* [135] and Ukraintsev and Harrison [134] for the excitation pathway leading to desorption of O_2 and formation of CO_2 from $CO/O_2/Pt(111)$.

6.3.3 Femtochemistry of $CO/O_2/Pt(111)$

The following section presents and discusses our experiments on photochemistry of $CO/O_2/Pt(111)$ induced with subpicosecond laser pulses. In particular, we wished to investigate whether the femtochemistry of $CO/O_2/Pt(111)$ leads to different results from those obtained in linear photochemistry. As discussed in Sec.6.2, very high electronic temperatures can be reached with very intense subpicosecond laser pulses. This may open up unique excitation pathways to desorption and reaction. We studied the femtochemistry of $CO/O_2/Pt(111)$ over a wide range of fluences and at three different wavelengths (267 nm, 400 nm, and 800 nm).

Experimental procedure

Details of the experimental setup are given in Sec. 6.4. Figure 6.6 shows a schematic of the experimental apparatus.

Results

We measured the O_2 and CO_2 yields as a function of laser fluence in the range $0.1\ \mu J/mm^2 < F < 50\ \mu J/mm^2$ for 0.3 ps pulses with wavelengths of 267 nm, 400 nm, and

SIONYX1403000045.0008

SAMSUNG EX. 1002 - 966/4148

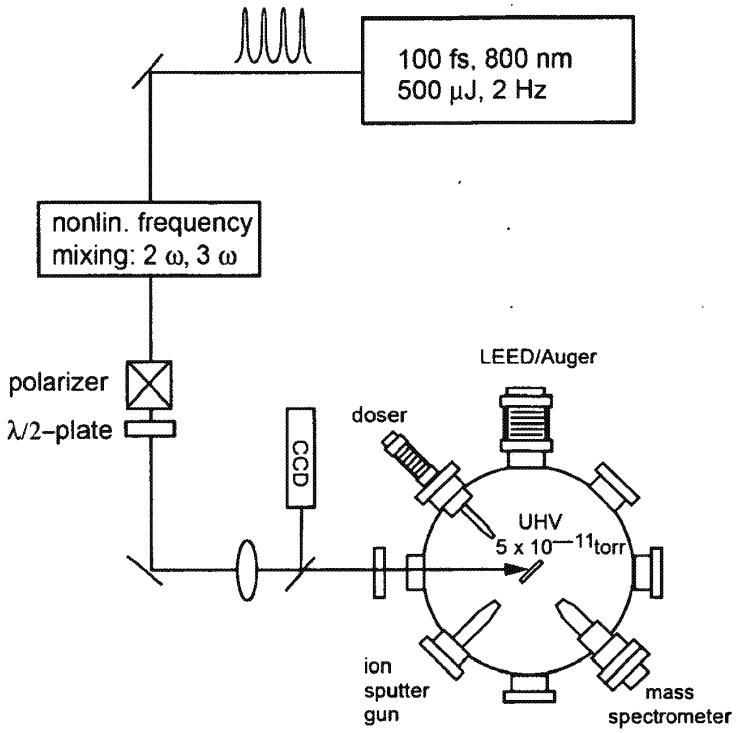


Figure 6.6: Schematic of the experimental apparatus used in the femtochemistry experiments.

800 nm. The data show two different regimes of the yields' dependence on fluence. The transition from one fluence regime to the other occurs roughly at $F = 10\ \mu\text{J/mm}^2$:

$F < 10\ \mu\text{J/mm}^2$

For fluences $F < 10\ \mu\text{J/mm}^2$ the results are very similar to those obtained with low-intensity light sources: CO_2- production and O_2- desorption is observed for wavelengths 267 nm and 400 nm, but not for 800 nm. These experiments were the first to demonstrate that photochemistry of $CO/O_2/Pt(111)$ induced with low-intensity femtosecond laser pulses results in a linear dependence of yield on fluence. The exponent is $p = 1.1 \pm 0.1$ for $\lambda = 267$ nm and $p = 0.9 \pm 0.1$ for $\lambda = 400$ nm. We observe that higher cross sections are obtained for higher photon energies (267 nm yields > 400 nm yields). The branching ratio of the O_2 and CO_2 yields is roughly 1.

SIONYX1403000045.0009

SAMSUNG EX. 1002 - 967/4148

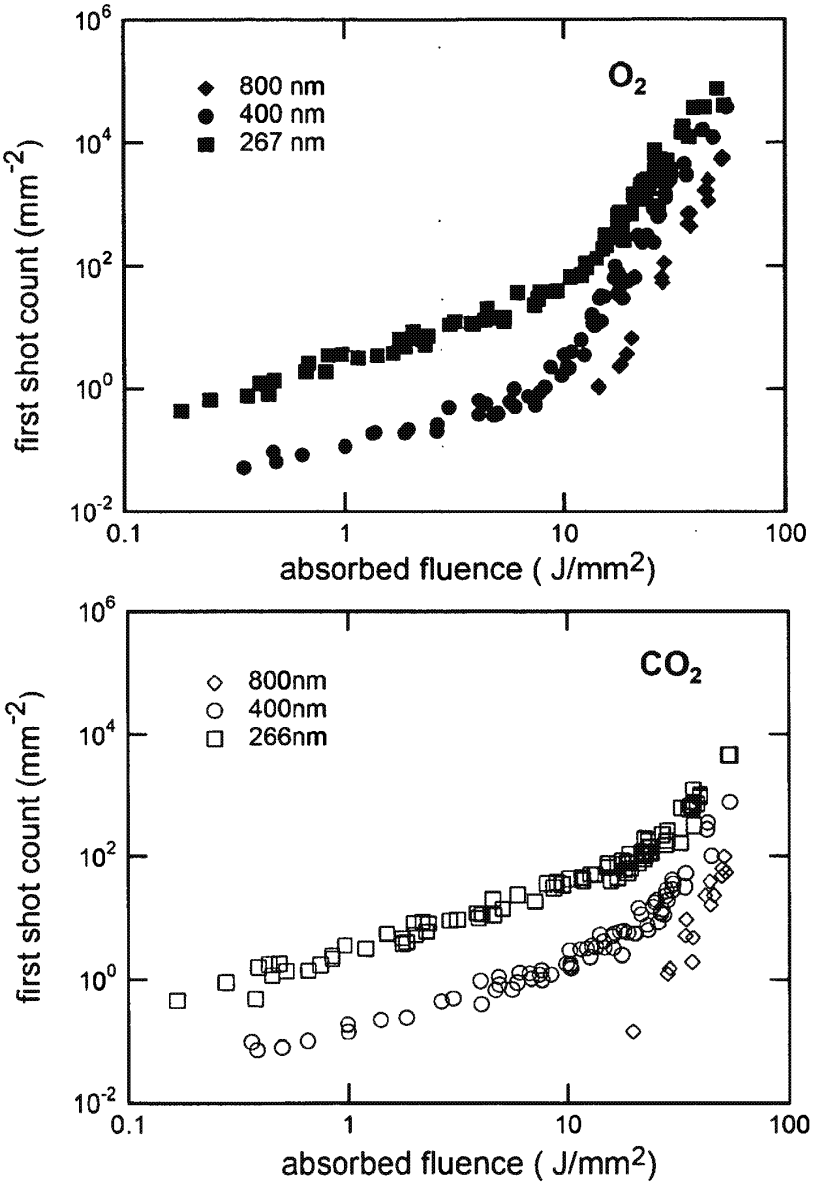


Figure 6.7: (*a*) O_2 and (*b*) CO_2 yields as a function of laser fluence using 267 nm, 400 nm, and 800 nm light as the excitation wavelength.

SIONYX1403000045.0010

SAMSUNG EX. 1002 - 968/4148

$F > 10\ \mu J/mm^2$

For $F > 10\ \mu J/mm^2$ we observe a drastically different behavior of the yields. The yields scale nonlinearly with the fluence and can be described by $Y = F^p$ $(p > 1)$. Compared to the yields using fluences below F=10 $\mu J/mm^2$, the yields are higher by several orders of magnitude. In addition, the branching ratio of O_2 desorption and CO_2 production is much larger than 1. These results are in agreement with the observations of Kao *et al.* [135]

We observe O_2- desorption and CO_2- production at 267 nm, 400 nm and, in contrast to the results of linear photochemistry, also at 800 nm excitation wavelength. Unlike Kao *et al.* we detect a 3-fold wavelength dependence of the yields:

1. The yields increase with decreasing wavelength.
2. The power exponent p decreases with decreasing wavelength.
3. The branching ratio of O_2: CO_2 decreases with decreasing wavelength.

The wavelength dependencies of both fluence regimes are summarized in tables 6.1 - 6.3. [26]

Table 6.1: Wavelength dependence of O_2 and CO_2 yields

Fluence	267 nm	400 nm	800 nm
1 $\mu J/mm^2$	3 ± 0.5	0.1 ± 0.02	0
30 $\mu J/mm^2$	8000 ± 1500	2000 ± 500	120 ± 25

Table 6.2: Wavelength dependence of power law exponent

Fluence	267 nm	400 nm	800 nm
$F < 10\mu J/mm^2$	1.1 ± 0.1	0.9 ± 0.1	n.a.
$F > 10\mu J/mm^2$	4.8 ± 0.1	6.0 ± 0.1	7.2 ± 0.1

Table 6.3: Wavelength dependence of O_2:CO_2 yields

Fluence	267 nm	400 nm	800 nm
$F < 10\mu J/mm^2$	1 ± 0.1	1 ± 0.1	n.a.
$F > 10\mu J/mm^2$	25 ± 5	55 ± 15	70 ± 10

Discussion

The striking differences in the behavior of the yields in the two fluence regimes suggest that different mechanisms are responsible for desorption and reaction using fluences

SIONYX1403000045.0011

SAMSUNG EX. 1002 - 969/4148

above and below $F = 10\ \mu J/mm^2$. DIET, which successfully explains the results of linear photochemistry, cannot explain the high desorption and reaction yields nor the nonlinear dependence of the yields on fluence observed for fluences exceeding $F > 10\ \mu J/mm^2$. The high yields and the nonlinearity of the yields are characteristics of surface photochemistry induced with subpicosecond laser pulses and have also been observed by other groups. [147, 135] In order to explain the results for fluences exceeding $F > 10\ \mu J/mm^2$, a generalized DIET model, DIMET (desorption induced by multiple electronic transitions) was invoked to explain the results of surface femtochemistry. [147, 148, 149]

High-intensity subpicosecond laser pulses lead to very high electronic temperatures. In DIMET, these high electronic temperatures can lead to successive electronic excitations of the adsorbate before the vibrationally excited molecule loses its excess energy to phonons. Figure 6.8 illustrates this process; if there are sufficient cycles of excitations and deexcitations, the adsorbate can finally acquire enough energy to desorb, dissociate, or react with other adsorbates. DIMET can account for the high yields we observe, because successive electronic excitations greatly enhance the probability of desorption and reaction. The nonlinearlity of the yields to increased fluence also follows from this model: multiple electronic excitation of the adsorbate lead to a nonlinear dependence of the yield on fluence. DIMET, however, cannot explain the threefold wavelength dependence that we observe. DIMET assumes thermalized electrons (electrons that have a well-defined temperature) are responsible for the excitation and our results clearly indicate though that the excitation cannot be associated with thermalized electrons. Nonthermalized electrons have to play an important role in order to account for the wavelength-dependent behavior of the yields, the power law, and the branching ratios. We therefore conclude that a theoretical model for subpicosecond photochemistry has to include non-thermalized electrons as part of the excitation mechanism.

SIONYX1403000045.0012

SAMSUNG EX. 1002 - 970/4148

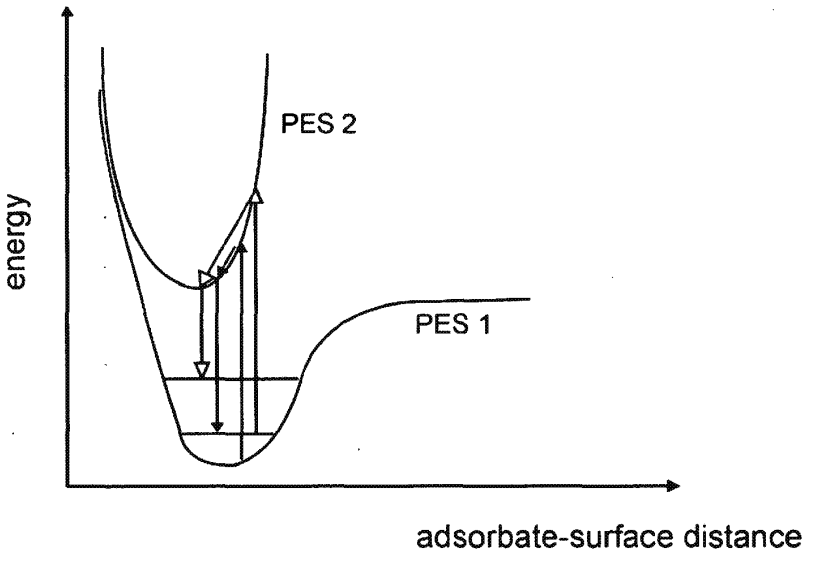


Figure 6.8: Schematic diagram of the excitation and de-excitation cycles in DIMET. Shown are two cycles. The first excitation path is depicted using filled arrows, the second excitation cycle is depicted using hollow arrows. After the first excitation cycle the adsorbate-substrate complex starts out vibrationally excited.

6.4 Reaction Pathways to CO_2-Formation from $CO/O_2/Pt(111)$

The following material appeared in Chemical Physics Letters, volume 274, pages 499-504 (1997).

SIONYX1403000045.0013

SAMSUNG EX. 1002 - 971/4148

Chapter 7

Conclusion

7.1 Formation of silicon microspikes with femtosecond laser pulses

Highly intense femtosecond laser pulses incident on a silicon surface cause microstructuring of the surface. Sharp spikes are produced if the irradiation takes place in an environment of a halogenated gas. These spikes form only under certain laser and gas conditions. They form gradually over hundreds of laser pulses; the spike height increases with increasing laser fluence and decreases with increasing laser pulse duration. Sharp spikes likewise form on germanium but not on InP or GaAs. The spikes are mostly crystalline with a high density of structural defects and contain a high concentration of sulfur and fluorine. The spikes form most likely via a mechanism involving both preferential ablation and chemical etching.

The spiked surface has remarkable light absorption properties; it absorbs nearly all incident radiation for wavelengths ranging from the ultraviolet to the infrared. The strong absorption of below-band gap radiation is most likely associated with impurities.

This light absorption can enhance the efficiency of existing photovoltaic devices in the visible range after passivation of the surface. For certain below-band gap radiation, spiked silicon devices produce significantly more photocurrent than ordinary silicon devices (without passivation), and thus may be used to extend the wavelength range of existing photovoltaic devices.

Silicon surfaces microstructured in air luminesce strongly in the visible. The pho-

SIONYX1403000045.0014

SAMSUNG EX. 1002 - 972/4148

toluminescence is related to the oxygen embedded in the surface, most likely in the form of SiO_x. The photoluminescence characteristics change with the laser parameters used to produce the luminescent silicon surface: the luminescence intensity increases with increasing laser fluence and the peak wavelength blue-shifts with increasing number of laser pulses. Results from annealing experiments indicate that the green luminescence possibly comes from defects and that the red luminescence likely stems from quantum-confined silicon nanoclusters embedded in the silicon-oxide matrix.

7.2 Femtochemistry of $CO/O_2/Pt(111)$

The nonequilibrium condition created by the high-intensity femtosecond laser pulses enable high-yield excitation pathways that depend nonlinearly on the absorbed laser fluence. The transition from linear to nonlinear fluence dependence at 10 $\mu mJ/mm^2$ indicates a change in the nature of the excitation. This change may be a transition from a single to multiple electronic excitation of the substrate. We observe a threefold wavelength dependence of the yields: the O_2 and CO_2 yields, the power law, and the branching ratio of the O_2:CO_2 yields. The wavelength dependence excludes the dominance of thermalized electrons in the excitation process.

Given the required high efficiency of capturing a dissociated oxygen atom to form CO_2, the atomic pathway is not likely to account for the observed CO_2 production. If the CO_2 is formed via the molecular pathway, then the intermediate CO_3^* has very inequivalent oxygen atoms.

SIONYX1403000045.0015

SAMSUNG EX. 1002 - 973/4148

Bibliography

[1] T.-H. Her, R.J. Finlay, C. Wu, and E. Mazur, Appl. Phys. A **70**, 383 (2000).

[2] L. C. Feldman, J. W. Mayer, and S. Thomas Picraux, *Materials analysis by ion channeling* (Academic Press, 1982).

[3] E. D. Palik, *Handbook of optical constants of solids* (Academic Press, Inc., 1985).

[4] E. Janzén, R. Stedman, G. Grossmann, and H.G. Grimmeiss, Phys. Rev. B **29**, 1907 (1984).

[5] Radiation Monitoring Devices (RMD).

[6] X.-L. Zhou and J.M. White, in *Laser spectroscopy and photochemistry on metal surfaces Part II* (World Scientific Publishing Co. Pte. Ltd., 1995), Chap. 25.

[7] S. Deliwala, Ph.D. thesis, Harvard University, 1995.

[8] W.D. Mieher and W. Ho, J. Chem. Phys. **99**, 9279 (1993).

[9] J.F. Young, J.S. Preston, H.M. van Driel, and J.E. Sipe, Phys. Rev. B **27**, 1155 (1983).

[10] S. Nolte, C. Momma, H. Jacobs, A Tünnermann, B.N. Chikov, B. Wellegehausen, and H. Welling, J. Opt. Soc. Am. B **14**, 2716 (1997).

[11] A.K. Jain, V.N. Kulkarni, D.K. Sood, and J.S. Uppol, J. Appl. Phys. **52**, 4882 (1981).

[12] J.F. Young, J.E. Sipe, and H.M van Driel, Phys. Rev. B **30**, 2001 (1984).

[13] E.N. Glezer and E. Mazur, Appl. Phys. Lett. **71**, 882 (1997).

[14] A. Smirl, T.F. Boggess, and S. C. Moss, J. Appl. Phys. **60**, 1169 (1986).

SIONYX1403000045.0016

SAMSUNG EX. 1002 - 974/4148

[15] P. M. Fauchet, *Light Emission in Silicon* (Academic Press, 1998).

[16] D. Jost, W. Lüthy, and H.P. Weber, Appl. Phys. Lett. **49**, 625 (1986).

[17] J.E. Rothenberg and R. Kelly, Nucl. Instrum. Meth. Phys. Res. B **1**, 291 (1984).

[18] S. Ameer-Berg, W. Perrie, S. Rathbone, J. Wright, and W. Weaver, Appl. Surf. Sci. **127–129**, 875 (1998).

[19] W. Kautek and J. Krueger, *Materials Science Forum* (Trans Tech Publications, Switzerland, 1995), Vol. 173–174, pp. 17–22.

[20] B.N. Chikov, C. Momma, S. Nolte, and F. von Alvensleben, Appl. Phys. A **63**, 109 (1996).

[21] D. von der Linde, K. Sokolowski-Tinten, and J. Bialkowski, Appl. Surf. Sci. **109/110**, 1 (1997).

[22] K. Sokolowski-Tinten, J. Bialkowski, M. Boing, A. Cavalleri, and D. von der Linde, Phys. Rev. B **58**, R11 805 (1998).

[23] A. Cavalleri, K. Sokolowski-Tinten, J. Bialkowski, M. Schreiner, and D. von der Linde, J. Appl. Phys. **65**, 3301 (1999).

[24] K. Sokolowski-Tinten, J. Bialkowski, and D. von der Linde, Phys. Rev. B **51**, 14186 (1995).

[25] A.J. Pedraza, J. D. Fowlkes, and D. H. Lowndes, Appl. Phys. Lett. **74**, 2322 (1999).

[26] R. J. Finlay, Ph.D. thesis, Harvard University, 1997.

[27] T.-H. Her, Ph.D. thesis, Harvard University, 1998.

[28] A. Zangwill, *Physics at Surfaces* (Cambridge University Press, 1988).

[29] D.P. Woodruff and T.A. Delchar, *Modern techniques of surface science* (Cambridge University Press, 1986).

[30] R.G. Wilson, F.A. Stevie, and C.W. Magee, *Secondary Ion Mass Spectrometry* (Wiley, NY, 1989).

SIONYX1403000045.0017

SAMSUNG EX. 1002 - 975/4148

[31] E. Yablonovitch and N. Bloembergen, Phys. Rev. Lett. **29**, 907 (1972).

[32] A.C. Tien, S. Backus, H. Kapteyn, M. Mournane, and G. Mourou, Phys. Rev. Lett. **82**, 3883 (1999).

[33] W.S. Fann, R. Storz, H.W.K. Tom, and J. Boker, Surface Science **283**, 221 (1993).

[34] D. v.d. Linde, J. Kuhl, and H. Klingenberg, Phys. Rev. Lett. **44**, 1505 (1980).

[35] P. Stampfli and K.H. Bennemann, Phys. Rev. B **42**, 7163 (1990).

[36] P. Stampfli and K.H. Bennemann, Phys. Rev. B **46**, 10686 (1992).

[37] N. Bloembergen, in *Laser-Solid Interactions and Laser Processing - 1978* (1979).

[38] M.C. Downer, R.L. Fork, and C.V. Shank, J. Opt. Soc. Am. B **2**, 595 (1984).

[39] H.W.K. Tom, G.D. Aumiller, and C.H. Brito-Cruz, Phys. Rev. Lett. **60**, 1483 (1983).

[40] P. Saeta, J.-K. Wang, Y.Siegal, N. Bloembergen, and E. Mazur, Phys. Rev. Lett **67**, 1023 (1991).

[41] C.V. Shank, R. Yen, and C. Hirlimann, Phys. Rev. Lett. **51**, 900 (1983).

[42] K. Sokolowski-Tinten, H. Schulz, J. Bialkowski, and D. von der Linde, Appl. Phys. A **53**, 227 (1991).

[43] J.A. van Vechten, R. Tsu, and F.W. Saris, Phys. Lett. A **74**, 422 (1979).

[44] P. Stampfli and K.H. Bennemann, Phys. Rev. B **49**, 7299 (1994).

[45] A. Miotello and R. Kelly, Appl. Phys. Lett. **67**, 3535 (1995).

[46] P.P. Pronko, S.K. Dutta, and D. Du, J. Appl. Phys **78**, 6233 (1995).

[47] *CRC Handbook of chemistry and physics* (CRC Press, 1999-2000).

[48] P.P. Pronko, in *Advanced Laser-Processing of Materials - Fundamentals and Applications* (1996), pp. 45–51.

[49] P.E. Dyer, S.D. Jenkins, and J. Sidhu, Appl. Phys. Lett. **49**, 453 (1986).

SIONYX1403000045.0018

SAMSUNG EX. 1002 - 976/4148

[50] R.S. Taylor, L.E. Leopold, D.L. Singleton, G. Paraskevopoulos, and R.S. Irwin, J. Appl. Phys. **64**, 2815 (1988).

[51] S.R. Foltyn, R.C. Dye, K.C. Ott, E. Peterson, K.M. Hubbard, W. Hutchinson, R.E. Muenchausen, R.C. Estler, and X.D. Wu, Appl. Phys. Lett. **59**, 594 (1991).

[52] O. Auciello, A.R. Krauss, J. Santiago-Ausles, P.F. Schreiner, and D.M. Gruen, Appl. Phys. Lett. **52**, 239 (1988).

[53] D.J. Krajnovich and J.E. Vasquez, J. Appl Phys. **73**, 3001 (1992).

[54] D.J. Krajnovich, J. E. Vasquez, and R.J. Savoy, Science **259**, 1590 (1992).

[55] G.K. Wehner and D.J. Hajicek, J. Appl. Phys. **42**, 1145 (1971).

[56] J. D. Fowlkes, A. J. Pedraza, and D. H. Lowndes, Appl. Phys. Lett. **77**, 1629 (2000).

[57] T.J. Chuang, Surface Science Reports **3**, 1 (1983).

[58] J.H. Thomas III and L.H. Hammer, J.Vac. Sci. Technol. B **5**, 1617 (1987).

[59] K. Seeger and R.E. Palmer, Appl. Phys. Lett. **74**, 1627 (1999).

[60] R. Ortega Martinez, T.R. Verhey, P.K. Boyer, and J.J. Rocca, J. Vac. Sci. Technol. B **6**, 1581 (1988).

[61] T.J. Chuang, J. Chem. Phys. **74**, 1453 (1981).

[62] T.J. Chuang, J. Chem. Phys. **72**, 6303 (1980).

[63] F. Raksi, K. Wilson, Z. Jiang, A. Ikhlef, C.Y. Cote, and J. Kieffer, J. Chem. Phys. **104**, 6066 (1996).

[64] E. Hecht, *Optics* (Addison-Wesley, 1998).

[65] J. M. Palmer, *Handbook of Optics* (McGraw-Hill, 1995).

[66] J.D. Jackson, *Classical Electrodynamics* (John Wiley & Sons, Inc., 1975).

[67] C.F. Klingshirn, *Semiconductor Optics* (Springer-Verlag, 1995).

[68] G. R. Fowles, *Introduction to modern optics* (Dover Publications, New York, 1975).

SIONYX1403000045.0019

SAMSUNG EX. 1002 - 977/4148

[69] Melles Griot, *Catalogue 1995/96.*

[70] E. S. Kolesar Jr., V.M. Bright, and D. M. Sowders, Thin Solid Films **290–291**, 23 (1996).

[71] D.H. Raguin and G.M. Morris, Appl. Opt. **32**, 1154 (1993).

[72] I.T. Ritchie and B. Window, Appl. Opt. **16**, 1438 (1977).

[73] Lord Rayleigh, Lond. Math. Soc. **11**, 51 (1880).

[74] P. B. Clapham and M.C. Hutley, Nature **244**, 281 (1973).

[75] C.G. Bernhard, Endeavour **26**, 79 (1967).

[76] J.I. Gittleman and E.K. Sichel, Appl. Phys. Lett. **35**, 742 (1979).

[77] H.G. Craighead, R.E. Howard, and D.M. Tennant, Appl. Phys. Lett. **37**, 653 (1980).

[78] J.P. Zheng, K.L. Jiao, W.P. Shen, W.A. Anderson, and H.S. Kwok, Appl. Phys. Lett. **61**, 459 (1992).

[79] M.K. Lee, H. Wang, and C.H. Chu, IEEE J. Quant. Elec. **33**, 2199 (1997).

[80] K. Grigoras, A. Krotkus, V. Pacebutas, J. Kavaliauskas, and I. Simkiene, Thin Solid Films **276**, 228 (1996).

[81] N. W. Ashcroft and N. David Mermin, *Solid State Physics* (Saunders College Publishing, 1976).

[82] R.A. Forman, Appl. Phys. Lett. **37**, 776 (1980).

[83] D.R. Myers and W.E. Phillips, Appl. Phys. Lett. **32**, 756 (1978).

[84] T.H. Ning and C.T. Sah, Phys. Rev. B **4**, 3482 (1971).

[85] W. Fahrner and A. Goetzberger, Appl. Phys. Lett. **21**, 329 (1972).

[86] J. Pankove, *Optical processes in semiconductors* (Dover, 1975).

[87] R.G. Wilson, J. Appl. Phys. **55**, 3490 (1984).

SIONYX1403000045.0020

SAMSUNG EX. 1002 - 978/4148

[88] C.H. Seager, P.M. Lenahan, K. L. Brower, and R.E. Mikawa, J. Appl. Phys. **58**, 2704 (1985).

[89] W.B. Jackson, N.M. Johnson, and D.K. Biegelsen, Appl. Phys. Lett. **43**, 195 (1983).

[90] W.B. Jackson and N.M. Amer, Phys. Rev. B **25**, 5559 (1982).

[91] C.H. Seager and P.M. Lenahan, J. Appl. Phys. **58**, 2709 (1985).

[92] R. C. Jaeger, *Vol. V: Introduction to Microelectronic Fabrication* (Addison-Wesley, 1988).

[93] H. Grebel and K.J. Fang, J. Appl. Phys. **77**, 367 (1995).

[94] G. Hahn, C. Zechner, M. Rino, P. Fath, G. Willeke, and E. Bucher, J. Appl. Phys. **68**, 7179 (1999).

[95] B. El-Kareh, *Fundamentals of semiconductor processing* (Kluwer Academic Publisher, 1995).

[96] R.A. Ditizio, G. Liu, S.J. Fonash, B.-C. Hseih, and D.W. Greve, Appl. Phys. Lett. **56**, 1140 (1990).

[97] T.C. Lee and G.W. Neudeck, J. Appl. Phys. **54**, 199 (1983).

[98] K. Baert, H. Murai, K. Kobayashi, H. Namizaki, and M. Nunoshita, Jpn. J. Appl. Phys. **32**, 2601 (1993).

[99] S.M. Sze, *Physics of semiconductor devices* (John Wiley & Sons, Inc., 1981).

[100] T. Sameshima, M. Skiya, M. Hara, and N. Sano, J. Appl. Phys. **76**, 7377 (1994).

[101] B.E.A. Saleh and M.C. Teich, *Fundamentals of Photonics* (John Wiley & Sons, Inc., 1991).

[102] R. T. Collins, P. M. Fauchet, and Michael A. Tischler, Physics Today 24 (1997).

[103] L.T. Canham, Appl. Phys. Lett. **57**, 1046 (1990).

[104] A.J. Kenyon, P.F. Trwoga, C.W. Pitt, and G. Rehm, J. Appl. Phys. **79**, 9291 (1996).

[105] T. Shimizu-Iwayama, S. Nakao, and K. Saitoh, Appl. Phys. Lett. **65**, 1814 (1994).

SIONYX1403000045.0021

SAMSUNG EX. 1002 - 979/4148

[106] G. Ghislotti, B. Nielsen, P. Asoka-Kumar, K.G. Lyn, A. Gambhir, L.F. Di Mauro, and C.E. Bottani, J. Appl. Phys. **79**, 8660 (1996).

[107] C. Itho, T. Suzuki, and N. Itho, Phys. Rev. B **41**, 3794 (1990).

[108] T. Komoda, J. P. Kelly, A. Nejim, K.P. Homewood, P.L.F. Hemment, and B.J. Sealy, Mat. Res. Soc. Symp. Proc. **358**, 163 (1995).

[109] Shimizu-Iwayama, K. Fujita, S. Nakao, K. Saitoh, T. Fujita, and N. Itoh, J. Appl. Phys. **75**, 7779 (1994).

[110] Y. Ishikawa and N. Shibata, Nucl. Instrum. Methods **91**, 520 (1994).

[111] Y. Ono, M. Nagase, M. Tabe, and Y. Takahashi, Jpn. J. Appl. Phys. **34**, 1728 (1995).

[112] T. Fischer, T. Muschik, R. Schwarz, D. Kovalev, and F. Koch, Mater. Res. Soc. Symp. Proc. **358**, 851 (1995).

[113] G.S. Tompa, D. C. Morton, B.S. Sywe, Y. Lu, E. W. Forsythe, J. A. Ott, D. Smith, J. Khurgin, and B.A. Khan, Mater. Res. Soc. Symp. Proc. **358**, 701 (1995).

[114] M. Zhu, Y. Han, R. B. Wehrspohn, C. Godet, R. Etemadi, and D. Ballutaud, J. Appl. Phys. **83**, 5386 (1998).

[115] S. Hayashi, T. Nagareda, Y. Kanzawa, and K. Yamamoto, Jpn. J. Appl. Phys. **32**, 3840 (1993).

[116] S. Nozaki, H. Nakamura, H. Ono, H. Morisaki, and N. Ito, Jpn. J. Appl. Phys. **34**, 122 (1994).

[117] D. Dimova-Malinovska, M. Tzolov, N. Malinowski, and Ts. Marinova, Appl. Surf. Sci. **96–98**, 457 (1996).

[118] K. Hoh, H. Koyama, K. Uda, and Y. Miura, Jpn. J. Appl. Phys. **19**, L375 (1980).

[119] Y.S. Liu, S.W. Chiang, and F. Bacon, Appl. Phys. Lett. **38**, 1005 (1981).

[120] E. Fogarassy, C.W. White, A. Slaoui, C. Fuchs, P. Siffert, and S.J. Pennycook, Appl. Phys. Lett. **53**, 1720 (1988).

[121] A. Cros and F. Salvan, Appl. Phys. A **28**, 241 (1982).

SIONYX1403000045.0022

SAMSUNG EX. 1002 - 980/4148

[122] www.genplot.com, RUMP (Simulation program for Rutherford Backscattering Spectrometry).

[123] B.A. Joyce and J.H. Neave, Surface Science **27**, 499 (1971).

[124] B. Carriére and J. P. Deville, Surface Science **80**, 278 (1979).

[125] X.-Y. Zhu, S.R. Hatch, A. Campion, and J.M. White, J. Chem. Phys. **91**, 5011 (1989).

[126] B.H. Augustine, E.A. Irene, Y.J. He, K.J. Price, L.E. McNeil, K.N. Christensen, and D.M. Maher, J. Appl. Phys. **78**, 4020 (1995).

[127] T. Engel and G. Ertl, in *Advances in Catalysis* (Academic Press, Inc., 1979), Chap. 1, p. 1.

[128] I. Langmuir, Trans. Faraday Soc. **17**, 672 (1922).

[129] T. Matsushima and H. Asada, J. Chem. Phys **85**, 1658 (1986).

[130] T. Matsushima, Surface Science **127**, 403 (1983).

[131] C.B. Mullins, C.T. Rettner, and D.J. Auerbach, J. Chem. Phys. **95**, 8649 (1991).

[132] J. Hall and B. Kasemo, Surface Science **316**, L1099 (1994).

[133] C.E. Tripa, C.R. Arumaninayagam, and J.T. Yates, J. Chem. Phys. **105**, 1691 (1996).

[134] V.A. Ukraintsev and I. Harrison, J. Chem. Phys. **96**, 6307 (1992).

[135] F.-J. Kao, D.G. Busch, D.G. da Costa, and W. Ho, Phys. Rev. Lett. **70**, 4098 (1993).

[136] T.-H. Her, R.J. Finlay, C. Wu, and E. Mazur, J. Chem. Phys. **108**, 8595 (1998).

[137] S. Deliwala, R.J. Finlay, J.R. Goldman, T.-H. Her, W.D. Mieher, and E. Mazur, Chem. Phys. Lett. **242**, 617 (1995).

[138] W.S. Fann, R. Storz, H.W.K. Tom, and J. Boker, Phys. Rev. Lett. 2834 (1992).

[139] S.I. Anisimov, B.L. Kapeliovich, and T.L. Perel'man, Sov. Phys. JETP **39**, 375 (1974).

[140] J.A. Misewich, T.F. Heinz, P.Weigand, and A. Kalamarides, in *Laser spectroscopy and photochemistry on metal surfaces Part II* (World Scientific Publishing Co. Pte. Ltd., 1995), Chap. 19, p. 764.

SIONYX1403000045.0023

SAMSUNG EX. 1002 - 981/4148

[141] J. L. Gland and E. B. Kollin, J. Chem. Phys. **78**, 963 (1983).

[142] K.-H. Allers, H. Pfnür, P. Feulner, and D. Menzel, J. Chem. Phys. **100**, 3985 (1994).

[143] T. Matsushima, Surface Science **157**, 306 (1985).

[144] D. Menzel and R. Gomer, J. Chem. Phys. **41**, 3311 (1964).

[145] P.A. Redhead, Can. J. Phys. **42**, 886 (1964).

[146] J.W. Gadzuk, in *Laser Spectroscopy and Photochemistry on Metal Surfaces, Part II* (World Scientific Publishing Co. Pte. Ltd., 1995), Chap. 21, p. 897.

[147] J.A. Misewich, T.F. Heinz, and D.M. Newns, Phys. Rev. Lett. **68**, 3737 (1992).

[148] S. Gao, Phys. Rev. B **55**, 1876 (1997).

[149] T. Seideman and H. Guo, J. Chem. Phys. **107**, 8627 (1997).

SIONYX1403000045.0024

SAMSUNG EX. 1002 - 982/4148

Near-unity below-band-gap absorption by microstructured silicon

C. Wu
Department of Physics, Harvard University, Cambridge, Massachusetts 02138

C. H. Crouch, L. Zhao,[a] and J. E. Carey
Division of Engineering and Applied Sciences, Harvard University, Cambridge, Massachusetts 02138

R. Younkin
Department of Physics, Harvard University, Cambridge, Massachusetts 02138

J. A. Levinson
Department of Chemistry, Harvard University, Cambridge, Massachusetts 02138

E. Mazur[b]
Department of Physics and Division of Engineering and Applied Sciences, Harvard University, Cambridge, Massachusetts 02138

R. M. Farrell, P. Gothoskar, and A. Karger
Radiation Monitoring Devices, Inc., 44 Hunt Street, Watertown, Massachusetts 02472

(Received 19 December 2000; accepted for publication 30 January 2001)

We increased the absorptance of light by silicon to approximately 90% from the near ultraviolet (0.25 μm) to the near infrared (2.5 μm) by surface microstructuring using laser-chemical etching. The remarkable absorptance most likely comes from a high density of impurities and structural defects in the silicon lattice, enhanced by surface texturing. Microstructured avalanche photodiodes show significant enhancement of below-band-gap photocurrent generation at 1.06 and 1.31 μm, indicating promise for use in infrared photodetectors. © *2001 American Institute of Physics.* [DOI: 10.1063/1.1358846]

Light absorption by unmodified silicon is limited by two factors: silicon is highly reflective across the electromagnetic spectrum, and the band gap of silicon is 1.07 eV, making unmodified silicon essentially transparent to wavelengths longer than 1.1 μm. Both factors limit the useful wavelength range, sensitivity, and efficiency of silicon-based optoelectronic devices. Because of silicon's technological importance, overcoming these limitations would open up new possibilities for applications.

In this letter, we report increasing the optical absorptance of silicon from a few percent to roughly 90% in the near-infrared region (1.1–2.5 μm) as well as from roughly 60% to roughly 90% at shorter wavelengths (0.25–1.1 μm). The increased absorptance leads to photoelectron generation by 1.31 μm illumination of a microstructured avalanche photodiode (APD) with a bias voltage of 500 V. For bias voltages below 900 V, an unstructured APD gives no response to 1.31 μm illumination, and for higher bias voltages, the signal is a factor of 3 lower than that obtained from the structured device. The microstructured APD response to 1.06 μm illumination is similarly improved. These properties are obtained by microstructuring the surface of silicon using laser-assisted chemical etching.[1–3]

One well-established strategy for reducing reflection is surface texturing. In silicon, various texturing techniques[4–10] have been used to reduce the total hemispherical reflectance (i.e., specular and diffuse reflectance combined) for normal incidence to a few percent for visible light and somewhat more for infrared radiation. While reducing reflectance increases absorptance for visible wavelengths, reducing reflectance below the band gap without simultaneously introducing absorbing states into the gap leads primarily to increased transmittance.

We produced microstructured silicon surfaces that have visible to near-infrared reflectance of a few percent and absorptance of about 90%. The surfaces are microstructured by irradiating a Si(111) surface with a train of 800 nm, 100 fs laser pulses in the presence of SF_6.[1] This process creates a quasiordered array of sharp conical microstructures up to 50 μm high that are about 0.8 μm wide near the tip and up to 10 μm wide near the base. The pattern forms spontaneously without the use of masks, and forms only in the region illuminated by the laser. Figure 1 shows scanning electron micrographs of the surface after 10, 25, 100, and 450 laser pulses with fluence 10 kJ/m^2. Areas up to 10 mm$\times$10 mm were microstructured by scanning the laser beam across the sample; the laser parameters and scan speed determine the height of the spikes.[2] On the sides of the spikes, nanoscale structures (10–100 nm across) are formed, as shown in Fig. 2(a); many of these surface nanostructures disappear after annealing in vacuum at 1200 K for 3 h, as shown in Fig. 2(b). The spikes themselves, however, are not significantly altered by annealing.

We measured total hemispherical (specular and diffuse) reflectance (R) and transmittance (T) to determine the absorptance ($A=1-R-T$) of the microstructured surfaces. Measurements were performed with a Hitachi U-4001 UV–VIS spectrophotometer equipped with an integrating sphere

[a]Present address: Department of Physics, Fudan University, Shanghai, China.
[b]Electronic mail: mazur@physics.harvard.edu

 © 2001 American Institute of Physics

SIONYX1403000045.0025

SAMSUNG EX. 1002 - 983/4148

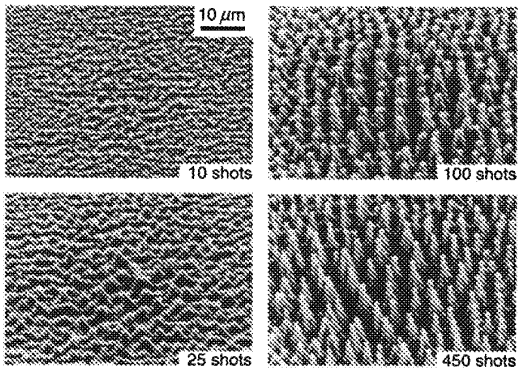


FIG. 1. Scanning electron micrographs of silicon spikes formed in SF_6 after 10, 25, 100, and 450 laper pulses (pulse duration: 100 fs; fluence: 10 kJ/m^2). Spike height increases with increasing number of laser pulses.

detector. Figure 3 shows the absorptance for three microstructured surfaces of varying spike heights (1–2, 4–7, and 10–12 μm), for an annealed sample (spike height 10–12 μm), and for the substrate silicon prior to microstructuring [n-Si(111), 260 μm thick, with resistivity $\rho = 8-12\,\Omega$ m].[11] Removing the native oxide layer by etching with HF does not affect the absorptance. Annealing was performed in vacuum for 3 h at 1200 K. The absorptance is 90% or more over the range 0.3–2.5 μm for the surface with 10–12 μm spikes, and decreases somewhat for surfaces with shorter spikes. The absorptance of the annealed sample is essentially unchanged above the band gap ($\lambda < 1.1\,\mu$m), but decreases significantly below the band gap ($\lambda > 1.1\,\mu$m).[12]

We observe significantly enhanced photocarrier production in microstructured silicon at infrared wavelengths near and below the band gap. We microstructured half of the light collection area of ordinary silicon APDs, leaving half unaltered. With no further processing of the devices, we measured the response (photocurrent) of both areas to illumination from the 1.064 μm line of a Nd:YAG pulsed laser and from a 1.310 μm diode laser (cw, chopped at 100 Hz). Figure 4 shows the response of the flat and the microstructured areas to 1.310 μm light (response at 1.064 μm is similar).

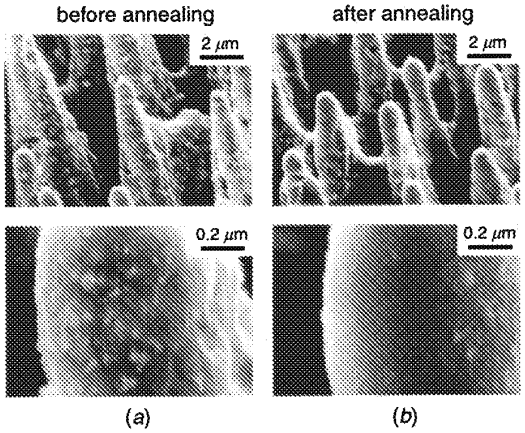


FIG. 2. Scanning electron micrograph of the sides of the spikes (a) before and (b) after annealing in vacuum at 1200 K for 3 h. Note that annealing eliminates many of the surface nanostructures.

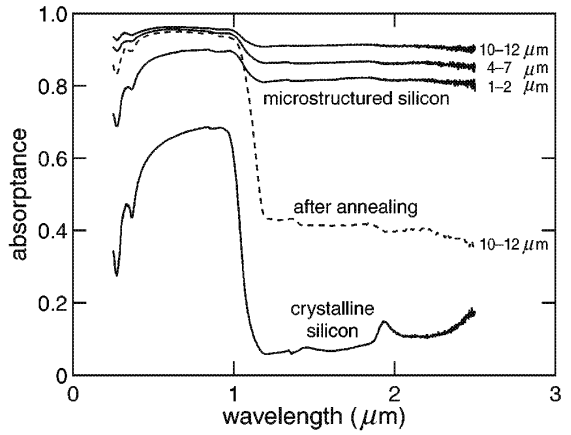


FIG. 3. Absorptance (A) of microstructured silicon surfaces and unstructured silicon substrate.

Illuminating the microstructured area generates a response at bias voltage 500 V and higher, whereas the unstructured area shows no measurable response for bias voltage less than 900 V. For a bias of 900 V or greater, at both 1.064 and 1.310 μm, photocarrier production from the microstructured area is at least three times that from the unstructured area. There is no detectable difference in noise from the two areas.

To identify a mechanism for the observed below-band-gap absorption and photocarrier production of microstructured silicon, we analyzed the chemical composition and the structure of the spikes. We performed secondary ion mass spectrometry (SIMS) to determine the chemical composition of our samples to a depth of approximately 1 μm. The results reveal an extremely high concentration of sulfur after microstructuring (~1 part in 10^3), and a substantially lower, but still significant, concentration of fluorine (~1 part in 10^5). Both the sulfur and fluorine content are highest just below the surface and decrease deeper into the sample. After annealing for 3 h at 1200 K, both concentrations decrease by roughly a factor of 2.

We examined the crystallinity of microstructured silicon with electron backscattering and ion channeling. The electron backscattering measurements show that the surface lay-

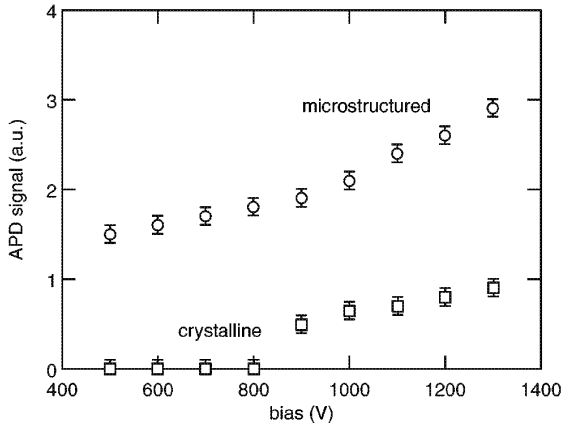


FIG. 4. Photocurrent from 1.310 μm excitation of microstructured and ordinary silicon detection areas of an avalanche photodiode (APD).

SIONYX1403000045.0026

SAMSUNG EX. 1002 - 984/4148

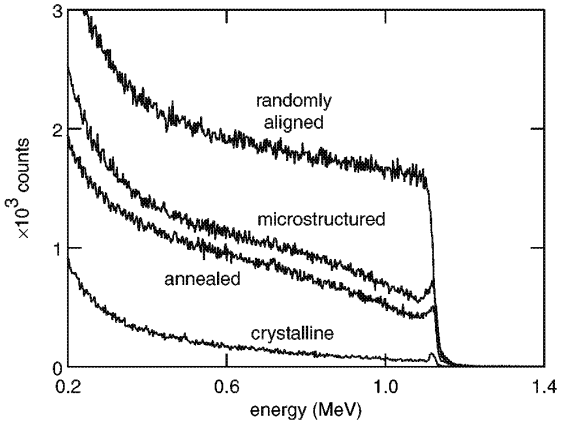


FIG. 5. Ion channeling spectra of the microstructured silicon surface with 10–12 μm spikes before and after annealing for 3 h at 1200 K in vacuum. For comparison, ion channeling spectra of a crystalline sample and of a randomly aligned sample (indicating maximum disorder) are also shown. Ion channeling spectra were measured with 2.0 MeV alpha particles backscattered into an annular solid-state detector.

ers have crystalline order, but do not exclude the possibility of a high density of defects. The ion channeling spectra (Fig. 5) show a background level higher than that of crystalline silicon but lower than that of a randomly aligned sample, which has a spectrum identical to that of amorphous silicon.[13] These measurements indicate that the material is crystalline and is likely to have a high density of defects. The background remains high in ion channeling spectra from samples annealed for 3 h at 1200 K, indicating that a significant amount of disorder in the microstructured material is unaffected by annealing under these conditions.

The high infrared absorptance of microstructured silicon most likely comes from the incorporation of a high density of impurities and structural defects into the lattice in the microstructuring process. Sulfur impurities are likely to be particularly important; sulfur is known to introduce states into the band gap of silicon, both near the band edge and in the middle of the gap, and structural defects are known to introduce infrared-absorbing states near the band edge.[14–17] The intrinsic absorptance caused by impurities and defects is enhanced by multiple reflections that reduce the reflectance significantly for the wavelength range shown in Fig. 3. The high, featureless infrared absorptance suggests that the extremely high concentration of sulfur impurities forms a band of infrared-absorbing states, since otherwise one would expect to see features in the infrared absorptance corresponding to sulfur impurity states. Bands of impurity states can form at concentrations as low as $10^{16}/\text{cm}^3$.[18] Such bands would also explain the observed below-band-gap carrier generation; carrier generation via impurity levels, known as the impurity photovoltaic effect (IPV), has been previously demonstrated to improve the efficiency of silicon solar cells.[19,20]

In conclusion, we have developed a microstructured form of silicon with roughly 90% light absorption at wavelengths from the near ultraviolet to the near infrared. Photocarriers are generated in this material by below-band-gap radiation. We find that in the microstructuring process, a high concentration of impurities and structural defects are incorporated into the silicon lattice, most likely producing bands of impurity states in the band gap that can absorb infrared radiation. The resulting subgap absorption is enhanced by the surface texture. These remarkable properties may make possible silicon-based detectors for infrared radiation. In order to optimize microstructured silicon infrared detectors, we are investigating further the optoelectronic properties of this material and the dependence of these properties on surface morphology such as spike height and density.

This work was supported by the U.S. Army Research Office (DAAD 19-99-1-0009) and by the NSF (DMR-98-09363). One of the authors (C.W.) acknowledges a Cusanuswerk fellowship and one of the authors (J.C.) the NDSEG Fellowship. The authors thank John Chervinsky, Yuan Lu, Tom Mates, and Jennifer Sage for experimental assistance, and Michael J. Aziz, Jonah Erlebacher, Paul Evans, William Paul, Frans Spaepen, and the members of the Mazur research group at Harvard University for helpful conversations. Two of the authors (C.W. and C.H.C.) made equal contributions to this work.

[1] T. H. Her, R. J. Finlay, C. Wu, S. Deliwala, and E. Mazur, Appl. Phys. Lett. **73**, 1673 (1998).
[2] T. H. Her, R. J. Finlay, C. Wu, and E. Mazur, Appl. Phys. A: Mater. Sci. Process. **70**, 383 (2000).
[3] A. J. Pedraza, J. D. Fowlkes, and D. H. Lowndes, Appl. Phys. Lett. **74**, 2322 (1999).
[4] E. S. Kolesar, V. M. Bright, and D. Sowders, Thin Solid Films **270**, 10 (1995).
[5] E. S. Kolesar, V. M. Bright, and D. M. Sowders, Thin Solid Films **290–291**, 23 (1996).
[6] H. G. Craighead, R. E. Howard, and D. M. Tennant, Appl. Phys. Lett. **37**, 653 (1980).
[7] J. I. Gittleman, E. K. Sichel, H. W. Lehmann, and R. Widmer, Appl. Phys. Lett. **35**, 742 (1979).
[8] J. Zhao, A. Wang, M. Green, and F. Ferrazza, Appl. Phys. Lett. **73**, 1991 (1998).
[9] J. P. Zheng, K. L. Jiao, W. P. Shen, W. A. Anderson, and H. S. Kwok, Appl. Phys. Lett. **61**, 459 (1992).
[10] E. Chen and S. Chou, Appl. Phys. Lett. **70**, 753 (1980).
[11] Our previous results (1, 2) indicate that microstructure formation is independent of the doping and the crystal plane of the substrate silicon.
[12] Another sample made and annealed under the same conditions shows an even greater drop in infrared absorptance than that shown in Fig. 3. Prior to annealing, we see a few percent variation in the infrared absorptance of samples made under the same conditions; we surmise that annealing enhances the underlying structural differences which produce these variations.
[13] L. C. Feldman, J. W. Mayer, and S. T. Picraux, *Materials Analysis by Ion Channeling* (Academic, New York, 1982).
[14] E. Janzen, R. Stedman, G. Grossmann, and H. G. Grimmeiss, Phys. Rev. B **29**, 1907 (1984).
[15] W. Fahrner and A. Goetzberger, Appl. Phys. Lett. **21**, 329 (1972).
[16] D. L. Camphausen, H. M. James, and R. J. Sladek, Phys. Rev. B **2**, 1899 (1970).
[17] C. H. Seager, P. M. Lenahan, K. L. Brower, and R. E. Mikawa, J. Appl. Phys. **58**, 2704 (1985).
[18] J. I. Pankove, *Optical Processes in Semiconductors* (Dover, New York, 1971), p. 9.
[19] M. J. Keevers and M. A. Green, Sol. Energy Mater. Sol. Cells **41/42**, 195 (1996).
[20] M. J. Keevers, F. W. Saris, G. C. Zhang, J. Zhao, and M. A. Green, *Proceedings of the 13th European Photovoltaic Solar Energy Conference and Exhibition* (1995) (unpublished).

SIONYX1403000045.0027

SAMSUNG EX. 1002 - 985/4148

Visible luminescence from silicon surfaces microstructured in air

C. Wu,[a] C. H. Crouch, L. Zhao,[b] and E. Mazur[c]
Department of Physics and Division of Engineering and Applied Sciences, Harvard University, Cambridge, Massachusetts 02138

(Received 7 March 2002; accepted for publication 10 July 2002)

We report visible luminescence from SiO_x formed by microstructuring silicon surfaces with femtosecond laser pulses in air. Incorporation of oxygen into the silicon lattice occurs only where the laser beam strikes the surface. Laser microstructuring therefore offers the possibility of writing submicrometer luminescent features without lithographic masks. The amount of oxygen incorporated into the silicon surface depends on the laser fluence; the peak wavelength of the primary luminescence band varies between 540 and 630 nm and depends on the number of laser shots. Upon annealing, the intensity of the primary luminescence band increases significantly without any change in the luminescence peak wavelength, suggesting that the luminescence comes from defects rather than quantum confinement. © *2002 American Institute of Physics.*
[DOI: 10.1063/1.1504868]

Optoelectronic devices play an important role in information and communication technologies. These devices typically use direct band gap semiconductors such as GaAs. Developing silicon-based optoelectronic devices would permit easy integration with silicon-based circuits. However, unmodified silicon is a poor light emitter due to its indirect band gap.[1] Many strategies have been developed to improve silicon's light emission efficiency, such as band gap engineering, quantum confinement in low-dimensional structures, or impurity-mediated luminescence.[2] While porous silicon[3] luminesces brightly, it is fragile and highly reactive, oxidizing spontaneously in air, and the luminescence is unstable and degrades with time.

A promising luminescent form of silicon is silicon-rich silica ($SiO_x, x<2$), which consists of silicon nanoclusters embedded in a SiO_2 matrix. The emission properties of SiO_x are similar to those of porous silicon, but unlike porous silicon, SiO_x is chemically and structurally stable.[4–6] Previously developed methods of producing SiO_x include sputtering, ion implantation, and various chemical vapor deposition techniques.[6] SiO_x has also been produced by pulsed-laser ablation[7] and by irradiation of silicon with nanosecond laser pulses.[8]

Here we report visible luminescence from SiO_x formed by microstructuring silicon with femtosecond laser pulses in air. Formation of SiO_x occurs only where the laser beam strikes the surface, making it possible to write submicrometer features without masks. At room temperature the luminescence is visible to the naked eye with less than 10 mW excitation at 488 nm. The peak wavelength of the primary luminescence band varies between 540 and 630 nm, depending on the average number of laser shots per unit area $\langle N \rangle$, which is determined by the size of the laser spot and the speed at which the surface is scanned beneath the laser beam.[9] We find that both the luminescence intensity and the amount of oxygen incorporated into the silicon increase with the laser fluence used for microstructuring. Upon annealing, the intensity of the primary luminescence band increases roughly fourfold without significant change in the peak wavelength, and an additional red luminescence band appears.

We produced microstructured, luminescent silicon by irradiating a silicon (111) surface in air with a train of 800 nm, 100 fs laser pulses at a 1 kHz repetition rate.[10,11] Luminescent silicon patches (2 mm×2 mm) are produced by translating the silicon chip at constant speed during irradiation in the plane perpendicular to the laser beam.[12] The height and morphology of the surface microstructures depend on the laser fluence and the number of laser shots.

Figure 1 shows scanning electron micrographs of surfaces microstructured with $\langle N \rangle = 1000$ and laser fluences of 2.8, 11, and 33 kJ/m^2. The height of the microstructures, and consequently the surface area of the sample, increases with increasing fluence. The microstructures formed with high fluence [Fig. 1(c)] resemble those made in SF_6 as previously reported,[10] but are blunt and less regular, and are covered

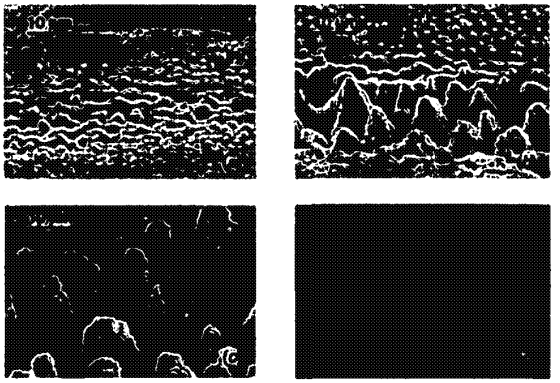


FIG. 1. Scanning electron micrographs of the surfaces made with $\langle N \rangle = 1000$ and laser fluences (a) 2.8 kJ/m^2, (b) 11 kJ/m^2, and (c) 33 kJ/m^2. (d) Dendritic microstructures 10–100 nm in size cover the microstructures.

[a]Present address: OFS, 791 Keyport-Holmdel Rd., Holmdel, NJ 07733.
[b]Present address: Laboratory of Materials Modification, Fudan University, Shanghai, China.
[c]Electronic mail: mazur@physics.harvard.edu

 © 2002 American Institute of Physics

SIONYX1403000045.0028

SAMSUNG EX. 1002 - 986/4148

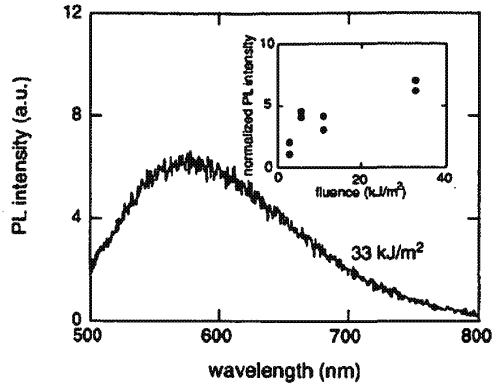


FIG. 2. PL spectrum from a sample made with $\langle N \rangle = 1000$ and laser fluence 33 kJ/m^2. Inset: Peak luminescence intensity from samples made with fluences 2.8, 5.5, 11, and 33 kJ/m^2, normalized to the intensity from the sample made with 2.8 kJ/m^2. Two measurements of intensity were made for each sample.

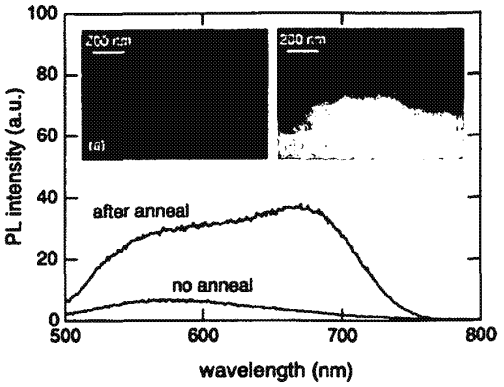


FIG. 3. PL spectrum of the sample made with 22 kJ/m^2 ($\langle N \rangle = 1000$) before and after annealing at 1300 K for 5 h. Vertical scale is the same as in Fig. 2(a). Inset: Scanning electron micrographs of surface of microstructures (a) before annealing and (b) after annealing.

with dendritic nanostructures roughly 10–100 nm in size [Fig. 1(d)].

We obtained photoluminescence (PL) spectra by exciting the samples with the 488 nm line of a 50 mW Ar^+-ion laser and measuring the luminescence from 500 to 800 nm with 0.6 nm resolution using a double monochromator and a thermoelectrically cooled GaAs photomultiplier tube. All measurements were performed with the sample at room temperature in air.

Figure 2 shows the PL spectrum from the sample made with 33 kJ/m^2 and $\langle N \rangle = 1000$. The peak wavelength, which is approximately 560 nm, is the same for three other samples made with the same $\langle N \rangle$ but different fluences. The peak luminescence intensity increases with increasing laser fluence, as shown in the inset.

To determine the origin of the PL, we analyzed the chemical composition of the microstructures by Rutherford backscattering spectrometry (RBS) with 2 MeV alpha particles. The RBS spectra[9] display a peak at 0.67 MeV, corresponding to oxygen impurities in the silicon. As the laser fluence used to structure the surfaces increases, this oxygen peak grows while the silicon peak at 1.1 eV shrinks, indicating that the amount of oxygen incorporated into the surface increases with increasing fluence. The growth in the oxygen peak may correspond to a higher atomic ratio of oxygen to silicon; it may also reflect the increased surface area of the microstructures formed with higher fluence. Simulations of the RBS spectra suggest that if the increased oxygen signal were entirely due to changes in composition, the atomic ratio of oxygen to silicon would range from roughly 0.1 (for the sample made with 2.8 kJ/m^2) to 0.4 (for the sample made with 33 kJ/m^2).[13]

The increase of both luminescence intensity and RBS oxygen signal with laser fluence suggests that the PL comes from oxidized silicon on the microstructure surfaces. Two additional results support this hypothesis: the luminescence disappears when oxidized silicon is removed from the sample surfaces by etching in hydrofluoric acid, and silicon surfaces microstructured in vacuum (10^{-4} Torr) rather than air do not luminesce.

Annealing the sample produces dramatic changes in the luminescence spectrum. Figure 3 shows the PL spectrum of a sample made with 22 kJ/m^2 ($\langle N \rangle = 1000$) before and after annealing for 5 h at 1300 K in vacuum ($p = 10^{-7}$ Torr). The annealing increases the intensity of the green luminescence peak by more than a factor of 4 without changing its peak wavelength, and a red peak centered at 620 nm appears. Electron microscopy reveals that most of the surface nanostructures disappear upon annealing (Fig. 3 inset). Figure 4 shows the luminescence of a sample made with 7.5 kJ/m^2 ($\langle N \rangle = 2000$), prior to annealing and after 0.5, 1, and 3 h of annealing at 1300 K in vacuum. The red luminescence peak, which appears upon annealing, both increases in intensity and shifts to longer wavelengths with increased annealing time.

Surface oxidation of silicon upon laser irradiation in an oxygen-rich atmosphere has been reported before.[14–17] The laser irradiation heats or melts the surface, causing diffusion of oxygen into the silicon substrate and enhancing oxidation. (The diffusion coefficient of oxygen in liquid silicon is six orders of magnitude greater than that in solid silicon.[18]) The greater oxygen content we observe for samples fabricated at

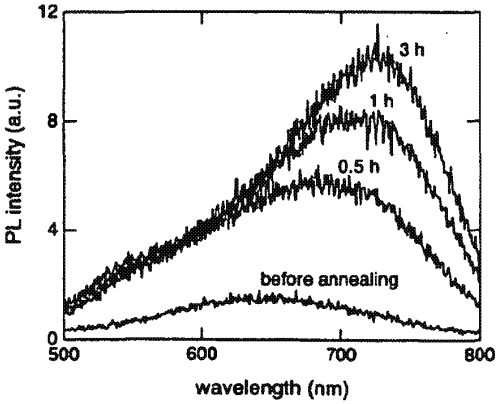


FIG. 4. PL spectrum of the sample made with 7.5 kJ/m^2 ($\langle N \rangle = 2000$), before annealing and after annealing for 0.5, 1, and 3 h at 1300 K. Vertical scale is the same as in Figs. 2(a) and 3.

SIONYX1403000045.0029

SAMSUNG EX. 1002 - 987/4148

higher fluence may therefore be attributable to a greater increase in the surface temperature, and therefore a larger melt depth upon laser irradiation.

Several recent reports of visible luminescence from SiO_x also describe two luminescence bands, one red and one green, at wavelengths similar to the bands we observe.[4–6,19] These reports attribute the green band to recombination of carriers at defects ("defect luminescence") and the red band to recombination of confined excitons in silicon nanoclusters ("quantum confinement").[4–6,20] The behavior of the luminescence upon annealing is one way to distinguish these two mechanisms. Annealing increases the size of Si clusters within the SiO_2 matrix by diffusion of Si,[21,22] a process known as Ostwald ripening.[6,19] Luminescence resulting from quantum confinement should therefore show a wavelength shift to lower energies upon annealing, as the cluster size increases and the excitonic energy decreases. By contrast, for defect luminescence, annealing may eliminate radiative or nonradiative defect sites (or both, potentially at different rates), and thus may alter the intensity, but should not alter the peak wavelength substantially.

We observe an increase in both green luminescence intensity (Fig. 2) and oxygen content as the laser fluence used to structure the samples increases, indicating that oxygen-related defects are the most likely source of this luminescence. The peak wavelength of the green luminescence band remains unchanged upon annealing, although the intensity increases, providing further evidence that the green luminescence arises from defects. As annealing both increases the luminescence intensity and eliminates most of the dendritic nanostructures, this indicates that the visible dendritic nanostructures are not responsible for the green luminescence. Finally, secondary ion mass spectroscopy indicates that nitrogen as well as oxygen is present in our material, although the nitrogen is present in much lower concentrations (roughly 0.01%–0.1%). This is consistent with a report that luminescence from thin films containing amorphous silicon-rich oxynitride (SiO_xN_y:H) shows an increase in green luminescence intensity with high annealing temperatures;[23] those authors suggest that nitrogen stabilizes the defect luminescence.

The appearance of the red luminescence with annealing, and its redshift with increased annealing time, suggest it is most likely caused by quantum confinement. Again, the surface nanostructures do not appear to contribute to the luminescence, as they disappear with annealing while the luminescence increases in intensity. Rather, we expect the quantum confinement responsible for the red luminescence is in silicon nanoclusters that form within the surface oxide. The increased luminescence intensity with annealing time must come from reducing the number of nonradiative recombination sites or increasing the efficiency of radiation from embedded nanoclusters, rather than increasing the surface area, as annealing reduces the surface area.

In conclusion, we observe photoluminescence from SiO_x formed by laser-structuring silicon surfaces with femtosecond laser pulses in air. The luminescence shows two bands: a green band which is most likely associated with defects and a red band that most likely comes from quantum confinement in silicon nanocrystals embedded in the silica matrix. The luminescence intensity increases with increased oxygen content, unlike the luminescence from porous silicon, which degrades upon oxidation. Laser production of luminescent SiO_x offers the possibility of precise, localized SiO_x production on silicon chips without the use of masks or multistep processing; other methods of producing luminescent SiO_x lack this versatility.

This work was supported by the U.S. Army Research Office (contract No. DAAD 19-99-1-0009) and by the NSF through the Harvard MRSEC (Grant No. NSF/DMR-98-09363). One of the authors (C.W.) acknowledges a Cusanuswerk fellowship. We thank K. Smith of UniSil for wafers, and J. Chen, J. Chervinsky, Y. Lu, T. Mates, D. Pang, and J. Sage for experimental assistance.

[1] R. T. Collins, P. M. Fauchet, and M. A. Tischler, Phys. Today **50**, 24 (1997).
[2] D. J. Lockwood, in *Light Emission in Silicon: From Physics to Devices, Semiconductors and Semimetals*, edited by D. J. Lockwood (Academic, New York, 1998), Vol. 49.
[3] L. T. Canham, Appl. Phys. Lett. **57**, 1046 (1990).
[4] T. Shimizu-Iwayama, S. Nakao, and K. Saitoh, Appl. Phys. Lett. **65**, 1814 (1994).
[5] G. Ghislotti, B. Nielsen, P. Asoda-Kumar, K. G. Lyn, A. Gambhir, L. F. Di Auro, and C. E. Bottani, J. Appl. Phys. **79**, 8660 (1996).
[6] A. J. Kenyon, P. F. Trwoga, C. W. Pitt, and G. Rehm, J. Appl. Phys. **79**, 9291 (1996).
[7] J. R. Heath, Y. Liu, S. C. O'Brien, Q.-L. Zhang, R. F. Curl, F. K. Tittel, and R. E. Smalley, J. Chem. Phys. **83**, 5520 (1985).
[8] D. Dimova-Malinovska, M. Tzolov, N. Malinowski, and T. Marinova, Appl. Surf. Sci. **457**, 96 (1996).
[9] C. Wu, Ph.D. thesis, Harvard University, 2001.
[10] T.-H. Her, R. J. Finlay, C. Wu, S. Deliwala, and E. Mazur, Appl. Phys. Lett. **73**, 1673 (1998).
[11] T.-H. Her, R. J. Finlay, C. Wu, and E. Mazur, Appl. Phys. A: Mater. Sci. Process. **70**, 383 (2000).
[12] C. Wu, C. H. Crouch, L. Zhao, J. E. Carey, R. Younkin, J. A. Levinson, E. Mazur, R. M. Farrell, P. Gothoskar, and A. Karger, Appl. Phys. Lett. **78**, 1850 (2001).
[13] Simulations were performed with a program called RUMP (www.genplot.com); the microstructured surfaces are treated as a set of 300-nm-thick layers of material of uniform composition, and the oxygen concentration is assumed to decrease with increasing depth.
[14] I. W. Boyd, Mater. Res. Soc. Symp. Proc. **105**, 23 (1988).
[15] E. Fogarassy, C. W. White, A. Slaoui, C. Fuchs, P. Siffert, and S. J. Pennycook, Appl. Phys. Lett. **53**, 1720 (1988).
[16] Y. S. Liu, S. W. Chiang, and F. Bacon, Appl. Phys. Lett. **38**, 1005 (1981).
[17] A. Cros, F. Salvan, and J. Derrien, Appl. Phys. A: Mater. Sci. Process. **28**, 241 (1982).
[18] K. Hoh, H. Koyama, K. Uda, and Y. Miura, Jpn. J. Appl. Phys. **19**, L375 (1980).
[19] T. Shimizu-Iwayama, K. Fujita, S. Nakao, K. Saitoh, T. Fujita, N. Itoh, J. Appl. Phys. **75**, 7779 (1994).
[20] Others report observing three luminescence bands in SiO_x films of different stoichiometries (prepared with chemical vapor deposition), and attribute all three to luminescence from different types of defects: M. Zhu, Y. Han, R. B. Wehrspohn, C. Godet, R. Etemadi, and D. Ballutaud, J. Appl. Phys. **83**, 5386 (1998).
[21] L. A. Nesbit, Appl. Phys. Lett. **46**, 38 (1985).
[22] F. Rochet, G. Dufar, H. Roulet, B. Pelloie, J. Perriere, E. Fogarassy, A. Slaoui, and M. Froment, Phys. Rev. B **37**, 6468 (1988).
[23] B. H. Augustine, E. A. Irene, Y. J. He, K. J. Price, L. E. McNeil, K. N. Christensen, and D. M. Maher, J. Appl. Phys. **78**, 4020 (1995).

SIONYX1403000045.0030

SAMSUNG EX. 1002 - 988/4148

BLACK SILICON

Claudia Wu
Catherine Crouch
Tsing-Hua Her
Eric Mazur

Harvard University

UPS '99
Taipei, Taiwan

SIONYX1403000045.0031

SAMSUNG EX. 1002 - 989/4148

Outline

- Black silicon: what is it?

SAMSUNG EX. 1002 - 990/4148

Outline

- Black silicon: what is it?
- Conditions for formation

SAMSUNG EX. 1002 - 991/4148

Outline

- Black silicon: what is it?
- Conditions for formation
- Mechanism

SAMSUNG EX. 1002 - 992/4148

Outline

- Black silicon: what is it?
- Conditions for formation
- Mechanism
- Light absorption

SAMSUNG EX. 1002 - 993/4148

Black Silicon: What is it?

SAMSUNG EX. 1002 - 994/4148

Black Silicon: what is it?

irradiate with 100 fs 10 kJ/m^2 laser pulses

SAMSUNG EX. 1002 - 995/4148

Black Silicon: What is it?

SAMSUNG EX. 1002 - 996/4148

Black Silicon: What is it?

SAMSUNG EX. 1002 - 997/4148

Conditions for formation

Effects of Gas

SF_6, Cl_2 → sharp spikes

N_2, He, Ar, air, vacuum → blunt structures

SIONYX1403000045.0040

SAMSUNG EX. 1002 - 998/4148

SAMSUNG EX. 1002 - 999/4148

Conditions for formation

Conditions for formation

pulse duration dependence

SAMSUNG EX. 1002 - 1001/4148

Conditions for formation

s-polarized

p-polarized

circularly polarized

SAMSUNG EX. 1002 - 1002/4148

0000
15mm 10kV
20µm
X2000
#3548
512 X 480

X2000 20um 10kV 15mm
#5548 512 X 480
0001

SAMSUNG EX. 1002 - 1005/4148

SAMSUNG EX. 1002 - 1006/4148

SAMSUNG EX. 1002 - 1007/4148

SIONYX1403000045.0050

SAMSUNG EX. 1002 - 1009/4148

SAMSUNG EX. 1002 - 1010/4148

SAMSUNG EX. 1002 - 1011/4148

SAMSUNG EX. 1002 - 1012/4148

SIONYX1403000045.0055